National Library of Canada
Acquisitions and Bibliographic Services Branch
395 Wellington Street
Ottawa, Ontario
K1A 0N4

Bibliothèque nationale du Canada
Direction des acquisitions et des services bibliographiques
395, rue Wellington
Ottawa (Ontario)
K1A 0N4

Your file Votre référence

Our file Notre référence

NOTICE

The quality of this microform is heavily dependent upon the quality of the original thesis submitted for microfilming. Every effort has been made to ensure the highest quality of reproduction possible.

If pages are missing, contact the university which granted the degree.

Some pages may have indistinct print especially if the original pages were typed with a poor typewriter ribbon or if the university sent us an inferior photocopy.

Reproduction in full or in part of this microform is governed by the Canadian Copyright Act, R.S.C. 1970, c. C-30, and subsequent amendments.

AVIS

La qualité de cette microforme dépend grandement de la qualité de la thèse soumise au microfilmage. Nous avons tout fait pour assurer une qualité supérieure de reproduction.

S'il manque des pages, veuillez communiquer avec l'université qui a conféré le grade.

La qualité d'impression de certaines pages peut laisser à désirer, surtout si les pages originales ont été dactylographiées à l'aide d'un ruban usé ou si l'université nous a fait parvenir une photocopie de qualité inférieure.

La reproduction, même partielle, de cette microforme est soumise à la Loi canadienne sur le droit d'auteur, SRC 1970, c. C-30, et ses amendements subséquents.

Canadä

UNIVERSITY OF ALBERTA

LIQUEFACTION AND POST-EARTHQUAKE DEFORMATION ANALYSIS

By

WEI-HUA GU ©

A thesis submitted to the Faculty of Graduate Studies and Research in partial fufillment of the requirements for the degree of Doctor of Philosophy.

DEPARTMENT OF CIVIL ENGINEERING

Edmonton, Alberta

FALL 1992

National Library
of Canada

Acquisitions and
Bibliographic Services Branch

395 Wellington Street
Ottawa, Ontario
K1A 0N4

Bibliothèque nationale
du Canada

Direction des acquisitions et
des services bibliographiques

395, rue Wellington
Ottawa (Ontario)
K1A 0N4

Your file Votre référence

Our file Notre référence

The author has granted an irrevocable non-exclusive licence allowing the National Library of Canada to reproduce, loan, distribute or sell copies of his/her thesis by any means and in any form or format, making this thesis available to interested persons.

L'auteur a accordé une licence irrévocable et non exclusive permettant à la Bibliothèque nationale du Canada de reproduire, prêter, distribuer ou vendre des copies de sa thèse de quelque manière et sous quelque forme que ce soit pour mettre des exemplaires de cette thèse à la disposition des personnes intéressées.

The author retains ownership of the copyright in his/her thesis. Neither the thesis nor substantial extracts from it may be printed or otherwise reproduced without his/her permission.

L'auteur conserve la propriété du droit d'auteur qui protège sa thèse. Ni la thèse ni des extraits substantiels de celle-ci ne doivent être imprimés ou autrement reproduits sans son autorisation.

ISBN 0-315-77425-8

Canada

UNIVERSITY OF ALBERTA

RELEASE FORM

NAME OF AUTHOR: WEI-HUA GU

TITLE OF THESIS: LIQUEFACTION AND POST-EARTHQUAKE DEFORMATION ANALYSIS

DEGREE: DOCTOR OF PHILOSOPHY

YEAR THIS DEGREE GRANTED: 1992

Permission is hereby granted to the University of Alberta Library to reproduce single copies of this thesis and to lend or sell such copies for private, scholarly or scientific research purposes only.

The author reserves all other publication and other rights in association with the copyright in the thesis, and except as hereinbefore provided neither the thesis nor any substantial portion thereof may be printed or otherwise reproduced in any material from whatever without the author's prior written permission.

(SIGNED) Gu Wei

PERMANENT ADDRESS:
#5 11504 - 132ST
Edmonton Alberta.
T5M 1G3

DATED July 23/92

UNIVERSITY OF ALBERTA

FACULTY OF GRADUATE STUDIES AND RESEARCH

The undersigned certify that they have read, and recommend to the Faculty of Graduate Studies and Research for acceptance, a thesis entitled LIQUEFACTION AND POST-EARTHQUAKE DEFORMATION ANALYSIS submitted by WEI-HUA GU in partial fulfillment of the requirements for the degree of DOCTOR OF PHILOSOPHY.

Dr. N. R. Morgenstern

PK Robertson
Dr. P. K. Robertson

DC Sego
Dr. D. C. Sego

T. Hrudey
Dr. T. M. Hrudey

AW Lipsett
Dr. A. W. Lipsett

W. D. Liam Finn
Prof. W. D. Liam Finn
(External Examiner)

June 08, 1992

To my beloved mother

ABSTRACT

Liquefaction failure is usually related to earthquake or dynamic loading even though it may occur under static condition. It is a complicated process involving dynamic loading, excess pore water pressure, strain softening of materials, stress redistribution and reconsolidation. Therefore, any assessment of the stability of an earth structure with liquefiable materials must necessarily include consideration of deformations.

The deformation of an earth structure during or following an earthquake may be composed of three parts: the deformation caused by earthquake loading, the deformation caused by stress redistribution and the deformation caused by reconsolidation. The deformations caused directly by the earthquake loading are usually small and of short duration and somehow can be considered as the triggering conditions for subsequent large deformations or flow failure. The large deformations or flow failure are caused by stress redistribution and reconsolidation. The deformations caused by stress redistribution and reconsolidation are the subject of the post-earthquake deformation process studied in this research.

The stress redistribution during or following an earthquake describes a two dimensional or even three dimensional process in terms of a progressive failure mechanism. The stress redistribution is caused by the strain softening behaviour of liquefied materials. When the liquefied materials undergo strain softening from peak strength to residual strength, they will

release unbalanced loads that cause stress redistribution within the earth structure. The deformations developed during stress redistribution can be large enough to cause the failure of an earth structure. This is the main reason for the undrained flow failure of dams, slopes and foundations and can occur in a short period from a few seconds to a few minutes after earthquake shaking.

The deformation during reconsolidation is associated with the dissipation of excess pore water pressures. It is the main reason for the drained failure of earth structures and may occur in a period from a few hours to a few days after the earthquake. Excess pore water pressures may be generated or accumulated during earthquake shaking, stress redistribution and pore water pressure redistribution. As a result, further liquefaction, and hence further stress redistribution may occur due to dissipation of excess pore water pressures. Undrained flow failure may also occur after some time of dissipation of excess pore water pressures.

Post-earthquake deformation analysis is an essential process in the safety evaluation of earth structures composed of liquefiable materials, because stress redistribution and reconsolidation cannot be avoided in these structures. Zones that may have liquefied during the earthquake may expand during post-earthquake deformation.

The results obtained in this research show that the finite element method is a powerful tool to address this problem. To simulate the undrained behaviour of liquefied material during stress redistribution, an undrained boundary surface model is developed and implemented in a finite element program based on the theory of critical state boundary surface, the concepts of steady state deformation and collapse surface, a hyperbolic strain softening relationship and the behaviour of liquefiable soils.

To investigate the effects of reconsolidation during dissipation of excess pore water pressures, a finite element simulation of Biot's theory has been adopted in this research.

The capability of the methods have been evaluated by back analyses of two case histories; the post-earthquake deformation of the Lower San Fernando Dam during the 1971 earthquake and the post-earthquake deformation of the Wildlife Site during the 1987 earthquake.

In the post-earthquake deformation analysis of the Lower San Fernando Dam, the progressive failure of the upstream shell after the earthquake has been simulated by observing the expansion of liquefied zone and yielding zone during stress redistribution. The results show that the initial liquefied zone due to the earthquake which triggers failure of an earth structure may be much smaller than previously predicted because of the expansion of the liquefied zone during stress redistribution.

The post-earthquake deformation analysis of the Wildlife Site reveals that the delayed behaviour of the pore water pressures observed during and following the earthquake may be due to stress redistribution and reconsolidation. The lateral spreading of the ground surface at the Wildlife Site is mainly due to stress redistribution. Additional local liquefaction during dissipation of excess pore water pressures has been observed in this analysis.

ACKNOWLEDGEMENT

The author wishes to express his gratitude to his supervisor Dr. N. R. Morgenstern for his guidance in this arduous subject. His supports, ideas, enthusiasm and valuable discussions throughout the course of this research in making it a success are very much appreciate. Without his supports on this subject, this research would not have been possible.

The author would like to express his thanks to Dr. P. K. Robertson for his valuable discussions, suggestions and guidance during the analyses. His time, ideas and enthusiasm on the research are very much appreciate. Many thanks to Dr. D. H. Chan for his valuable discussions and suggestions on the numerical analyses. His kind help and permission in using and modifying his programs are very much appreciate. The computer facilities provided by the University of Alberta in making the numerical work possible is acknowledged. The author would like to acknowledge the financial support of the Natural Science and Engineering Research Council of Canada (NSERC).

The author wishes to thank his wife Yan Liu and son Lei Gu for their supports and understanding throughout the five years program. The author also wishes to express his thanks to his father, brothers and sisters for their encouragement and support for his study abroad. During his five years' study, they have

borne whole duties to look after his mother in hospital for which he fell very much in debts.

Finally, the author wishes to dedicate this thesis to his beloved mother, Liu Xiu-ying, for her encouragement throughout his life and study. Her wish and love have provided him a power in overcoming many obstacles in his studies.

Table of Contents

Chapter Page

1. INTRODUCTION 1
  1.1. Outline of Problem 1
  1.2. Delayed Phenomenon in Liquefaction Effects. 5
  1.3. Deformation Analysis and Liquefaction Failure. 10
  1.4. Purpose of The Research and Scope of The Thesis. 16
2. BEHAVIOUR OF LIQUEFIABLE SOILS AND A MODIFIED CRITICAL STATE BOUNDARY SURFACE 19
  2.1. Liquefaction of Soils.. 19
  2.2. Steady State Line 24
  2.3. Strain Softening Behaviour 26
  2.4. Triggering Condition For Strain Softening 30
    2.4.1. Effective stress path method .30
    2.4.2. The strain control method. 36
  2.5. Phase Transformation Line and Stress Mobility Behaviour. 39
  2.6. Summary of Behaviours of Liquefiable Soils 41
3. A SIMPLIFIED ELASTO-PLASTIC MODEL FOR LIQUEFACTION DEFORMATION ANALYSIS 45
  3.1. State Boundary Surface For Liquefiable Soils. 45
  3.2. Simplified Three Zones and Shearing Yielding Surface Under Undrained Conditions 50

3.3. Hyperbolic Strain Softening Model For Liquefiable Soils. 59

4. POST-EARTHQUAKE DEFORMATION DUE TO STRESS RE-DISTRIBUTION IN EARTH STRUCTURES. 68

4.1. Strain Softening Behaviour of Liquefiable Soils and Stress Re-distribution in Earth Structures. 68

4.2. The Yielding Surface For Strain Softening. 70

4.3. The Unbalanced Load Caused by Contracting of Yielding Surface During Strain Softening. 75

4.4. The Governing Equation for Stress Re-distribution Analysis. 77

4.5. Iteration Scheme For Stress Re-distribution Analysis 79

5. POST-EARTHQUAKE DEFORMATION DUE TO EXCESS PORE WATER PRESSURE. 90

5.1. The Mechanism of Re-consolidation Induced by Excess Pore Pressure. 90

5.2. Flow Continuity Equation for Re-consolidation with Excess Pore Pressure Development. 98

5.3. Pore Water Pressure Caused by Undrained Cyclic Loadings. 102

5.4. Pore Water Pressure Caused by Undrained Monotonic Loadings. 105

5.4.1. Pore water parameters A and B 105

5.4.2. Effective stress path model for liquefiable soils 110

5.5. Unbalance Load Caused by the Excess Pore Pressure. 118

5.6. Iteration Scheme for Excess Pore Pressure under Fully Undrained Condition. 120

6 STABILITY EVALUATION BY FINITE ELEMENT DEFORMATION ANALYSIS 124

6.1. Deformation Analysis and Stability Evaluation. 124

6.2. Contours of Yield Ratio and Safety Evaluation of Slopes. 126

6.3. Definition of Yield Ratio. 129

6.4. Displacement Field from Finite Element Analysis. 134

6.5. Slip Surface Determined by Finite Element Results. 137

6.6. The Factor of Safety FS Evaluation by The Finite Element Results 142

7. POST-EARTHQUAKE DEFORMATION ANALYSIS OF THE LOWER SAN FERNANDO DAM. 145

7.1. Review of The Failure Behaviour of The Lower San Fernando Dam. 145

7.2. The Properties of Materials in The Lower San Fernando Dam 150

7.3. Initial Effective Stress Analysis. 160

7.4. The Post-earthquake Deformation Analysis. 169

7.4.1. Progressive Failure of The Lower San Fernando Dam 172

7.4.2. Stability and Steady State Strength 174

7.5. Discussions on Liquefaction Instability of Earth Structures. 175

8. POST-EARTHQUAKE DEFORMATION ANALYSIS OF THE WILDLIFE SITE, IMPERIAL VALLEY, CALIFORNIA. 204
8.1. Review of The Liquefaction Behaviour of The Wildlife Site. 204
8.2. Characteristics of Sediments and Properties of Materials. 211
8.3. Initial Effective Stress Analysis. 213
8.4. Post-earthquake Deformation Due To Stress Re-distributions. 214
8.5. Post-earthquake Deformation Due to Re-consolidation. 221
8.6. Discussion on the Liquefaction Behavior of Wildlife Site During 1987 Superstition Hills Earthquake. 224
9. CONCLUSIONS. 258
9.1. Conclusions. 258
9.2. Recommendations. 264
BIBLIOGRAGHY 267
APPENDIX 275
A. Finite Element Formulation For Post-earthquake Deformation Analysis. .275
B. Finite Element Solution For Un-stable Structures 294
C Simplified Analysis Scheme 304

List of Tables

Table Page

1.2.1. Delayed Phenomenon in Liquefaction Effects . . . . .8 to 9

1.3.1. Pseudo-static Analysis of Dams With Slope Failure During Earthquake(after Seed, 1976) .12

5.4.1. The Pore Pressure Parameters For Liquefiable Soils 116

7.2.1. Parameters For Nonlinear Static Stress Analysis Given By Lee and Seed et.al(1975) 153

7.2.2. Steady State Strength of Hydraulic Fill in The Lower San Fernando Dam.(Psf) 155

7.3.1. Parameters For Initial Static Stress Analysis 162

7.4.1. Parameters For Post-earthquake Deformation Analysis 170

7.4.2. Steady State Strength Su kPa(psf) in Analysis. 171

8.3.1. Parameters For Deformation Analysis of Wildlife Site 228

8.4.1. Normalized Pore Water Pressures During Post-earthquake Deformation Analysis. 229

List of Figures

Figure Page

2.1.1 Zero Effective Stress Definition and Its Limitation 20

2.1.2. Flow Structure and Loss in Shear Strength 23

2.2.1. Steady State Line For Liquefiable Soils.. 25

2.3.1. Typical Liquefaction Behaviour 28

2.4.1. Collapse Surface. 32

2.4.2. Behaviour of Liquefiable Soils Suggested By McRoberts Sladen (1990) 33

2.4.3. Strain Control Triggering Condition in Poulos' Procedure(1985). 37

2.6.1. Idealized Soil Behaviour Under Undrained Monotonic Loading 42

2.6.2. Idealized Soil Behaviour Under Undrained Cyclic Loading 44

3.1.1. State Boundary Surface Defined By Roscoe et.al(1958) 46

3.1.2. State Boundary Surface For Liquefiable Soils. 49

3.2.1. Effective Stress Paths On an Undrained Plane. 51

3.2.2. Three Zones On an Undrained Plane For Liquefiable Soils. 52

3.2.3. Stress-strain Behaviour in Three Zones. .53

3.2.4. The Two Yield Surface Model Given By Provest(1975) 55

3.2.5. The Shear Yield Surface For Liquefiable Soils 58

3.3.1. The Hyperbolic Strain Softening Model Given By Chan and Morgenstern(1986) 65

3.3.2. Post-peak Behaviour in The Hyperbolic Strain Softening Model (after Chan, 1986) 66
3.3.3. The Hyperbolic Strain Softening Model For Liquefiable Soils 67
4.2.1. Perpendicular Projection Method For Contraction of Yield Surface 73
4.2.2. Pore Water Pressure During Contraction of Yield Surface For Liquefiable Soils 74
4.5.1. Newton-Raphson Method 84
4.5.2. Modified Newton-Raphson Method 85
4.5.3. Eular Forward Method (after Chan, 1986) 86
4.5.4. Improved Eular Forward Method (after Chan, 1986) 87
4.5.5. Total Loading Step Scheme 88
4.5.6. Incremental Iteration Loading Scheme 89
5.1.1. Mechanism of Excess Pore Pressure and Re-consolidation . . . . .92 to 93
5.1.2. Mechanism of Excess Pore Pressure 94
5.2.1. Mechanism of Re-consolidation Associated With Pore Water Pressure Generation 99
5.4.1. Factors Influencing Parameter A 109
5.4.2. The Effective Stress Paths Under Undrained Condition 111
5.4.3. The Numerical Effective Stress Path Model for Liquefiable Soils 112
5.4.4. Pore Water Pressure in Zone 2 117
5.4.5. Pore Water Pressure in Zone 3 117
5.6.1. Effective Stress Scheme During Iteration of Unbalanced Load 122

5.6.2. Total Stress Scheme During Iteration of Unbalanced Load 123
6.2.1. Contours of Yield Ratio and Stability Evaluation 128
6.3.2. Yield Ratio For Elasto-plastic Models 130
6.3.3. The Yield Ratio For Liquefiable Soils 133
6.4.1. Stability Evaluation By Displacement Field in Finite Element Analysis 136
6.5.1. The Kinematically Possible Slip Surface 139
6.5.2. Failure Surface and Kinematically Possible Slip Surface 140
6.6.1. An Example of The Two Steps in Safety Evaluation By the Results of Finite Element Analysis 144
7.1.1. Liquefaction Failure of The Lower San Fernando Dam (after Seed, 1979) 146
7.1.2. Liquefaction Evaluation By Seed et.al(1979) 148
7.1.3. Stability Evaluation By Seed et.al (1979) 149
7.2.1. Material Distribution of The Lower San Fernando Dam 151
7.2.2. Steady State Strengths Determined By Laboratory Tests or Field Conditions (after Seed, 1989) 157
7.2.3. Collapse Surface For RPI Tests' Results 159
7.3.1. Finite Elements of The Lower San Fernando Dam 163
7.3.2(a). Contours of Initial Effective Stress σ_x 164
7.3.2(b). Contours of Initial Effective Stress σ_y 165
7.3.2(c). Contours of Initial Effective Stress τ_{xy} 166
7.3.3. Contours of Initial Seepage Pore Water Pressure 167
7.3.4. Initial Stress State of The Lower San Fernando Dam 168

7.4.1. Contours of Initial Yield Ratio 179

7.4.2. Contours of Yield Ratio When U/Um=0.1-0.8 180

7.4.3(a). Contours of Yield Ratio When Unbalanced Load
Iteration = 0 181

7.4.3(b). Contours of Yield Ratio When Unbalanced Load
Iteration = 5 182

7.4.3(c). Contours of Yield Ratio When Unbalanced Load
Iteration = 7 183

7.4.3(d). Contours of Yield Ratio When Unbalanced Load
Iteration = 10 184

7.4.3(e). Contours of Yield Ratio When Unbalanced Load
Iteration = 20 185

7.4.3(f). Contours of Yield Ratio When Unbalanced Load
Iteration = 100 186

7.4.4(a). Displacement Field When Unbalanced Load
Iteration = 20 187

7.4.4(b). Displacement Field When Unbalanced Load
Iteration = 100 188

7.4.5(a). Contours of Effective Stress σ_x after
Iteration of Unbalanced Load 189

7.4.5(b). Contours of Effective Stress σ_y .after
Iteration of Unbalanced Load 190

7.4.5(c). Contours of Effective Stress τ_{xy} after
Iteration of Unbalanced Load 191

7.4.6. The Effective Stress Paths For The Elements Liquefied
Directly By The Excess Pore Water Pressure Generated
By The Earthquake 192

7.4.7. The Effective Stress Paths For The Elements Liquefied By The Stress Re-distribution 193

7.4.8. Factor of Safety During Iteration of Unbalanced Load 194

7.4.9. Strain Softening Behaviour For The Elements Liquefied Directly By the Earthquake 195

7.4.10. Strain Softening Behaviour For The Elements Liquefied By The Stress Re-distribution 196

7.4.11(a). Contours of Yield Ratio When Su=21 kPa(441 psf) 197

7.4.11(b). Contours of Yield Ratio When Su=28 kPa(580 psf) 198

7.4.11(c). Contours of Yield Ratio When Su=33 kPa(690 psf) 199

7.4.11(d). Contours of Yield Ratio When Su=36 kPa(745 psf) 200

7.4.11(e). Contours of Yield Ratio When Su=38 kPa(800 psf) 201

7.4.12. Factor of Safety vs Steady State Strength 202

7.4.13. Horizontal Displacement vs Steady State Strength 203

8.1.1. Cross Section of Wildlife Site 207

8.1.2. Normalized Pore Water Pressures at Wildlife Site 208

8.1.3. Displacements on Ground Surface of The Wildlife Site 209

8.1.4. Sand Boils Observed at Wildlife Site During 1987 Earthquake 210

8.3.1. Finite Elements and Material Distribution For Wildlife Site 230

8.3.2. Larger Finite Element Mesh For Wildlife Site 231

8.3.3. Contours of Initial Effective Stress σ_x 232

8.3.4. Contours of Initial Effective Stress σ_y 233

8.3.5. Contours of Initial Effective Stress τ_{xy} 234

8.3.6. Contours of Initial Yield Ratio 235

8.4.1. Delayed Behaviour Due To Stress Re-distribution 236

8.4.2. Displacements After Stress Re-distribution For Group 1 Steady State Strenght 237

8.4.3. Displacements After Stress Re-distribution For Group 2 Steady State Strenght 238

8.4.4. Distribution of Movement on Ground Surface 239

8.4.5. E-W Components of Displacements on Ground Surface 240

8.4.6(a). Contours of Yield Ratio After Stress Re-distribution When Using Group 1 Steady State Strength 241

8.4.6(b). Contours of Yield Ratio After Stress Re-distribution When Using Group 2 Steady State Strength 242

8.4.7. Contours of Effective Stress σ_x After Stress Re-distribution 243

8.4.8. Contours of Effective Stress σ_y After Stress Re-distribution 244

8.4.9. Contours of Effective Stress τ_{xy} After Stress Re-distribution 245

8.4.10. Displacement Field By Using Larger Finite Element Mesh 246

8.4.11. Distribution of Displacement on Ground Surface 247

8.4.12. Contours of Yield Ratio After Stress Re-distribution

For Larger Finite Element Mesh 248
8.5.1. Displacement Field After Re-consolidation 249
8.5.2. Settlements of Ground Surface During Re-consolidation 250
8.5.3. Relationship Between Settlements and Pore Pressures in Underneath Soils 251
8.5.4. Pore Water Pressures During Re-consolidation 252
8.5.5. Contours of Effective Stress σ_x After Re-consolidation. 253
8.5.6. Contours of Effective Stress σ_y After Re-consolidation 254
8.5.7. Contours of Effective Stress τ_{xy} After Re-consolidation 255
8.5.8. Effective Stress Paths For Soils in Liquefied Zones 256
8.5.9. Effective Stress Paths For Soils in Lower Pore Pressure Pockets 257
B-1. Two Schemes For Limit Equilibrium Solution 297
B-2. Load Transfer Between Two Materials 298
B-3. A Typical Finite Element Displacement Solution For an Un-stable Structure 299
B-4. A Typical Displacement Distribution For a Divergent Result 300
B-5. Errors During Iteration of Unbalanced Loads For a Convergent Solution 301
B-6. Errors During Iteration of Unbalanced Loads For an Un-stable Solution 302
B-7. Errors During Iteration of Unbalanced Loads For a

Divergent Solution 303
C-1. Outline of Liquefaction Failure Analysis 304
C-2. Simplified Analysis Scheme .... .308

1. INTRODUCTION

1.1. Outline of Problem.

Liquefaction failures of earth structures have caused extensive concerns in earthquake engineering since the 1964 Niigata earthquake in Japan and the 1971 San Fernando earthquake in USA. In the 1964 Niigata earthquake, settlements, tilting or uplift of all kinds of structures occurred gradually due to liquefaction following the earthquake. In the 1971 San Fernando earthquake, the upstream shell of the Lower San Fernando Dam failed some 30 seconds after the main shaking. Several large blocks of soil floating on the liquefied materials moved about 46 meters into the reservoir.

In the following years, much research work and laboratory tests were concentrated on the liquefaction behaviour of soil related directly to dynamic loading. This work was usually based on the definition of liquefaction introduced by Seed et al (1966, 1975) in which the initial liquefaction was defined as a condition of zero effective stress or a certain magnitude of cyclic axial strain.

Castro (1975), based on the "critical void ratio" concept defined by Casagrande (1936) and the supportive results of undrained monotonic loading tests on saturated sands, proposed that liquefaction be considered a phenomenon wherein the shear resistance of a mass of soil decreases when subjected to monotonic, cyclic or dynamic loading at constant volume. The mass undergoes very large unidirectional shear strains, it appears to flow, until the shear stresses are as low as or lower than the reduced shear resistance. The reduced shear strength was called "steady state strength" by Castro (1975) and steady state deformation was defined more precisely by Poulos (1981).

In this definition, the authors pointed out a very important fact that a residual strength or shear resistance still exists in the liquefied soils and the liquefaction failure only occurs when the static driving shear stress is higher than the residual shear strength.

A similar result was also observed in saturated clay soil by Sangrey et al (1969). They reported that a critical level of repeated stress existed. Below this critical level, a state of nonfailure equilibrium was reached while above the critical level of repeated stress, failure occurred.

The effects of static shear stress on liquefaction of soils were also noticed by Seed et al (1969) and Finn et al (1976) by observing the results of undrained cyclic tests on anisotropically consolidated samples. They have shown that stress reversal is required if a condition of initial liquefaction, i.e. effective stress equal to zero, is to be achieved, and without such stress reversal, the pore water pressures stabilize at values that depend on the anisotropic consolidation ratio and the magnitude of the cyclic shear stress ratio.

Castro (1975) insisted that at least two clearly different phenomena should be distinguished. They were referred as "liquefaction" and "cyclic mobility" respectively.

Liquefaction occurs by generation of excess pore water pressures when the static driving shear stress is higher than the steady state strength and cyclic mobility occurs by generation of excess pore water pressures when the static driving shear stress is lower than the steady state strength.

Sladen et al (1985) suggested that there is a "collapse surface" that defines the onset of collapse for contractant sands in undrained loading. They showed that when contractant saturated sands were loaded in undrained triaxial tests, they reached a maximum shear stress before strain softening to steady state.

The monotonic undrained triaxial tests on very loose to medium dense sands conducted by Ishihara et al (1991) confirm almost all of the important concepts for liquefiable soils. In these tests, the behaviour on an undrained plane including steady state, collapse surface, effective stress paths and stress-strain relationships can be clearly observed.

All of this research and these laboratory tests are important background to understand the behaviour of liquefiable soils and they provide a base to study the most important problem: the mechanism of the liquefaction failure of earth structures.

Liquefaction failure of an earth structure is a very complicated process involving dynamic loading, excess pore water pressure generation and redistribution, material softening and stress redistribution. The characteristics of liquefaction failure include:

(1). pore water pressure generation and redistribution during and following an earthquake.

(2). stress redistribution when liquefied materials undergo strain softening from their peak strength to residual strength during and following an earthquake.

(3). back influence on the dynamic response of earth structures by changes in stresses during stress redistribution and reconsolidation.

(4). volumetric strain caused by dynamic densification and reconsolidation and their subsequent influence on both dynamic response and stress redistributions.

Liquefaction failure of an earth structure may occur under various conditions without earthquake shaking. It may occur under some cyclic loading caused by ocean waves, wind or machine vibrations. It may also occur under some static conditions by changes in pore water pressures. The assessment of the stability of an earth structure with liquefiable materials must necessarily include consideration of deformations because stress redistribution and reconsolidation cannot be avoided in these structures.

The deformations related to the liquefaction failure of an earth structure can be usually indicated into three parts: the deformation caused directly by the dynamic loadings, the deformation caused by stress redistribution and the deformation caused by reconsolidation. The deformations caused by stress redistribution and reconsolidation are called post-earthquake deformations in this research. The delayed phenomena in liquefaction effects reinforce the importance of post-earthquake deformation in safety evaluation of earth structures under liquefaction conditions.

1.2. Delayed Phenomenon in Liquefaction Effects.

Delayed failure is a common phenomenon in liquefaction effects on earth dams and foundations. After an investigation on the performance of dams in the 1939 Ojika earthquake in Japan, as cited by Seed(1979), Akiba and Semba (1941) made an important conclusion that there were very few failures of earth dams that occurred during the earthquake shaking. Most dam failures occurred either a few hours or up to 24 hours after the earthquake.

A very good review and discussion of liquefaction effects on earth dams was given by Seed (1979). The delayed failure phenomenon in liquefaction are reinforced by his report. A similar conclusion was also made in his report that the critical period for an embankment dam subjected to earthquake shaking is not only the period of shaking itself, but also a period of hours following an earthquake, possibly because piping may occur through cracks induced by the earthquake motions or because slope failures may result from pore pressure redistribution. For dams constructed of saturated cohesionless soils and subjected to strong shaking, a primary cause of damage or failure is the build-up of pore water pressures in the embankment and the possible loss of strength which may occur as a result of these pore pressures.

The seismoscope record on the crest of the Lower San Fernando Dam during the 1971 San Fernando earthquake showed that the slide movement involving the crest of the dam apparently did not take place during the main earthquake, but rather occurred some 30 seconds after the main shaking (Seed, 1979).

At the time of the Izu-Ohshima-Kinkai earthquake of January 15, 1978 in Japan, two dams retaining tailings from the Mochikoshi gold mine failed. One of the dams, No. 2 dike, failed about 24 hours after the earthquake at a time when there was no shaking (Ishihara, 1984).

A similar conclusion for liquefaction effects on ground surface deposits was given by Ambraseys and Sarma (1969). In their report, special attention was given to the delay with which liquefaction effects appear on surface deposits originally stable. As they concluded, liquefaction effects may appear on the surface of the ground with considerable delay, and moreover initially stable deposits near the surface may liquefy after the earthquake shaking is over. Structures may sink or float up, and damage to structures on loose deposits is due to foundation failure and sliding rather than due to earthquake shaking.

During the Haicheng earthquake in 1975 and the Tangshan earthquake in 1976 in China, sand boils were observed at a number of sites from a few minutes to some hours after the earthquake shaking was over (Liu and Qiao, 1984).

The simultaneous measurements of seismically induced pore water pressure changes in-situ during the 1987 Superstition Hills earthquake at the Wildlife Site, as reported by Holzer, Youd and Hanks (1989), are possibly the first measurements of pore water pressures building up to a lithostatic condition associated with earthquake induced liquefaction. It is more important that the measurements revealed that total pore pressures approached lithostatic conditions after the strong motion ceased. The earthquake shaking lasted for about 10 seconds, but the pore water pressures continued to climb for about 90 seconds.

Table 1.2.1 shows case histories in which the delayed phenomenon in liquefaction effects were observed.

Table 1.2.1. Delayed Phenomenon in Liquefaction Effects.

earthquake	liquefaction effects
Ojika earthquake, 1939.	Most dams failed a few hours or up to 24 hours after the earthquake.
San Fernando earthquake, 1971.	The upstream shell of the Lower San Fernando dam failed some 30 seconds after the main shaking.
Izu-Ohshima-Kinkai earthquake, 1978.	One dam retaining tailings from Mochikoshi gold mine failed about 24 hours after the earthquake.
Assam earthquake, June 12, 1897.	Ejection of sand and water continued for 20 to 30 minutes after the earthquake.
San Fernando earthquake, 18 April, 1906.	Sand were ejected for several minutes after the earthquake.
Kwanto earthquake, September 1, 1923.	The ejection of water and sand would stop and then resume a few seconds later, continuing long after the earthquake.
Bulgarian earthquake, April 18, 1928.	Water spouted in the Maritsa valley intermittently for tens of minutes after the earthquake. Carts and houses sank gradually into the ground.

Table 1.2.1. (Continue)

Bihar-Nepal earthquake January 15, 1934.	Hundreds of water spouts, throwing up water, sand and peat 6 feet high, continued to act for about 30 minutes.
Niigata earthquake, June 16, 1964 in Japan.	The ground around some buildings began to crack during or right after the earthquake, a minute or two later, water began to come out and continued for 3-4 minutes from around the buildings. Fountains of water continued to play for nearly 20 minutes. Settlements, tilting or rises of all kinds of structures occurred gradually following the earthquake.
Haicheng earthquake, 1975.	Ejection of sand and water continued for some minutes or up to 6 hours.
Tangshan earthquake, 1976.	Ejection of water and sand started after the earthquake and lasted for some minutes or up to 1 day, heavy structures sank into the ground, some houses collapsed a rather long time after the earthquake.
Superstition Hills earthquake, Nov.24, 1987.	The earthquake shaking lasted for about 10 seconds, the measured pore water pressures continued to climb to lithostatic conditions for about 90 seconds. Lateral spreading of ground surface towards the river was observed.

It is a common agreement that the delayed failure in liquefaction is caused by material softening, loss of strength and excess pore water pressure build-up and dissipation following an earthquake. Obviously, it is not possible to predict this type of failure by a traditional limit equilibrium stability analysis even by using the steady state strength for the liquefied zone along the slip surface. Deformation analyses to consider the stress redistribution caused by strain softening of liquefied materials and the reconsolidation caused by dissipation of excess pore water pressures become necessary. As Terzaghi anticipated, for any soil which builds up large pore pressures during earthquake shaking, the post-earthquake stability may need careful examination.

1.3. Deformation Analysis and Liquefaction Failure.

The stability of slopes depends on the characteristics of the slope forming materials, stress history, ground water condition and boundary condition. In some cases, the deformation consideration in stability evaluation of slopes may become necessary.

In 1965, based on the investigation of case histories and also on the results of model tests, Newmark (1965) made a conclusion that the peak acceleration may not be significant in determining the response of the dam. The effects of the velocities and of the ground displacement, and of the differential displacement of the ground leading to fissures in the ground surface, may be of equal or of even greater importance.

A similar conclusion was also made by Seed (1966) that any assessment of the stability of an embankment during an earthquake must necessarily involve a consideration of the magnitude of deformation or change in configuration. A large displacement of a section of the embankment would be considered a slope failure, a small downward movement of a section would be identified as a minor slump of the embankment, differential movements of several inches might be considered as a severe cracking and smaller movements as minor cracking.

Table 1.3.1 shows some case histories in which the failure of earth dams occurred even when the computed factor of safety was larger than unity.

Table 1.3.1. Pseudo-static analysis of dams with slope failure during earthquake (after Seed, 1979)

Dam	Seismic coefficient (g)	computed FS	effect of earthquake
Sheffield dam	0.10	1.20	complete failure
Lower San Fernando Dam	0.15	1.30	upstream slope failure
Upper San Fernando Dam	0.15	2.00 -2.50	downstream shell slipped about 6 ft
Tailing dam (Japan)	0.20	1.30	failure of dam with release of tailings.

The methods of deformation analysis for seismic stability of earth dams developed in the last three decades include:

(1). Newmark method (1965).

The yield acceleration (i.e. when FS=1) can be determined by a pseudo-static method. Displacement of blocks can be calculated by integration of the part of the acceleration history beyond the yield acceleration. Displacements caused by static driving stress and material softening were not considered in this method, although it could be extented to strain softening.

(2). Seed - Lee - Idriss Method (1975).

Dynamic response of the earth dam is calculated by finite element analysis. Pore water pressures are determined by the dynamic response and laboratory tests. Evaluate the factor of safety against failure based on the dynamic response and pore water pressure. The post-earthquake deformations have not been considered in this method.

(3). Zienkiewicz et.al Method (1990).

Permanent deformation and pore water pressure are calculated by finite element analysis. A generalized plasticity model is used. The steady state strength and triggering condition have not been considered in this method.

(4). Kuwano-Ishihara Method (1991).

The permanent deformation caused by softening parameters in moduli of soils was considered. The steady state strength, strain softening behaviour have not been considered in this method.

(5). Finn et.al method(1990).

The steady state strength and the permanent deformation caused by stress redistribution have been considered in this method. But, the post peak strain softening behaviour and the triggering condition have not been considered in this method.

The deformation related to liquefaction failure of an earth structure usually consists of three parts: the deformation caused directly by the dynamic loading, the deformation caused by stress redistribution and the deformation caused by reconsolidation.

The deformation caused by dynamic loading is usually relatively small and of short duration compared to the other two parts.

The deformation caused by stress redistribution can be very large depending on the properties of the materials. This part of the deformation may develop during and following an earthquake and it is the main reason for the gross failures of dams or foundations after the earthquakes. The stress redistribution can usually be completed in a short period from a few seconds to a few minutes. The failure caused by this part of the deformation is usually an undrained flow failure.

The deformation caused by reconsolidation is of the longest duration. This part of the deformation may be responsible for the failures of dams or foundations that have occurred some hours or days after earthquakes. During dissipation of excess pore water pressures, further liquefaction may occur, therefore the failure of earth structures may be also generated by the combined effects of reconsolidation and stress redistribution.

The post-earthquake deformation analysis for liquefaction problems should be able to consider the strain softening behavior, steady state strength and liquefaction triggering conditions.

Liquefaction failure is usually a large strain and discontinuity problem. A simpler and more economic approach is to capture the incipient liquefaction failure, i.e. to capture the deformation that may cause large liquefaction flow failures. This analysis can be done by small strain finite element analysis. It can provide a reasonable method to evaluate the factor of safety for some structures in which we are concerned about the safety of the structure rather than the flow distance of materials involved in the failure.

For an earth structure with a potentially small liquefied zone, the slip surface may be well defined. Then the traditional limit equilibrium method or the weak direction slip surface method (Chen, 1990) can be used to evaluate the safety of the structure. For earth structures with a potentially large liquefied area, the slip surface may be difficult or even impossible to define, e.g. the failure of the Lower San Fernando dam. In this case, a new method to evaluate the safety of the earth structure based on finite element results must be developed.

1.4. Purpose of The Research and Scope of The Thesis.

The basic purpose of this research is to investigate the relationship between liquefaction failure and post-earthquake deformation. Post-earthquake deformations are caused by stress redistribution and pore water pressure redistribution during and following an earthquake. The post-earthquake deformation for an earth structure with liquefiable soils is dependent upon the initial static driving shear stresses, the steady state and strain softening behavior of the liquefiable materials, and reconsolidation in the earth structure. The finite element method is a powerful tool to consider all of these features.

In order to achieve these goals, the following are needed:

(1). Develop a computer program or a group of programs which are capable of analyzing various geotechnical problems, including the analyses of initial stress, steady state seepage, stress redistribution and reconsolidation.

(2). Develop a soil model that can be used in finite element analyses to simulate the behavior of liquefiable materials, particularly, the strain softening, steady state, collapse triggering and effective stress paths.

(3). Evaluate the capability of the proposed analytical method by using the method to analyze documented case histories.

Chapter 2 reviews the behavior of liquefiable soils. The steady state line, strain softening behaviour, collapse surface, phase transformation line and cyclic mobility behaviours are discussed in this chapter. Chapter 3 develops a simplified model based on the review in chapter 2 and the following previous work: (1). the critical state boundary theory introduced by Roscoe et al. (1958), (2). steady state deformation theory introduced by Castro (1975) and Poulos (1981), (3). the concept of collapse surface introduced by Sladen et.al (1985), (4). the hyperbolic strain softening model developed by Chan et al. (1986), and (5). the phase transformation line defined by Ishihara et.al (1975). The post-earthquake deformation due to stress redistribution is discussed in chapter 4. The formulation of unbalanced load for liquefied materials by contraction of the yield surface during strain softening is also introduced in chapter 4. Post-earthquake deformation due to excess pore water pressure is discussed in chapter 5. The deformation discussed in chapter 5 includes the following two parts: (1) the deformation due to reconsolidation and (2) the deformation due to the unbalanced load of excess pore water pressures. Chapter 6 discussed the stability evaluation of earth structures by the finite element method. The evaluation is based on the contours of yielding ratio and the field of displacements. A definition of factor of safety by finite element results is also given in this chapter. To evaluate the analytical capability of the proposed method, the post-earthquake deformation analyses of the Lower San Fernando Dam during San Fernando earthquake, February 9, 1971 are discussed in chapter 7. This analysis reveals that progressive failure may be initiated by liquefaction of materials in an earth structure. Another case history of the Wildlife Site, Imperial Valley, during 1987 Superstition Hills earthquake, is introduced in chapter 8. The analysis has shown that the delayed pore water pressure response and large lateral spreading of the ground surface could have been due to stress redistribution. Further liquefaction during dissipation of excess pore water pressures are also observed in the analysis. Conclusions and recommendations for further research are given in chapter 9.

2. BEHAVIOUR OF LIQUEFIABLE SOILS

2.1. Liquefaction of Soils

A condition of zero effective stress caused by accumulation of excess pore water pressures during cyclic loading was defined as initial liquefaction by Seed et al (1966, 1975). At the heart of the definition is that the soil will lose the ability to carry any shear stress when the effective stress equals zero. However, the results of laboratory tests always show that the soils can still carry a certain amount of shear stress in either cyclic loading or monotonic loading even though the zero effective stress condition has apparently been reached due to the accumulation of excess pore water pressures. Figure 2.1.1(a) illustrates a typical effective stress path for liquefiable soils under cyclic loading conditions. During cyclic loading, pore water pressure will increase and the effective stress path will move towards the left. After reaching the origin with zero effective stress, the soil can still carry a certain amount of cyclic shear stress and the effective stress path will move up and down along an envelope. Any subsequent monotonic loading may still be applied after the soil has reached the initial liquefaction state by the cyclic loading.

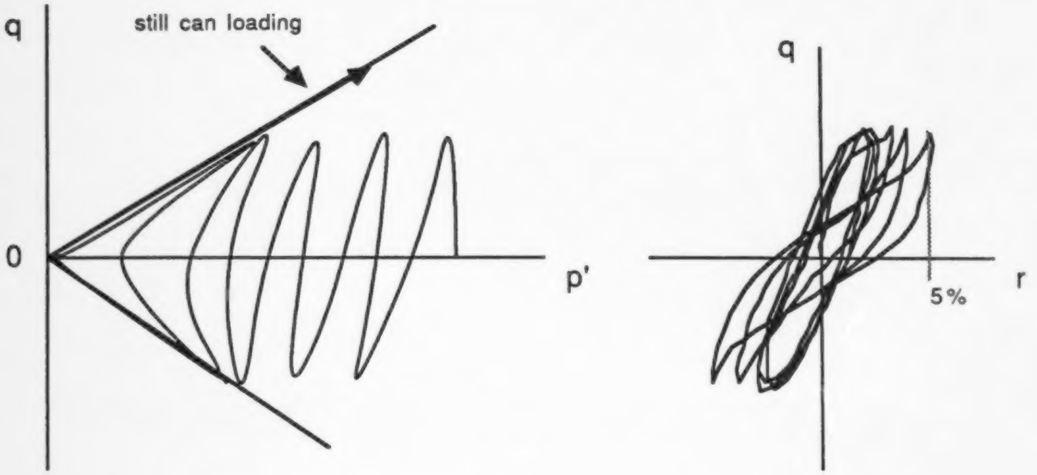
q
still can loading
0
p'
q
r
5%

(a) Soil behaviour under isotropically consolidated conditions.

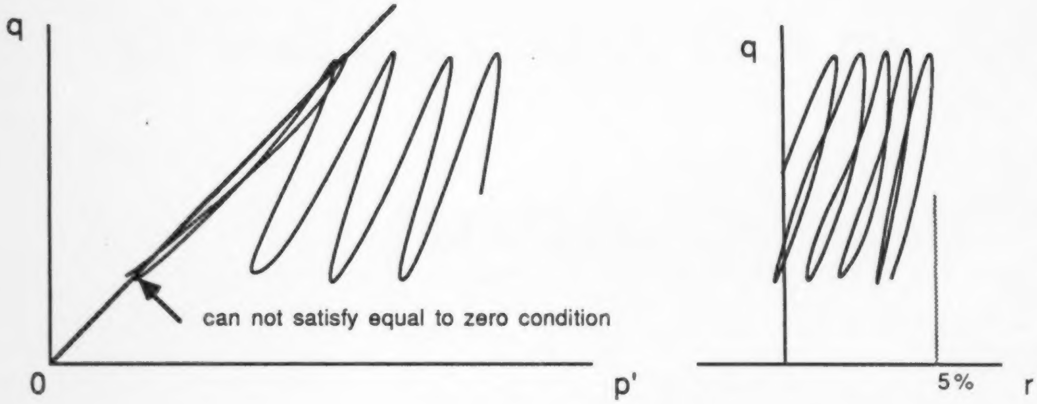
q
can not satisfy equal to zero condition
0
p'
q
5%
r

(b) Soil behaviour under anisotropically consolidated conditions.

Fig.2.1.1. Zero Effective Stress Definition and Its Limitations.

For soils consolidated anisotropically as shown in Figure 2.1.1(b), initial liquefaction will not occur if there is no shear stress reverse. Seed et al (1973) and Finn et al (1976) have noticed that principle stress reversal is required if a condition of initial liquefaction, i.e. effective stress equal to zero, is to be achieved. Under conditions without that stress reversal, the pore water pressures stabilize at values that depend on the anisotropic consolidation ratio and the magnitude of the cyclic shear stress ratio. Therefore, certain amounts of accumulated strain (e.g. 5 %) have been adopted to define liquefaction. The definition of initial liquefaction may cause confusion when one tries to determine a strength for liquefied materials in stability analysis.

Castro (1975) insisted that the term "liquefaction" should be used to refer to the steady flow of granular material as a result of high pore pressures and a sudden loss in shear strength due to either static or cyclic loading under undrained conditions. Figure 2.1.2 shows the behaviour of the steady flow of granular material and the sudden loss in shear strength under both monotonic and cyclic loading. When excess pore water pressures are caused by dynamic loading, monotonic loading or any other reason, the stress path moves to the left in p-q stress space and reaches a peak where the soil begins to undergo strain softening from the peak to a residual strength. The pore water pressure will continue to increase during strain softening until the residual strength is reached. The steady flow of granular material or large plastic strain develops at a constant level of shear stress representing the residual strength. The state of continuous deformation at constant resistance and constant volume, corresponds to Casagrande's concept of critical void ratio (Casagrande, 1936), and was defined as the critical state of the soil by Castro (1975). The deformation at this state was called steady state deformation and the residual strength was called steady state strength by Poulos (1981). Laboratory tests have shown that the stresses at the critical or steady state are independent of the manner in which the failure is initiated and are only a function of the void ratio of the sand after consolidation. The behaviour of sands in the laboratory is similar to the behaviour of sand in a flow slide in which the sand suffers such a substantial reduction of its shear strength that the mass of soil seems to flow like a liquid.

The definition of liquefaction given by Castro (1975) has been used in this thesis to consider the behaviour of contractant sands under undrained conditions. Liquefaction can only occur when drainage is impeded and pore pressures increase. If drainage is not impeded and the dissipation of excess pore pressures is fast enough, the void ratio of the soils will change, and liquefaction as an undrained failure will never occur.

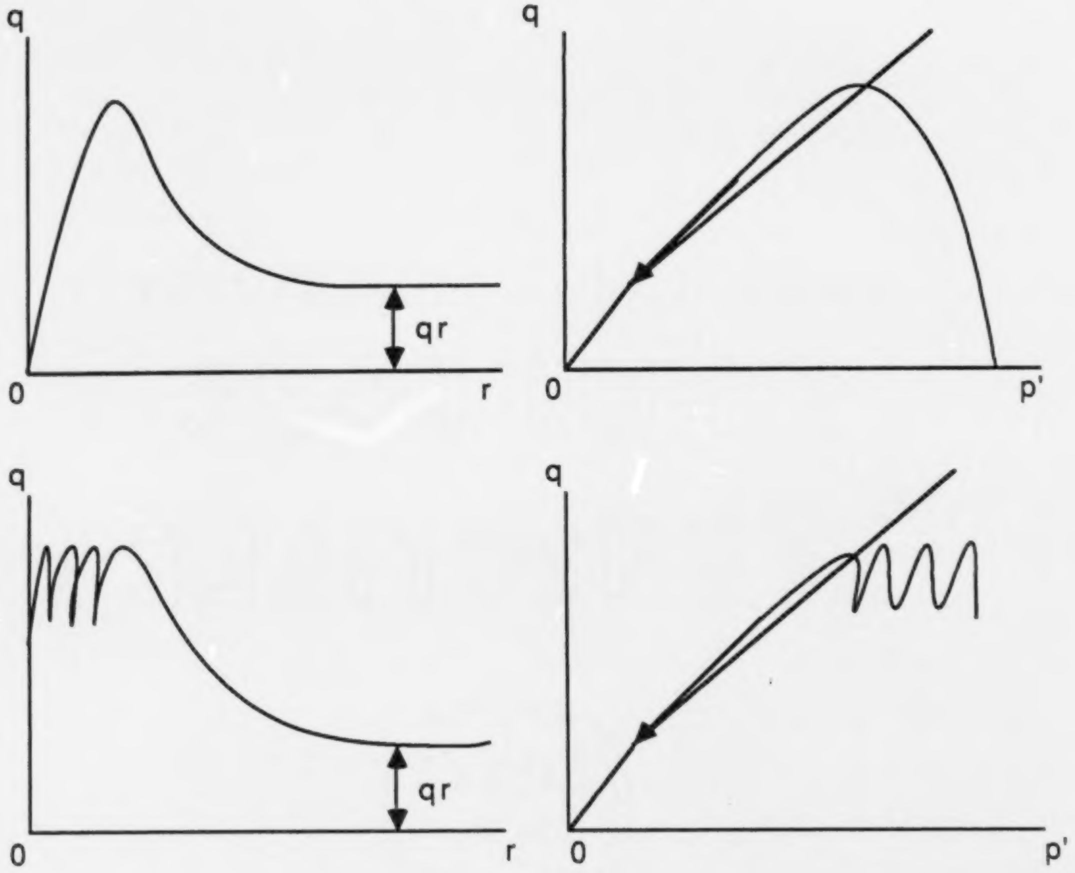

p' = normal effective stress;

q = shear stress;

qr = residual shear strength.

Fig.2.1.2. Flow Structure and Loss in Shear Strength.

2.2. Steady State Line

When loose saturated sands are loaded under undrained conditions, they may collapse and strain soften to a constant level of effective stress and shear strength. This condition has been called steady state by Castro(1975) and Poulos(1981). Poulos(1981) defined steady state as a condition of constant effective stress, constant shear stress, constant volume and constant velocity of deformation. The steady state of a particular sand can be represented by a line in $e - \sigma' - \tau$ space, as shown in Figure 2.2.1, where e is the void ratio, σ' is the effective normal stress and τ is the shear stress. The steady state is commonly represented by the projection of the steady state line (SSL) on to the $e - \sigma'$ plane or the $e - \tau$ plane, also shown in Figure.2.2.1. However, to fully understand the behaviour of sands subjected to undrained loading, it is important to follow the actual stress paths in three dimensional $e - \sigma' - \tau$ space. The steady state line is very similar to the critical state line defined by Roscoe et al. (1958) and its projection on the $e - \sigma'$ plane was called the critical void ratio line by Casagrande (1936). The critical void ratio line can also be determined by drained tests and it defines a boundary between contractant and dilatant behaviour of soils. During undrained loading conditions, pore water pressure will increase for soils on the contractant side of steady state. On the contrary, negative pore water pressure will develop for soils on the dilatant side of steady state during undrained loading.

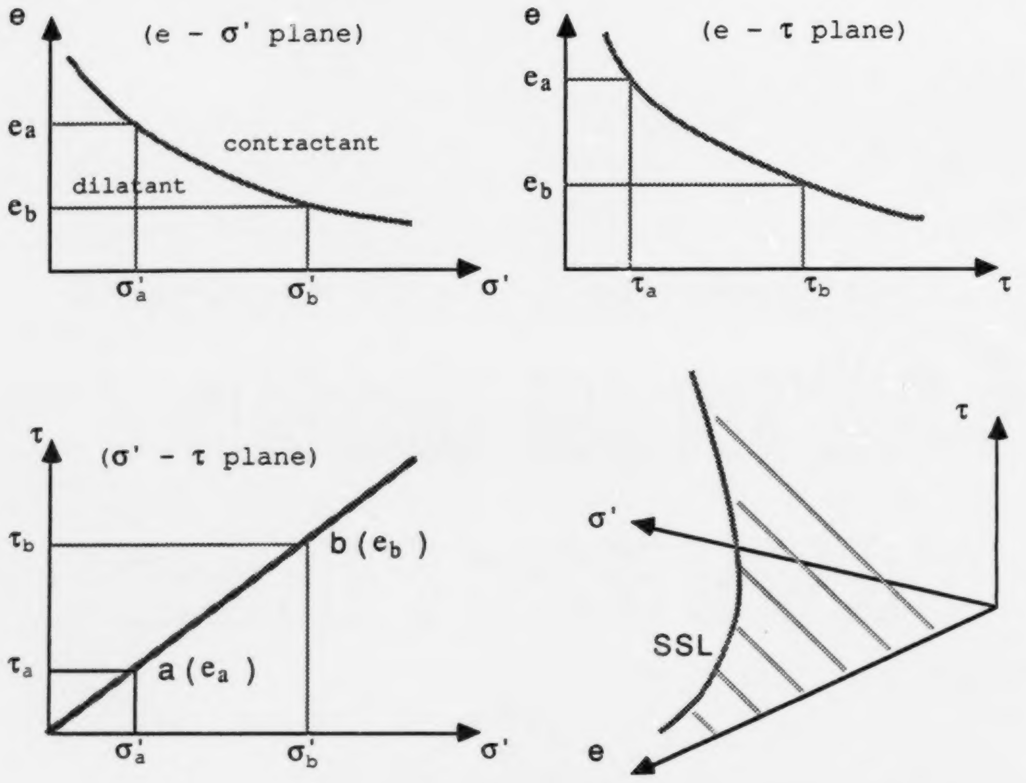
e
(e - σ' plane)
e_a
contractant
dilatant
e_b
σ'_a
σ'_b
σ'
e
(e - τ plane)
e_a
e_b
τ_a
τ_b
τ
τ
(σ' - τ plane)
τ_b
b (e_b)
τ_a
a (e_a)
σ'_a
σ'_b
σ'
τ
σ'
SSL
e

Fig.2.2.1. Steady State Line For Liquefiable Soils.

The development of the theory of steady state deformation provides us with the concept that a residual strength exists for liquefied soils. To use the residual strength in stability analysis is a limit design problem. The steady state strength can no longer be simply expressed as an undrained strength envelope in p-q space because the strength is independent of the stress paths under undrained conditions and it becomes a single point rather than an envelope in an undrained plane.

Most laboratory tests results show that for uniform materials, the steady state strength is independent of the effective stress path and initial effective stress state, but depends uniquely on the void ratio. After investigation on results for both compression and extension triaxial tests on water deposited sands, Vaid et al. (1990) concluded that the steady state strength, at a given void ratio, is smaller in extension than in compression and the difference increases as the sand gets looser. After examining the behaviour of a fine to medium, uniformly graded quartzitic sand, Been et al. (1991) argued that the steady states are equal and independent of stress path, sample preparation method and initial density and suggested that the mobilized friction angle at steady state in sands may be a function of the critical state void ratio.

2.3. Strain Softening Behaviour

For contractant soil under saturated undrained loading conditions, strain softening behaviour may occur after the effective stress path reaches a peak point. During strain softening, part of the load previously carried by the soil skeleton or grain structure will be transferred to the pore water which may cause further development of excess pore water pressure. The load transfer between the soil skeleton and pore water is due to the collapse of the soil skeleton during loading in shear and the development of excess pore water pressure. The collapse in the soil skeleton will weaken the global stiffness of the soil represented by a loss in shear strength. After the collapse, the soil structure may reach a relatively stable state, i.e. the steady state. Figure 2.3.1 illustrates typical liquefaction behaviour in an undrained monotonic test. During the undrained monotonic loading, the pore water pressure increases and the effective stress path bends to the left in p-q space. After reaching a peak strength defined by the intersection of the effective stress path and a peak strength envelope defined as the collapse surface by Sladen et. al (1985), the soil suddenly loses its strength and undergoes strain softening from the peak strength to the steady state strength. During strain softening, the pore water pressure continues to increase and causes the effective stress path to move along or slightly above the collapse surface. A critical state boundary of strain softening can be approximately defined by the collapse surface.

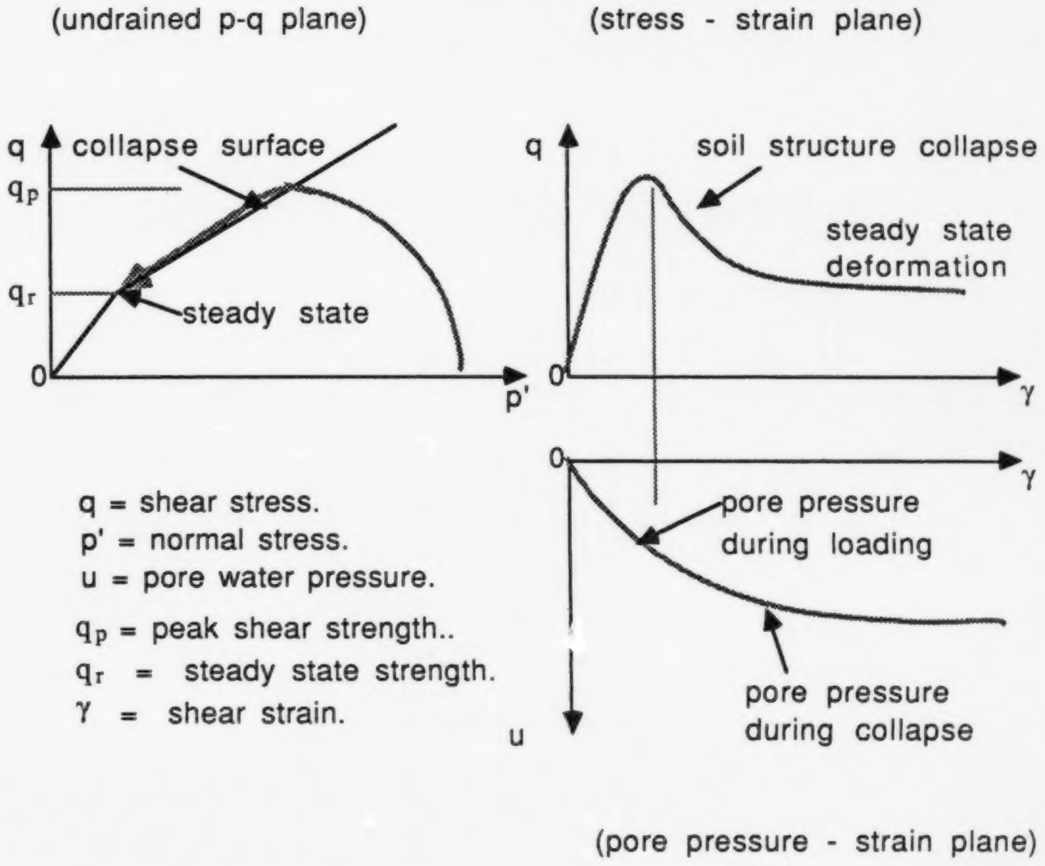
(undrained p-q plane)
(stress - strain plane)
q
collapse surface
q_p
q_r
steady state
0
p'
q
soil structure collapse
steady state deformation
0
γ
0
γ
pore pressure during loading
pore pressure during collapse
u
q = shear stress.
p' = normal stress.
u = pore water pressure.
q_p = peak shear strength..
q_r = steady state strength.
γ = shear strain.
(pore pressure - strain plane)

Fig. 2.3.1. Typical Liquefaction Behaviour.

The pore water pressure during strain softening is both the result and reason for the collapse. If the pore water pressure can dissipate fast enough, the soil would move away from the peak envelope and either elastic unloading or plastic hardening may occur. If the pore water pressure decreases due to any reason, the strength of the soil may recover and the effective stress path may move up again even though the steady state had been reached. This appears as an elbow in the effective stress path in p-q space. This behaviour was defined as limited liquefaction by Vaid et.al (1990). Negative pore water pressures during undrained laboratory tests may be generated by the tendency for dilation during orientation of sand particles. Alternatively volume changes develop caused by membrane penetration or small holes generated by angular particles.

The post-peak strain softening behaviour depends on the density of the material. For looser materials with a stress state much higher than the steady state strength, the strain softening may occur suddenly and the strength of soil may drop very fast from the peak strength to steady state strength. For denser material with a higher steady state strength, the soil usually behaves in a less brittle manner during strain softening from the peak point to the steady state.

The peak strength depends on the effective stress path and may also depend on the initial state of consolidation because the initial state of consolidation may influence both the peak envelope and the form of the effective stress path. A criterion or so called triggering condition for strain softening behaviour to occur needs to be defined before the concept of steady state strength can be used in a deformation and stability analysis.

2.4. Triggering Condition For Strain Softening

In order to decide when the steady state strength should be used in a stability analysis, or when strain softening occurs, a criterion needs to be defined. The criterion is called a "triggering condition" to describe the triggering of collapse in the soil structure. Triggering conditions can be generally divided into two groups. One defines the criterion in terms of effective stress state and the other defines the criterion in terms of accumulated shear strain. The first one can be called the " effective stress path method ", and the second one can be called the " strain control method ".

2.4.1. Effective stress path method

Sladen et.al (1985) suggested that there is a "collapse surface" in e-p'-q space for liquefiable materials, where e is the void ratio of soils, p' is the normal effective stress and q is the shear stress. On an undrained plane, this surface is presented by a straight line passing through the steady state strength which is a single point on this undrained plane. When undrained effective stress paths reach this surface, the applied shear stress will drop to the steady state strength.

The collapse surface can be observed clearly by plotting the results in a normalized p-q space. It is very convenient to think that the collapse surface can be defined in an undrained p-q plane and that the stress redistribution analysis due to liquefaction should also be conducted under fully undrained conditions. Figure 2.4.1 shows the effective stress paths obtained in triaxial compression tests reported by Sladen et al. (1985). The collapse surface can be observed clearly in these tests. Figure 2.4.2 illustrates the possible relationships among collapse surface, steady state strength, phase transformation and Hvorslev surface given by McRoberts and Sladen (1990)

As discussed by Sladen et.al (1985), the collapse surface is not a state boundary surface, a post peak soil state can pass slightly above it, as is evident in effective stress paths in figure 2.4.1, but it represents the limit of stability if drainage is impeded under load-controlled conditions.

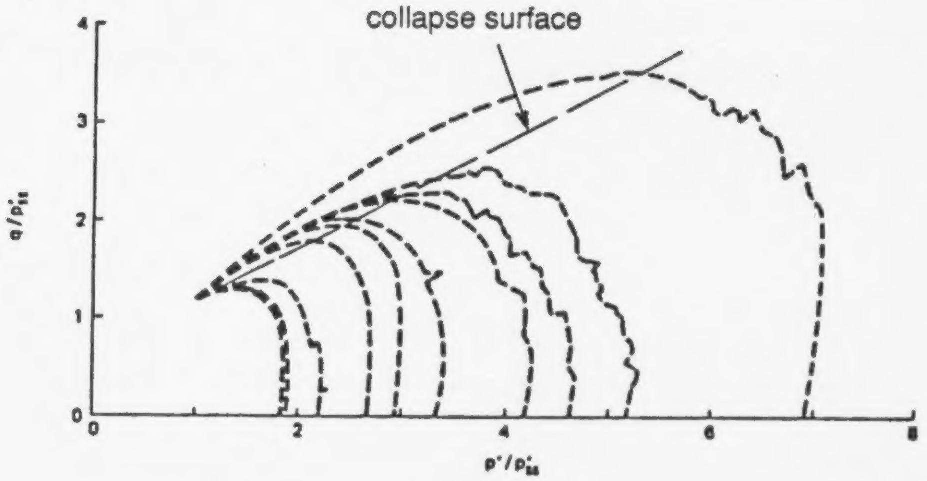

Fig.2.4.1. Collapse Surface

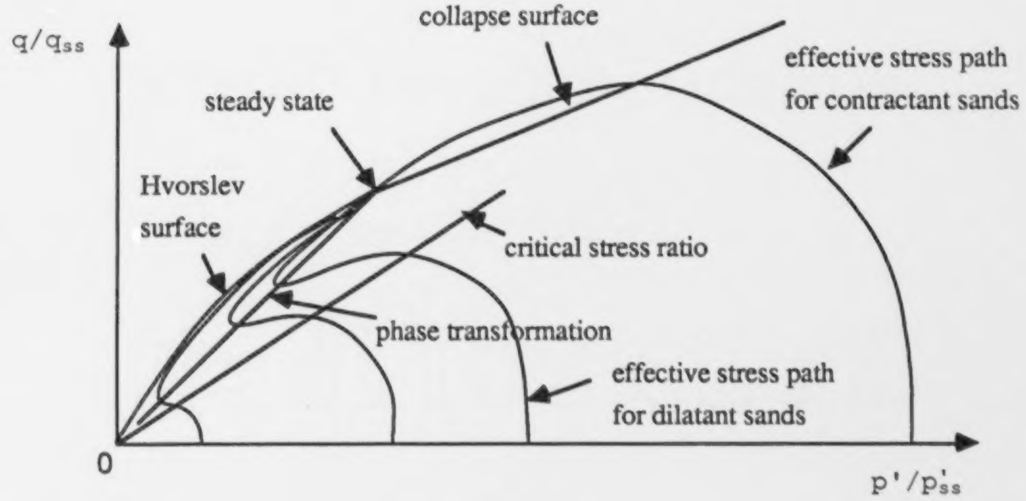
q/q_ss
collapse surface
effective stress path
for contractant sands
steady state
Hvorslev
surface
critical stress ratio
phase transformation
effective stress path
for dilatant sands
0
p'/p'ss

Fig. 2.4.2. Behaviour of Liquefiable Soils Suggested By McRoberts and Sladen (1990).

The significance of the collapse surface is that it defines the triggering condition for strain softening under undrained conditions. The unbalanced loads caused by strain softening are the main reasons for deformation during stress redistribution. The deformation caused by pore water pressure under undrained condition is very small. Therefore, a state boundary surface can be approximately defined by the collapse surface. The collapse surface defines a triggering condition and also a zone of strain softening under undrained loading conditions. When the soil undergoes strain softening from peak strength to steady state strength, the effective stress path can be assumed to move along the collapse surface.

It is possible that the slope of the collapse surface is to some degree dependent upon stress history. The results of tests on anisotropically consolidated samples reported by Castro et. al (1982), as cited by Sladen et. al (1985), suggested that the collapse surface for anisotropically consolidated soils may be slightly steeper than that for isotropically consolidated soils. Like the influence of stress history on yield surface, this possibility does not reject the collapse surface as a state boundary surface. In fact, the collapse surface defines a zone on which the continued contraction of yield surfaces occurs during plastic straining under undrained conditions.

One should strictly distinguish the collapse surface from any strength envelope. As a zone defining yield surfaces, the collapse surface describes the soil behaviour between the peak strength and the residual strength.

The collapse surface can be defined as a state boundary on which the yield surface may expand or contract depending on the drainage condition and stress path. If drainage is impeded, the contraction of the yield surface and the increase of pore water pressure may occur as plastic strains develop. If the drainage is not impeded and the water pressure may dissipate fast enough, the soil may behave in a strain hardening or strain softening manner when the effective stress path moves along the surface. In general, the collapse surface defines a special zone in p'- q - e space describing different behaviour of yield surface under various drainage conditions. This surface has not been described by any plasticity theory and cannot be simply adopted as a yield surface in any plasticity model.

In a study of triggering conditions on the undrained p-q plane, Mohamad and Dobry (1986), and Vasquez-Herrera and Dobry (1988) defined a triggering condition as a straight line in p-q space passing through the origin. The straight line is determined by the peak strengths obtained in undrained tests on samples at different void ratios. Vaid and Chern (1985) defined a similar triggering condition and called it the "critical stress ratio" surface. This definition cannot be used directly for an undrained stress analysis because different effective stress paths under fully undrained condition may reach different peak values representing different void ratios which is contrary to the undrained assumption.

2.4.2. The strain control method.

For the thickened tailings of lower permeability, Poulos et al. (1985) suggested a procedure for liquefaction stability analysis as:

(1) Determine the in-situ steady state strength and the stress-strain curve using field vane tests as that shown in Figure 2.4.3(a).

(2) Determine the driving shear stress and the factor of safety against liquefaction slide.

(3) If the factor of safety $F < 1$, determine the earthquake intensity needed to produce the strain obtained in (1) that is necessary to reduce the resistance below the driving shear stress.

(4) Compare the determined earthquake intensity with the design earthquake intensity.

To estimate the intensity of shaking that will trigger liquefaction, one needs to know: (1) the strain that is necessary to reduce the resistance below the driving shear stress, and (2) the strain that will be caused by a given shaking intensity. The strain needed to reduce the strength below the driving shear stress can be determined on the stress strain curve obtained in field van test as shown in figure 2.4.3(a). The strain caused by a given cyclic loading is defined as double amplitude shear strain in cyclic loading tests as that shown in figure 2.4.3(b).

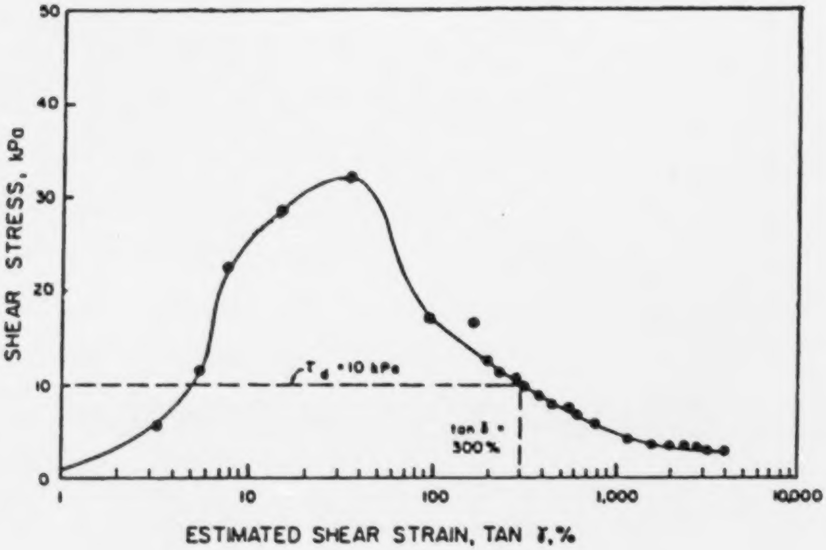

(a) stress-strain curve of in-situ van tests.

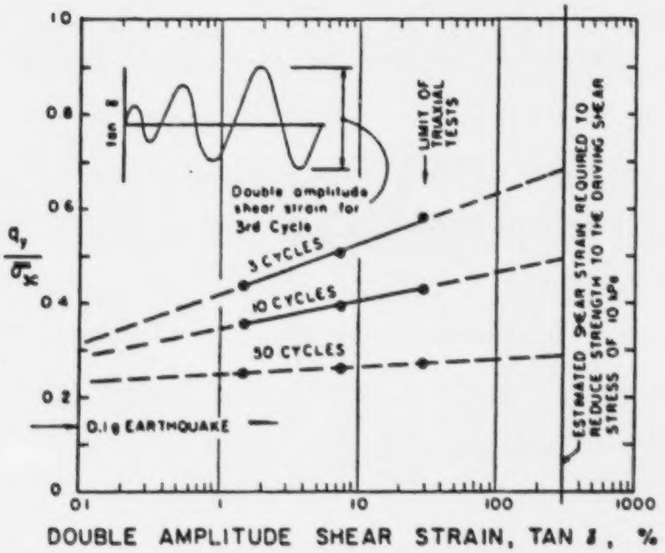

(b) strain caused by given cyclic loading.

Fig. 2.4.3. Strain Control Triggering Condition in Poulos' Procedure (1985).

To investigate the effects of anisotropic consolidation and cyclic shear strain magnitude on the triggering conditions, strain control undrained cyclic torsional tests and some monotonic tests were conducted by Vasquez-Herrera et al. (1988). The method defined by Vasquez-Herrera et al. includes the following steps:

(1). Dynamic analysis to determine the shear strain histories for potentially liquefiable materials in an earth structure.

(2). Determine the equivalent magnitude of shear strain and the number of cycles N from the shear strain histories obtained in step (1).

(3). Undrained strain controlled tests with the equivalent magnitude of shear strain are conducted under similar in-situ consolidation condition to determine the triggering cycles Nf that are necessary to induce liquefaction.

(4). If the equivalent number of cycles N is larger than the triggering cycles Nf, the steady state strength should be used for this material in stability analysis.

These methods provide another possibility to define the triggering condition by means of strains. The accumulated strain and the magnitude of cyclic strain during cyclic loading are needed in these methods. These methods are unable to consider the growth of the liquefied zone due to stress redistribution and cannot be applied to static liquefaction failures caused by changes in ground water conditions.

2.5. Phase Transformation Line and Cyclic Mobility Behaviour.

For a liquefiable soil, the peak value of shear stress before collapse depends on the effective stress path. Whether strain softening behaviour occurs or not depends on whether the peak shear stress is higher or lower than the steady state strength. If the effective stress path moves below the steady state strength, strain softening behaviour will not occur even if the effective stress path can reach a limit state. This situation is more likely to happen for dense materials and heavily over-consolidated materials. Before the effective stress path reaches the limit state, it may cross the phase transformation line defined by Ishihara et.al (1975). The phase transformation line represents the stress state where the pore water pressure decreases in loading and increases in unloading of shear stress under undrained condition. This behaviour is coincident with the dilatancy of material in loading under drained conditions. A limit state can be reached after the effective stress path crosses the phase transformation line. Cyclic mobility can be observed when the effective stress path reaches the limit state under undrained cyclic loading. In the limit state, exterior force, skeleton force and pore water pressure balance each other during loading and unloading. The pore water pressure decreases during loading and increases during unloading thus forcing the effective stress path to bend and move along a line. This line can be called a limit state rather than a failure envelope because the material is not at failure on this line. The strain behaviour can be elastic or strain hardening along this line depending on the density of material and the magnitude of loading in shear stress. The maximum load that can be applied in this state is controlled by the steady state strength (Castro, 1987). After crossing the phase transformation line, the effective stress paths in the limit state will be bounded by an envelope on an undrained plane. This envelope represents a surface in $e - \sigma' - \tau$ space. This surface is comparable to the Hvorslev surface indicated by Roscoe et.al (1958). For loose material, the phase transformation line is very close to the Hvorslev surface. According to the "critical void ratio" concept introduced by Casagrande (1936), the steady state strength represented by a point on an undrained plane separates the Hvorslev surface from the collapse surface. In $e - \sigma' - \tau$ three dimensional space, the steady state line is the boundary between the Hvorslev surface and the collapse surface.

2.6. Summary of Behaviour of Liquefiable Soils.

The idealized behaviour of contractant and dilatant sands during monotonic undrained loading is illustrated in Figure 2.6.1, in terms of their stress paths in p-q space and their associated stress-strain and pore pressure-strain curves. Contractant sands reach a peak undrained strength that can be conveniently defined by the collapse surface. After the peak strength is reached, contractant sands collapse to steady state with associated additional increase in pore pressure. The strain softening behaviour is evident during the collapse.

Dilatant sands, on the other hand, may show only a small increase in pore pressure before reaching the phase transformation line. After crossing the phase transformation line, the soil behaviour becomes strain hardening before reaching steady state and this is associated with a decrease in pore pressure when loading by shear stress. The maximum load that can be carried by the dilative sand is controlled by the steady state strength even though large deformations may develop.

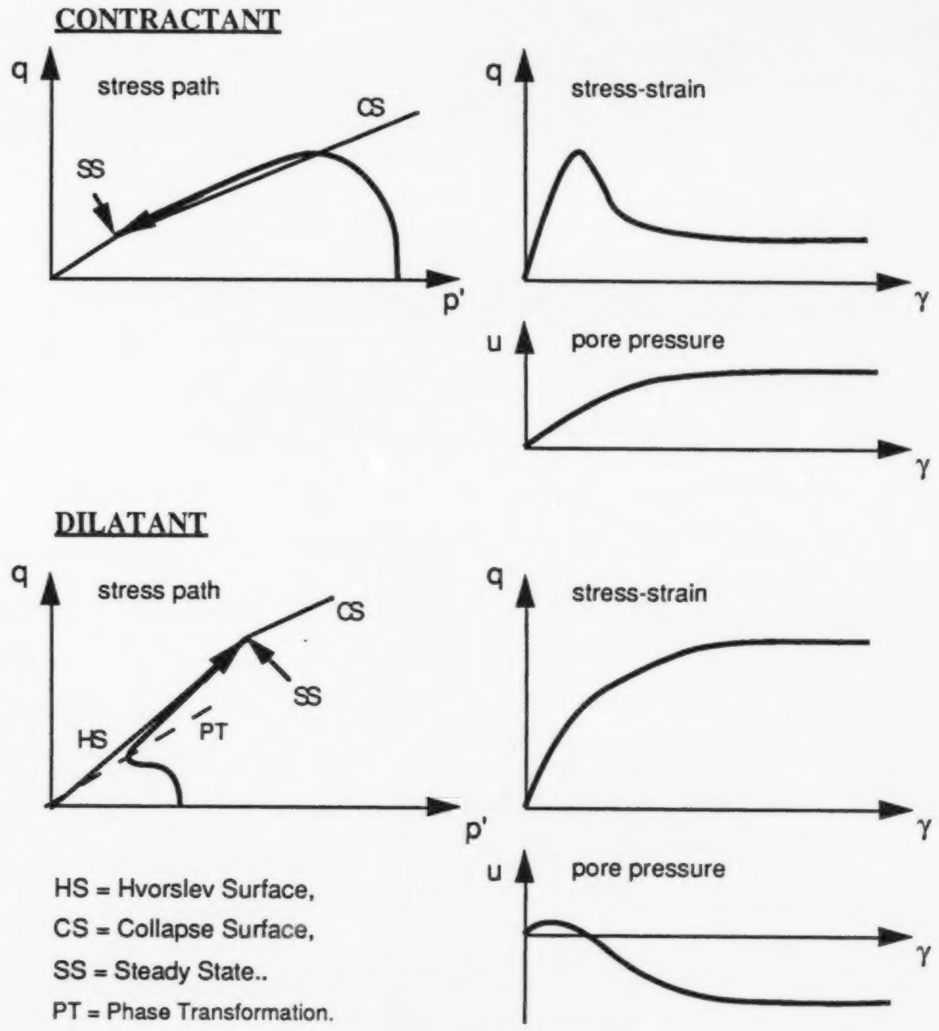
CONTRACTANT
q
stress path
CS
SS
p'
q
stress-strain
γ
u
pore pressure
γ
DILATANT
q
stress path
CS
SS
HS
PT
p'
q
stress-strain
γ
u
pore pressure
γ
HS = Hvorslev Surface,
CS = Collapse Surface,
SS = Steady State..
PT = Phase Transformation.

Fig.2.6.1. Idealized Soil Behaviour Under Undrained Monotonic Loading.

When sands experience undrained cyclic loading, a similar response can be observed for contractant and dilatant sands, as illustrated in Figure 2.6.2. For both contractant and dilatant sands, cyclic loads will induce positive pore pressures and effective stress paths will move towards the boundary surface formed by the collapse surface, steady state and Hvorslev surface. If the initial static driving shear stress is larger than the steady state strength, collapse and strain softening will result when the stress path reaches the collapse surface. If the static driving shear stress is less than the steady state strength, it is possible that the stress path can travel beneath the steady state line and move to the dilative side of steady state. After the stress path crosses the phase transformation line, pore pressures will decrease in loading by shear stress and increase in unloading by shear stress, and the soil may finally reach the Hvorslev surface. The cyclically induced strains, i.e. the cyclic mobility behaviour defined by Casagrande (1971) and Castro et al. (1975) can be observed when the cyclic stresses move up and down along the Hvorslev surface.

The monotonic undrained triaxial tests on very loose to medium dense sands reported by Ishihara et al (1991) confirms almost all the above described concepts on an undrained plane. In these tests, the behaviour of liquefiable soil on an undrained plane including steady state, collapse surface, effective stress paths and stress-strain relationship can be clearly observed.

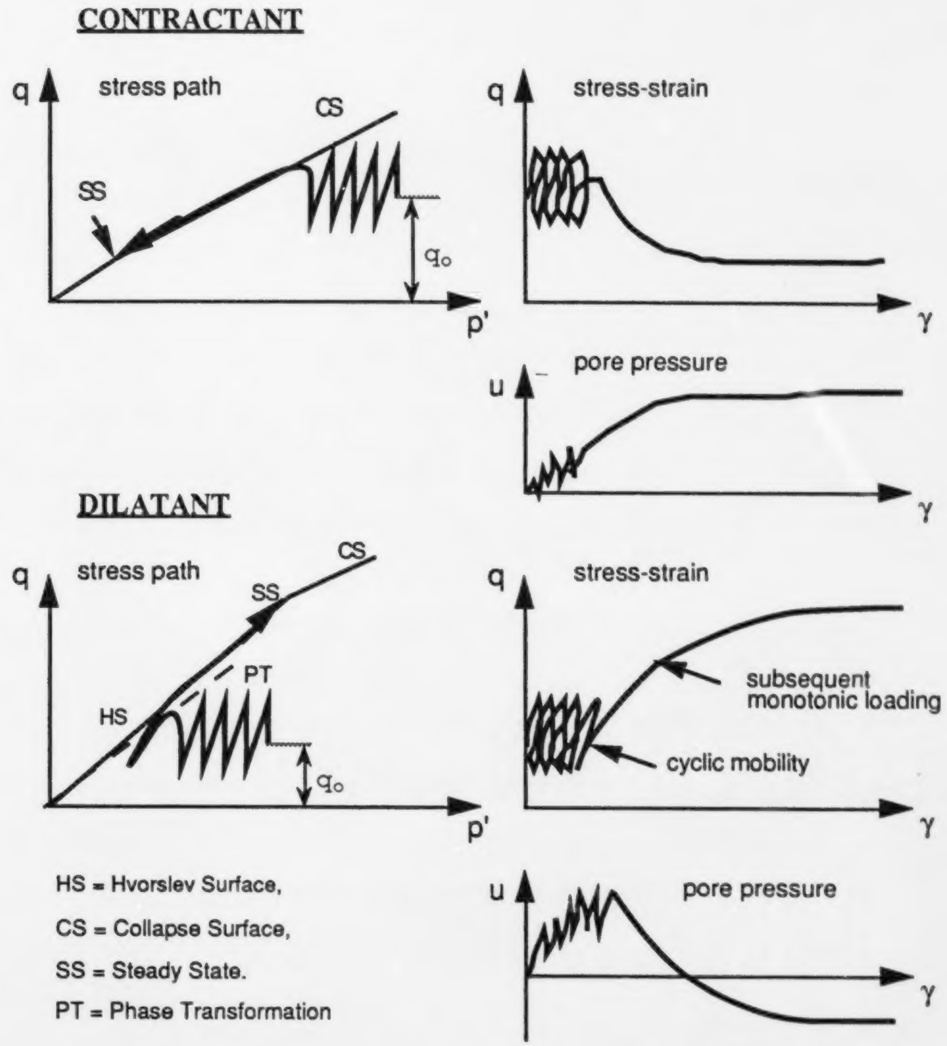
CONTRACTANT
q
stress path
CS
SS
qo
p'
q
stress-strain
γ
u
pore pressure
γ
DILATANT
q
stress path
CS
SS
PT
HS
qo
p'
q
stress-strain
subsequent monotonic loading
cyclic mobility
γ
u
pore pressure
γ
HS = Hvorslev Surface,
CS = Collapse Surface,
SS = Steady State.
PT = Phase Transformation

Fig.2.6.2. Idealized Soil Behaviour Under Undrained Cyclic Loading.

3. A SIMPLIFIED ELASTO-PLASTIC MODEL FOR LIQUEFACTION DEFORMATION ANALYSIS.

3.1. State Boundary Surface For Liquefiable Soils.

The critical state boundary surface model was developed mainly for clay materials by Roscoe and Schofield et.al (1958). A critical state line was defined as a joint ridge between the Roscoe surface and the Hvorslev surface in p-q-e space. Figure 3.1.1 shows the critical state boundary surface. Contractant behaviour occurs when shearing materials below the Roscoe surface and dilatant behaviour occurs when shearing materials below the Hvorslev surface under drained conditions. Therefore, the contractant side and dilatant side can be defined by the critical state line. The contractant or dilatant behaviour will be represented by an increase or decrease in pore pressures under undrained conditions. In both drained and undrained conditions, the material always fails on the critical state line. In the results of undrained tests on clay reported by Loudon (1967), the effective stress paths for overconsolidated materials, the contractant side, the dilatant side and the critical state can be clearly observed. The critical state line is a maximum yield point on an undrained plane. Roscoe et.al (1958) also reported the results of tests on granular media in a simple shear apparatus that confirms closely the applicability of the theory to the yielding of granular materials.

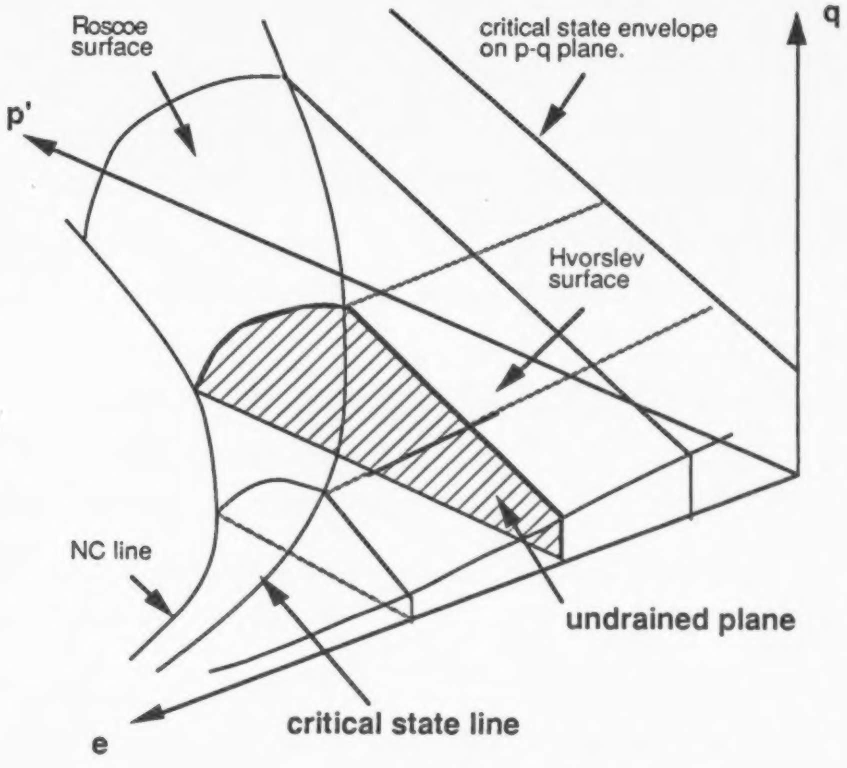
Roscoe surface
critical state envelope on p-q plane.
q
p'
Hvorslev surface
NC line
undrained plane
critical state line
e

Fig.3.1.1. State Boundary Surface Defined by Roscoe et.al (1958).

The state boundary surface determines the yielding of materials. The elastic behaviour is usually defined for the soils inside the state boundary surface. For some materials, plastic shear strain may occur inside the state boundary surface. A modification is usually made for this problem by introducing additional shear yielding surfaces inside the state boundary surface. In general, the state boundary surface is embeded in an elasto-plastic model with strain hardening.

For a liquefiable soil, the state boundary surface under undrained condition should be modified to consider the following characteristics:

(1). Strain softening behaviour occurs during the soil grain structure collapse caused by excess pore water pressure, and the excess pore water pressure will increase continuously until the effective stress path reaches steady state.

(2). A triggering condition should be defined for the collapse of the soil skeleton structure or the onset of strain softening behaviour, in which the shear yield surface will contract from its peak to the residual strength.

(3). Cyclic mobility behaviour should be considered when the effective stress path crosses the phase transformation line and reaches the Hvorslev Surface.

(4). The excess pore water pressure behaviour or the effective stress path should be defined below the critical state boundary surface.

Figure 3.1.2 shows a possible critical state boundary surface for liquefiable soils. The steady state line is a curve in the space connecting the collapse surface and the Hvorslev surface. The collapse surface is represented by a plane in this model between the Roscoe surface and the Hvorslev Surface. When the effective stress path reaches the collapse surface under undrained conditions, the strain softening behaviour will occur and the effective stress path will drop to the steady state line along the collapse surface on an undrained plane. Under drained condition, the soil can move towards or even on the collapse surface but cannot cross over the surface. For the soil sitting on or close to the collapse surface, any little disturbance may cause the soil to collapse undrained to the steady state even though the soil was brought to the position under a drained condition. The test result reported by Eckersley (1990) is a vivid example for this kind of failure in which the rise in water table under fully drained conditions brought the loose soil in a model embankment towards the collapse surface and finally caused undrained flow failure.

Whether the undrained flow failure occurs or not depends on the drainage conditions and stress path. If any generation of pore water pressure can dissipate rapidly during drained loading, the soil may move along the collapse surface without undrained flow failure. If the drainage is impeded or the dissipation of pore water pressure is not fast enough, a little increase of pore water pressures may cause undrained flow failure for the soils on the collapse surface even though the soil was previously brought to the collapse surface under fully drained conditions.

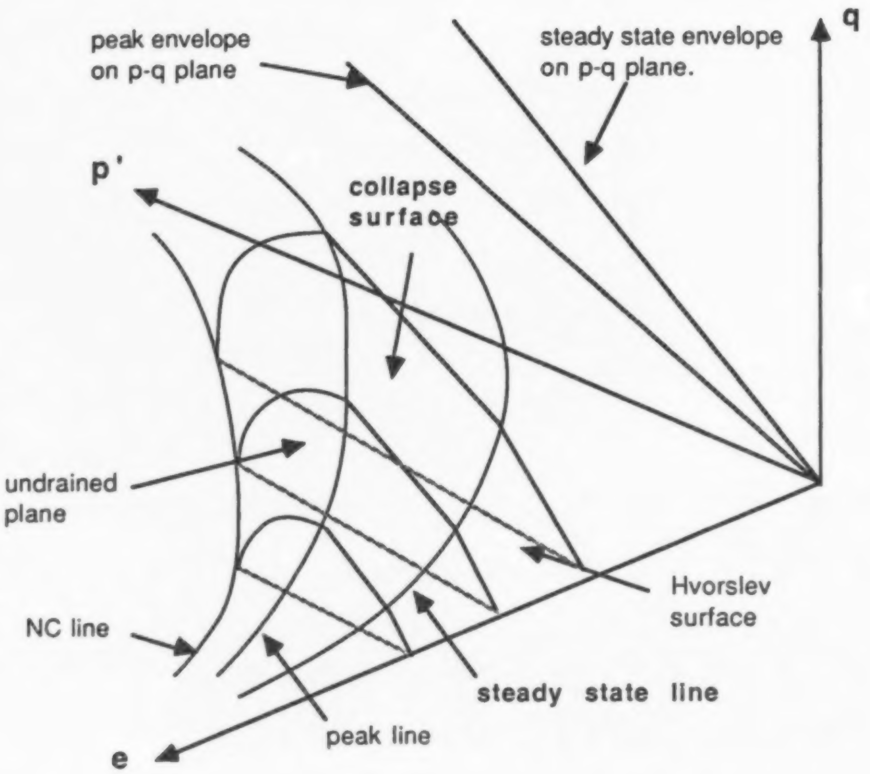
peak envelope on p-q plane
steady state envelope on p-q plane.
q
p'
collapse surface
undrained plane
Hvorslev surface
NC line
steady state line
peak line
e

Fig. 3.1.2. State Boundary Surface For Liquefiable Soils.

3.2. Simplified Three Zones and Shearing Yielding Surface Under Undrained Conditions

Liquefaction stability analysis should be conducted under fully undrained conditions. Therefore, the model for liquefiable material can be simplified to an undrained plane. Fig.3.2.1 shows the typical effective stress paths for liquefiable soils under undrained condition in which the steady state may be the maximum yield surface or the residual yield surface depending on the initial effective stress state. The stress-strain behaviour can be simplified into three zones. Fig.3.2.2 shows the three zones. In zone 1, the stress will follow the previously defined effective stress paths in loading and unloading under undrained condition. there are no volumetric strain when the soil moves along the previously defined effective stress paths. Therefore the shearing yield surface is the only yield surface to be defined in this zone under the assumption that either the elastic or the plastic volumetric strain will occur later in a re-consolidation phase. In zone 2 and zone 3, the soil is on the state boundary surface. Fig.3.2.3 shows the stress-strain behaviour on these boundary surfaces.

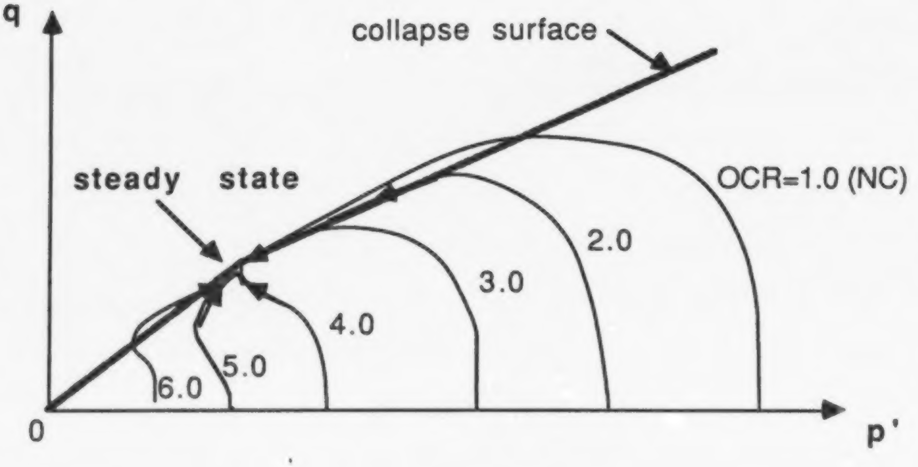
q
collapse surface
steady state
OCR=1.0 (NC)
2.0
3.0
4.0
5.0
6.0
0
p'

(a) effective stress for monotonic loading.

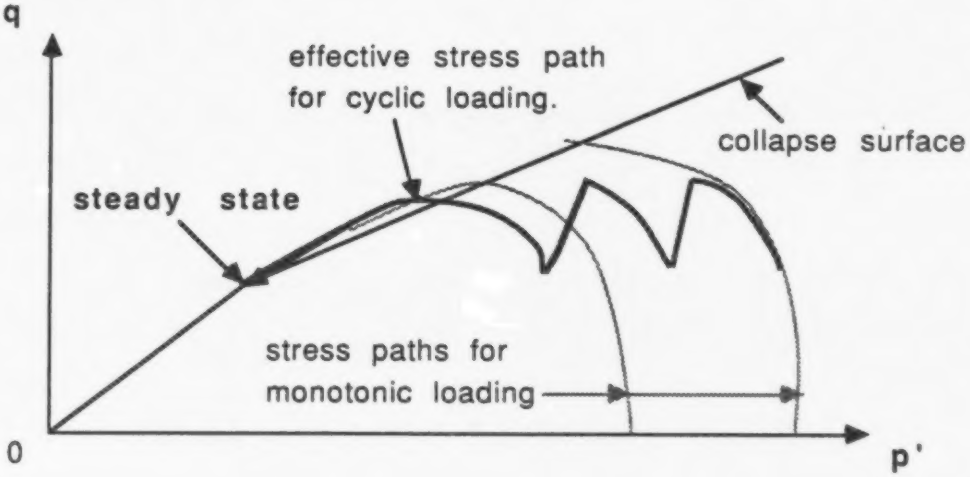
q
effective stress path
for cyclic loading.
collapse surface
steady state
stress paths for
monotonic loading
0
p'

(b) effective stress path for cyclic loading.

Fig. 3.2.1. Effective Stress Paths On An Undrained Plane.

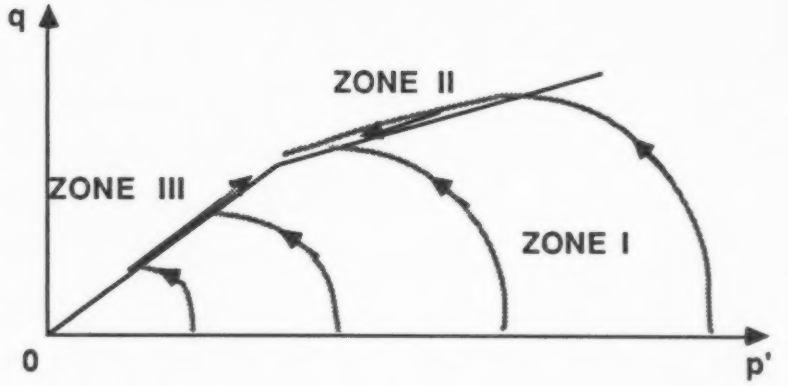
q
ZONE II
ZONE III
ZONE I
0
p'

Fig, 3.2.2. Three Zones on an Undrained Plane For Liquefiable Soils.

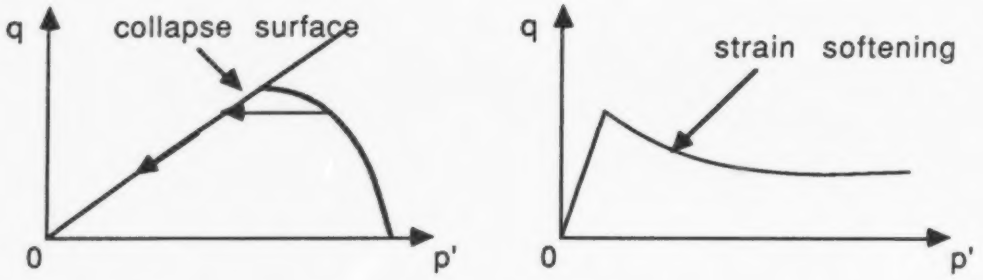
q
collapse surface
0
p'
q
strain softening
0
p'

(a). strain softening on collapse surface.

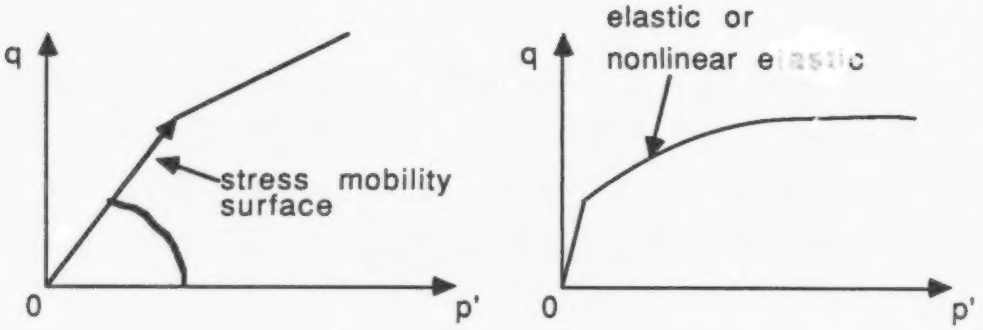
q
stress mobility surface
0
p'
elastic or
nonlinear elastic
q
0
p'

(b). strain hardening on stress mobility surface.

Fig. 3.2.3. Stress-strain Behaviour in Three Zones.

The soil behaviour for a liquefiable soil can be summarized as follows:

Zone 1: Elastic or strain hardening behaviour may occur. The elastic model, nonlinear elastic model or elastoplastic model can be used in this zone. The excess pore water pressure may increase or decrease during cyclic or monotonic loading defined by an effective stress path model.

Zone 2: Soil skeleton structure collapse, a strain softening behaviour occurs, excess pore water pressures increase during the collapse, and the soil reaches the steady state strength after the collapse.

Zone 3: Elastic or strain hardening behaviour may occur, excess pore water pressure decreases during loading and increases during unloading in shear.

The elasto-plastic model for undrained loading condition can be expressed by two yield surfaces. Fig.3.2.4 shows a two yield surface model given by Prevost and Hoeg (1975). In this model, both the volumetric and shear yield surface are defined as a straight line. During undrained loading conditions, the effective stress path A-B cannot cross the volumetric yield surface, because this would imply volume change. Thus, when the effective stress path reachs point A, it must bend over and follow the volumetric yield surface locus to the point B'. The shift between the effective and total stress paths gives the magnitude of the excess pore water pressure. For the effective stress path C-D inside the volumetric yield surface, the elastic behaviour of volumetric strain has been defined by the surface. But plastic shear strain can occur inside the volumetric yield surface when the effective stress path crosses over the shear yield surface. Strictly speaking, this model should be established under an assumption that the elastic volumetric strain is small compared with the plastic volumetric strain. Otherwise, the undrained condition cannot be satisfied, i.e. the total volumetric strain is zero when the effective stress path travels under the volumetric yield surface.

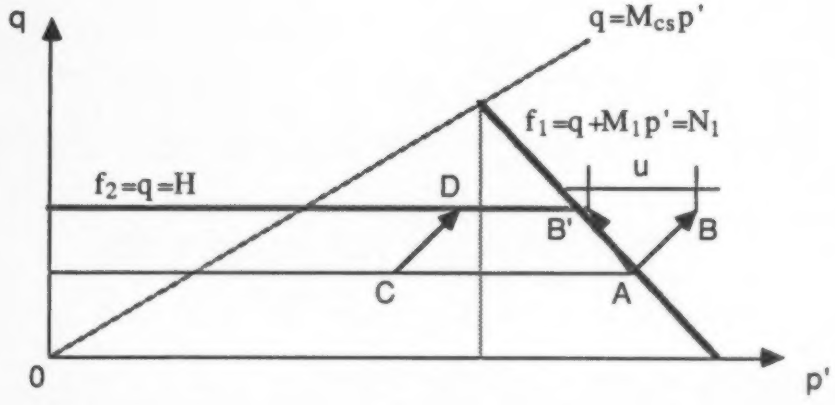

Fig. 3.2.4. The Two Yield Surface Model Given By Prevost and Hoeg (1975)

For liquefiable soils under undrained loading condition, we cannot simply define a volumetric yield surface, because the excesss pore water pressure will develop when the effective stress path moves inside the volumetric yield surface. This means that volumetric strain can occur under drained conditions for this kind of soil. Even for the undrained loading condition, the volumetric strain will sooner or later occur during the re-consolidation caused by the dissipation of excess pore water pressure. This problem has provoked a great improvement in the concept about yielding surfaces in plasticity theory. In the generalized plasticity model given by Pastor and Zienkiewicz (1986) and the bounding surface model given by Dafalias (1982), a loading surface is defined rather than a yielding surface. For liquefiable soils, the effective stress paths in zone 1 can be very well defined in laboratory undrained tests. When stress moves along these effective stress paths, total volumetric strain will not occur. It is a reasonable assumption to simplify the undrained stress analysis that either the elastic or plastic volumetric strain will occur later in re-consolidation analysis. Therefore, defining a volumetric yield surface can be replaced by defining an effective stress path. In other words, the stress has to move along the effective stress paths to satisfy the undrained condition, i.e. there is no volumetric strain, either elastic or plastic, during loading or unloading. In fact, the effective stress paths are zero volumetric strain loading surfaces. In the later re-consolidation analysis, the volumetric yield surface should be re-defined according to the effective stress state obtained in the undrained stress analysis. The plastic shear strains in zone 1 are relatively small compared with the strain at steady state and on the collapse surface for contractive materials. Therefore, it is reasonable to adopt an elastic behaviour in zone 1. Fig.3.2.5 shows a model in which the horizontal shear yield surface in p-q space is used to simulate the strain softening with the effective stress path dropping from its peak to the residual strength. For the soil behaviour during the soil skeleton structure collapse, i.e. the effective stress path dropping from the peak strength to the residual strength, the hyperbolic strain softening or brittle plastic model can be used. The shear yield surface can be simply defined by either Von Mises, Tresca or Mohr Coulomb yield surface. In this analysis, the Von Mises yield surface and the hyperbolic strain softening model defined by Chan and Morgenstern (1986,1989) are adopted.

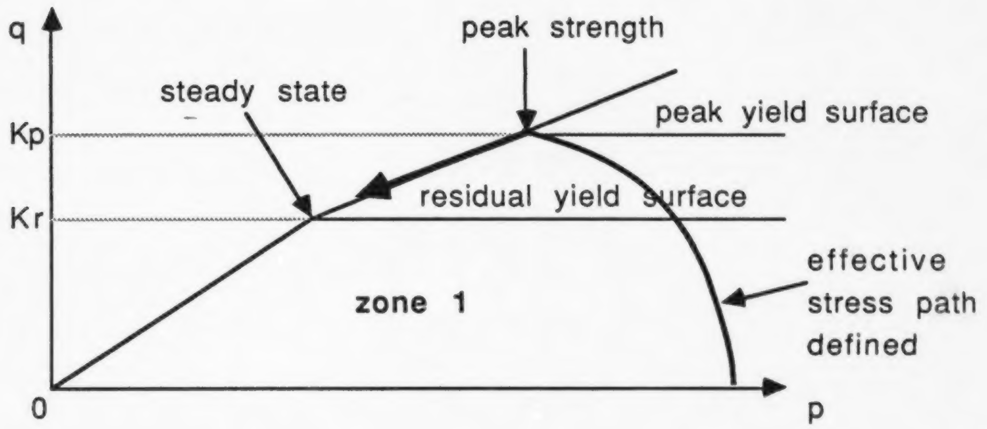
q
peak strength
steady state
Kp
peak yield surface
Kr
residual yield surface
effective stress path defined
zone 1
0
p

Fig. 3.2.5. The Shear Yield Surface For Liquefiable Soils.

3.3. Hyperbolic Strain Softening Model For Liquefiable Soils.

An elasto-plastic strain softening model was introduced by Prevost and Hoeg (1975) to simulate the deformation behaviour under undrained conditions. In this model, the loading function, i.e. yield function is given by:

$$F = q - k \tag{3.3.1}$$

where:

$$q = \sqrt{3J_2}$$

and

$$k = a\left[\frac{b(\bar{\varepsilon}^p)^2 + \bar{\varepsilon}^p}{1 + (\bar{\varepsilon}^p)^2}\right] \tag{3.3.2}$$

where: J_2 is the second stress invariant, a, b are material parameters,

$$\bar{\varepsilon}^p = \int d\bar{\varepsilon}^p \text{ = equivalent plastic strain}$$

$$d\bar{\varepsilon}^p = \left(\frac{2}{3} de^p_{ij} de^p_{ij}\right)^{1/2}$$

$$de^p_{ij} = d\varepsilon^p_{ij} - d\varepsilon^p_{kk}\delta_{ij}/3$$

and

$d\varepsilon_{ij}^{p}$ = increment of plastic strain

The parameter a can be determined by letting $\bar{\varepsilon}^p = \infty$ in equation (3.3.2) and k = kr, kr is the residual strength, then:

$$a = kr / b \qquad (3.3.3)$$

The parameter b is dependent only upon the amount of post peak softening. Using the brittleness index introduced by Bishop (1967) which can be expressed as:

$$I_b = 1 - kr/kp \qquad (3.3.4)$$

where: kp is the peak strength. The parameter b is given by:

$$b = \frac{1 - I_b}{2\sqrt{I_b}} \qquad (3.3.5)$$

In this model, the parameters a and b are often related to the peak and residual strength of the material. Once the peak and residual strengths are specified, the peak strain and post-peak softening behaviour for the material are determined and cannot be varied independently. This model is therefore restricted to only one stress strain relationship for one value of peak strength and residual strength.

In order to model a variety of stress strain relationships, i.e. to specify the peak strength, residual strength, peak strain and post peak softening behaviour independently, a hyperbolic strain softening model was introduced by Chan and Morgenstern (1986). The feature to specify the peak strength, residual strength, peak strain and post peak strain softening behaviour independently becomes more important to describe the behaviour of liquefable soils. For liquefable soils, the peak strength is no longer a constant, it depends on the effective stress path. If the post-peak strain softening behaviour and peak strength cannot be specified independently, the stress-strain behaviour becomes uncontrollable for this kind of material.

In the hyperbolic strain softening model, four parameters are introduced to describe the materials. They are the peak strength, the residual strength, the peak strain and the rate of post peak strain softening. This model is based on the plasticity formulation with a variable rate of post peak softening. The post peak behaviour is approximated by an inverted hyperbola asymptotic to the residual strength value.

The hyperbolic strain softening model assumes linear elastic behaviour for deformation prior to peak strength. Generalized Hooke's laws will be used for elastic deformation. At peak strength, yielding is defined as:

$$F = q - kp = 0 \tag{3.3.6}$$

where: $q = \sqrt{3J_2}$

and kp = uniaxial compressive peak strength.

The strength of the material decreases gradually after peak and the yield function in the post-peak region is defined as:

$$F = q - k = 0 \tag{3.3.7}$$

where:

$$k = kp\left(1 - \frac{\bar{\varepsilon}^p}{a + b\bar{\varepsilon}^p}\right) \tag{3.3.8}$$

and

$$\bar{\varepsilon}^p = \int d\bar{\varepsilon}^p = \text{equivalent plastic strain}$$

$$d\bar{\varepsilon}^p = \left(\frac{2}{3} de^p_{ij} de^p_{ij}\right)^{1/2}$$

$$de^p_{ij} = d\varepsilon^p_{ij} - d\varepsilon^p_{kk}\delta_{ij}/3$$

$$d\varepsilon^p_{ij} = \text{increment of plastic strain}$$

a and b are material parameters.

Substitute $\bar{\varepsilon}^p = \infty$ into equation (3.3.8), one has:

$$b = 1 / (1 - kr/kp) \tag{3.3.9}$$

The b parameter depends only on the amount of softening of the material. The parameter a can be determined by differentiating k with respect to $\bar{\varepsilon}^p$ in equation (3.3.8).

$$\frac{\partial k}{\partial \bar{\varepsilon}^p} = -a\, kp / (a + b\bar{\varepsilon}^p)^2 \tag{3.3.10}$$

let $\bar{\varepsilon}^p = 0$

$$\frac{\partial k}{\partial \bar{\varepsilon}^p} = -\left(\frac{kp}{a}\right) \tag{3.3.11}$$

In other words, kp/a is the tangent of the initial slope of the post peak stress strain relationship of the material. A typical stress-strain relationship of this model and the meaning of the a and b parameters are illustrated in Figure 3.3.1. The b value defines the residual strength and the a value defines the post-peak strain softening behaviour. Figure 3.3.2 shows the relationship between the a value and the post-peak strain softening behavior. The soil behaves in a more brittle manner when the a value decreases.

For a liquefiable soil, the peak strength kp is dependent on the effective stress path. Therefore, the parameter b (equation 3.3.9) is also dependent on the effective stress path. The parameter a and peak strain are still constants. This means that the post-peak softening behaviour can be specified independently which is desired for liquefiable materials. Figure 3.3.3 shows the hyperbolic strain softening model for liquefiable soils. When the undrained effective stress paths are defined in zone 1, the peak strength for any effective stress state can be determined by the point of intersection between the undrained effective stress path and the collapse surface. An numerical effective stress path model and the method to determine the peak strength kp for liquefiable soils will be discussed in Chapter 5.

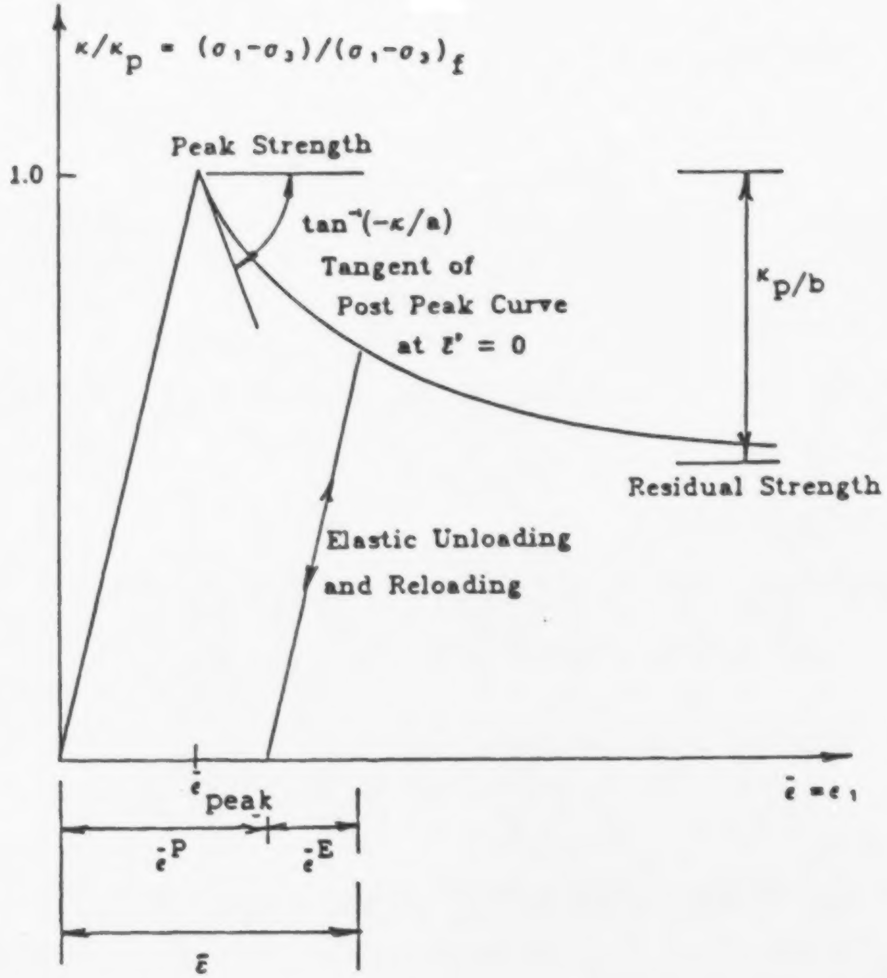
κ/κp = (σ1-σ3)/(σ1-σ3)f
Peak Strength
1.0
tan⁻¹(-κ/a)
Tangent of
Post Peak Curve
at ε̄' = 0
κp/b
Residual Strength
Elastic Unloading
and Reloading
ε̄peak
ε̄ = ε1
ε̄P
ε̄E
ε̄

Fig.3.3.1. The Hyperbolic Strain Softening Model
(after Chan, 1986)

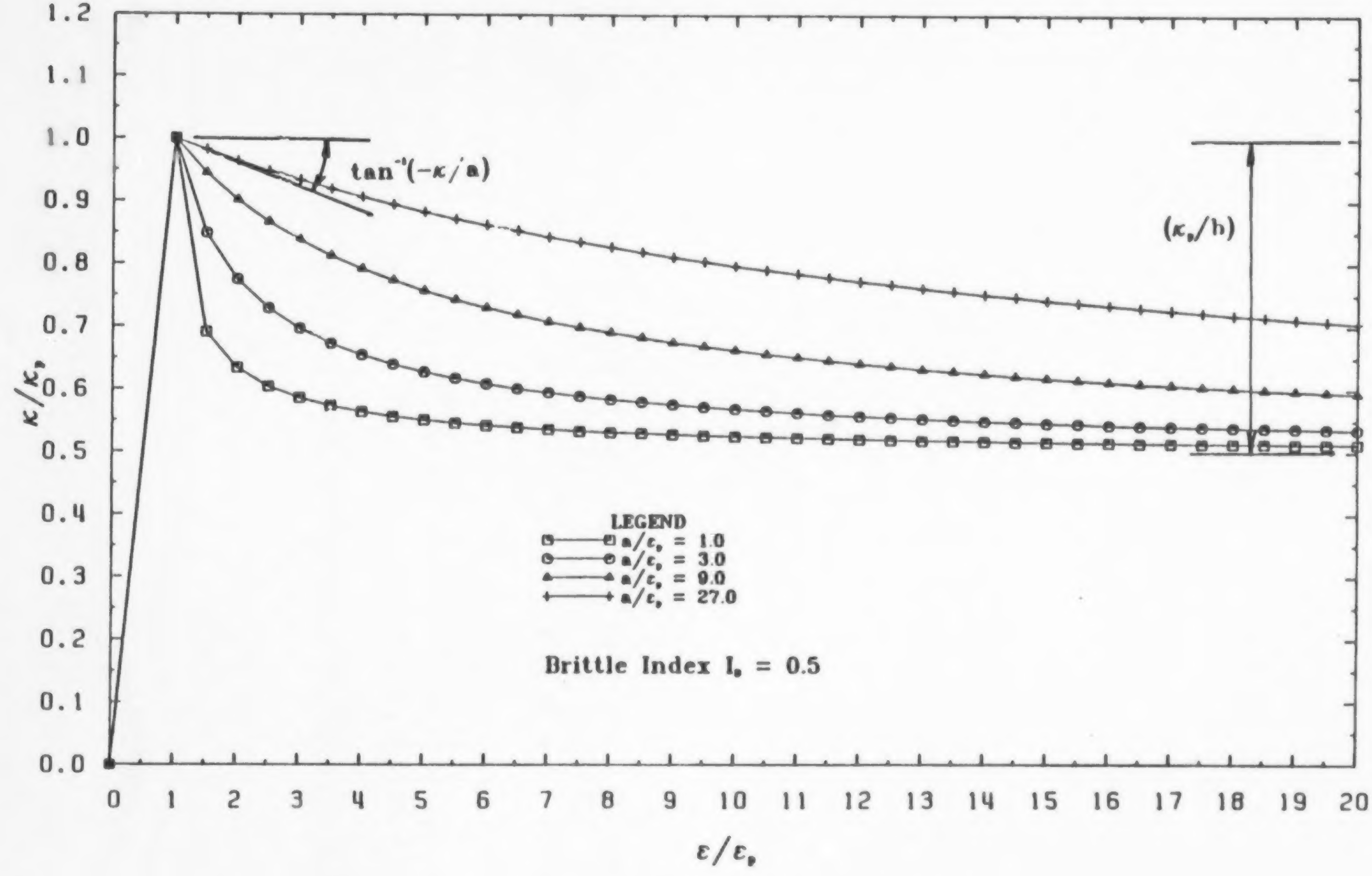

Fig.3.3.2. Post-peak Behaviour in The Hyperbolic Strain Softening Model. (after Chan, 1986)

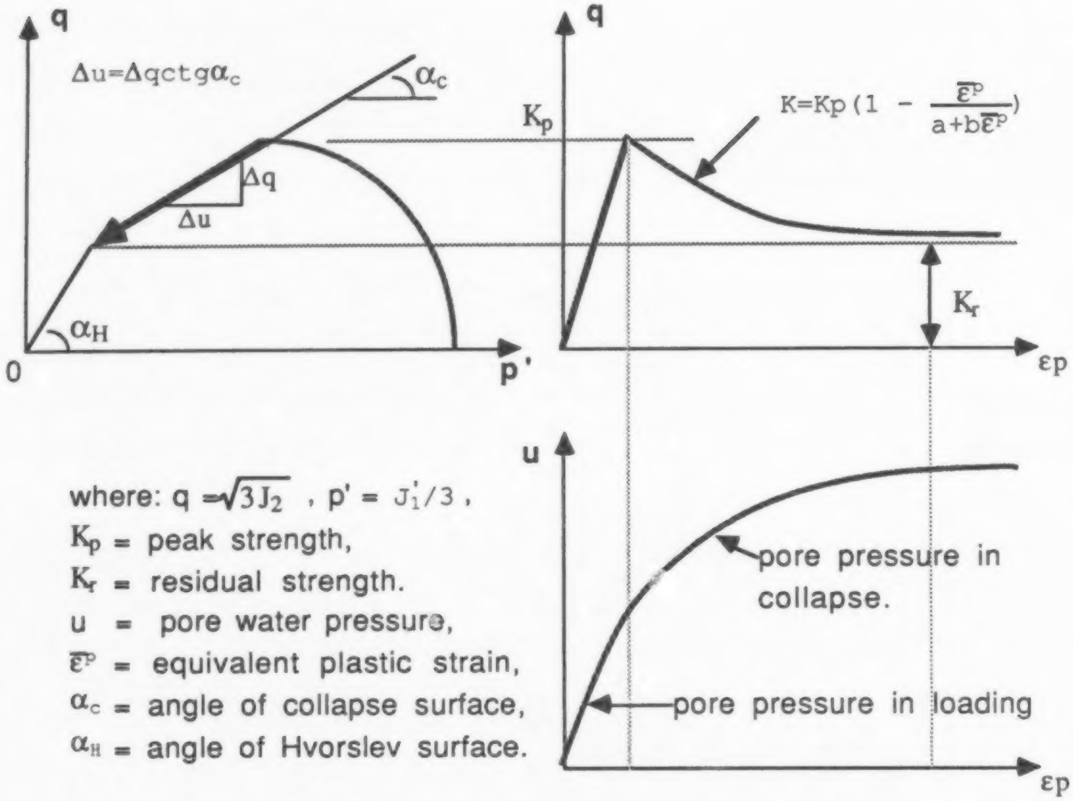
q
$\Delta u = \Delta q \, ctg \alpha_c$
α_c
Δq
Δu
α_H
0
p'
q
K_p
$K = Kp(1 - \frac{\bar{\varepsilon}^p}{a + b\bar{\varepsilon}^p})$
K_r
εp
u
pore pressure in collapse.
pore pressure in loading
εp

where: $q = \sqrt{3J_2}$, $p' = J_1'/3$,
K_p = peak strength,
K_r = residual strength.
u = pore water pressure,
$\bar{\varepsilon}^p$ = equivalent plastic strain,
α_c = angle of collapse surface,
α_H = angle of Hvorslev surface.

Fig.3.3.3. Hyperbolic Strain Softening Model For Liquefiable Soils.

4. POST-EARTHQUAKE DEFORMATION DUE TO STRESS RE-DISTRIBUTION IN EARTH STRUCTURES.

4.1. Strain Softening Behaviour of Liquefiable Soils and Stress Re-distribution in Earth Structures.

The strain softening behaviour of liquefiable soils can be observed when the following conditions are satisfied:

(1).The soils are fully saturated and loaded under undrained conditions.

(2). The effective stress path reaches the critical state boundary surface by generation of excess pore water pressure induced by either earthquake shaking or monotonic loading.

(3). The driving shear stress must be higher than the steady state strength.

The release of driving shear stress from its peak to the steady state for a liquefied material must induce re-distribution of stresses in an earth structure, particularly, when the liquefied material is located in higher shear zones. The deformation caused by the stress re-distribution may become large enough to fail the earth structure depending on the amount of energy released during strain softening or the amount of released driving shear stress, as well as the boundary conditions.

It can be expected that the deformation caused by excess pore water pressures under fully saturated and undrained conditions will be very small, because the assumption of incompressibility of inter-skeleton water and soil particles is usually adopted. Therefore, the liquefaction failure of earth structures are caused directly by the stress re-distribution and indirectly by the pore water pressures. In other words, the excess pore water pressure is just a condition for triggering failure that brings soil to the collapse surface and the stress re-distribution as a result of release in driving shear stress is the direct reason for the failure of the earth structure. On the other hand, the stress re-distribution in earth structures may cause further development in excess pore water pressures that in turn may cause further release in driving shear stress and hence further stress re-distribution.

In concept, the stress re-distribution caused by strain softening of liquefied materials is quite similar to the progressive failure defined by Bjerrum et.al (1967). In fact, the progressive failure analysis defined by Bjerrum et.al is a method to describe the stress re-distribution on a given slip surface. For earth structures with a large area of strain softening material rather than a thin layer of strain softening material, progressive failure should be considered to occur, at least in two dimensions.

To consider the stress re-distribution in a two-dimensional earth structure, a deformation analysis becomes essential.

Obviously, the finite element method is a powerful tool for this analysis.

4.2. The Yielding Surface For Strain Softening.

In the theory of plasticity, the stress-strain relationship can be expressed as:

$$\{d\sigma\} = [\ C\ ]\{d\varepsilon\} \qquad (4.2.1)$$

in which:

$$\{d\varepsilon\} = \{d\varepsilon^e\} + \{d\varepsilon^p\} \qquad (4.2.2)$$

and

$$[\ C\ ] = [\ C\ ]^e - \frac{[\ C\ ]^e\{\frac{\partial Q}{\partial \sigma}\}<\frac{\partial F}{\partial \sigma}>[\ C\ ]^e}{<\frac{\partial F}{\partial \sigma}>[\ C\ ]^e\{\frac{\partial Q}{\partial \sigma}\} - <\frac{\partial F}{\partial \varepsilon^p}>\{\frac{\partial Q}{\partial \sigma}\}} \qquad (4.2.3)$$

where: $\{d\sigma\}$ is the stress increment,

$\{d\varepsilon\}$ is the strain incement,

$\{d\varepsilon^e\}$ is the elastic strain increment,

$\{d\varepsilon^p\}$ is the plastic strain increment,

$[\ C\ ]$ is the elasto-plastic constitutive matrix,

$[\ C\ ]^e$ is the elastic constitutive matrix,

F is the yield function and Q is the plastic potential function.

Under the assumption of associated flow rule, $Q = F$.

The material behaviour can be described by the yield function as follows:

(1). For elastic deformation.

$$F(\sigma_{ij}, \varepsilon^{p}_{ij}) < 0, \qquad F(\sigma_{ij}+\Delta\sigma_{ij}, \varepsilon^{p}_{ij}+\Delta\varepsilon^{p}_{ij}) < 0 \qquad (4.2.4)$$

(2). For elastic unloading.

$$F(\sigma_{ij}, \varepsilon^{p}_{ij}) = 0, \qquad F(\sigma_{ij}+\Delta\sigma_{ij}, \varepsilon^{p}_{ij}+\Delta\varepsilon^{p}_{ij}) < 0$$

and (4.2.5)

$$<\frac{\partial F}{\partial \sigma_{ij}}>\{d\sigma_{ij}\} < 0$$

(3). For plastic deformation and strain hardening.

$$F(\sigma_{ij}, \varepsilon^{p}_{ij}) = 0, \qquad F(\sigma_{ij}+\Delta\sigma_{ij}, \varepsilon^{p}_{ij}+\Delta\varepsilon^{p}_{ij}) = 0$$

and (4.2.6)

$$<\frac{\partial F}{\partial \sigma_{ij}}>\{d\sigma_{ij}\} > 0$$

(4). For plastic deformation and strain softening.

$$F(\sigma_{ij}, \varepsilon^{p}_{ij}) = 0, \qquad F(\sigma_{ij}+\Delta\sigma_{ij}, \varepsilon^{p}_{ij}+\Delta\varepsilon^{p}_{ij}) = 0$$

and (4.2.7)

$$<\frac{\partial F}{\partial \sigma_{ij}}>\{d\sigma_{ij}\} < 0$$

For strain softening behaviour, the material is undergoing unloading but the stress state remains on the yield surface. In other words, the unloading is caused by contracting of the yield surface. This is different to elastic unloading in which the yield surface will not contract with the unloading in stress. During the collapse of liquefied materials, the stress state will remain on the collapse surface that can be satisfied by a contracting yielding surface and increasing pore water pressures.

During the stress calculation, the yield criterion should be satisfied within allowable tolerance, then an iteration procedure is used to bring the stress state back to the yield surface. This situation always occurs for strain softening materials when the yield surface contracts. The contraction of the yield surface after the peak strength will leave the state of stress outside the yield surface which is inadmissible in plasticity analysis. Therefore, the stress state after the peak strength will be projected onto the yield surface frequently during the contracting in the yield surface. In this analysis, the perpendicular projection method defined by Chan (1986) is used. This method is illustrated in Figure 4.2.1.

For the liquefiable soils, the pore water pressure will increase during the unloading in the projection of the stress state from its current yield surface to the contracted yield surface. Figure 4.2.2. shows the increment of pore water pressure and the projection of stress state for liquefiable materials. This figure shows that the effective stress state remains on the collapse surface during the projection of stress state caused by the contracting yield surface.

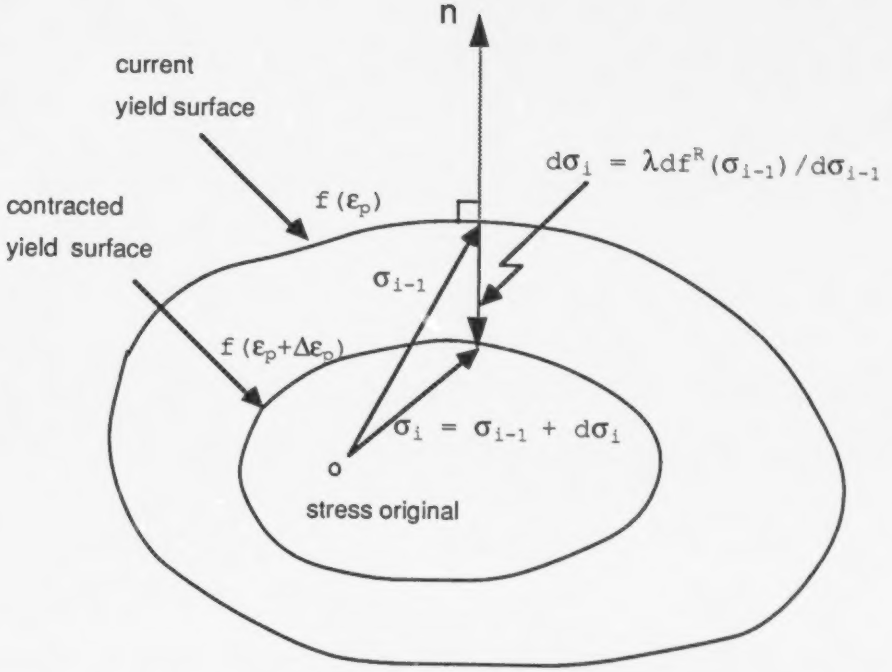
n
current
yield surface
$d\sigma_i = \lambda df^R(\sigma_{i-1})/d\sigma_{i-1}$
contracted
yield surface
$f(\varepsilon_p)$
σ_{i-1}
$f(\varepsilon_p+\Delta\varepsilon_p)$
$\sigma_i = \sigma_{i-1} + d\sigma_i$
o
stress original

Fig. 4.2.1. Perpendicular Projection Method For Contraction of Yield Surface.

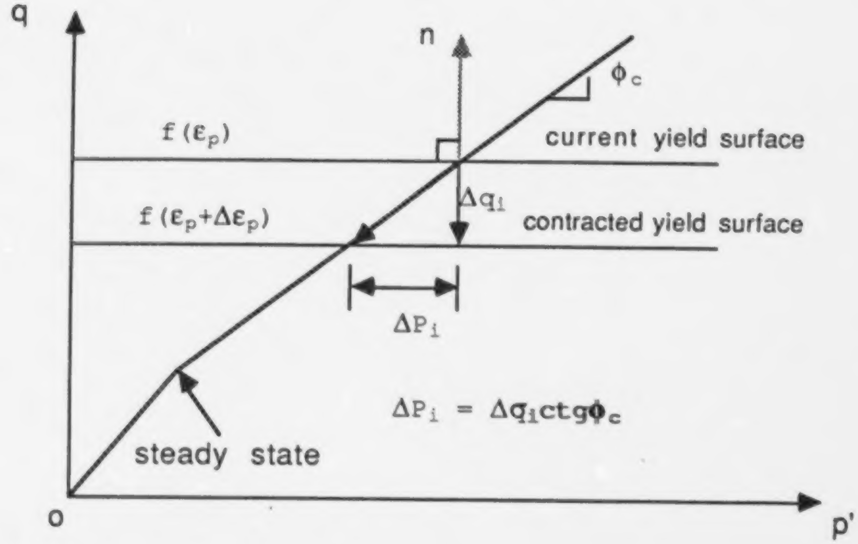
q
n
ϕ_c
$f(\varepsilon_p)$
current yield surface
Δq_i
$f(\varepsilon_p+\Delta\varepsilon_p)$
contracted yield surface
ΔP_i
$\Delta P_i = \Delta q_i \mathrm{ctg}\phi_c$
steady state
o
p'

Fig. 4.2.2. Pore Water Pressure During Contraction of Yield Surface For Liquefiable Soils.

4.3. The Unbalanced Load Caused by Contracting of Yielding Surface During Strain Softening.

Let $< \sigma^b >$ and F^b be the stress state and yield function before contraction of yield surface and $< \sigma^a >$ and F^a be the stress state and yield function after contraction of yield surface. Then:

$$F^b(\sigma^b) = 0 \tag{4.3.1}$$

before contraction of yield surface, and

$$F^a(\sigma^a) = 0 \tag{4.3.2}$$

after contraction of yield surface.

The difference in stresses $< d\sigma >$ is assumed to be perpendicular to the yield surface at the contracted stress state. That is:

$$\{ d\sigma \} = \lambda \left\{ \frac{\partial F^a(\sigma^b)}{\partial \sigma} \right\} \tag{4.3.3}$$

Since

$$dF = < \frac{\partial F^a(\sigma^b)}{\partial \sigma} > \{ d\sigma \} = F^a(\sigma^b) - F^b(\sigma^b) = F^a(\sigma^b) \tag{4.3.4}$$

therefore:

$$F^{a}(\sigma^{b}) = < \frac{\partial F^{a}(\sigma^{b})}{\partial \sigma} > \lambda \{ \frac{\partial F^{a}(\sigma^{b})}{\partial \sigma} \} \tag{4.3.5}$$

and

$$\lambda = \frac{F^{a}(\sigma^{b})}{< \frac{\partial F^{a}(\sigma^{b})}{\partial \sigma} > \{ \frac{\partial F^{a}(\sigma^{b})}{\partial \sigma} \}} \tag{4.3.6}$$

The change in stresses is given by:

$$\{ d\sigma \} = \frac{F^{a}(\sigma^{b})}{< \frac{\partial F^{a}(\sigma^{b})}{\partial \sigma} > \{ \frac{\partial F^{a}(\sigma^{b})}{\partial \sigma} \}} \{ \frac{\partial F^{a}(\sigma^{b})}{\partial \sigma} \} \tag{4.3.7}$$

Where $\{ d\sigma \} = \{ \Delta\sigma \}$ are the incremental stresses released during contracting yield surface. The unbalanced load in incremental finite element analysis can be expressed as:

$$\{ \Delta R \} = \int_{v} [B]^{T} \{ \Delta\sigma \} dV \tag{4.3.8}$$

where: [B] is the strain displacement matrix,

V = entire volume of the body.

4.4. The Governing Equation for Stress Re-distribution Analysis.

The incremental finite element equilibrium equation given by Bathe(1982) is:

$$\int_{v} [\ B\ ]^{T} \{\ \Delta\sigma\ \}\ dV = \{\ \Delta F\ \} \tag{4.4.1}$$

where: $\{\ \Delta F\ \}$ = increment of external applied load vector. The load vector includes the body force and surface traction:

$$\{\ \Delta F\ \} = \int_{v} [\ N\ ]^{T} \{\ \Delta\gamma\ \}\ dV + \int_{s} [\ N\ ]^{T} [\ N\ ] \{\ \Delta P\ \}\ dS \tag{4.4.2}$$

where: $[\ N\ ]$ = interpolation function matrix ,

$\{\ \Delta\gamma\ \}$ = incremental body force vector,

$\{\ \Delta P\ \}$ = incremental nodal surface traction vector,

S = surface subjected to external traction.

In finite element methods, the equation (4.4.1) can be rewritten as:

$$\sum_{e=1}^{n} \int_{V_e} [\ B\ ]^T \{\ \Delta\gamma\ \}\ dV = \{\ \Delta F\ \}^e \tag{4.4.3}$$

where: Ve = volume of element e, n = total number of elements.

The summations are performed to ensure nodal equilibrium and compatibility. Introducing the incremental constitutive relationship of the material:

$$\{\ \Delta\sigma\ \} = [\ C\ ]\ \{\ \Delta\varepsilon\ \} \tag{4.4.4}$$

and the strain displacement relationship:

$$\{\ \Delta\varepsilon\ \} = [\ B\ ]\ \{\ \Delta\delta\ \} \tag{4.4.5}$$

one gets the following matrix equation for incremental displacement:

$$[\ K\ ]\ \{\ \Delta\delta\ \} = \{\ \Delta F\ \} \tag{4.4.6}$$

where:

$$[\ K\ ] = \sum_{e=1}^{n} \int_{V_e} [\ B\ ]^T [\ C\ ]\ [\ B\ ]\ dV \tag{4.4.7}$$

and $\{\ \Delta\delta\ \}$ = incremental of displacement.

For stress re-distribution analysis under an assumption of zero incremental body force and surface traction, we have:

$$\{ \Delta F \} = \int_V [B]^T \{ \Delta\sigma \} dV \tag{4.4.8}$$

where $\{ \Delta\sigma \}$ are the incremental stresses released during contraction of yield surface for strain softening behaviour of liquefied materials.

Since the incremental constitutive relationship [C] and the contracted yield function F^a depend on the stress state and the plastic strain, an iteration procedure is required to obtain the solution with an acceptable degree of accuracy.

4.5. Iteration Scheme For Stress Re-distribution Analysis.

The Newton-Raphson or modified Newton-Raphson iteration scheme are widely used methods in non-linear finite element analysis. In the Newton-Raphson method, the finite element equilibrium requires:

$$f(u^*) = R(u^*)^{t+\Delta t} - F(u^*)^{t+\Delta t} = 0 \tag{4.5.1}$$

where: R is the external load vector, F is the equivalent load vector corresponding to internal stresses.

Assuming that in the iteration, we have evaluated $u_i^{t+\Delta t}$, then a Taylor series expansion gives:

$$f(u^*) = f(u_{i-1}^{t+\Delta t}) + \left[\frac{\partial f}{\partial u}\right]_{i-1}^{t+\Delta t} (u^* - u_{i-1}^{t+\Delta t}) + \cdots = 0 \tag{4.5.2}$$

neglecting higher-order terms, one has:

$$\left[\frac{\partial f}{\partial u}\right]_{i-1}^{t+\Delta t} \Delta u_i = R^{t+\Delta t} - F_{i-1}^{t+\Delta t} \tag{4.5.3}$$

and

$$\left[\frac{\partial f}{\partial u}\right]_{i-1}^{t+\Delta t} = K_{i-1}^{t+\Delta t} \tag{4.5.4}$$

then:

$$K_{i-1}^{t+\Delta t} \Delta u_i = R^{t+\Delta t} - F_{i-1}^{t+\Delta t} \tag{4.5.5}$$

For the modified Newton-Raphson method:

$$K^t \Delta u_i = R^{t+\Delta t} - F_{i-1}^{t+\Delta t} \tag{4.5.6}$$

Figure 4.5.1 and Figure 4.5.2 shows the two methods respectively. Solving equation (4.5.5) or equation (4.5.6), one has:

$$u_i^{t+\Delta t} = u_{i-1}^{t+\Delta t} + \Delta u_i \tag{4.5.7}$$

The initial conditions in this iteration are:

$$K_0^{t+\Delta t} = K^t, \quad F_0^{t+\Delta t} = F^t, \quad u_0^{t+\Delta t} = u^t \tag{4.5.8}$$

In static stress analysis by the incremental finite element method, the Δt is not an increment in real time, but a loading step.

The final approximate solution can be obtained when certain convergence criteria are satisfied. The convergence criteria include: the displacement criterion, the out-of-balance load criterion and the internal energy criterion. In this analysis, both displacement criteria and out-of-balance load criterion are used. The displacement criterion is:

$$\frac{\| \Delta u_i \|_2}{\| u_i \|_2} < \varepsilon_u \tag{4.5.9}$$

where: $\| \Delta u_i \|_2$ is the Euclidean norm of the incremental nodal displacements of the whole structure at iteration i; $\| u_i \|_2$ is the Euclidean norm of the total nodal displacement of the whole structure at iteration i; and ε_u is the displacement tolerance criterion for convergence. The tolerance ε_u is usually set to be less than 0.01%.

The out-of-balance load criterion is:

$$\frac{\left\| R^{t+\Delta t} - F_i^{t+\Delta t} \right\|_2}{\left\| R^{t+\Delta t} - F^t \right\|_2} < \varepsilon_f \tag{4.5.10}$$

where: ε_f is the unbalanced load tolerance. It is a useful factor to study the features of convergence.

The Newton-Raphson method can be sometimes very expensive since the stiffness matrix is updated at every iteration. Combining the Newton-Raphson and the modified Newton-Raphson method to update the stiffness at selected intervals can give a more effective solution scheme. Experience indicates that updating the stiffness at every 3 to 5 iterations for strain hardening materials provides a good rate of convergence. Usually updating the stiffness matrix at every iteration is necessary for strain softening materials to obtain stable convergence.

To determine the equivalent load vector $F_i^{t+\Delta t}$, the stresses corresponding to the displacement $u_i^{t+\Delta t}$ have to be calculated by a nonlinear stress-strain relationship. In the stress calculation, the Euler Forward scheme, the improved Euler scheme or the Runge-Kutta scheme can be used. A very good discussion and comparison can be found in the thesis by Chan(1986). Figure 4.5.3 shows the Euler Forward method. Figure 4.5.4 shows the Improved Euler method.

To avoid the accumulation of error during iteration, the stress calculation is usually carried out corresponding to the total incremental displacement for each load step $\Delta u = u_i^{t+\Delta t} - u^t$, not the incremental displacement during iteration Δu_i . This means that the equilibrium equation is always satisfied for each load step rather than the incremental unbalanced load during iteration. This method can be called the total loading step method. Figure 4.5.5 shows the method.

In some special cases, the initial stiffness cannot be very well defined, e.g. the loading from zero for nonlinear-elastic hyperbolic model, the above mentioned total loading step method may cause divergence. In this case, the stress calculation using incremental displacement Δu_i during iteration of unbalanced load rather than the using the incremental displacement Δu for each loading step may give a stable solution with acceptable degree of accuracy. We call this method the incremental iteration unbalance load method. Figure 4.5.6 illustrates the method. In this method, the accumulation of error may be minimized by adopting smaller subintervals in stress calculations.

Combining the total load step method and the incremental iteration unbalance load method for stress calculation can give a more effective scheme to obtain stable and more accurate solutions.

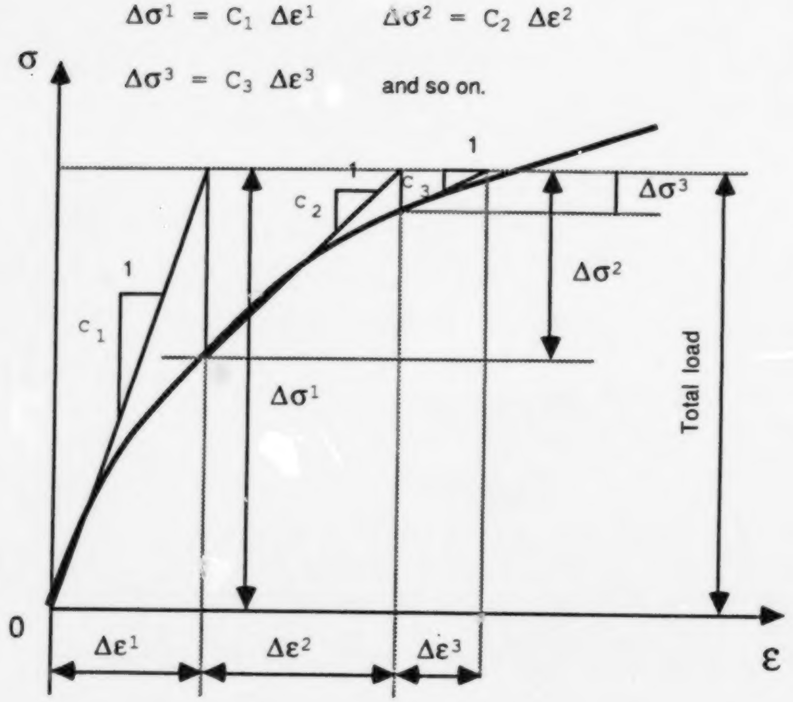
Δσ¹ = C₁ Δε¹
Δσ² = C₂ Δε²
Δσ³ = C₃ Δε³
and so on.
σ
1
c 1
1
c 2
1
c 3
Δσ³
Δσ²
Δσ¹
Total load
0
Δε¹
Δε²
Δε³
ε

Fig. 4.5.1. Newton - Raphson Method.

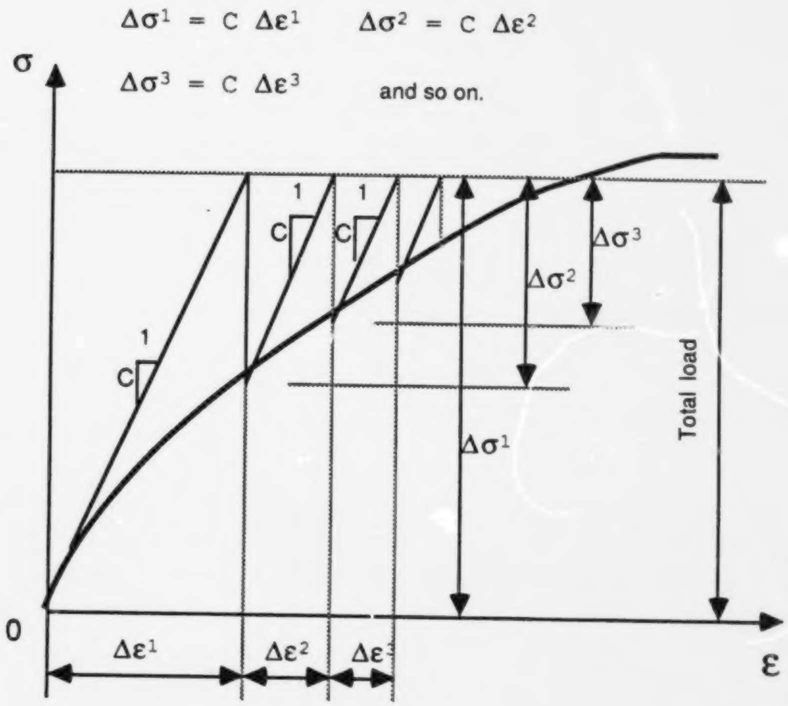
$\Delta\sigma^1 = C\ \Delta\varepsilon^1$
$\Delta\sigma^2 = C\ \Delta\varepsilon^2$
$\Delta\sigma^3 = C\ \Delta\varepsilon^3$
and so on.
σ
1
C
1
C
1
C
$\Delta\sigma^3$
$\Delta\sigma^2$
$\Delta\sigma^1$
Total load
0
$\Delta\varepsilon^1$
$\Delta\varepsilon^2$
$\Delta\varepsilon^3$
ε

Fig. 4.5.2. Modified Newton - Raphson Method.

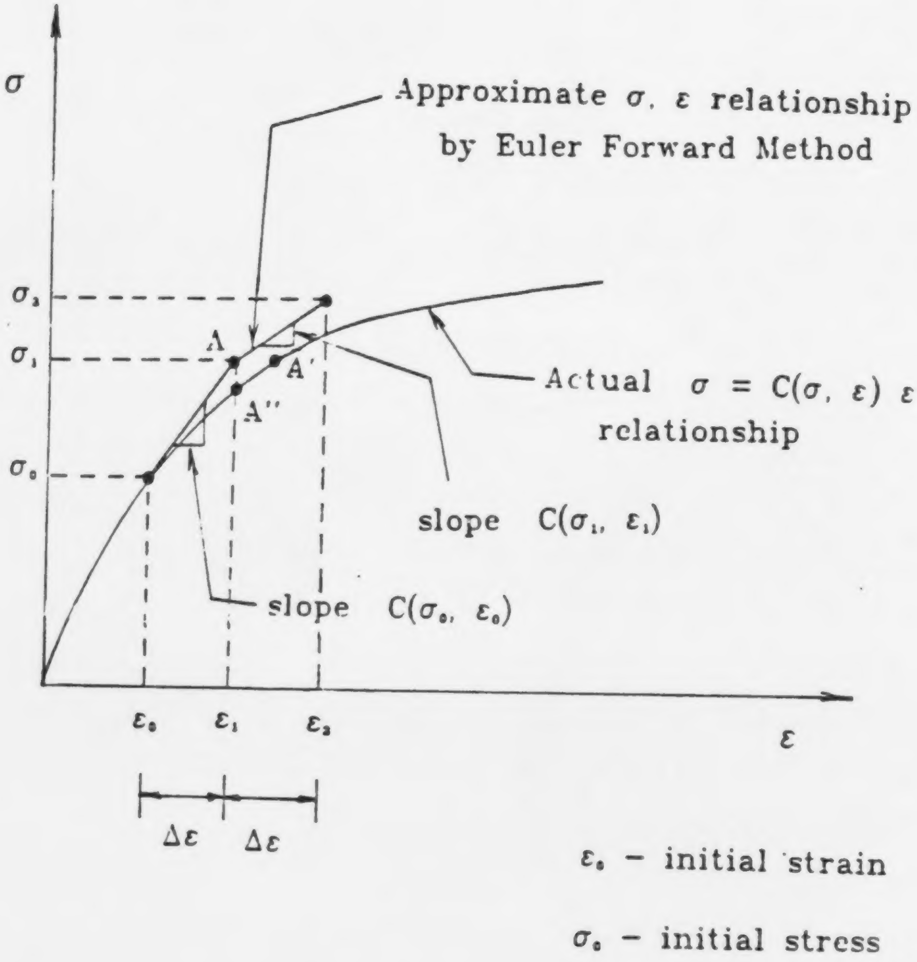
σ
Approximate σ, ε relationship by Euler Forward Method
σ_2
σ_1
σ_0
A
A'
A''
Actual σ = C(σ, ε) ε relationship
slope C(σ_1, ε_1)
slope C(σ_0, ε_0)
ε_0
ε_1
ε_2
ε
Δε
Δε
ε_0 – initial strain
σ_0 – initial stress

Fig. 4.5.3. Euler Forward Method (after Chan, 1986).

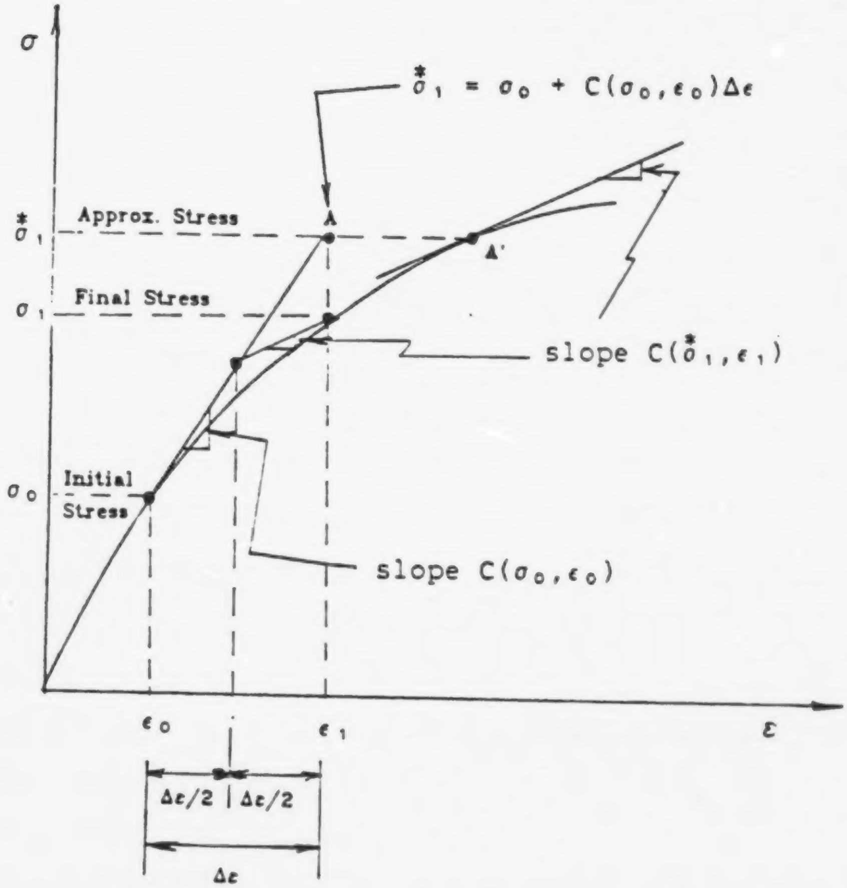
σ
$\overset{*}{\sigma}_1 = \sigma_0 + C(\sigma_0,\epsilon_0)\Delta\epsilon$
$\overset{*}{\sigma}_1$
Approx. Stress
A
A'
σ_1
Final Stress
slope $C(\overset{*}{\sigma}_1,\epsilon_1)$
σ_0
Initial Stress
slope $C(\sigma_0,\epsilon_0)$
ϵ_0
ϵ_1
ε
Δε/2
Δε/2
Δε

Fig. 4.5.4. Improved Euler Forward Method (after Chan, 1986).

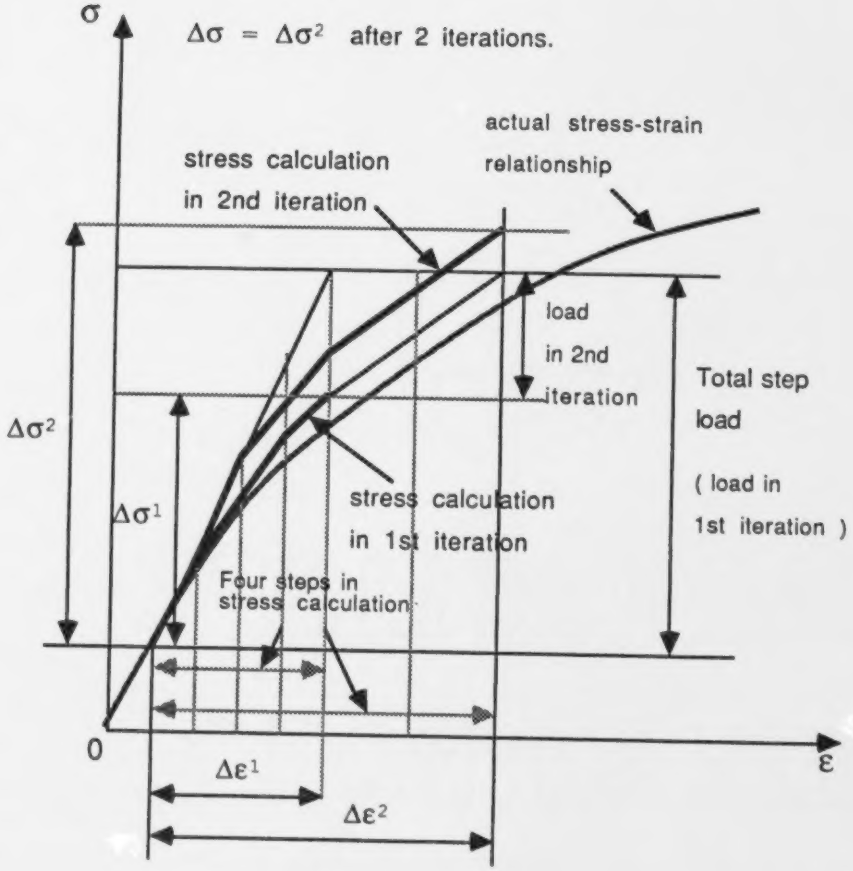
σ
Δσ = Δσ² after 2 iterations.
actual stress-strain relationship
stress calculation in 2nd iteration
load in 2nd iteration
Total step load
(load in 1st iteration)
Δσ²
Δσ¹
stress calculation in 1st iteration
Four steps in stress calculation
0
ε
Δε¹
Δε²

Fig. 4.5.5. Total Loading Step Scheme.

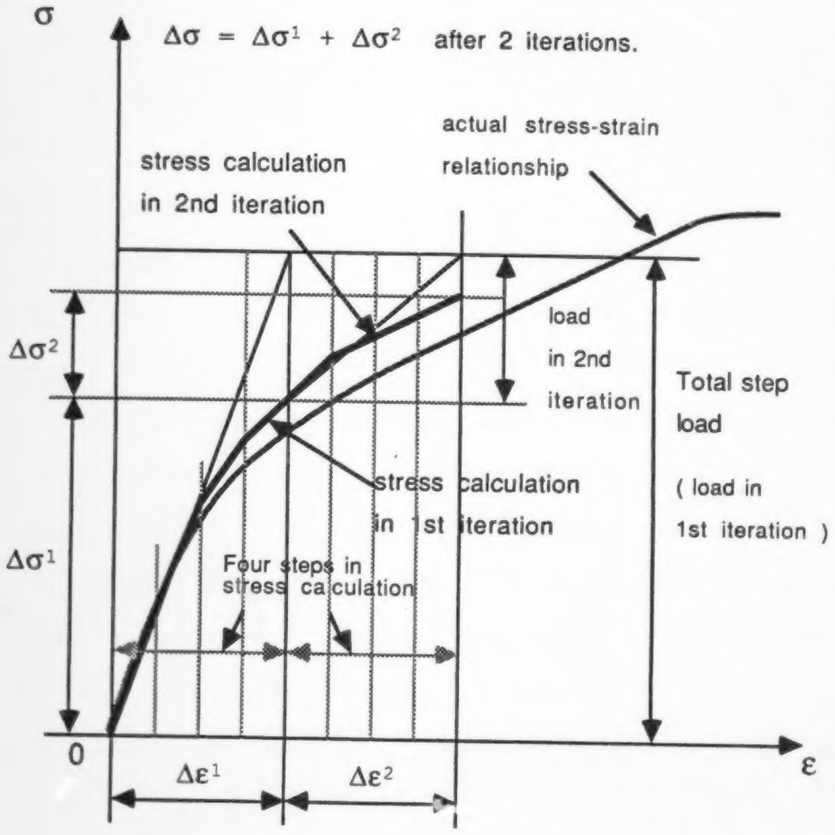
σ
Δσ = Δσ¹ + Δσ² after 2 iterations.
actual stress-strain relationship
stress calculation in 2nd iteration
Δσ²
load in 2nd iteration
Total step load
(load in 1st iteration)
stress calculation in 1st iteration
Δσ¹
Four steps in stress calculation
0
ε
Δε¹
Δε²

Fig. 4.5.6. Incremental Iteration Loading Scheme.

5. POST-EARTHQUAKE DEFORMATION DUE TO EXCESS PORE WATER PRESSURE.

5.1. The Mechanism of Re-consolidation Induced by Excess Pore Pressure.

For contractive saturated soils, the soil skeleton or grain structure can fully or partly collapse during earthquake shaking. Therefore, part of the load previously carried by the soil structure will be transferred to pore water in a short period causing the development of excess pore water pressures. The excess pore water pressures will sooner or later dissipate depending on the drainage conditions. During the dissipation, re-consolidation occurs until a new stable soil structure is formed and the excess pore water pressures reduce to zero again. Figure 5.1.1 illustrates the process. Figure 5.1.1(a) shows an initial stable soil structure in which the external static normal stress P and shear stress τ are totally carried by the stable soil structure and the excess pore water pressure $\Delta u=0$. Figure 5.1.1(b) shows the partial collapse in soil structure due to earthquake shaking τ_d. The connection between partical A and B is disturbed by the earthquake shaking and hence part of the initial static external normal stress P will be transferred to pore water causing excess pore water pressure Δu. On other hand, part of the initial static shear stress may be released because the stiffness of the soil structure becomes less. Figure 5.1.1(c) shows the re-consolidation during the dissipation of excess pore water pressure Δu. After re-consolidation, the excess pore water pressure becomes zero again, a new stable soil structure is formed and settlement Δs occurs.

A mechanism for excess pore water pressure generation during cyclic loading was introduced by Martin, Finn and Seed (1975) under an assumption that the increment of excess pore water pressure under undrained cyclic loading condition is coincident with the increment of volumetric strain under drained cyclic loading condition. Figure 5.1.2 shows the mechanism. In order to satisfy the condition of zero volumetric strain under undrained conditions, the increment of elastic rebound volumetric strain due to excess pore water pressure must equal to the increment of permanent volumetric strain that may occur under drained cyclic loading conditions. It is interesting to notice that the plastic volumetric strain caused by cyclic loading under drained condition can be obtained by a re-consolidation analysis using elastic soil behaviour.

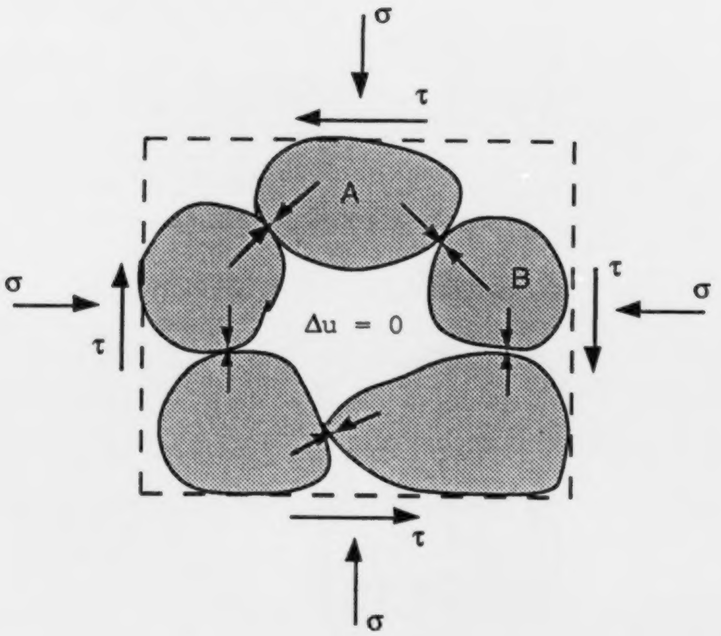
σ
τ
A
B
σ
τ
Δu = 0
τ
σ
τ
σ

(a) initial stable soil structure.

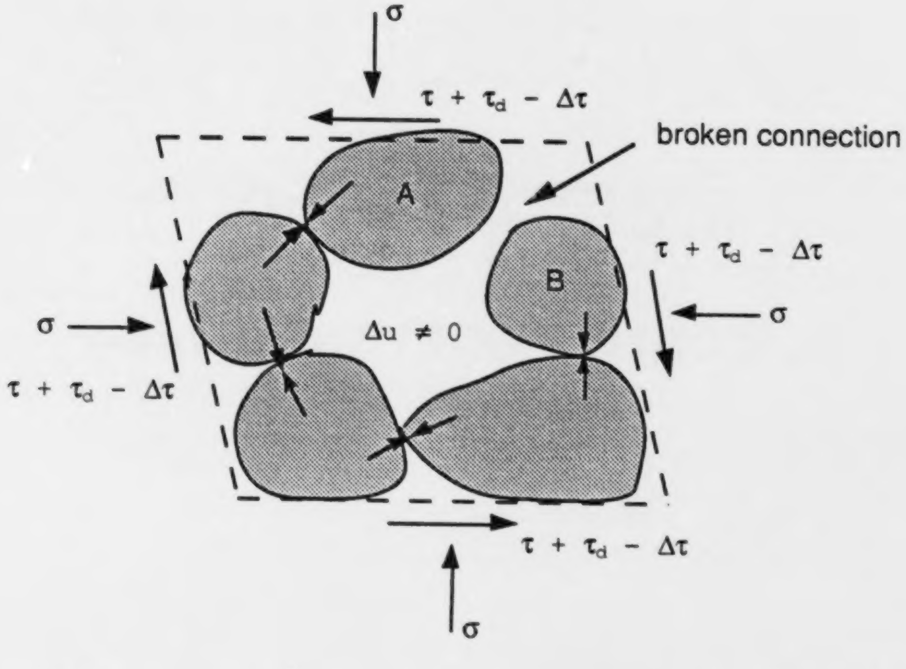
σ
τ + τd − Δτ
broken connection
A
τ + τd − Δτ
B
σ
σ
Δu ≠ 0
τ + τd − Δτ
τ + τd − Δτ
σ

(b) pore pressure due to part of collapse in soil structure

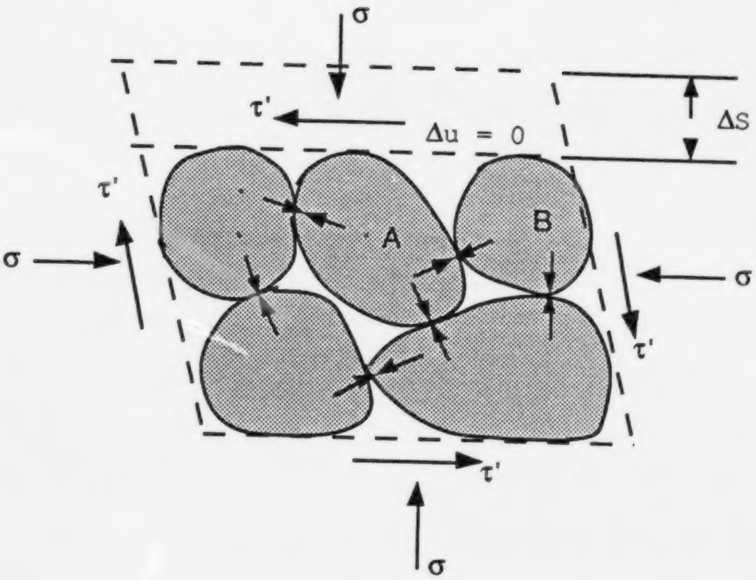
σ
τ'
Δu = 0
ΔS
τ'
σ
A
B
σ
τ'
τ'
σ

(c) settlement after re-consolidation.

Fig. 5.1.1. **Mechanism of Excess Pore Pressure and Re-consolidation.**

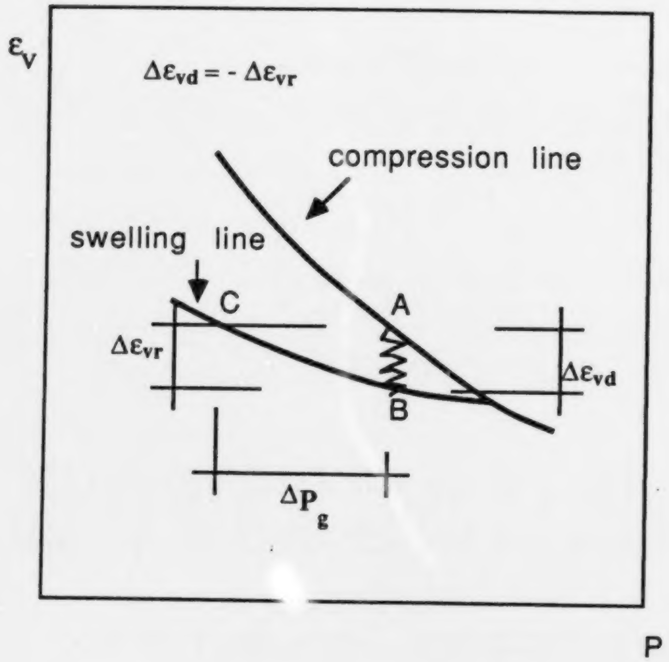
ε_v
$\Delta\varepsilon_{vd} = -\Delta\varepsilon_{vr}$
compression line
swelling line
C
A
B
$\Delta\varepsilon_{vr}$
$\Delta\varepsilon_{vd}$
ΔP_g
P

Fig.5.1.2. Mechanism of Excess Pore Pressure.

The deformation during re-consolidation can be determined by Biot's theory with rebound parameters of soils. In Biot's theory, the soils satisfy the stress equilibrium condition and the flow continuity condition simultanously. The equilibrium equation in effective stress form can be written as:

$$
\begin{aligned}
&\frac{\partial \sigma'_x}{\partial x}+\frac{\partial \tau_{xy}}{\partial y}+\frac{\partial \tau_{zx}}{\partial z}+\frac{\partial p}{\partial x}=0\\
&\frac{\partial \tau_{xy}}{\partial x}+\frac{\partial \sigma'_y}{\partial y}+\frac{\partial \tau_{yz}}{\partial z}+\frac{\partial p}{\partial y}=0 \qquad (5.1.1)\\
&\frac{\partial \tau_{zx}}{\partial x}+\frac{\partial \tau_{yz}}{\partial y}+\frac{\partial \sigma'_z}{\partial z}+\frac{\partial p}{\partial z}=-\gamma
\end{aligned}
$$

Where: σ'_x, σ'_y and σ'_z are effective normal stresses in x, y, z direction respectively, τ_{xy} is the shear stress, p is the pore water pressure and γ is the unit weight of soils.

For elastic behaviour, the stress strain relationship can be expressed by Hooke's law:

$$
\begin{aligned}
\sigma'_x &= 2G\left(\frac{\mu}{1-2\mu}\varepsilon_v + \varepsilon_x\right)\\
\sigma'_y &= 2G\left(\frac{\mu}{1-2\mu}\varepsilon_v + \varepsilon_y\right) \qquad (5.1.2)\\
\sigma'_z &= 2G\left(\frac{\mu}{1-2\mu}\varepsilon_v + \varepsilon_z\right)\\
\tau_{xy} &= G\gamma_{xy},\ \tau_{zx} = G\gamma_{zx},\ \tau_{yz} = G\gamma_{yz}
\end{aligned}
$$

where: ε_x, ε_y and ε_z are normal strain compornances in x, y, z direction respectively, γ_{xy} is the shear strain, $\varepsilon_v = \varepsilon_x + \varepsilon_y + \varepsilon_z$

is the volumetric strain, μ is the poisson's ratio and G is the shearing modulus, and:

$$G = \frac{E}{2(1+\mu)} \tag{5.1.3}$$

in which: E is the Young's modulus.

The strain displacement relationship under small strain conditions are:

$$\begin{aligned} \varepsilon_x &= -\frac{\partial u}{\partial x},\ \varepsilon_y = -\frac{\partial v}{\partial y},\ \varepsilon_z = -\frac{\partial w}{\partial z} \\ \gamma_{xy} &= -(\frac{\partial v}{\partial x}+\frac{\partial u}{\partial y}),\ \gamma_{zx} = -(\frac{\partial u}{\partial z}+\frac{\partial w}{\partial x}),\ \gamma_{yz} = -(\frac{\partial w}{\partial y}+\frac{\partial v}{\partial z}) \end{aligned} \tag{5.1.4}$$

where: u, v, w are components of displacements in x y z direction respectively, the minus in these equations means the definition of positive in compression in soil mechanics.

Substitute (5.1.2) and (5.1.4) into (5.1.1), the equilibrium equation can be rewritten in displacements and pore water pressures as:

$$\begin{aligned} -G\nabla^2 u + \frac{G}{1-2\mu}\frac{\partial}{\partial x}(\frac{\partial u}{\partial x}+\frac{\partial v}{\partial y}+\frac{\partial w}{\partial z}) + \frac{\partial p}{\partial x} &= 0 \\ -G\nabla^2 v + \frac{G}{1-2\mu}\frac{\partial}{\partial x}(\frac{\partial u}{\partial x}+\frac{\partial v}{\partial y}+\frac{\partial w}{\partial z}) + \frac{\partial p}{\partial y} &= 0 \\ -G\nabla^2 w + \frac{G}{1-2\mu}\frac{\partial}{\partial x}(\frac{\partial u}{\partial x}+\frac{\partial v}{\partial y}+\frac{\partial w}{\partial z}) + \frac{\partial p}{\partial z} &= -\gamma \end{aligned} \tag{5.1.5}$$

Therefore, the incremental equilibrium equation are:

$$-G\nabla^2\Delta u + \frac{G}{1-2\mu}\frac{\partial}{\partial x}\left(\frac{\partial \Delta u}{\partial x}+\frac{\partial \Delta v}{\partial y}+\frac{\partial \Delta w}{\partial z}\right)+\frac{\partial \Delta p}{\partial x}=0$$

$$-G\nabla^2\Delta v + \frac{G}{1-2\mu}\frac{\partial}{\partial x}\left(\frac{\partial \Delta u}{\partial x}+\frac{\partial \Delta v}{\partial y}+\frac{\partial \Delta w}{\partial z}\right)+\frac{\partial \Delta p}{\partial y}=0 \qquad (5.1.6)$$

$$-G\nabla^2\Delta w + \frac{G}{1-2\mu}\frac{\partial}{\partial x}\left(\frac{\partial \Delta u}{\partial x}+\frac{\partial \Delta v}{\partial y}+\frac{\partial \Delta w}{\partial z}\right)+\frac{\partial \Delta p}{\partial z}=0$$

For a saturated material under an assumption of incompressible inter-skeleton fluid and soil particles, the flow continuity equation is:

$$\frac{\partial \varepsilon_v}{\partial t} = -\frac{1}{\gamma_w}\left(k_x\frac{\partial^2 p}{\partial x^2}+k_y\frac{\partial^2 p}{\partial y^2}+k_z\frac{\partial^2 p}{\partial z^2}\right) \qquad (5.1.7)$$

Substitute (5.1.4) into (5.1.7), one has:

$$\frac{\partial}{\partial t}\left(\frac{\partial u}{\partial x}+\frac{\partial v}{\partial y}+\frac{\partial w}{\partial z}\right)-\frac{1}{\gamma_w}\left(k_x\frac{\partial^2 p}{\partial x^2}+k_y\frac{\partial^2 p}{\partial y^2}+k_z\frac{\partial^2 p}{\partial z^2}\right)=0 \qquad (5.1.8)$$

The equation (5.1.8) can be re-written in an incremental form as:

$$\left(\frac{\partial \Delta u}{\partial x}+\frac{\partial \Delta v}{\partial y}+\frac{\partial \Delta w}{\partial z}\right)-\frac{\Delta t}{\gamma_w}\left(k_x\frac{\partial^2 \Delta p}{\partial x^2}+k_y\frac{\partial^2 \Delta p}{\partial y^2}+k_z\frac{\partial^2 \Delta p}{\partial z^2}\right)=$$

$$=\frac{\Delta t}{\gamma_w}\left(k_x\frac{\partial^2 p^t}{\partial x^2}+k_y\frac{\partial^2 p^t}{\partial y^2}+k_z\frac{\partial^2 p^t}{\partial z^2}\right) \qquad (5.1.9)$$

The incremental displacements and pore water pressures can be obtained by solving equation (5.1.6) and (5.1.9). The finite element method can be used to solve the equations.

5.2. Flow Continuity Equation for Re-consolidation with Excess Pore Pressure Development.

Fig. 5.2.1. shows the mechanism of the re-consolidation associated simultanously with the generation of the excess pore water pressure. In the figure, $\Delta\varepsilon_{vs}$ is the volumetric strain during re-consolidation, $\Delta\varepsilon_{vd}$ is the volumetric strain due to dynamic densification under drainage condition and $\Delta\varepsilon_{vr}$ is the rebound volumetric strain due to the increase of pore water pressure. The volumetric strain $\Delta\varepsilon_{vs}$ during re-consolidation associated with generation of excess pore water pressure should equal to the summation of the volumetric strain $\Delta\varepsilon_{vd}$ due to dynamic densification and the rebound volumetric strain $\Delta\varepsilon_{vr}$ due to the increase in excess pore water pressure. Under a positive definition of compression, $\Delta\varepsilon_{vr}$ is a negative value, $\Delta\varepsilon_{vd}$ should be a positive value for contractive soils and $\Delta\varepsilon_{vs}$ is a positive value during re-consolidation. The relationship among these three components of volumetric strain is:

$$\Delta\varepsilon_{vs} = \Delta\varepsilon_{vr} + \Delta\varepsilon_{vd} \qquad (5.2.1)$$

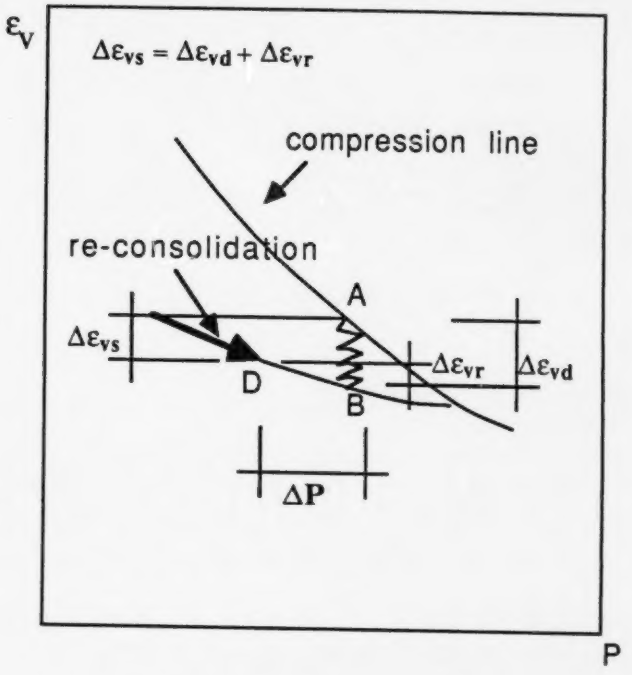
ε_V
$\Delta\varepsilon_{vs} = \Delta\varepsilon_{vd} + \Delta\varepsilon_{vr}$
compression line
re-consolidation
A
$\Delta\varepsilon_{vs}$
D
B
$\Delta\varepsilon_{vr}$
$\Delta\varepsilon_{vd}$
ΔP
P

Fig.5.2.1. **Mechanism of Re-consolidation Associated With Pore Water Pressure Generation.**

The flow continuity equation can be expressed as:

$$\nabla^2\left(\frac{k}{\gamma_w}P\right) = -\frac{\partial\varepsilon_{vs}}{\partial t} = -\frac{\partial\varepsilon_{vr}}{\partial t} - \frac{\partial\varepsilon_{vd}}{\partial t} \qquad (5.2.2)$$

the left term is the net flow of water into an element of soil, the middle term is the increment of volumetric strain due to re-consolidation, the first term of the right side is the increment of volumetric strain due to the changes in effective stresses, the second term of right side is the increment of accumulated volumetric strain due to dynamic loading. The increment of volumetric strain due to the changes of effective stresses can be determined by equilibrium equations and the increment of accumulated volumetric strain during dynamic loadings should be determined by dynamic analysis.

The incremental equation of flow continuity from t to t + Δt can be expressed as:

$$\Delta\varepsilon_{vr} + \Delta t\nabla^2\left(\frac{k}{\gamma_w}\Delta P\right) = -\Delta t\nabla^2\left(\frac{k}{\gamma_w}P^t\right) - \Delta\varepsilon_{vd} \qquad (5.2.3)$$

The increment of accumulated volumetric strain during dynamic loading can be expressed by the increment of excess pore water pressure as:

$$\Delta\varepsilon_{vd} = M_{v3}\,\Delta P_g \qquad (5.2.4)$$

In which: M_{v3} =1/B, and B is the bulk modulus:

$$B = \frac{E}{3(1-2\mu)} \tag{5.2.5}$$

Then, the equation (5.2.3) can be re-written as:

$$\Delta\varepsilon_{vr} + \Delta t\nabla^2(\frac{k}{\gamma_w}\Delta P) = -\Delta t\nabla^2(\frac{k}{\gamma_w}P^t) - M_{v3}\Delta P_g \tag{5.2.6}$$

This equation is similar to equation (5.1.9) except for the last term on the right hand side.

The rebound volumetric strains due to the changes in effective stress are elastic strains rather than plastic strains because the effective stress paths are moving on an elastic wall inside the volumetric yield surface. Then, we have the following relationship:

$$-\frac{\partial\varepsilon_{vr}}{\partial t} = \frac{3(1-2\mu)}{E}\left[\frac{\partial P}{\partial t} - \frac{1}{3}(\frac{\partial\sigma_x}{\partial t} + \frac{\partial\sigma_y}{\partial t} + \frac{\partial\sigma_z}{\partial t})\right] \tag{5.2.7}$$

Finally we have:

$$\nabla^2(\frac{k}{\gamma_w}P) = \frac{3(1-2\mu)}{E}\left[\frac{\partial P}{\partial t} - \frac{1}{3}(\frac{\partial\sigma_x}{\partial t} + \frac{\partial\sigma_y}{\partial t} + \frac{\partial\sigma_z}{\partial t})\right] - M_{v3}\frac{\partial P_g}{\partial t} \tag{5.2.8}$$

If there is no change in total stresses, the increment of isotropic effective stresses are:

$$\Delta\sigma'_x = \Delta\sigma'_y = \Delta\sigma'_z = -\Delta P \tag{5.2.9}$$

By Hooke's stress strain relationship, we have:

$$\nabla^2\left(\frac{k}{\gamma_w}P\right) = M_{v3}\left(\frac{\partial P}{\partial t} - \frac{\partial P_g}{\partial t}\right) \tag{5.2.10}$$

This equation is similar to the equation given by Seed et.al. (1977).

For the one-dimensional consolidation problem, equation (5.2.10) can be re-written as:

$$\frac{\partial P}{\partial t} = \overline{E}_r \frac{\partial}{\partial z}\left(\frac{k_z \partial P}{\gamma_w \partial z}\right) + \overline{E}_r \frac{\partial \varepsilon_{vd}}{\partial t} \tag{5.2.11}$$

This is the same as given by Finn et.al (1977).

5.3. Pore Water Pressure Caused by Undrained Cyclic Loadings.

The increment of excess pore water pressure caused by undrained cyclic loading can be predicted by the following models:

(1). Martin-Finn-Seed Model.

$$\Delta P = E_r \Delta\varepsilon_{vd} \tag{5.3.1a}$$

and

$$\Delta\varepsilon_{vd} = C_1(\gamma - C_2\varepsilon_{vd}) + \frac{C_3\varepsilon_{vd}^2}{(\gamma + C_4\varepsilon_{vd})} \tag{5.3.1b}$$

(2). Zienkiewicz Model

$$dp = -\beta \, d\varepsilon_v^0 \qquad (5.3.2a)$$

where:

$$\beta = \frac{1}{\left(\frac{n}{Kf} + \frac{1}{Ks}\right)} \approx Ks \qquad (5.3.2b)$$

$$d\varepsilon_v^0 = \frac{-A}{1 + B\,k}\, dk \qquad (5.3.2c)$$

$$dk = d\xi \, e^{\theta\,\gamma} \qquad (5.3.2d)$$

and

$$d\xi = \sqrt{(de_{ij}de_{ij}} \qquad (5.3.2e)$$

(3) Finn 's Endochronic Model

$$\frac{u}{\sigma_o'} = (A / B) \ln (1 + B\,k) \qquad (5.3.3a)$$

where:

$$k = \xi \, e^{\lambda\,\gamma} \qquad (5.3.3b)$$

$$d\xi = \sqrt{(\frac{1}{2} d\varepsilon_{ij} d\varepsilon_{ij}} \qquad (5.3.3c)$$

(4) Modified Finn-Seed Equations.

$$\frac{u}{u_m} = \frac{1}{2} + \frac{1}{\pi}\left[\sin^{-1}(2 (\frac{N}{N_m})^{\alpha} - 1 \right] \tag{5.3.4a}$$

where:

$$u_m = \sigma_0 - \frac{\sigma_1 - \sigma_3}{2 \sin\varnothing} + c \tan\varnothing \tag{5.3.4b}$$

$$N_m = (\frac{\tau_d}{A\ \sigma_3})^{\frac{1}{B}} \tag{5.3.4c}$$

$$A = \alpha_1 (Kc - 1)^2 + \alpha_2 \tag{5.3.4d}$$

and

$$B = \alpha_3 (Kc - 1)^2 + \alpha_4 \tag{5.3.4e}$$

5.4. Pore Water Pressure Caused by Undrained Monotonic Loadings.

5.4.1. Pore water parameters A and B

For a three-dimensional undrained loading, the total change in volume of the soil skeleton is:

$$\Delta V_s = V_o\,(\,C_c^1\,\Delta\sigma_1' + C_c^2\,\Delta\sigma_2' + C_c^3\,\Delta\sigma_3'\,) \qquad (5.4.1)$$

where: C_c^1, C_c^2, and C_c^3 are compressibilities of soil skeleton in σ_1', σ_2', σ_3' directions respectively, $\Delta\sigma_1'$, $\Delta\sigma_2'$, $\Delta\sigma_3'$ are the increments of principal stresses, and V_o is initial total volume of soil-water system.

The change in volume of fluid is:

$$\Delta V_f = n\,V_o\,C_w\Delta P_s \qquad (5.4.2)$$

where: C_w is the compressibility of water and n is the porosity of soil.

For undrained condition, one has:

$$\Delta V_f = \Delta V_s \qquad (5.4.3)$$

Hence:

$$nC_w \, \Delta P_s = C_c^1 \Delta\sigma_1' + C_c^2 \Delta\sigma_2' + C_c^3 \Delta\sigma_3' \qquad (5.4.4)$$

By the definition of effective stress:

$$\Delta\sigma' = \Delta\sigma - \Delta P_s \qquad (5.4.5)$$

then we have:

$$\Delta P_s = \frac{1}{nC_w + C_c^1 + C_c^2 + C_c^3} \left(C_c^1 \, \Delta\sigma_1 + C_c^2 \Delta\sigma_2 + C_c^3 \Delta\sigma_3 \right) \qquad (5.4.6)$$

For the increments of isotropic stresses, i.e. $\Delta\sigma_1 = \Delta\sigma_2 = \Delta\sigma_3$, and an isotropic soil element, i.e. $C_c^1 = C_c^2 = C_c^3 = C_c$, then we have:

$$\frac{\Delta P_s}{\Delta\sigma} = \frac{1}{1 + nC_w/C_c} = B \qquad (5.4.7)$$

For an increment of uniaxial stress, one has:

$$\Delta\sigma_1' = \Delta\sigma_1 - \Delta P_s \qquad \Delta\sigma_2' = \Delta\sigma_3' = -\Delta P_s \qquad (5.4.8)$$

then, from (5.4.4), we have:

$$\frac{\Delta P_s}{\Delta\sigma_1} = \frac{1}{1 + n\frac{C_w}{C_c^1} + \frac{C_c^2}{C_c^1} + \frac{C_c^3}{C_c^1}} \qquad (5.4.9)$$

if soil is isotropic and pore fluid is incompressible, we have:

$$\frac{\Delta \mathbf{P_s}}{\Delta\sigma_1} = \frac{1}{1 + 2\,\dfrac{\mathbf{C_c^3}}{\mathbf{C_c^1}}} = \mathbf{A} \qquad (5.4.10)$$

For an element of soil subjected to a triaxial loading, we have:

$$\Delta\sigma_2 = \Delta\sigma_3 \qquad (5.4.11)$$

This three-dimensional loading can be considered to be made up of an isotropic stress plus a deviator stress, then, we have:

$$\Delta \mathbf{P_s} = \mathbf{B}\ \Delta\sigma_3 + \mathbf{A}\ (\Delta\sigma_1 - \Delta\sigma_3) \qquad (5.4.12)$$

The pore water pressure generated due to the changes in total stresses under undrained condition can be expressed in a general form given by Henkel (1960).

$$\Delta u = \frac{\beta}{3}(\Delta\sigma_1+\Delta\sigma_2+\Delta\sigma_3)+$$

$$+\alpha\sqrt{(\Delta\sigma_1-\Delta\sigma_2)^2+(\Delta\sigma_2-\Delta\sigma_3)^2+(\Delta\sigma_3-\Delta\sigma_1)^2} \qquad (5.4.13)$$

where: $\Delta\sigma_1, \Delta\sigma_2, \Delta\sigma_3$ are the changes in total principal stresses, and α, β are pore pressure parameters. These parameters can be easily related to the Skempton pore pressure parameters A and B in equation (5.4.12).

The parameter β is for the pore pressure developed by an increment of mean hydrostatic stress, or isotropic stress caused by three dimensional loading. It is a function of saturation degree of materials and equals unity for fully saturated materials.

The parameter α is for the pore pressure developed by an increment of the second stress invariant. It is usually more complicated than the parameter β. The parameter α depends on the following factors:

(1). The strain to which the soil element has been subjected during undrained loading.

(2). The initial stress state, i.e. isotropic or anisotropic consolidation conditions.

(3). The stress history, i.e. normally consolidated or over-consolidated.

(4). The loading or unloading.

Figure 5.4.1. shows these factors.

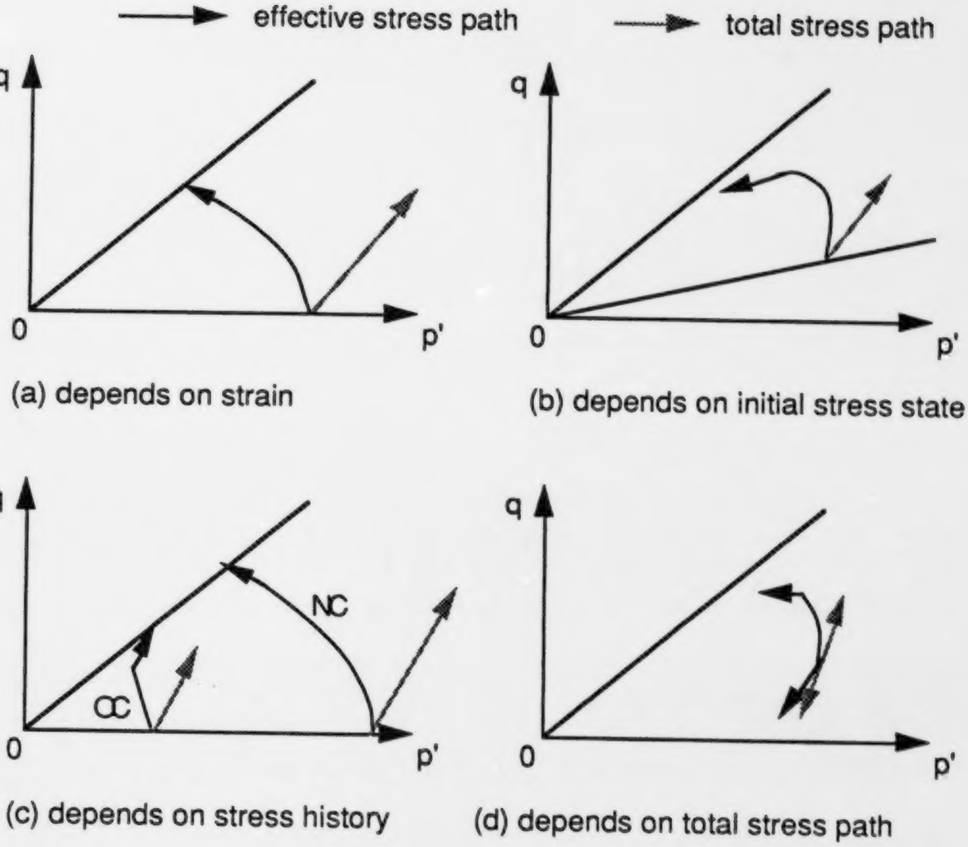
effective stress path
total stress path
q
0
p'
q
0
p'
q
NC
OC
0
p'
q
0
p'

(a) depends on strain

(b) depends on initial stress state

(c) depends on stress history

(d) depends on total stress path

Fig.5.4.1. Factors Influencing Parameter A.

5.4.2. Effective stress path model for liquefiable soils .

For liquefiable soils, the residual strength, i.e. steady state strength is independent of the effective stress state, but the peak strength is very much dependent on the effective stress state. The effective stress state can be changed by either the excess pore water pressure during undrained loading condition or consolidation during drained loading. When the effective stress paths are defined in zone 1, we can determine the peak strength for any effective stress state without difficulty.

Fig. 5.4.2 shows the typical effective stress paths and the contours of shear strain for liquefiable soils. The contours of shear strain are quite well coincident with the contours of q/p ratio. It is a flexible method to express the function numerically.

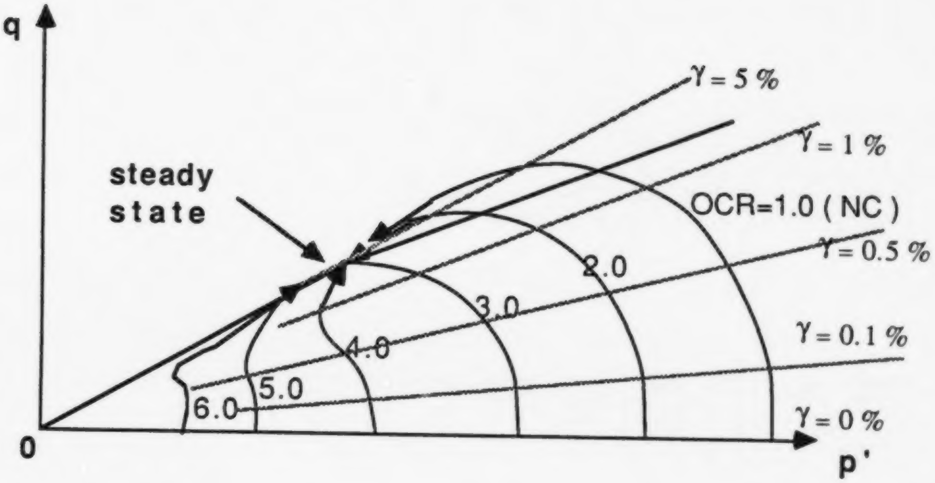
q
γ = 5 %
γ = 1 %
steady
state
OCR=1.0 (NC)
γ = 0.5 %
2.0
3.0
γ = 0.1 %
4.0
5.0
6.0
γ = 0 %
0
p'

Fig.5.4.2. The Effective Stress Paths under Undrained Condition.

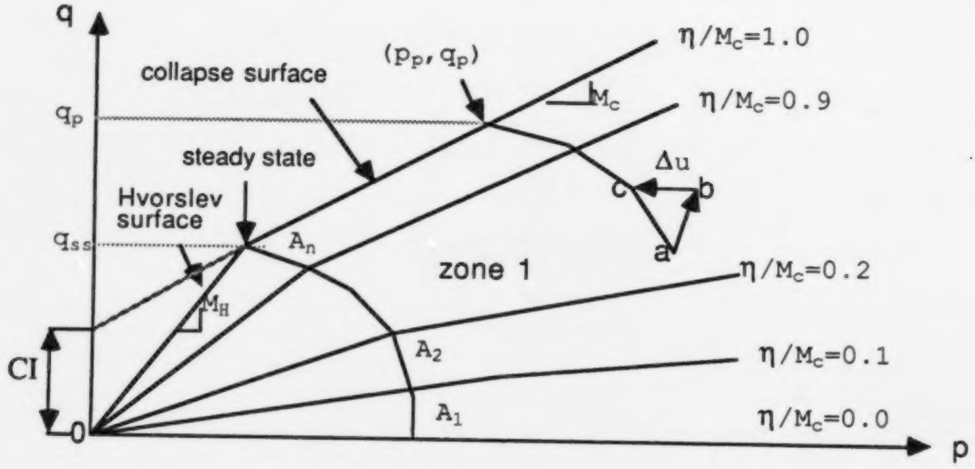
q
collapse surface
(p_p, q_p)
$\eta/M_c=1.0$
M_c
$\eta/M_c=0.9$
q_p
steady state
Δu
c
b
Hvorslev
surface
a
q_{ss}
A_n
zone 1
$\eta/M_c=0.2$
M_H
A_2
$\eta/M_c=0.1$
CI
0
A_1
$\eta/M_c=0.0$
p

Fig. 5.4.3. The Numerical Effective Stress Path Model for Liquefiable Soils.

Figure 5.4.3 shows a numerical effective stress path model. In this model, zone 1 is divided into a number of q/p ratio intervals. The pore pressure parameter A value can be determined approximately by a linear function between the minimum q/p interval and maximum q/p interval. The A value in the minimum q/p interval can be expressed as Ao, and the A value in the maximum q/p interval can be expressed as Am. Then the A value in the i q/p interval can be expressed as:

$$Ai = Ao + (Am - Ao)(i - 1)/(n - 1) \tag{5.4.14}$$

where: n is the total number of intervals.

If we know an effective stress state(p, q) in the i interval, then, we can express the effecive stress on i +1 contour line of q/p ratio (p_{i+1}, q_{i+1}) as follows:

$$\frac{(p - p_{i+1})}{(q_{i+1} - q)} = Ai \tag{5.4.15}$$

$$\frac{q_{i+1}}{p_{i+1} + c/\tan\phi_p} = \eta_{i+1} \tag{5.4.16}$$

where: c is an imagined cohesion obtained by extending the collapse surface line to the q axis, ϕ_p is the angle of the collapse surface, and the η_{i+1} is the q/p value of the i+1 contour line of the q/p ratio. If zone-1 is divided into n equal increments of q/p values, then η_{i+1} can be simply expressed as $\eta_{i+1} = i/n$. Solving the equation group (5.4.15) and (4.4.16), one has:

$$p_{i+1} = \frac{A_i q + p - A_i \eta_{i+1} c/\tan\phi_p}{1 + A_i \eta_{i+1}} \tag{5.4.17}$$

$$q_{i+1} = \frac{(A_i q + p + c/\tan\phi_p)\eta_{i+1}}{1 + A_i \eta_{i+1}} \tag{5.4.18}$$

Similarly, we can calculate p_{i+2}, q_{i+2} by p_{i+1}, q_{i+1} as follows:

$$p_{i+2} = \frac{A_{i+1} q_{i+1} + p_{i+1} - A_{i+1} \eta_{i+2}\ c/\tan\phi_p}{1 + A_{i+1} \eta_{i+2}} \tag{5.4.19}$$

$$q_{i+2} = \frac{(A_{i+1} q_{i+1} + p_{i+1} + c/\tan\phi_p)\eta_{i+2}}{1 + A_{i+1} \eta_{i+2}} \tag{5.4.20}$$

By repeating the calculation, finally we can get the values of p_{n+1}, q_{n+1} on the collapse surface, i.e. the peak strength (p_p, q_p) for the known effective stress state (p, q). The p_p and q_p can be expressed as:

$$p_p = \frac{A_n q_n + p_n - A_n \eta_{n+1}\ c/\tan\phi_p}{1 + A_n \eta_{n+1}} \tag{5.4.21}$$

$$q_p = \frac{(\ A_n q_n + p_n + \ c/\tan\phi_p\ )\eta_{n+1}}{1 + A_n \eta_{n+1}} \tag{5.4.22}$$

in which: $\eta_{n+1} = 1.0$.

If $q_p < q_s$, q_s is the steady state strength, then p_p, q_p should be re-calculated by repeating the above procedure, but letting c = 0 and $\phi_p = \phi_s$, where ϕ_s is the angle of the steady state envelope.

The increment of pore water pressure generated during strain softening, i.e. the shear yield surface contracting in zone2, can be calculated by:

$$\Delta u = \frac{\beta}{3}(\Delta\sigma_1+\Delta\sigma_2+\Delta\sigma_3)+$$

$$+\frac{\tan\phi_p}{\sqrt{2}}\sqrt{(\Delta\sigma_1-\Delta\sigma_2)^2+(\Delta\sigma_2-\Delta\sigma_3)^2+(\Delta\sigma_3-\Delta\sigma_1)^2} \qquad (5.4.23)$$

The increment of pore water pressure generated during loading on the stress mobolity surface(zone-3) can be expressed as:

$$\Delta u = \frac{\beta}{3}(\Delta\sigma_1+\Delta\sigma_2+\Delta\sigma_3) -$$

$$-\frac{\tan\phi_s}{\sqrt{2}}\sqrt{(\Delta\sigma_1-\Delta\sigma_2)^2+(\Delta\sigma_2-\Delta\sigma_3)^2+(\Delta\sigma_3-\Delta\sigma_1)^2} \qquad (5.4.24)$$

The increment of pore pressure during unloading in zone-3 is:

$$\Delta u = \frac{\beta}{3}(\Delta\sigma_1+\Delta\sigma_2+\Delta\sigma_3)+$$

$$+\frac{\tan\phi_s}{\sqrt{2}}\sqrt{(\Delta\sigma_1-\Delta\sigma_2)^2+(\Delta\sigma_2-\Delta\sigma_3)^2+(\Delta\sigma_3-\Delta\sigma_1)^2} \qquad (5.4.25)$$

The pore pressure parameters α, β in equation (5.4.13) for a liquefiable soil can be summarized in following table 5.4.1.

Table 5.4.1. The pore pressure parameters for liquefiable soils.

zone	loading		unloading	
	α	β	α	β
1	$\alpha(q/p)$	1.0	0	1.0
2	–	–	$\tan\phi_p/\sqrt{2}$	1.0
3	$-\tan\phi_s/\sqrt{2}$	1.0	$\tan\phi_s/\sqrt{2}$	1.0

Fig.5.4.4 shows the pore water pressure increase in zone 2. The pore water pressure increases with the decrease in shear stress during shear yield surface contraction. Fig 5.4.5 shows the pore water pressure increase or decrease when the effective stress paths move up and down along the Hvorslev surface.

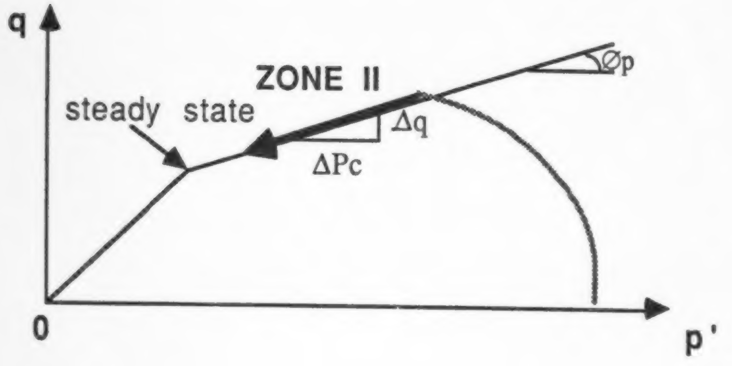
q
ZONE II
steady state
Øp
Δq
ΔPc
0
p'

Fig.5.4.4. Pore Water Pressure in Zone 2.

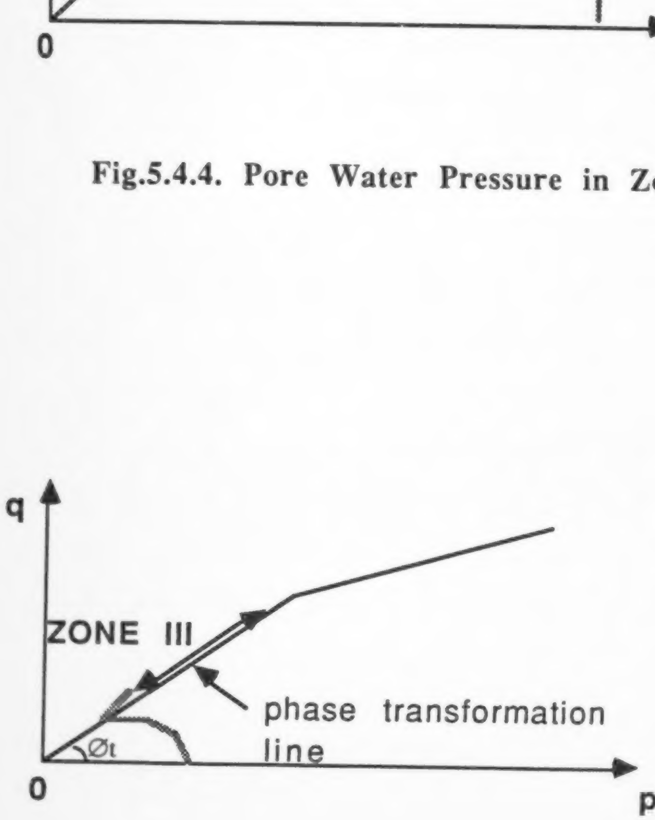
q
ZONE III
phase transformation line
Øt
0
p'

Fig.5.4.5. Pore Water Pressure in Zone 3.

5.5. Unbalanced Load Caused by the Excess Pore Pressure.

The incremental finite element equilibrium equation based on virtual displacement is given by Bathe (1982):

$$\int_{v} [\ B\ ]^{T} \{\ \Delta\sigma\ \}\ dV = \{\ \Delta R\ \} \qquad (5.5.1)$$

where: $\{\ \Delta\sigma\ \}$ is the incremental total stress vector.
From the defination of effective stress, we have:

$$\{\ \Delta\sigma\ \} = \{\ \Delta\sigma'\ \} + \{\ \Delta u\ \} \qquad (5.5.2)$$

where: $\{\ \Delta\sigma'\ \}$ = incremental of effective stress vector,
$\{\ \Delta u\ \}$ = incremental of pore water pressure vector.

From (5.5.1), we have:

$$\int_{v} [\ B\ ]^{T} \{\ \Delta\sigma'\ \}\ dV = \{\ \Delta R\ \} - \int_{v} [\ B\ ]^{T} \{\ \Delta u\ \}\ dV \qquad (5.5.3)$$

in which, the second term on right hand side is the unbalanced load vector caused by the pore water pressures.

The stress- strain relationship is usually expressed in terms of effective stress. Therefore, we have:

$$\{\Delta\varepsilon\} = [\ D\ ]\{\Delta\sigma'\} = [\ D\ ]\{\Delta\sigma\} - [\ D\ ]\{\Delta u\} = \{\Delta\varepsilon^{\sigma}\} - \{\Delta\varepsilon^{u}\}$$

(5.5.4)

For the elastic plane strain problem:

$$\begin{bmatrix} \Delta\varepsilon_x^{\sigma} \\ \Delta\varepsilon_y^{\sigma} \\ \Delta\gamma_{xy}^{\sigma} \end{bmatrix} = \frac{(1+\mu)}{E} \begin{bmatrix} 1-\mu & -\mu & 0 \\ -\mu & 1-\mu & 0 \\ 0 & 0 & 2 \end{bmatrix} \begin{bmatrix} \Delta\sigma_x \\ \Delta\sigma_y \\ \Delta\tau_{xy} \end{bmatrix} \tag{5.5.5}$$

$$\begin{bmatrix} \Delta\varepsilon_x^{u} \\ \Delta\varepsilon_y^{u} \\ \Delta\gamma_{xy}^{u} \end{bmatrix} = \frac{(1+\mu)}{E} \begin{bmatrix} 1-\mu & -\mu & 0 \\ -\mu & 1-\mu & 0 \\ 0 & 0 & 2 \end{bmatrix} \begin{bmatrix} \Delta u \\ \Delta u \\ 0 \end{bmatrix} \tag{5.5.6}$$

When $\mu = 0.5$, i.e. the fully undrained condition, one has:

$$\begin{bmatrix} \Delta\varepsilon_x^{u} \\ \Delta\varepsilon_y^{u} \\ \Delta\gamma_{xy}^{u} \end{bmatrix} = \begin{bmatrix} 0 \\ 0 \\ 0 \end{bmatrix} \tag{5.5.7}$$

Therefore, we have:

$$\{\Delta\varepsilon\} = [\ D\ ]\{\Delta\sigma'\} = [\ D\ ]\{\Delta\sigma\} \tag{5.5.8}$$

One cannot use exactly $\mu = 0.5$ in an analysis. The deformation due to pore water pressures under fully undrained saturated conditions ($\mu \approx 0.5$) will be very small. Therefore, we can use either a total stress scheme or an effective stress scheme for stress re-distribution analysis in which the fully undrained and satuated conditions are usually assumed. If one wants to use the effective stress scheme, an iteration for pore water pressure has to be considered because they are always changing during stress re-distribution.

5.6. Iteration Scheme for Excess Pore Pressure under Fully Undrained Condition.

For the stress re-distribution analysis under drained conditions or for materials under unsaturated conditions, the effective stress scheme should be used. Even for the stress re-distribution analysis under fully undrained and saturated conditions, there will be an error caused by the pore water pressure term in the equilibrium equation(5.5.3) because one cannot use exactly $\mu = 0.5$ in this analysis. To minimize the error, the effective stress scheme should used. The effective stress iteration scheme can be described as follows:

In first step of the iteration, the total stress equilibrium equations are solved:

$$\int_v [\ B\ ]^T \{\Delta\sigma\}_1 \, dV = \{\Delta R\}_1 \tag{5.6.1}$$

The incremental pore pressure Δu can be obtained from the increment of total stress. Then, in the second step of iteration, the effective stress equilibrium equations are solved:

$$\int_{v} [\ B\ ]^{T}\ \{\Delta\sigma'\}_2\ dV = \{\Delta R\}_2 - \int_{v} [\ B\ ]^{T}\ \{\Delta u\}_1\ dV \tag{5.6.2}$$

Figure 5.6.1 illustrates the effective stress iteration scheme.

For the total stress iteration scheme, the incremental pore water pressure can be calculated by the final convergent total stress increment in one loading stage. The stress path A-C-D in Figure 5.6.2 illustrates the scheme.

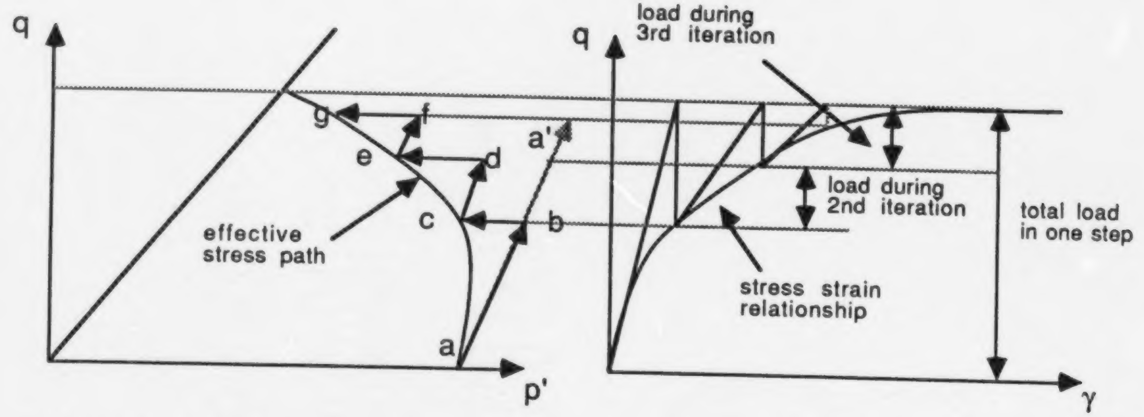
q
effective
stress path
g
f
e
d
c
b
a'
a
p'
q
load during
3rd iteration
load during
2nd iteration
total load
in one step
stress strain
relationship
γ

b - c is pore pressure unbalanced load during 2nd iteration.
d - e is pore pressure unbalanced load during 3rd iteration.
f - g is pore pressure unbalanced load during 4th iteration.
a - a' is total stress path after 3rd iteration.
a - b - c - d - e - f - g is effective stress path during iterations.

Fig. 5.6.1. Effective Stress Scheme During Iteration of Unbalanced Load.

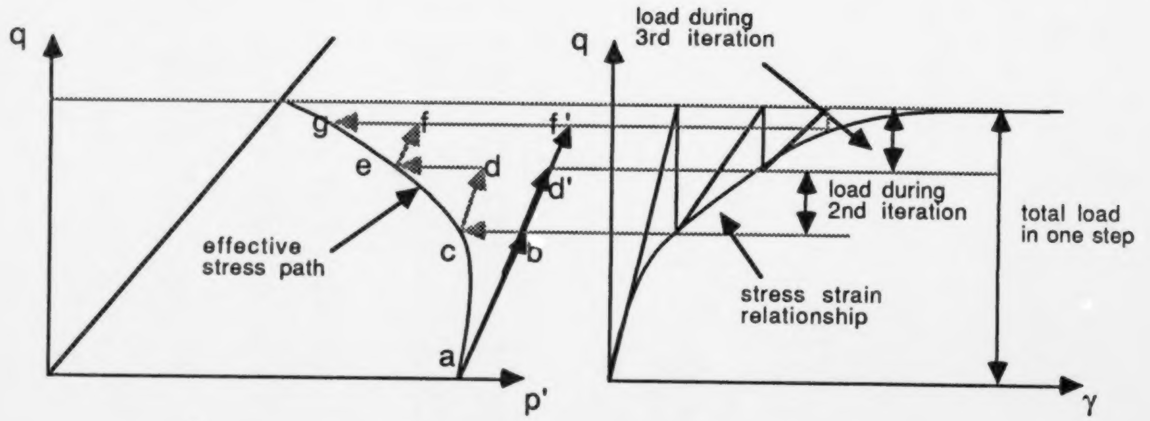
q
effective stress path
a
b
c
d
d'
e
f
f'
g
p'
q
load during 3rd iteration
load during 2nd iteration
stress strain relationship
total load in one step
γ

b - c is pore pressure increment after 1st iteration.
d - e is pore pressure increment after 2nd iteration.
f - g is pore pressure increment after 3rd iteration.
a - b - d' - f' is total stress path during iterations.

Fig. 5.6.2. Total Stress Scheme During Iteration of Unbalanced Load.

6 STABILITY EVALUATION BY FINITE ELEMENT DEFORMATION ANALYSIS

6.1. Deformation Analysis and Stability Evaluation.

The stability evaluation of slopes are commonly analyzed by limit equilibrium methods. These methods are used in design to determine the magnitude of the Factor of Safety. The development of analytical techniques for these methods can be represented mainly by improvement in the postulating of slip mechanisms. In the simpler configurations, the slopes are assumed to fail along planes (Janbu,1973) or circular sliding surfaces (Taylor,1937, Terzaghi,1950, Bishop,1955). For non-uniform conditions, an arbitrary shape of sliding surface and variation of strength can be considered by the method of slices (Morgenstern and Price,1965). The Factor of Safety defined by Morgenstern and Sangrey (1978) is as follows:

> " The Factor of Safety is that factor by which the shear strength parameters may be reduced in order to bring the slope into a state of limiting equilibrium along a given slip surface."

This definition has been adopted in limit equilibrium stability analyses. An iteration scheme is used to bring the slope into the state of limiting equilibrium along a given slip surface. A stable slope can be determined by a Factor of Safety larger than unity.

When strain softening is the dominant soil behaviour in an earth structure, the traditional limit equilibrium method cannot be used alone in determining a factor of safety. The strain softening describes the soil behaviour dropping from its peak strength to its residual strength. Stress re-distribution will occur when the strengths of material are lower than the actual shear stresses in any earth structure. Progressive failure processes described by Bjerrum (1967) can be used to consider the stress re-distribution along a slip surface. In fact, most slope failures are triggered by local failure at one point or several points in the slope, and the triggering failure points are not necessary on the final slip surface. Failure is preceded by continuous expansion of material yielding in two-dimensions or even three-dimensions. Obviously, the failure process is closely dependent upon the deformation of the material. For some more complicated cases, such as the liquefaction failure of earth structures, deformation analysis may become a method that is not only necessary for predicting the deformation but also necessary for evaluating the stability of the slope. The factors to be considered for a method to predict deformation to an acceptable degree of accuracy are summarized by Morgenstern and Sangrey (1978) as follows:

1. Representative stress-strain relations, including behaviour from peak to residual shear strength.
2. Anisotropy.
3. Variable pore pressure distributions.
4. Nonhomogeneity arising from variation of material properties with depth, layering, and discontinuities.
5. Influence of initial stress.
6. Construction sequence.

The developments of finite element methods have made it possible to consider most of these factors. The finite element deformation analysis may become more and more important in evaluation of stability of earth structures, particularly for complicated failure behaviour, such as the liquefaction failure or flow failure of earth structures because the assessment of progressive failure cannot be avoided.

6.2. Contours of Yield Ratio and Safety Evaluation of Slopes.

The results from a finite element deformation analysis are usually given in two forms, i.e. the stress field and the displacement field. These two fields cannot be used directly to evaluate the stability of slopes. Like any traditional safety evaluation, the strength of materials has to be introduced into the evaluation of stability analysis. A field of yield ratio can be determined directly from the stress field obtained from this finite element analysis and the strength of materials. The yield ratio is defined as real shear stress over real shear strength of the material. In this definition, we no longer use the concept of strength in the same manner as that used in limit equilibrium analysis. Obviously, the stress field satisfies the equilibrium condition at any time in the finite element anaysis. If we can capture the incipient failure by finite element analysis, then we can capture the stress field to satisfy limit equilibrium conditions. But, it will make things unnecessarily complicated, or even totally incorrect, to try to capture incipient failure or a stress field required by limit equilibrium by changing material strengths in the analysis in a manner that is similar to the determination of the Factor of Safety to reduce the strength parameters along a slip surface that is required by limit equilibrium . Therefore, the concept of safety evaluation or the definition of the Factor of Safety has to be modified in finite element analysis. Actually, it is a more direct method to evaluate the stability by observing the expansion of yield zones in earth structures.

Fig.6.2.1 shows the possible distribution of yield ratio and the principle to evaluate the safety of earth structures. When the contour line with unit yield ratio (yield zone) is contained by contour lines with lower yield ratio, one may say the structure is in a stable state. When the contour line with unit yield ratio reaches more than two points on the free boundary of structure, failure may occur.

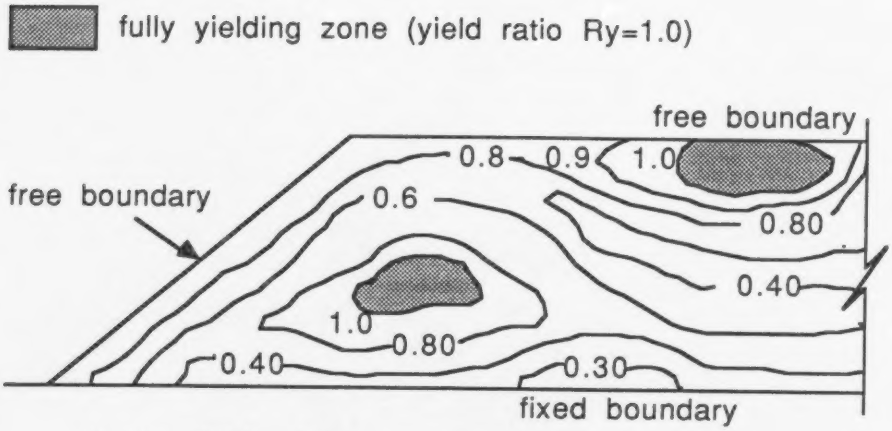
▨ fully yielding zone (yield ratio Ry=1.0)
free boundary
free boundary
0.8
0.9
1.0
0.6
0.80
0.40
1.0
0.80
0.40
0.30
fixed boundary

(a) stable state.

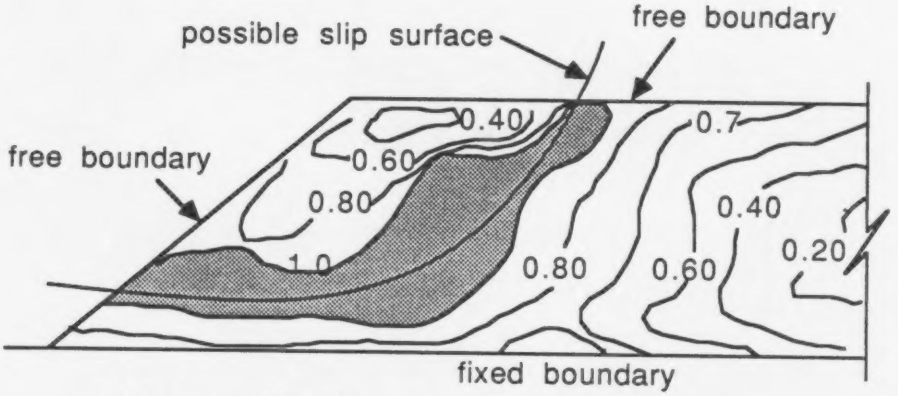
possible slip surface
free boundary
free boundary
0.40
0.7
0.60
0.80
0.40
1.0
0.80
0.60
0.20
fixed boundary

(b) unstable state.

Fig.6.2.1. Contours of Yield Ratio and Stability Evaluation

6.3. Definition of Yield Ratio.

The yield ratio can be defined as a ratio of shear stress over shear strength. The shear stress can be determined from finite element analysis. The shear strength is very much dependent upon the properties of material, drainage condition and initial stress state. For some materials, e.g. contractive cohesionless liquefiable materials, the shear strength is also dependent on the effective stress paths and deformations. Therefore, it is impossible to define the yield ratio as a single criterion in terms of strength. In other words, we have to use different criteria to define the yield ratio in different models for different materials.

For an elastic or non-linear elastic model, the yield ratio can be defined as:

$$R_y = \frac{\tau_m}{\tau_s} \qquad (6.3.1)$$

in which:

$$\tau_m = \frac{\sigma_1 - \sigma_3}{2} \qquad (6.3.2)$$

$$\tau_s = c \cos\varphi + \left(\frac{\sigma_1 + \sigma_3}{2} \right) \sin\varphi \qquad (6.3.3)$$

where: c = cohesion, φ = friction angle, σ_1 and σ_3 are maximum and minimum principal stresses.

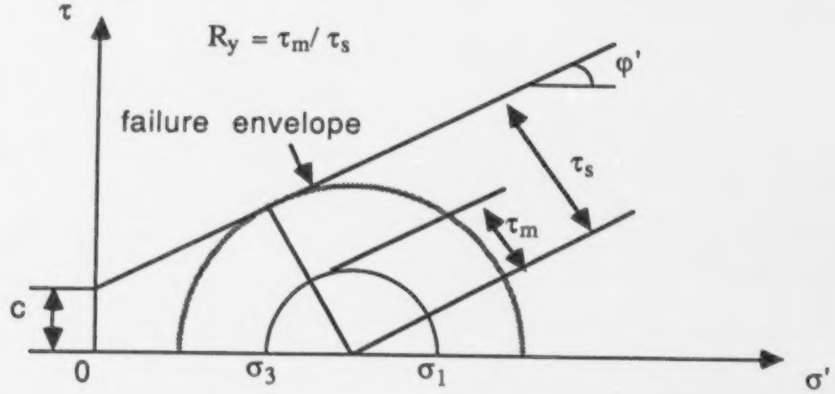
τ
$R_y = \tau_m / \tau_s$
φ'
failure envelope
τ_s
τ_m
c
0
σ_3
σ_1
σ'

Fig.6.3.1. Yield Ratio for Elastic or Nonlinear Elastic Model

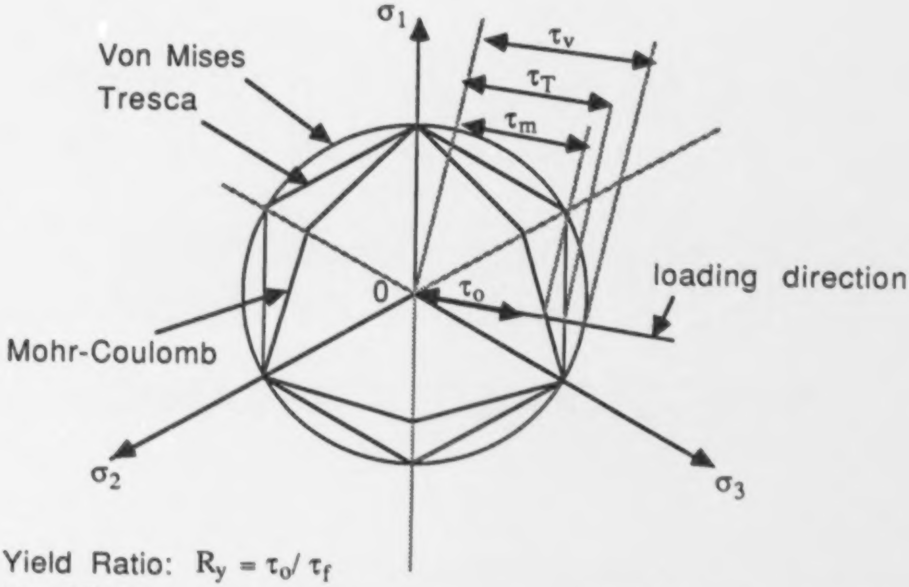
σ_1
τ_v
τ_T
τ_m
Von Mises
Tresca
0
τ_o
loading direction
Mohr-Coulomb
σ_2
σ_3

Yield Ratio: $R_y = \tau_o / \tau_f$

Von Mises : $\tau_f = \tau_v$, Tresca:: $\tau_f = \tau_T$, Mohr-Coulomb : $\tau_f = \tau_m$.

Fig.6.3.2. Yield Ratio for Elasto-plastic Models.

Fig.6.3.1 shows the definition of yield ratio for an elastic or nonlinear elastic model. In this definition, the Mohr-Coulomb failure criterion is introduced.

For an elasto-plastic model with Von Mises' yield criterion, the yield ratio can be expressed as:

$$R_y = \sqrt{3}\,\overline{\sigma} \,/\, Y \tag{6.3.4}$$

where: $\overline{\sigma} = \sqrt{J_2}$, $J_2 = \sigma^d_{ij}\sigma^d_{ij} \,/\, 2$, $\sigma^d_{ij} = \sigma_{ij} - \delta_{ij}\sigma_{kk} \,/\, 3$, δ_{ij} is the Kronecker delta. Y = uniaxial yield strength.

For an elasto-plastic model with Tresca yield criterion, the yield ratio can be expressed as:

$$R_y = 2\,\overline{\sigma}\,\cos\theta_o \,/\, Y \tag{6.3.5}$$

where:

$$\theta_o = \frac{1}{3}\sin^{-1}\left[(-3\sqrt{3}J_2)/(2J_2^{3/2})\right] \tag{6.3.6}$$

For an elasto-plastic model with Mohr-Coulomb yield criterion, the yield ratio can be defined as:

$$R_y = \frac{\overline{\sigma}\,(\cos\theta_o + \sin\theta_o\sin\varphi \,/\sqrt{3})}{(\sigma_m \sin\varphi + c\cos\varphi)} \tag{6.3.7}$$

where: $\sigma_m = \sigma_{kk}/3$, c, φ are Mohr-Coulomb cohesion and friction parameters.

Fig.6.3.2 shows the definitions of yield ratio for elasto-plastic models.

For liquefiable materials, the peak strength depends on the effective stress. During strain softening with the effective stress path dropping along the collapse surface from its peak to residual strength, the material is continuously on a contracting yield surface until it reaches the minimum yield surface at residual strength, i.e. the steady state strength. Therefore, the yield ratio is always equal to unity on the collapse surface. During stress mobility, i.e. the effective stress path reachs a limit state lower than the steady state strength, then the material can only fail when the effective stress path reaches the maximum yield surface, or the steady state strength, in loading along the stress mobility surface. Therefore, the yield ratio can be defined as:

$$R_y = q / q_p \qquad (q_p > q_s) \qquad (6.3.8)$$

$$R_y = q / q_s \qquad (q_p < q_s) \qquad (6.3.9)$$

where: q_p is the peak strength that can be calculated by the numerical effective stress path model defined in Chapter 4, q_s is the steady state strength, and $q = \sqrt{3J_2}$. Fig.6.3.3 shows the definition of yield ratio for liquefiable materials.

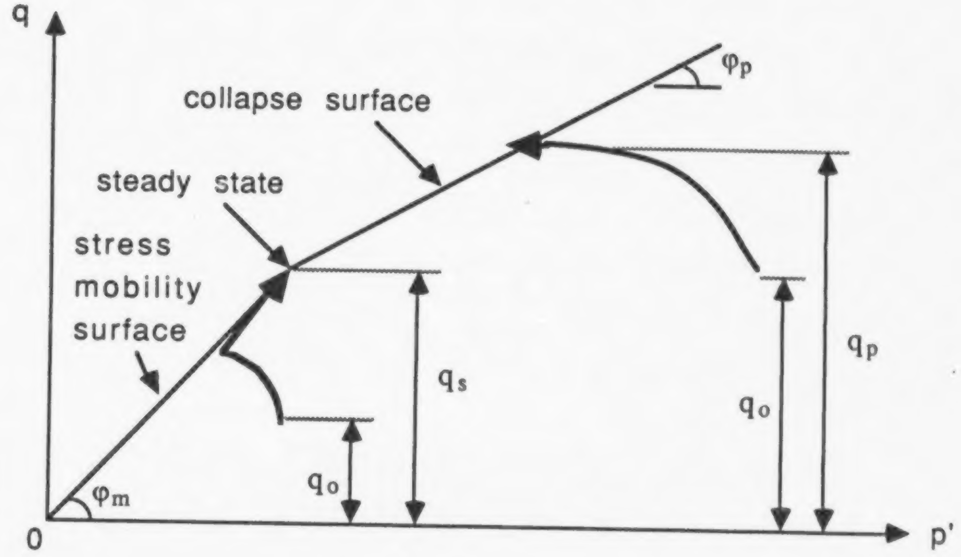
q
φ_p
collapse surface
steady state
stress mobility surface
q_s
q_o
q_p
q_o
φ_m
0
p'

Yield Ratio: $R_y = q_o / q_p \quad (q_p > q_s)$

$R_y = q_o / q_s \quad (q_p < q_s)$

Fig.6.3.3. The Yield Ratio For Liquefiable Soils.

6.4. Displacement Field from Finite Element Analysis.

In finite element analyses, the safety evaluation of an earth structure should include the interpretation of both stress field and strain field. The computation of contours of yield ratio in this analysis is part of the interpretation of stress field, and the interpretation of displacements is part of the interpretation of strain field. The reasons to interpret both the stress field and the strain field with equal importance are as follows:

(1). The accuracy of the stress field is dependent on the accuracy of the strain field.

(2). The validity of the stress field should be checked by the strain field, or more directly, by the displacement field.

(3). The location and also the shape of kinematically posssible slip surfaces may be determined by observing the displacement field.

(4). The stability of an earth structure may be also controlled by observing the displacement field.

The interpretation of the strain field is usually associated with observing the displacement field, because the movement of an earth structure, and hence the shape and location of kinematically possible slip surfaces can be observed more clearly and directly. The displacement field can be plotted by vectors in which the magnitude of displacements are expressed by the length of the vectors and the direction of displacements are expressed by the indication of the vectors.

For a stable structure, the displacement field should be well-distributed. For an unstable structure, an uneven distribution of displacement field must occur in the incipient failure condition. Fig.6.4.1(a) shows a possible well-distributed displacement field for a stable structure, and Fig.6.4.1(b) shows a possible uneven distributed displacement field for an unstable structure.

The deformation analysis for liquefaction failure itself should be a large strain, large displacement and discontinuity problem. But, it is easier and more economic to capture incipient liquefaction failure, i.e. to capture the deformation that may cause a huge liquefaction flow failure. This analysis may be done by small strain finite element analysis, and it provides a reasonable basis for the evaluation of safety of structures in which safety is the main concern rather than the volume of materials and distance of the flow involved in the failure.

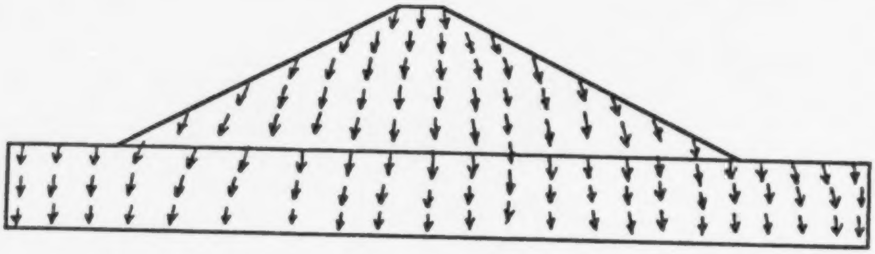

(a) well distributed displacement field for a stable structure.

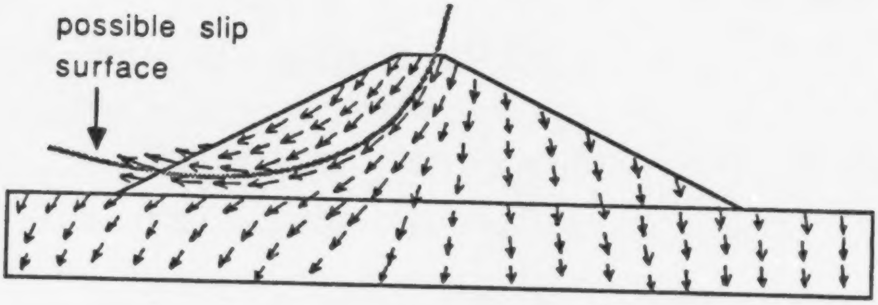

(b) un-even distributed displacement field for an unstable structure.

Fig.6.4.1. Stability evaluation by displacement field in finite element analysis.

For an earth structure with small liquefied zone, the slip surface may be well defined, then the limit equilibrium method or the stream line method (Chen,1989) can be used to evaluate the safety of a structure. But for an earth structure with a large liquefied zone, the slip surface may be difficult or even impossible to determine as in the failure of the lower San Fernando Dam in which the failure can be described by the movement of several huge blocks of soils floating on the liquefied material. In this case, the finite element deformation analysis by interpreting the contours of yield ratio and vector fields of displacement may become a necessary method in safety evaluation.

6.5. Slip Surface Determined by Finite Element Results.

The kinematically possible location and shape of a slip surface in an earth structure can be determined by interpreting both contours of yield ratio and vector distribution field of displacement obtained from the finite element analysis. This may be an another merit for finite element analysis in safety evaluation of earth structures. The kinematically possible slip surface can be defined as follows:

> "A kinematically possible slip surface is a surface on which all the displacement vectors point in the same clockwise or anti-clockwise tangent directions of the surface, and with two ends on the free boundary surface of the earth structure."

Fig.6.5.1. shows a kinematically possible slip surface and a kinematically impossible slip surface.

Finally, the failure surface can be defined as a kinematically possible slip surface passing through a yielding zone. Fig.6.5.2 shows the relationship between the failure surface and the kinematically possible slip surface.

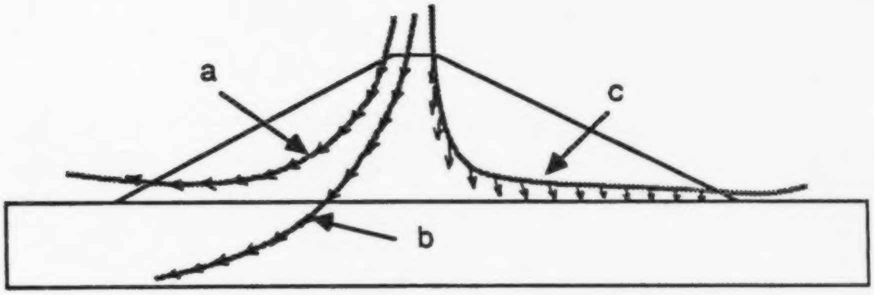

a ------ kinematically possible slip surface.

b ------ kinematically impossible slip surface with one end on a fixed boundary surface.

c ------ kinematically impossible slip surface with displacement vectors in directions other than the tangent direction of slip surface.

Fig. 6.5.1. The Kinematically Possible Slip Surface

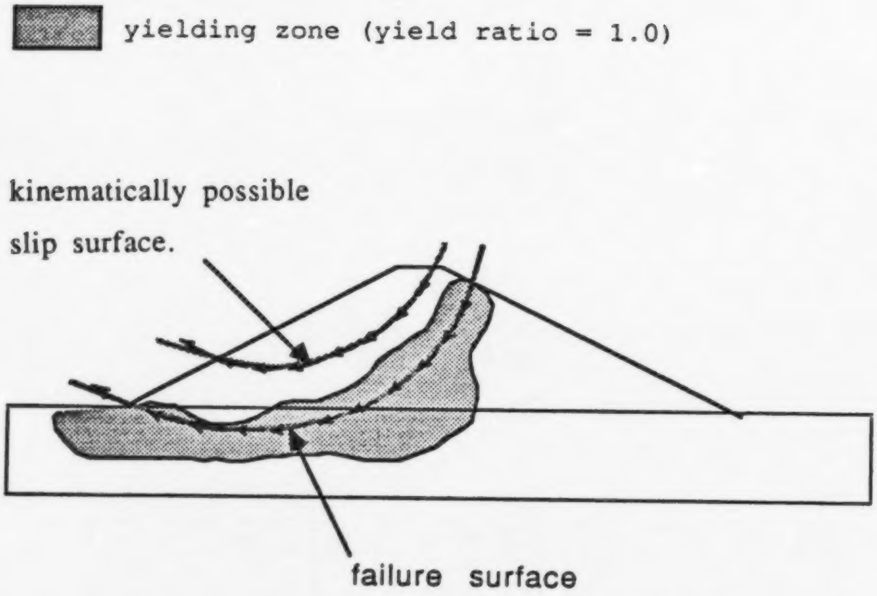
▨ yielding zone (yield ratio = 1.0)
kinematically possible slip surface.
failure surface

Fig.6.5.2. Failure surface and kinematically possible slip surface.

The kinematically possible slip surface can be determined by a streamline method given by Chen (1990). In this method, the kinematically possible slip surface, or the movement paths, is expressed by a function:

$$Y = f(x) \tag{6.5.1}$$

To satisfy the definition of kinematically possible slip surface, one has the following relationship:

$$\frac{dY}{dx} = \frac{\Delta v}{\Delta u} \tag{6.5.2}$$

where: u is the displacement in horizontal direction and v is the displacement in vertical direction.

Since:

$$\frac{dY}{dx} = \left(\frac{dY}{d\xi}d\xi + \frac{dY}{d\eta}d\eta\right) / \left(\frac{dx}{d\xi}d\xi + \frac{dx}{d\eta}d\eta\right) \tag{6.5.3}$$

Where: ξ, η are local coodinate for every element.
Then, one has:

$$\frac{d\xi}{d\eta} = \left(\frac{dY}{d\eta} - \frac{\Delta v}{\Delta u}\frac{dx}{d\eta}\right) / \left(\frac{\Delta v}{\Delta u}\frac{dx}{d\xi} - \frac{dY}{d\xi}\right) \tag{6.5.4}$$

The incremental displacements du and dv in any element can be determined by finite element analysis and the $\frac{dx}{d\xi}, \frac{dx}{d\eta}, \frac{dY}{d\xi}, \frac{dY}{d\eta}$ can be obtained from derivatives of the shape functions.

The coordinates of a slip surface are determined by integrating equation(6.5.3) which can be carried out by the Runge-Kutta method. In order to get an acceptable degree of accuracy, the integration should be carried out in a number of steps for any section of path within one element.

6.6. The Factor of Safety FS Evaluation by the Finite Element Results.

The Factor of Safety for any kinematically possible slip surface can be defined by the following integration:

$$FS = \frac{\int_L 1/R_y \, ds}{\int_L ds} \qquad (6.6.1)$$

where: R_y is the yield ratio, L is the length of slip surface.

The integration can be calculated numerically by:

$$FS = \frac{\sum_{i=1}^{n} 1/R_{yi}\Delta S_i}{\sum_{i=1}^{n} \Delta S_i} \tag{6.6.2}$$

where: $\Delta S_i=\sqrt{\Delta X_i^2+\Delta Y_i^2}$, R_{yi} is the yield ratio at the centre of ΔS_i , and $\Delta X_i, \Delta Y_i$ can be obtained in the integration of equation(6.5.3).

In finite element analysis, the stresses are usually output at each Gaussian integration point (2x2 or 3x3) because the accuracy of stress at Gaussian integration points is much better than the accuracy of stresses at the nodes or on the sides of an elements. In order to get the stresses at nodes or on the sides of element with more accuacy, the least square smoothing method may be required(Hinton, 1973).

In some cases, the numerical integration of equation(6.6.2) can even be carried out approximately by hand directly on the figure of contours of yield ratio. Fig.6.6.1 shows an example of two steps in safety evaluation by using the results of finite element analysis. The two steps are:

(1). The kinematically possible slip surfaces are determined from the displacement vector field.

(2). The Factor of Safety for any kinematically possible slip surface is calculated from the contours of yield ratio.

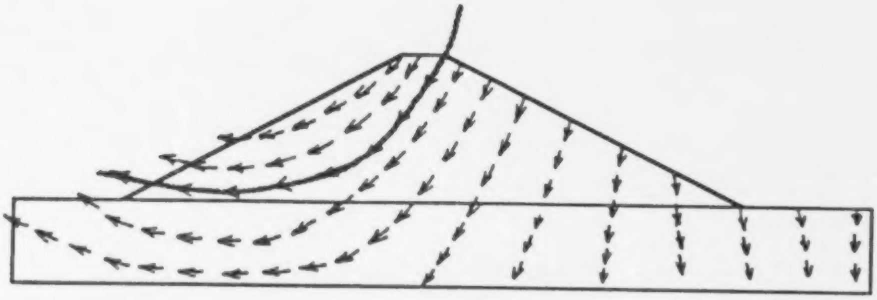

(a)Kinematically possible slip surface determined on the displacement field.

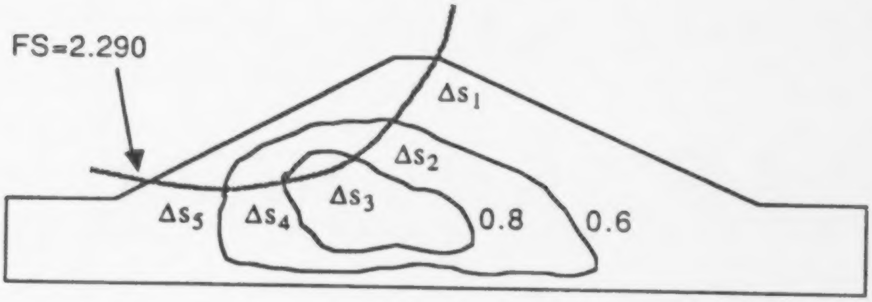
FS=2.290
Δs_1
Δs_2
Δs_3
Δs_4
Δs_5
0.8
0.6

$\Delta s_1 = 3.0$, $\Delta s_2 = 2.0$, $\Delta s_3 = 2.2$, $\Delta s_4 = 2.0$, $\Delta s_5 = 2.5$,
$R_{y1} = 0.3$, $R_{y2} = 0.7$, $R_{y3} = 0.8$, $R_{y4} = 0.7$, $R_{y5} = 0.3$.

$$FS = \frac{\sum_{i=1}^{5} \Delta s_i / R_{yi}}{\sum_{i=1}^{5} \Delta s_i} = \frac{\left(\frac{3.0}{0.3} + \frac{2.0}{0.7} + \frac{2.2}{0.8} + \frac{2.0}{0.7} + \frac{2.5}{0.3}\right)}{(3.0 + 2.0 + 2.2 + 2.0 + 2.5)} = 2.290$$

(b). factor of safety calculation for the Kinematically possible slip surface.

Fig.6.6.1. An example of the two steps in safety evaluation by the results of finite element analysis

7. THE POST-EARTHQUAKE DEFORMATION ANALYSIS OF THE LOWER SAN FERNANDO DAM.

7.1. Review of The Failure Behaviour of The Lower San Fernando Dam.

The slide failure in the upstream shell of the Lower San Fernando dam occurred in the earthquake of February 9, 1971 is probably the most important case history in liquefaction instability. Extensive research work including in-situ tests, laboratory tests and analytical studies have been conducted on this dam. The conclusion made by Seed et.al (1975) that is commonly accepted is that the failure had been initiated by liquefaction of the hydraulic sand fill in the lower section of the upstream shell, hence leading to extensive slide movements of the overlying soil and to slumping of the embankment crest. A major excavation was made into the embankment and across the slide area to determine the zone of failure. Extensive sampling was carried out to study the distribution of materials in the slide debris and detailed mapping in both plan and cross-section was performed to determine the mechanics of failure. Figure 7.1.1 shows the failure mechanics and the reconstructed cross-section reported by Seed(1979). As shown in this figure, the failure was a flow of several large blocks of soil floating on the liquefied soils. The blocks of soil moved about 46 meters into the reservoir.

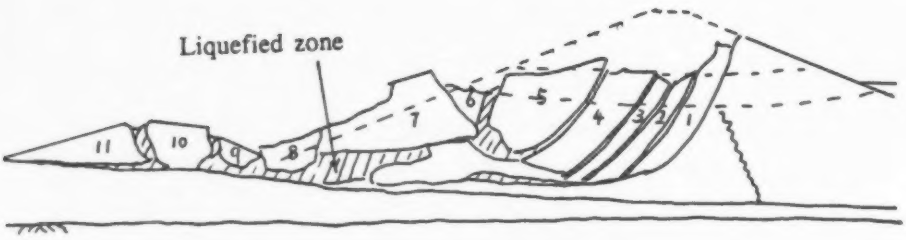
Liquefied zone
11
10
9
8
7
6
5
4
3
2
1

Cross-section after earthquake

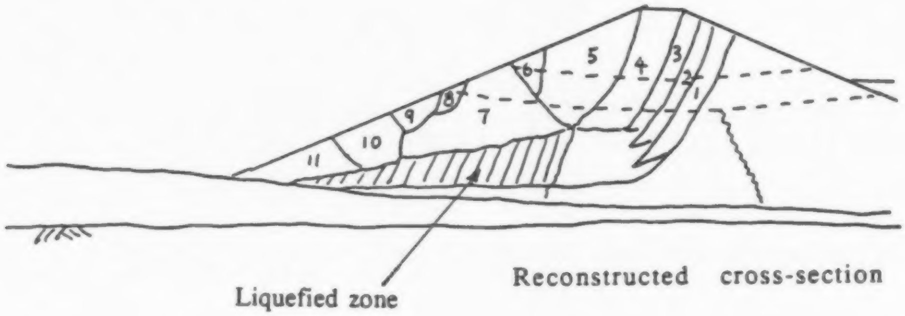
6
5
4
3
2
1
8
9
7
10
11
Liquefied zone

Reconstructed cross-section

Fig.7.1.1. Liquefaction Failure of The Lower San Fernando Dam.(after Seed, 1979)

A careful study of the seismoscope record from the instrument located on the crest of the embankment by Murray (1976), as cited by Seed (1979), leads to the conclusion that the slide movements involving the crest of the dam apparently did not take place during the main earthquake but, rather, they occurred some 30 seconds after the main shaking stopped. This conclusion would imply that the failure of the upstream shell in the Lower San Fernando dam was not caused directly by the inertia forces induced in the embankment by the earthquake shaking but, rather, was caused by the original static driving shear stresses in the embankment as a result of loss of strength in the liquefied soils. The loss in strength of the liquefied soils was caused by the generation of excess pore water pressure during and following the earthquake.

The first seismic stability analysis of the Lower San Fernando dam was conducted by Seed et.al (1975,1979) using the Seed-Lee-Idriss procedure. Figure 7.1.2 shows the results of dynamic response analysis and Figure 7.1.3 shows the results of stability analysis. The result of dynamic response analysis shows that the liquefaction first occurred in the hydraulic fill located at the lower corner of clay core and foundation of upstream shell, and then it expanded horizontally to the upstream toe and vertically to the rolled fill.

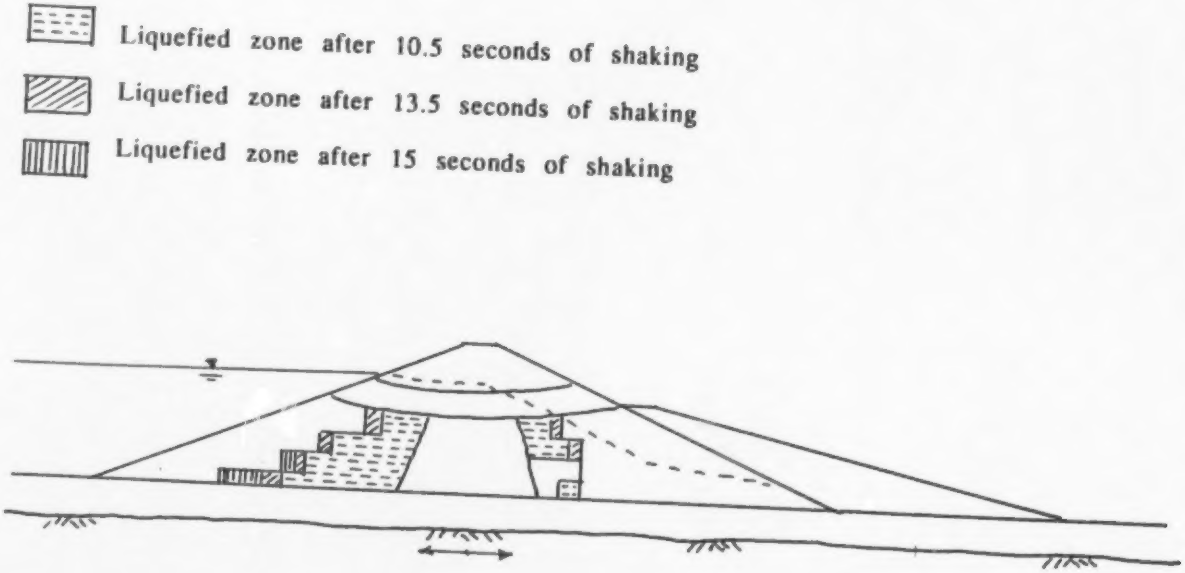
Liquefied zone after 10.5 seconds of shaking
Liquefied zone after 13.5 seconds of shaking
Liquefied zone after 15 seconds of shaking

Fig. 7.1.2. Liquefaction Evaluation of The Lower San Fernando Dam By Seed et. al (1979).

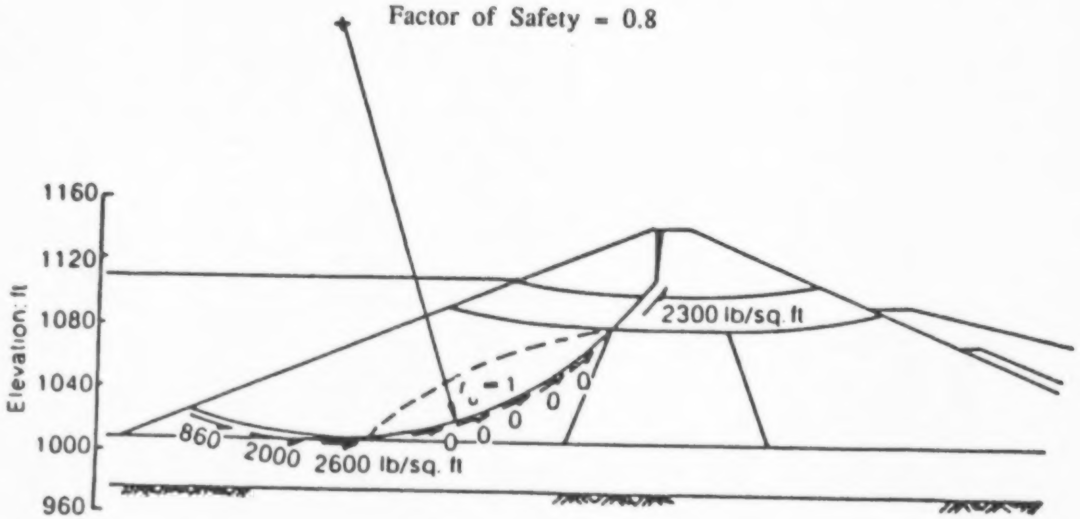
Factor of Safety = 0.8
1160
1120
1080
1040
1000
960
Elevation: ft
2300 lb/sq. ft
860
2000
2600 lb/sq. ft
c = 1
0
0
0
0
0
0

Fig. 7.1.3. Stability Evaluation of The Lower San Fernando Dam By Seed et. al (1979).

7.2. The Properties of Materials in The Lower San Fernando Dam

A detailed description of the construction and history of the Lower San Fernando dam can be found in the papers written by Seed (1975) and Lee, Seed et.al (1975). The Lower San Fernando dam was constructed on about 11m of alluvium and rose to a maximum height of about 43m above the original ground. The embankment was constructed by first making a broad dike of wagon-dumped and rolled fill at both the upstream and downstream edges. The large central area between the dikes was then filled by standard hydraulic fill procedures. After the dam had been constructed to about two-thirds of its final height, rolled fill was added with minimal compaction to bring the dam to the desired height. Finally, many years later, a downstream berm of rolled fill was added. Figure 7.2.1 shows the cross-section and material distribution in the Lower San Fernando dam.

To dertermine the properties of materials in the dam, an extensive program was conducted by Lee and Seed et.al (1975). The program included in-situ density tests, standard penetration tests, undisturbed sampling, index testing, seismic surveys, static and cyclic loading tests.

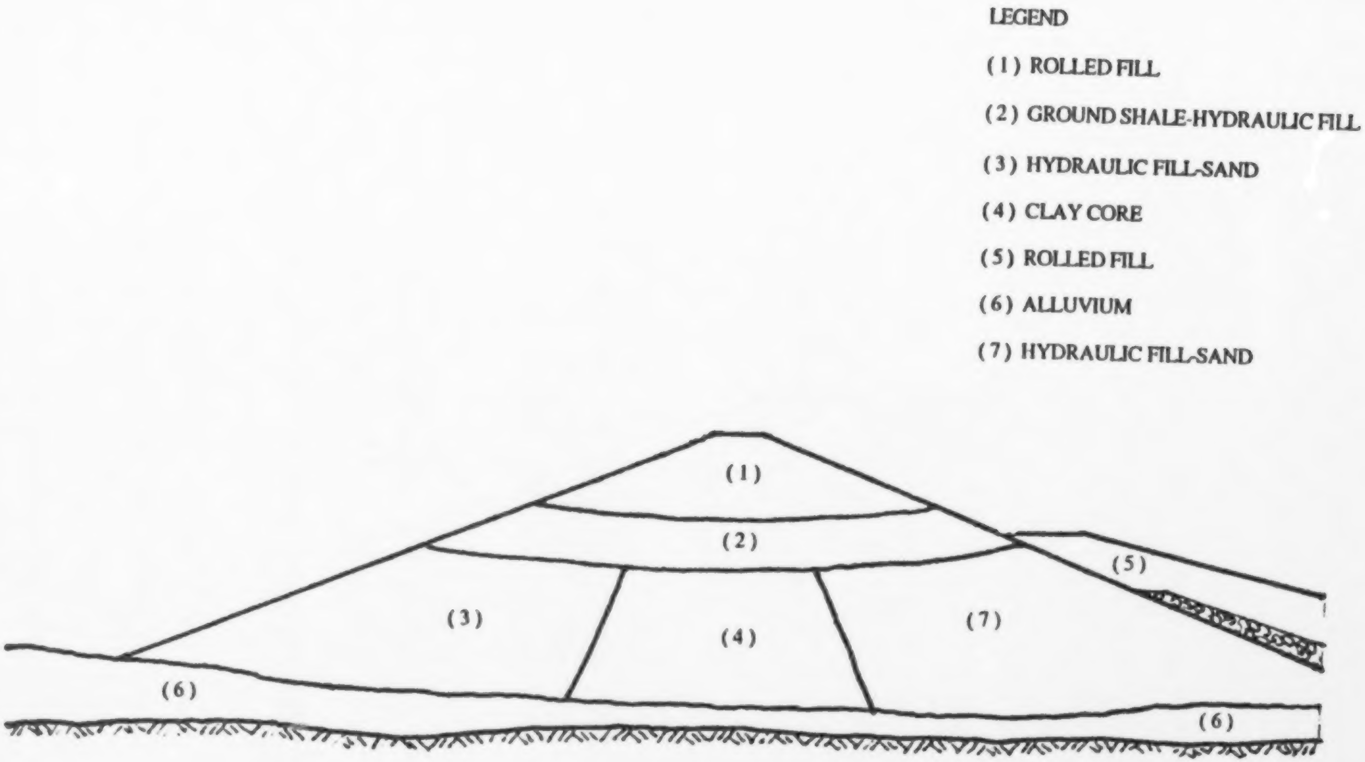
LEGEND
(1) ROLLED FILL
(2) GROUND SHALE-HYDRAULIC FILL
(3) HYDRAULIC FILL-SAND
(4) CLAY CORE
(5) ROLLED FILL
(6) ALLUVIUM
(7) HYDRAULIC FILL-SAND
(1)
(2)
(3)
(4)
(5)
(6)
(7)
(6)

Fig.7.2.1. Material Distribution of The Lower San Fernando Dam.

The field densities were determined by the sand cone method at several locations in the test trenches and in the bucket auger holes. The minimum density was determined in laboratory tests performed according to the American Society for Testing and Materials (ASTM) designation D2049-69. The maximum density was determined in laboratory tests performed according the modified American Association of State Highway Officials (AASHO) procedure. The relative density values range from 51% - 58 % for hydraulic fill and 65% - 70% for alluvium.

The maximum shear modulus was determined by seismic surveys using the cross hole method. The shear wave velocities and compression wave velocities were measured in the embankment and foundation soils at different depths.

The static loading triaxial tests were performed on undisturbed 3-in(76-mm) diam Shelby tube samples of the hydraulic fill sands and the alluvial materials. All of the tests were performed on isotropically consolidated samples at effective confining pressures ranging from 1 ton/sq.ft - 4 ton/sq.ft(96 kPa - 380 kPa) and sufficient back pressures were used to insure complete saturation. Both consolidated drained and consolidated undrained tests with pore pressure measurements were performed. Failure was defined as the peak axial stress developed during the test.

A summary of the parameters obtained from the static trixial tests on the hydraulic fill and alluvial soil is presented in Table 7.2.1.

Table 7.2.1. Parameters For Nonlinear Static Stress Analysis Given by Lee and Seed et.al(1975).

parameter		hydr. fill	alluvium
γ_d (pcf)		106	110
γ_b (pcf)		64	68
c (psf)		0	0
ϕ (o)		37	38
Young's modulus	Rf	0.72	0.76
	K	510	330
	n	0.54	0.41
Poisson's ratio	G	0.41	0.40
	F	0.23	0.16
	D	9.4	5.8

where: γ_d is the dry unit weight,
γ_b is the Buoyant unit weight,
c is the cohesion, ϕ is the friction angle and
Rf, K, n, G, F, D are parameters in non-linear elastic model defined by Duncan et. al(1970).

To determine the static undrained strength of clay soils, a fairly large number of small torvane shear tests were performed on the larger clay seams that were found in the Shelby tube and on the some clay seams exposed in the inspection trenches. When the measured shear strength Su was plotted versus the effective overburden pressure p, a fairly consistent relationship was Su=0.24p. Atterberg limit tests were performed on several samples of clay found in the hydraulic fill at both upper and lower dams. The liquid limit ranged from about 20 - 40. There was no clear distinction between the clays from the upper and lower dams. According to the empirical relation $Su/p = 0.11 + 0.0037\ PI$, the Su/p ratio ranged from 0.18 and 0.25 for normally consolidated soils. This correlates reasonably well with the measured value of Su/p=0.24.

The material properties in the Lower San Fernando dam, particularly the steady state strength of the hydraulic fill in the dam, were re-evaluated from 1985 to 1989 by a joint group. The joint group includes the Geotechnical Engineers Inc.(GEI), H. B. Seed, Inc., Rensselaer Polytechnic Institute(RPI) and the US Army Engineer Waterways Experiment State(WES). Principal investigators were Dr. Castro for GEI, Professor Seed for H. B. Seed, Inc., Professor Dobry for RPI and Dr. Franklin for WES.

Cyclic and monotonic load, consolidated undrained tests with pore pressure measurements were conducted in this investigation. The range in steady state strength is found to be quite large in all tests. Table 7.2.2 shows the range and average values of steady state strength Su determined by different groups.

Table 7.2.2. Steady state strength of hydraulic fill in the Lower San Fernando dam. (psf)

Group	upstream		downstream	
	range	average	range	average
GEI	291-1053	717	381-1322	896
Seed		640 1020	200-1600 200-2600	880 1380
RPI	150-2000	700		

The extensive range of steady state strength obtained in these laboratory tests makes it difficult to choose one reasonable value of steady state strength in stability analysis. Therefore, using several representative values of steady state strength in this analysis is not only necessary to study the behaviour of the dam but also useful in back-checking the reasonableness of these strengths.

In their investigation, Seed group suggested that the test data should be interpreted conservatively, rather than simply taking an average, to determine a reasonable value of steady state strength. This suggestion is supported by the back stability analysis of the lower San Fernando dam conducted by Seed et al (1975) and the study on the determination of steady state strength at field conditions (Seed, 1989). They also concluded that the use of the steady state testing approach, as proposed by Poulos et al (1985), is capable of predicting the onset of sliding in the upstream slope of the lower San Fernando dam. The approach used involves the assumption that the soil in the embankment would liquefy and a very conservative interpretation of a comprehensive set of test data. Ultimately, the 35-percentile steady state strength based on laboratory test data was strongly suggested by Seed group. Figure 7.2.2 shows a comparison of steady state strengths between the values obtained from laboratory tests and the values determined from field conditions.

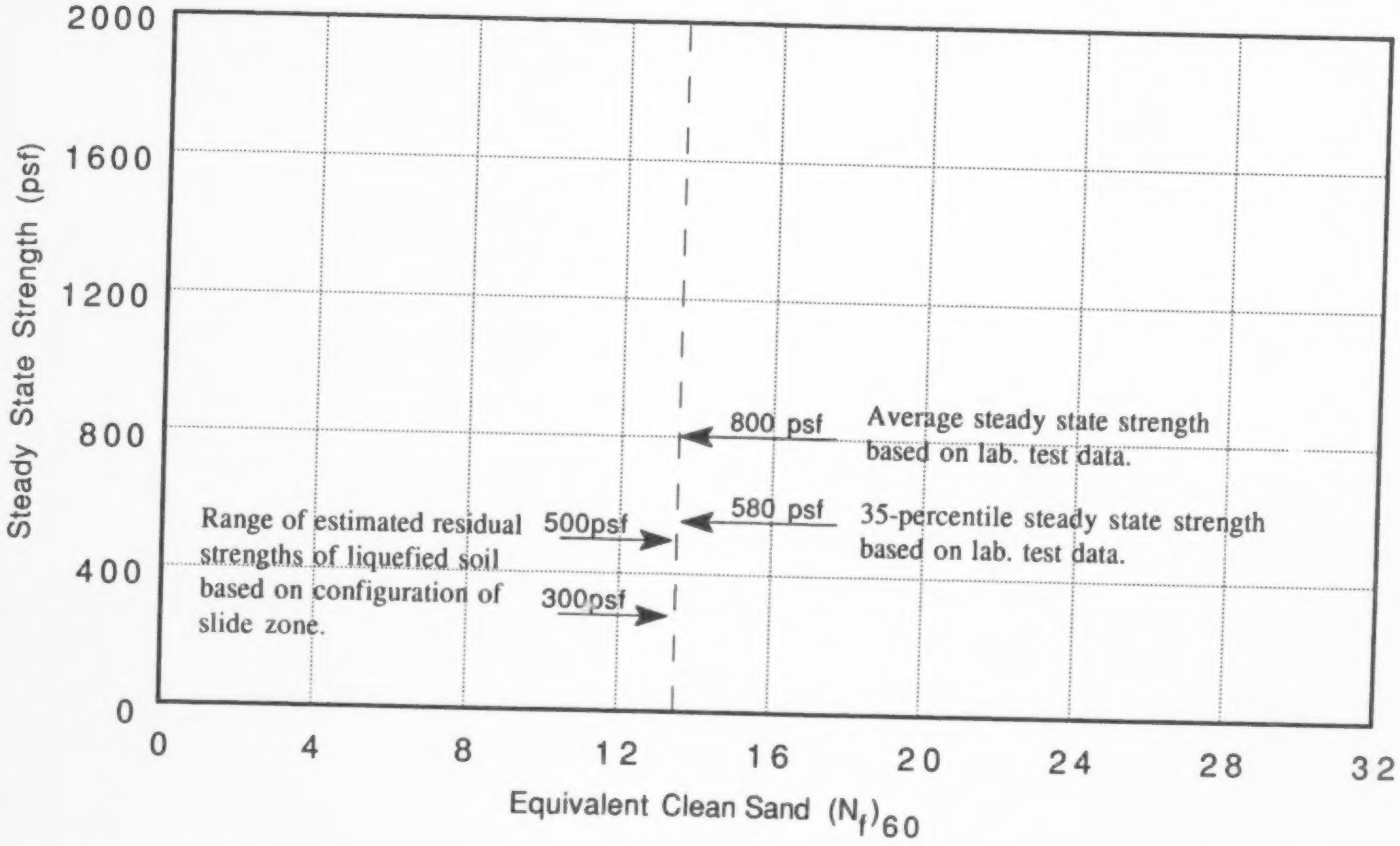

Fig. 7.2.2. Steady State Strength Determined By Laboratory Tests or Field Conditions. (after Seed et.al, 1985)

The RPI test results show that the angle of steady state strength envelope in p - q space is about 29°, and the peak strength envelope is about 22°. Here: $p = (\sigma_1+\sigma_3)/2$, $q = (\sigma_1-\sigma_3)/2$. To investigate the collapse surface defined by Sladen et.al(1985), we replot the results in a normalized p/ps - q/qs space, where ps is the steady state normal stress and qs is the steady state strength. The angle of collapse surface ranged from about 8° (Kc=1.0) to 22° (Kc=2.0) in p-q space. It seems that the angle of collapse surface depends on the initial consolidation condition. The angle increases with the increase in anisotropic consolidation ratio $Kc=\sigma_{1c}/\sigma_{3c}$. Figure 7.2.3 shows the results.

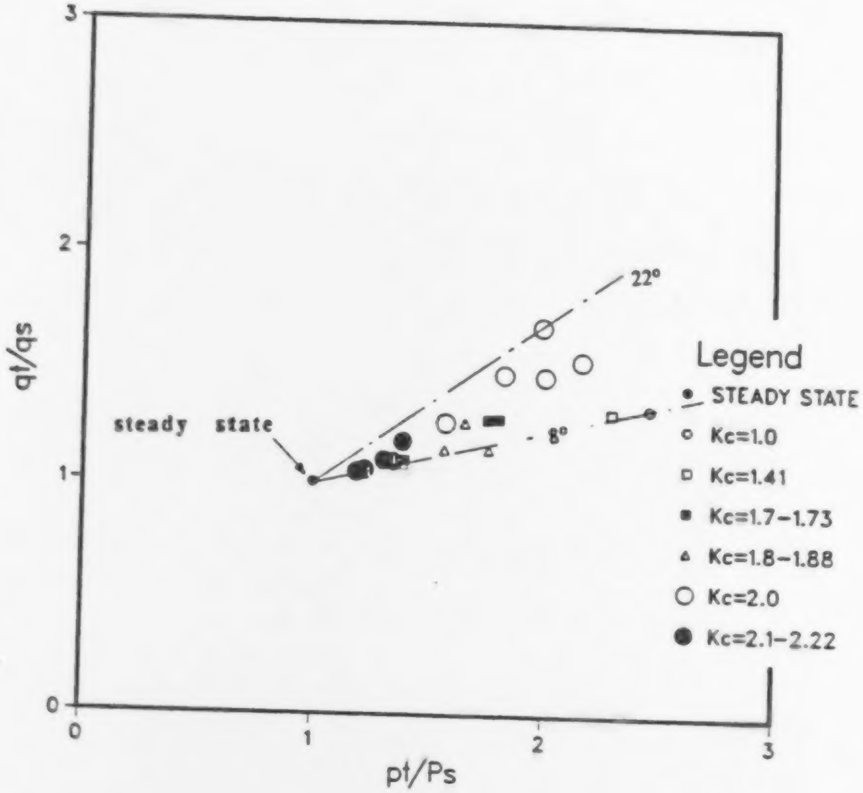

Fig.7.2.3 collapse surface for RPI tests.

7.3. Initial Effective Stress Analysis.

The initial effective stress was determined by the incremental finite element method simulating the construction sequence of the embankment. Figure 7.3.1 shows the finite element mesh and the distribution of materials. The boundary condition at the base was assumed fixed. The right and left side boundaries of alluvium foundation were assumed fixed in the horizontal direction but were free to move vertically.

The hyperbolic non-linear elastic model developed by Duncan and Chang (1970) and Kulhawy et.al. (1971) was used in this analysis for hydraulic fill and alluvium foundation. The properties of materials used in this analysis are given in Table.7.3.1. The properties were determined based on the test results reported by Lee and Seed et.al (1975) and the similar analyses conducted by Seed et.al (1975) and Stara-Gazetas et.al (1986).

The initial seepage pore water pressure was determined by a finite element analysis using the residual flow procedure for free surface flow in porous media given by Desai et. al (1983).

Figure 7.3.2(a) to Figure 7.3.2(c) shows the contours of initial effective stresses in the Lower San Fernando dam before the earthquake. The high shear zones can be observed near the clay core in the lower corners of the hydraulic fill in both upstream and downstream shells.

Figure 7.3.3 shows the free water table in the dam determined by the Desai method. The initial effective stress at all Gaussian integral points was also plotted in p - q space shown in Figure 7.3.4. Also shown on Figure 7.3.4 is the collapse surface for a steady state strength of Su=16 kPa, where Su is the undrained steady state strength on the σ'- τ plane. This figure shows that the initial effective stress states of the lower San Fernando dam are quite close to this collapse surface. In this case, a small amount of excess pore water pressure caused by either earthquake loading or some undrained loading associated with stress re-distribution could cause some elements in the dam to reach the collapse surface and lose strength down to their steady state strength.

Table.7.3.1. Parameters For Initial Static Stress Analysis.

No.	1	2	3&7	4	5	6
γ_s (kN/m^3)	21.05	19.17	19.79	19.17	21.05	20.42
c (kPa)	0	0	0	123.5	0	0
ϕ (o)	30	37	37	37	30	38
μ	0.35	0.35		0.40	0.40	
Rf			0.72			0.76
n			0.54			0.41
K			510			330
G			0.41			0.40
F			0.23			0.16
D			9.4			5.8
k (m/s)	0.001	0.001	0.001	0.0001	0.001	0.001

Key: γ_s = saturated unit weight, c = cohesion, ϕ = friction angle,

μ = Poisson's ratio, k = coefficients of permeability,

Rf, n, K, G, F, D are parameters in hyperbolic strain hardening model defined by Duncan et.al (1970).

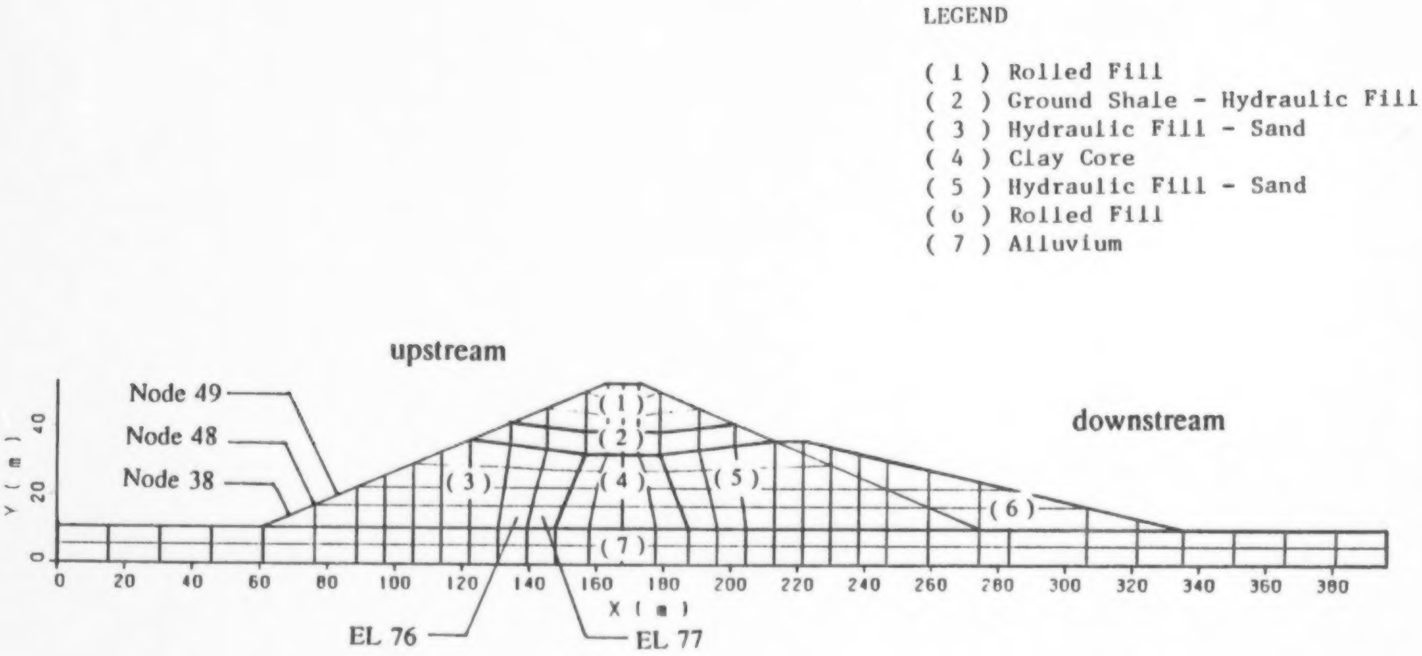
LEGEND
(1) Rolled Fill
(2) Ground Shale - Hydraulic Fill
(3) Hydraulic Fill - Sand
(4) Clay Core
(5) Hydraulic Fill - Sand
(6) Rolled Fill
(7) Alluvium
upstream
downstream
Node 49
Node 48
Node 38
(1)
(2)
(3)
(4)
(5)
(6)
(7)
EL 76
EL 77
Y (m)
0
20
40
X (m)
0
20
40
60
80
100
120
140
160
180
200
220
240
260
280
300
320
340
360
380

Fig. 7.3.1. Finite Elements of The Lower San Fernando Dam.

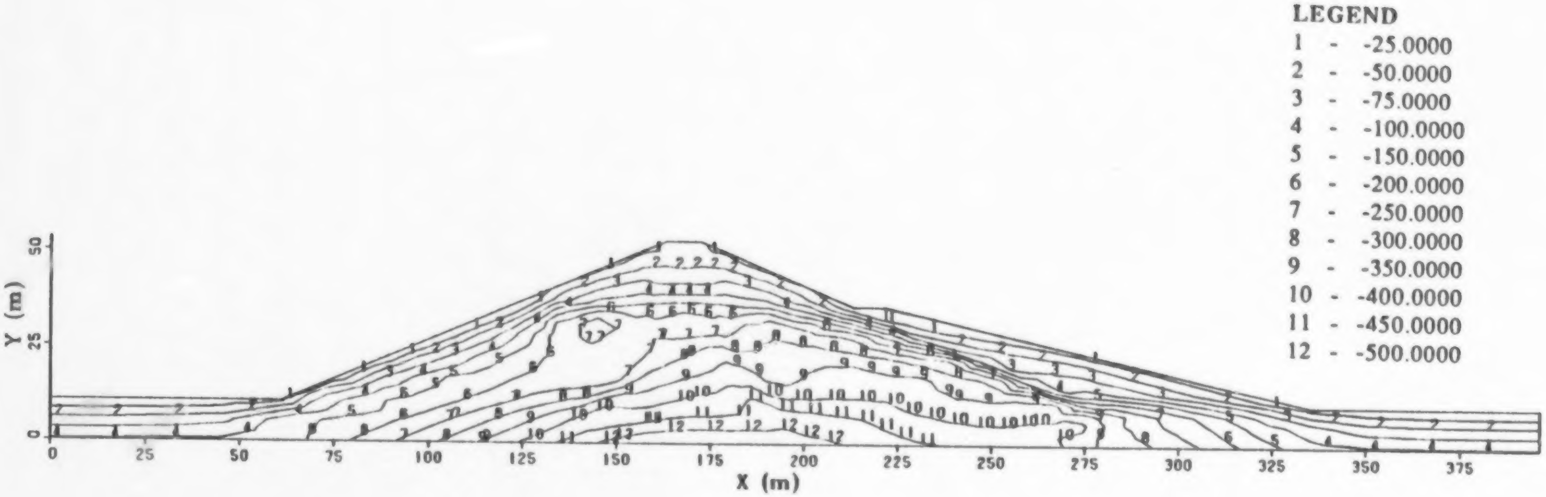

Fig. 7.3.2(a). Contours of Initial Effective Stress σ_x.

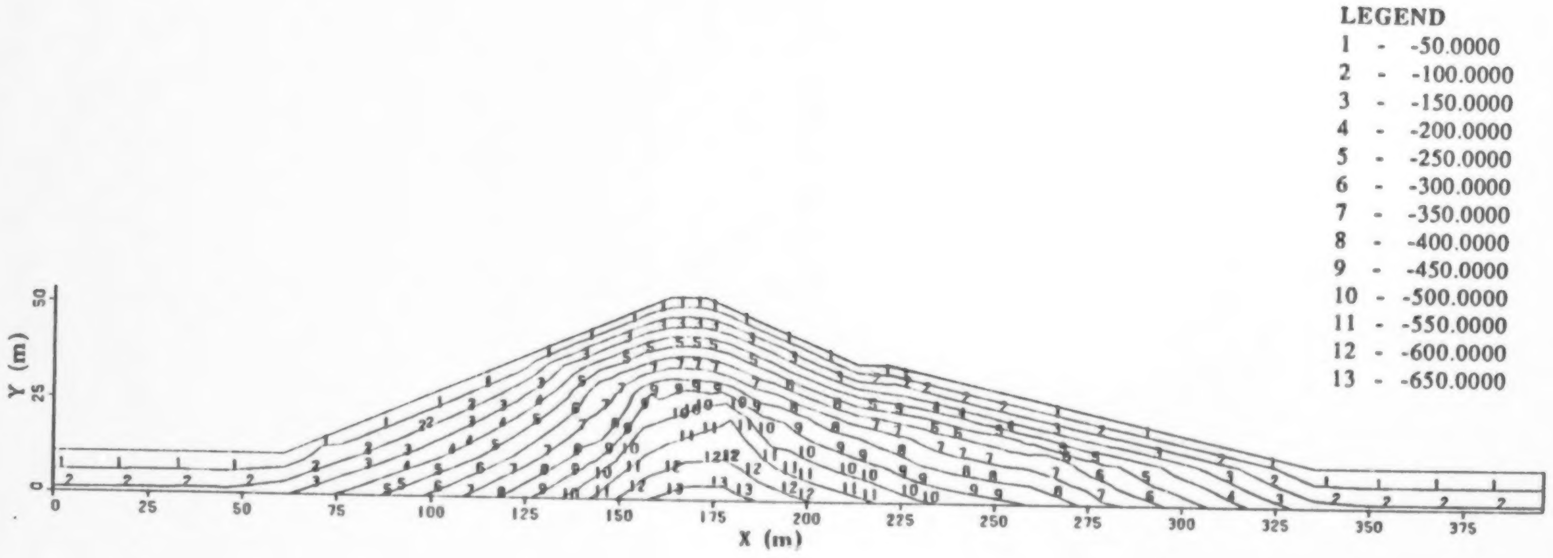

Fig. 7.3.2(b). Contours of Initial Effective Stress σ_y.

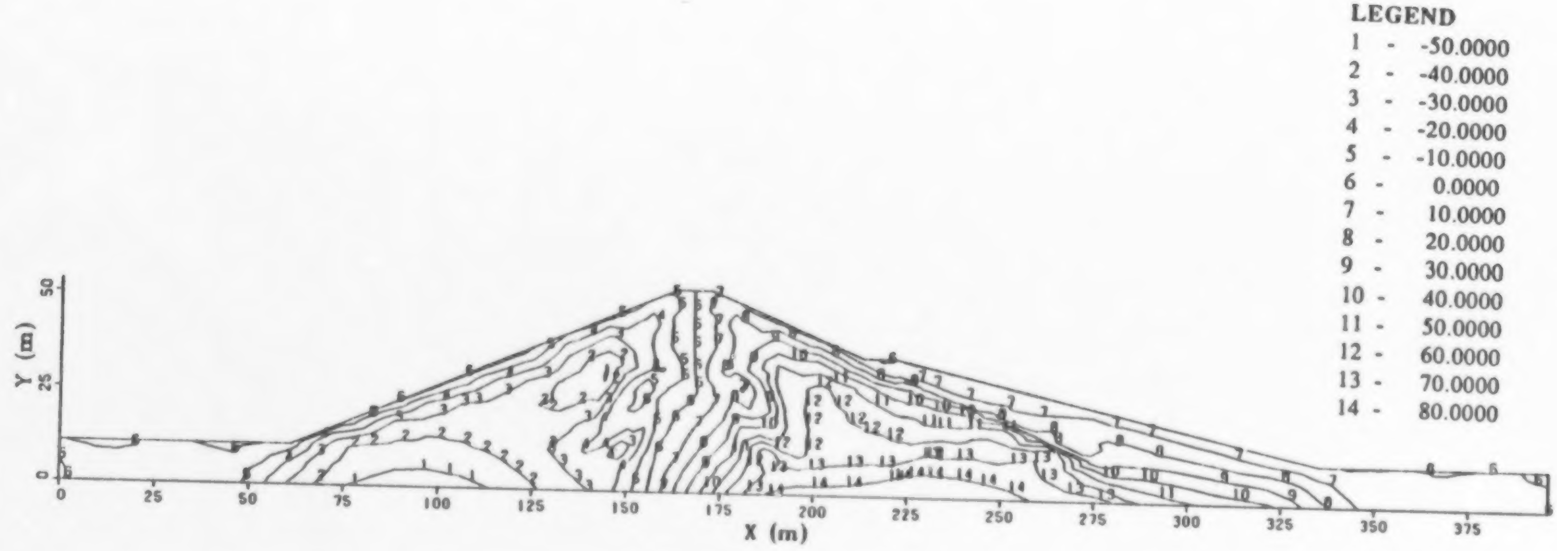

Fig. 7.3.2(c). Contours of Initial Effective Stress τ_{xy}.

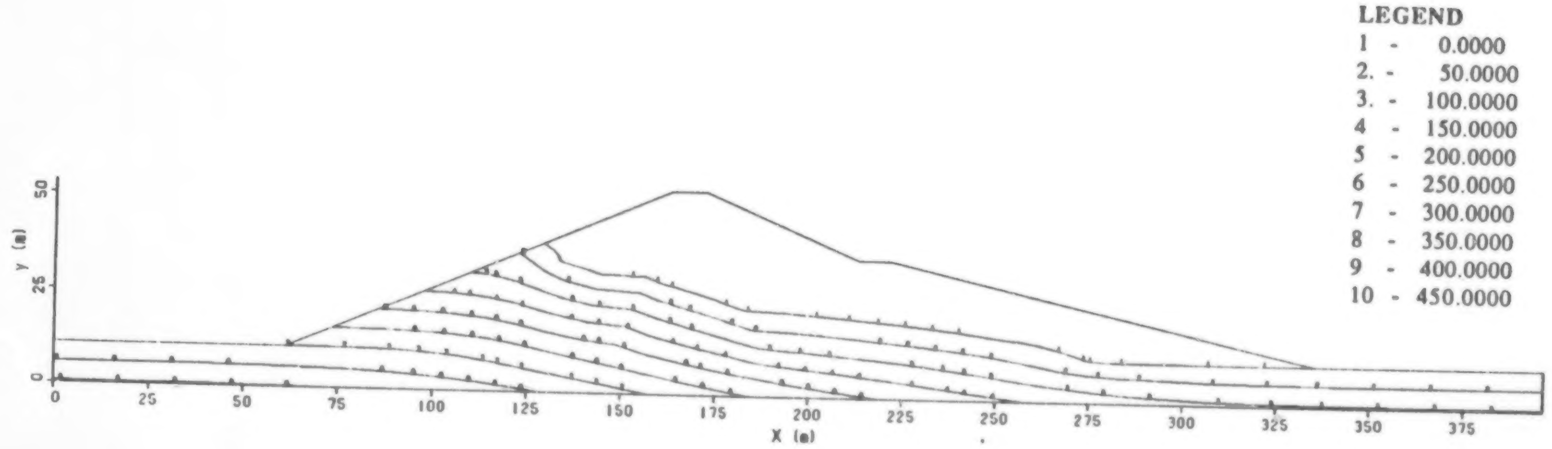

CONTOURS OF INITIAL PORE PRESSURE

Fig. 7.3.3. Contours of Initial Seepage Pore Water Pressure.

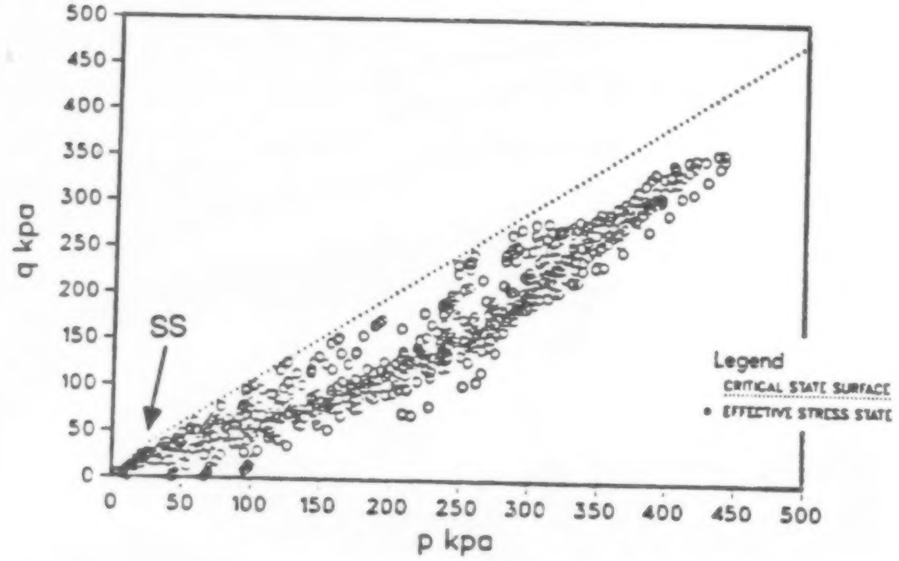

Fig.7.3.4. The initial effective stress state of the Lower San Fernando dam.

7.4. The Post-earthquake Deformation Analysis.

The post-earthquake deformation analysis was conducted under fully undrained conditions by the incremental finite element method. The same finite element mesh shown in Figure 7.3.1 was used in this analysis. The modified strain softening undrained boundary surface model defined in chapter 3 was used to simulate the behaviour of liquefied materials.

In this analysis, the excess pore water pressure caused directly by the earthquake are input by the pore water pressure ratio U/Um. The maximum pore water pressures Um are defined by the horizontal distance between the initial effective stress state and the undrained boundary surface. The distribution of the excess pore water ratio is determined based on the results of dynamic analysis reported by Seed et.al (1975) and Zienkiewicz et.al (1982). In their analyses, the highest pore water pressure was first developed in the lower corner of upstream hydraulic fill near the clay core and then expanded horizontally towards the upstream toe and vertically upwards the rolled materials.

The steady state strength and other parameters used in this analysis are determined based on the laboratory tests, in-situ tests and analytical study work conducted by Lee and Seed et.al(1975), Seed et. al (1975,1987,1989), Vasquez-Herrera (1988), Vasquez-Herrera and Dobry (1989), and Castro et. al

(1989). The properties of materials are given in Table.7.4.1. The steady state strengths used in this analysis are shown in Table 7.4.2.

Table. 7.4.1. Parameters For Post-earthquake Deformation Analysis.

No. of material	1	2	3&7	4	5	6
γ_s (kN/m^3)	21.05	19.17	19.79	19.17	21.05	20.42
c (kPa)	0	0		0	0	
ϕ (o)	30	37		18.4	30	
μ	0.35	0.35	0.48	0.48	0.40	0.48
α_H (o)			53.7			53.7
α_c (o)			43.0			43.0
a			0.05			0.10
Ao			0			0
Am			5			5
B			1.0			1.0

Key: γ_s = saturated unit weight, c = cohesion, ϕ = friction angle, μ = Poisson's ratio, α_H = angle of the Hvorslev surface on undrained p'-q plane, α_c = angle of collapse surface on undrained p'-q plane. a = post peak factor and Ao, Am, B are parameters in effective stress path model.

Table 7.4.2. Steady State Strength Su kPa(psf) in Analysis.

No. of analysis	upstream hydraulic fill	downstream hydraulic fill
1	16 (333)	22 (458)
2	21 (441)	27 (553)
3	28 (580)	36 (750)
4	33 (690)	44 (925)
5	36 (745)	49 (1013)
6	38 (800)	53 (1100)

7.4.1. Progressive Failure of The Lower San Fernando Dam.

In this analysis, the steady state strength were chosen in the range of steady state strength estimated by the back stability analysis conducted by Seed et al(1975,1987), i.e. the value of No.1 and No.2 shown in Table 7.4.2. For No.1 analysis, the undrained strength Su=16 KPa. The results are described as follows:

Figure 7.4.1 shows the initial contours of yield ratio when the excess pore water pressure ratio U/Um = 0 everywhere in the dam. A high yielding ratio zone (0.9) can be observed in the upstream hydraulic fill near the lower corner of clay core. But obviously, the dam is in stable condition. Then, the excess pore water pressures are input with the pore water pressure ratio U/Um = 0.1 - 0.8 distributed from the elements of hydraulic fill near the upstream slope surface with the minimum value of U/Um = 0.1 to the elements of hydraulic fill near the lower corner of the clay core in upstream shell with the maximum value of U/Um = 0.8 . The contours of yielding ratio are plotted in Figure 7.4.2. The figure shows the expansion of the high yielding ratio zone (0.9) in the horizontal direction from the clay core to the toe in upstream hydraulic fill.

When the excess pore water pressure ratio U/Um = 1.0 is input for elements 76 and 77 of the upstream hydraulic fill right beside the lower corner of the clay core where the liquefaction is assumed to occur first, according to the results of dynamic analysis reported by Seed et. al (1975) and Zienkiewicz et. al (1982), progressive failure behaviour occurs. Figure 7.4.3 (a) to Figure 7.4.3 (f) shows the expansion of yielding zone (yielding ratio = 1.0) during the iteration of unbalanced load caused by strain softening in liquefied element 76 and 77. Figure.7.4.4(a) and Figure 7.4.4(b) shows the displacement fields during the iteration of unbalanced load. The displacement in the upstream direction increased gradually and the slip surface was generated gradually during the iteration. The dam was in unstable state. Figure 7.4.5(a) to Figure 7.4.5(c) shows the contours of effective stresses after the iterations. The shear stress and also the normal stresses decrease significantly in the yielding zone because of the shear stress release and the pore water pressure generation during the soil skeleton structure collapse.

Figure 7.4.6 shows the effective stress paths for the elements liquefied directly due to the generation of excess pore water pressure caused by the earthquake. Figure 7.4.7 shows the effective stress paths for the elements liquefied by stress redistribution. The monotonic loading caused by the stress redistribution can be observed in Figure 7.4.7. The slopes of loading paths were defined by the pore pressure parameter A value in the effective stress path model defined in chapter 5.

Figure 7.4.8 shows the factor of safety for a possible slip surface during the iteration of unbalance load. Figure 7.4.9 and Figure 7.4.10 shows the stress-strain behaviour for the elements 76,77,71 and 94 liquefied by the development in excess pore water pressure induced by either earthquake (element 76,77) or by stress re-distribution (element 71,94).

7.4.2. Stability and Steady State Strength.

In order to investigate the relationship between stability and the undrained steady state strength of the hydraulic fill, additional analyses were performed, as shown in Table 7.4.2. The steady state strength of the upstream hydraulic fill was increased from the initial value of Su=16 kPa(333 psf) to Su=38 kPa(800 psf). These analyses reveal the decrease in size of the failure zone as the steady state strength increases. Figure 7.4.11(a) to Figure 7.4.11(e) shows the decrease in yield zones as the steady state strength increase. Figure 7.4.11(b) shows the yield zones after 100 iterations of unbalanced loads when the 35-percentile steady state strength Su=580 Psf was used. The progressive failure can be also observed in this analysis. Figure 7.4.11(e) shows the yield zone after stress redistribution when the average steady state strength Su=800 Psf based on laboratory tests given by Seed group was used. This figure reveals that evenhere there is a large liquefied zone in upstream hydraulic fill after stress re-distribution, although a stable result was obtained.

Figure 7.4.12 shows the relationship between the Factor of Safety and the steady state strength used for upstream hydraulic fill. The dam is stable for steady state strengths Su greater than about 36 kPa(745 psf). For the stress redistribution analyses using steady state strengths Su less than 33 kPa(690 psf), a numerically stable solution was not achieved after 100 iterations of unbalanced load and the processes of convergence are very slow.

Figure 7.4.13 shows the horizontal displacement of several nodes near the toe of upstream hydraulic fill vs the steady state strength. For stable solutions, the displacement after stress redistributions are used. For unstable solutions, the displacement after 100 iterations of unbalanced loads are used. The displacements for unstable solutions shown in these figures have no physical meanings. For an unstable solution, the displacement will continue to develop during further iteration of unbalanced loads.

7.5. Discussion on Liquefaction Instability of Earth Structures.

Liquefaction instability is a very complicated process. In this process, the excess pore water pressure build up. The excess pore water pressure can be caused by either earthquake shaking or stress redistribution. Therefore the soil can also be liquefied by either earthquake shaking or stress redistribution.

The soil skeleton structure may collapse when the stress state is brought to the collapse surface by the excess pore water pressure generation. During the collapse, the stored strain energy release and the load previously carried by the liquefied soils may be transferred to the surrounding materials, causing further liquefaction or yielding in surrounding areas. Obviously, it is not possible to predict this type of failure by a limit equilibrium stability method even by using the steady state strength for the liquefied zone. The liquefied zone after stress redistribution may be much larger than the previous liquefied zone caused directly by an earthquake. The common phenomenon of delayed failure in liquefaction instability of earth structures reinforces the conclusion that the post-earthquake deformation and the stress redistribution analysis are very important in liquefaction stability problem.

The progressive failure in liquefaction instability of the Lower San Fernando dam reveals that the liquefied zone necessary to cause the failure of an earth structure may be much smaller than expected. The progressive failure in liquefaction instability of an earth structure is preceded by continuous expansion of one or several yielding zones in the structure. The continuous expansion of the yielding zone is very much dependent on the release in unbalanced load when the material strength drops from its peak to residual. Therefore, the location of the initial liquefied zone is very important for liquefaction stability evaluation. Progressive failure more likely occurs when the initial liquefied zone is located in a high driving shear stress area. It is easy to understand that the liquefied materials in high driving shear stress conditions release more force and strain energy. Because the liquefied zone caused directly by an earthquake is usually smaller than the liquefied zone caused by stress redistribution during and following an earthquake, the limit equilibrium stability analysis even by using steady state strength for liquefied material may give a result on the un-safe side. The safety evaluation of an earth structure with liquefied materials is no longer a simple limit equilibrium problem. The appropriate resistance factor is not a function of material alone (Morgenstern,1989). It is a problem of stress path and deformation dependence.

To consider the effects of stress redistribution that must occur with liquefied materials, the post-earthquake deformation analysis becomes necessary. Because the deformation caused directly by the earthquake shaking is much smaller than the deformation caused by the stress redistribution when there are high unbalanced shear stress release during and following an earthquake, the post-earthquake deformation analysis may be more important in liquefaction stability analysis.

The results of these analysis also show that the progressive failure in the lower San Fernando dam may occur if the steady state strength for hydraulic fill is lower than the average value based on the laboratory tests given by the Seed group (1989) and slip failure may not occur if the steady state strength large or equal to the average value. This is in good agreement with the analysis conducted by Seed et.al or the stability analysis by using the steady state testing approach proposed by Poulos et.al (1985).

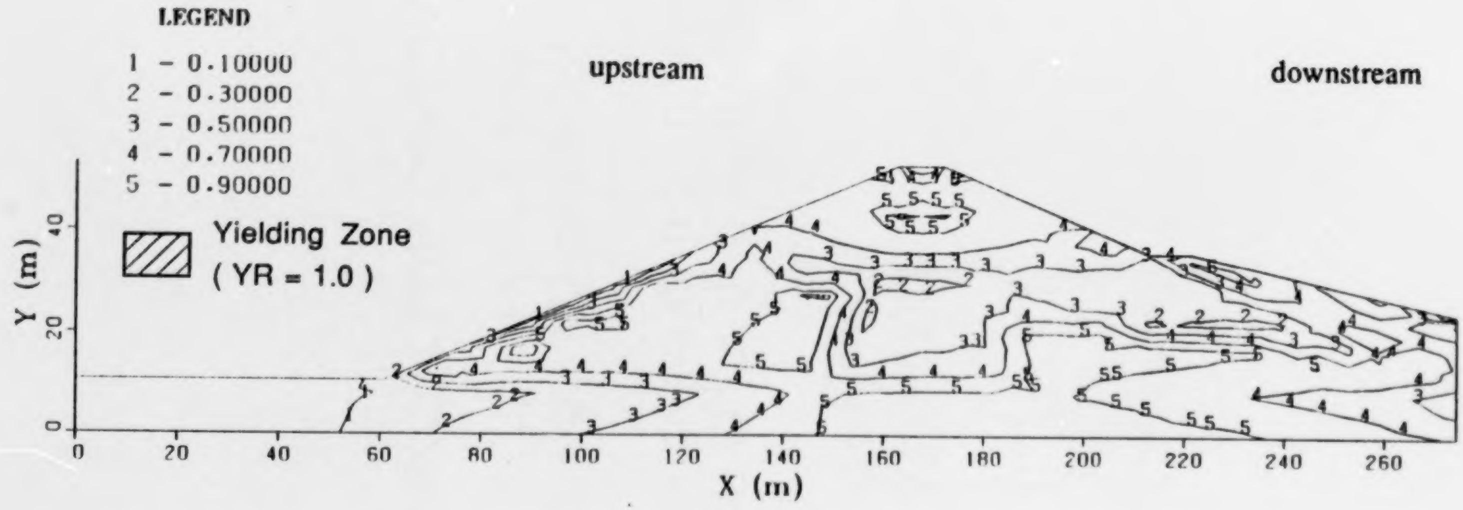

Fig. 7.4.1. Contours of Initial Yield Ratio.

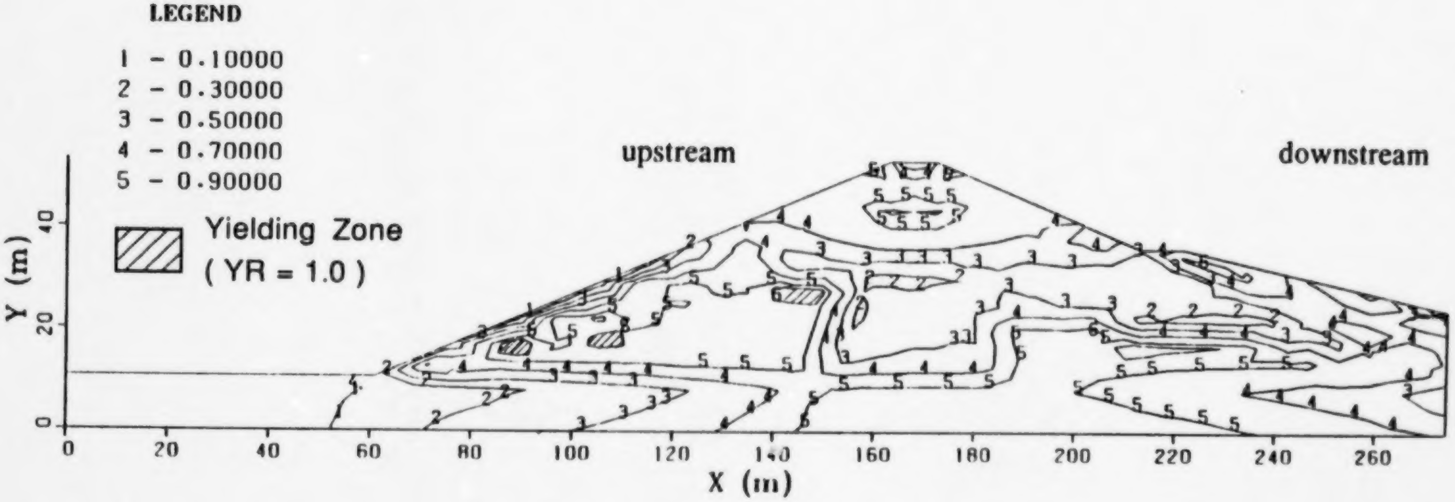

Fig. 7.4.2. Contours of Yield Ratio When U/Um=0.1 - 0.8.

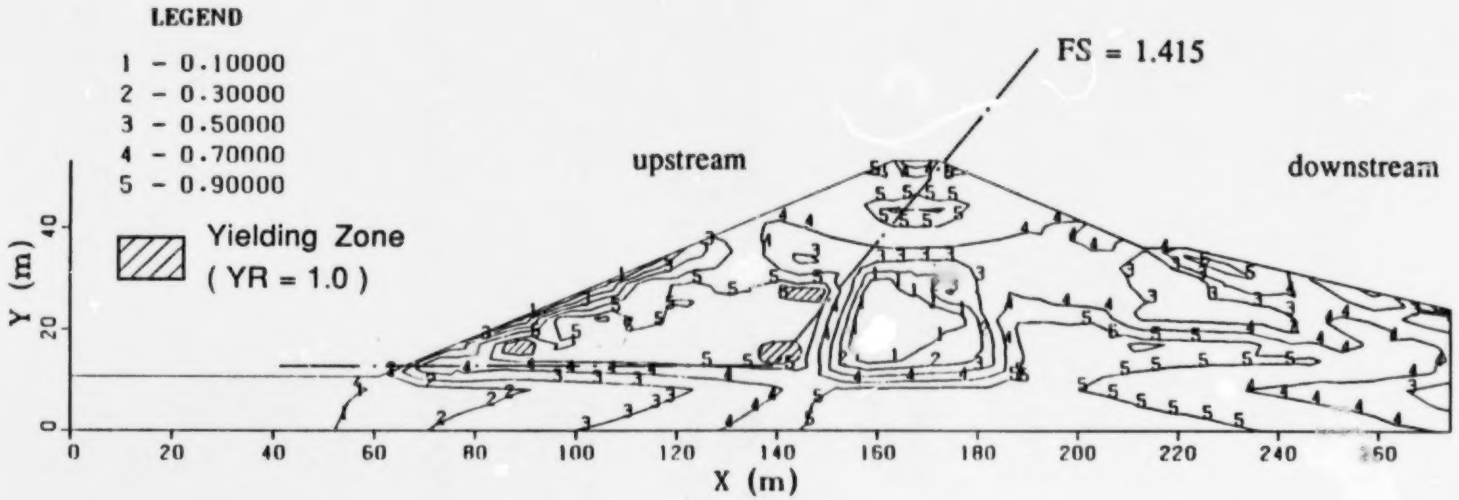

Fig. 7.4.3(a). Contours of Yield Ratio When Unbalanced Load Iteration = 0.

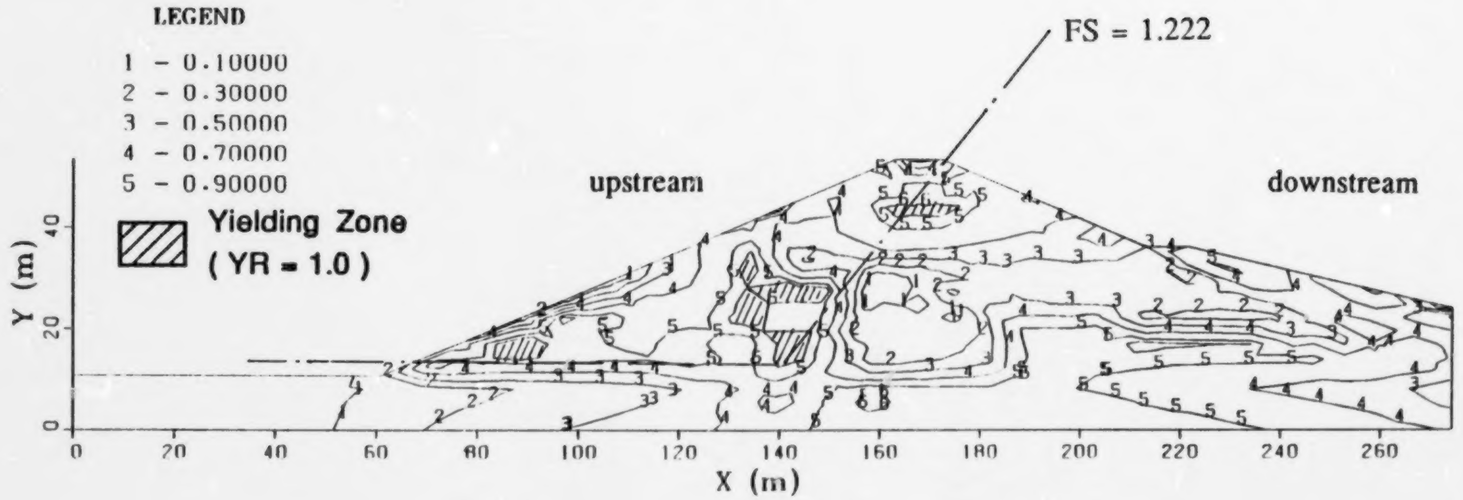

Fig. 7.4.3(b). Contours of Yield Ratio When Unbalanced Load Iteration = 5.

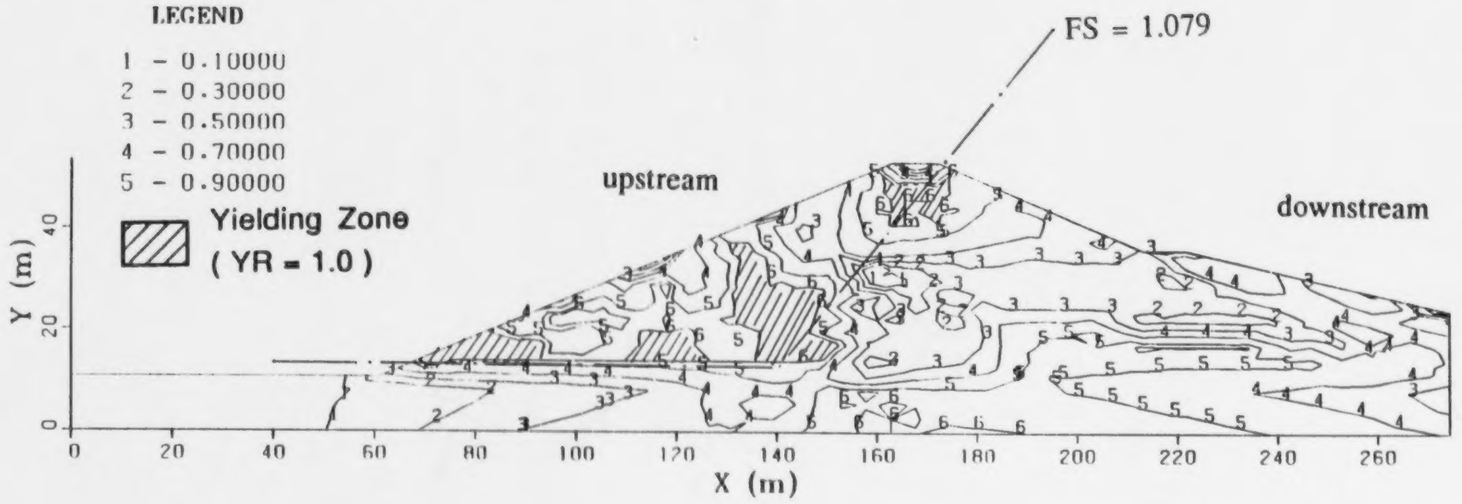

Fig. 7.4.3(c). Contours of Yield Ratio When Unbalanced Load Iteration = 7.

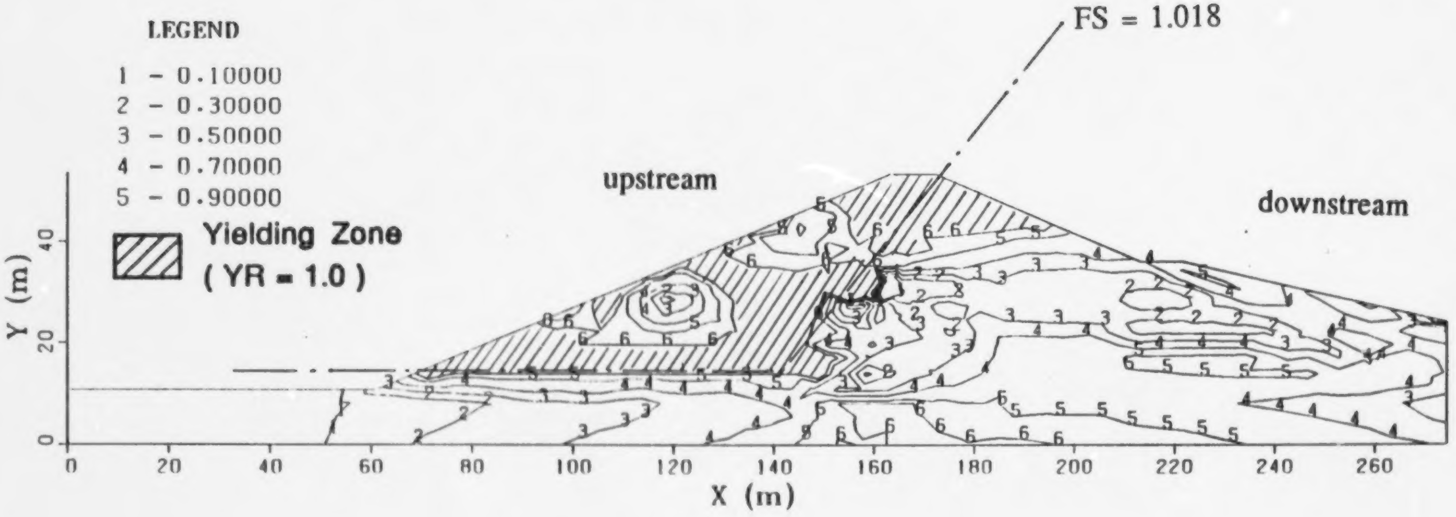

Fig. 7.4.3(d). Contours of Yield Ratio When Unbalanced Load Iteration = 10.

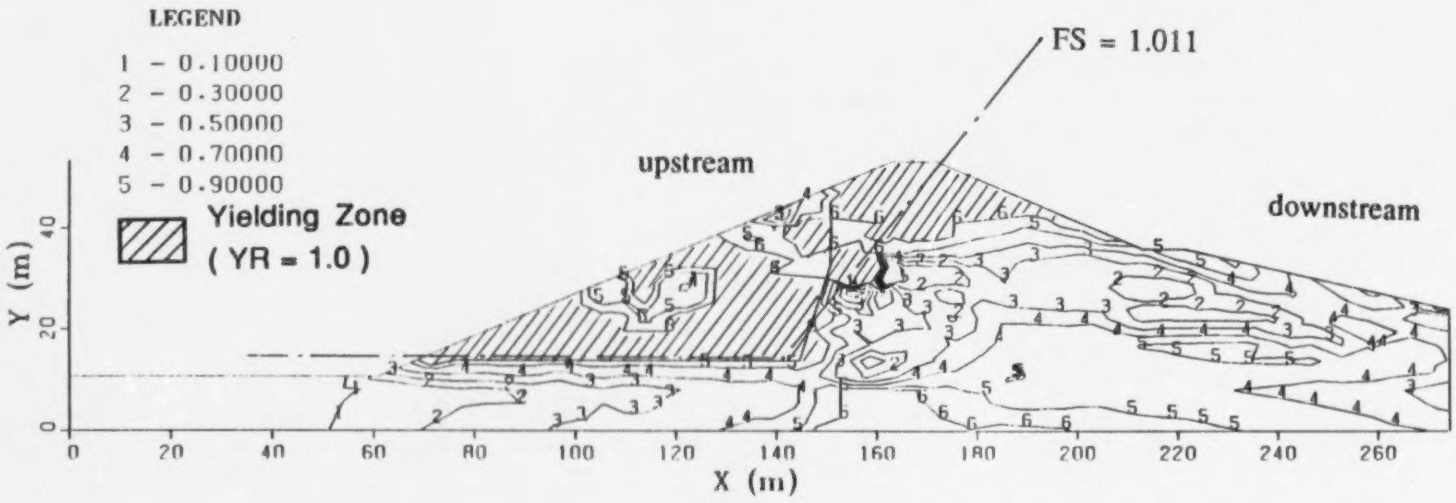

Fig. 7.4.3(e). Contours of Yield Ratio When Unbalanced Load Iteration = 20.

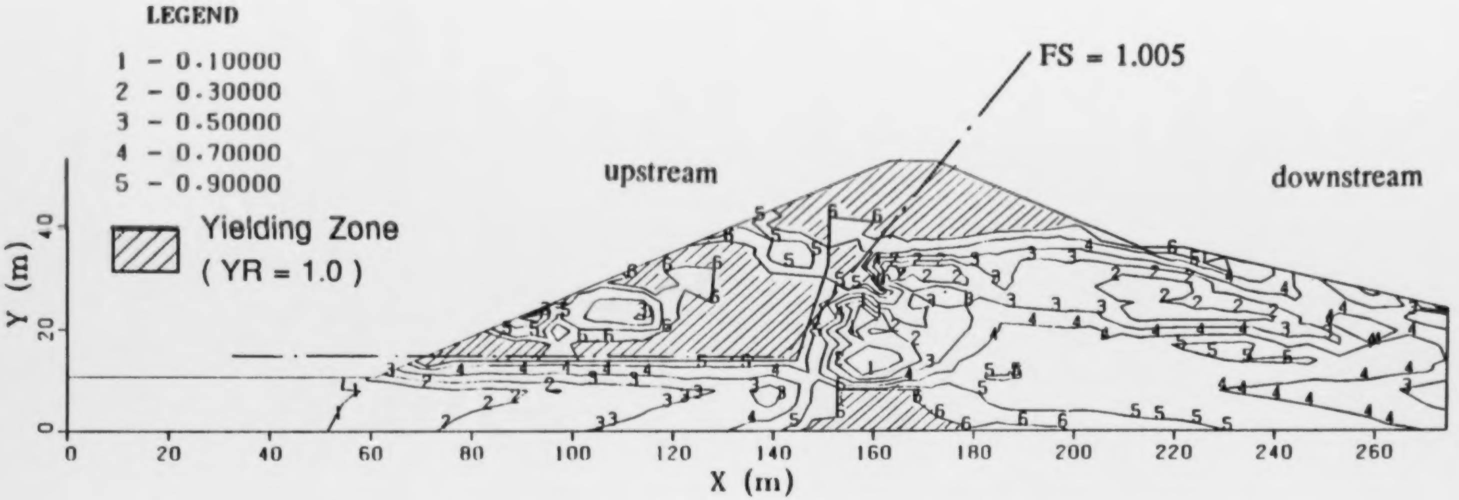

Fig. 7.4.3(f). Contours of Yield Ratio When Unbalanced Load Iteration = 100.

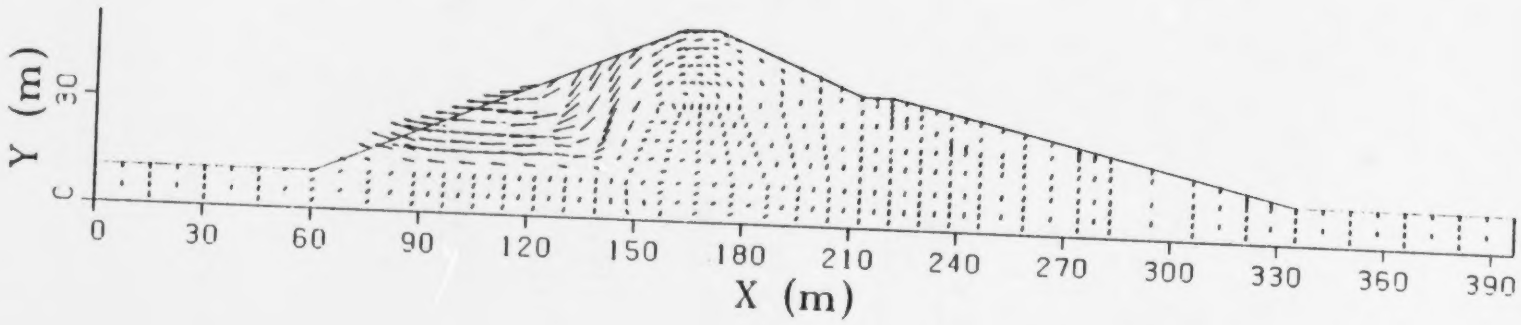

Fig. 7.4.4(a). Displacement Field When Unbalanced Load Iteration = 20.

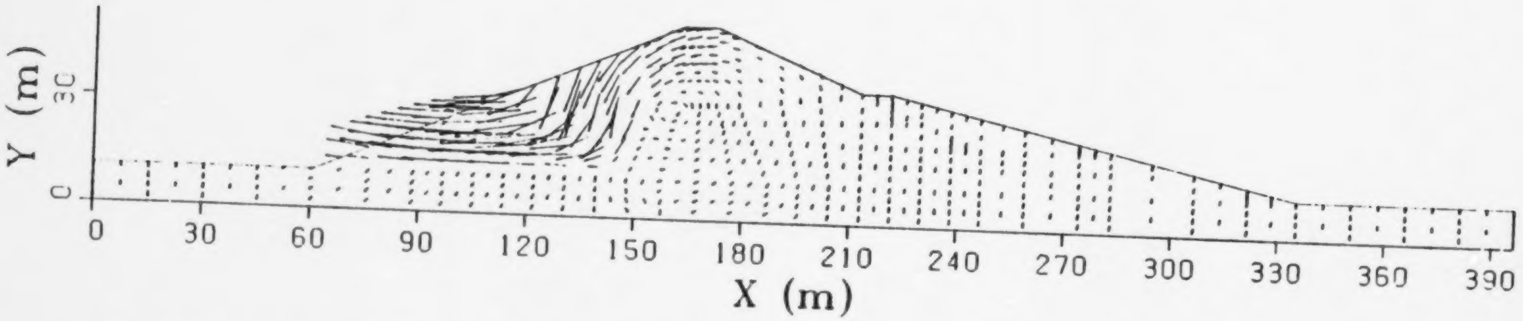

DISPLACEMENT DURING STRESS RE-DISTRIBUTION(it.=100,arrow=10xdispl.)

Fig. 7.4.4(b). Displacement Field When Unbalanced Load Iteration = 100.

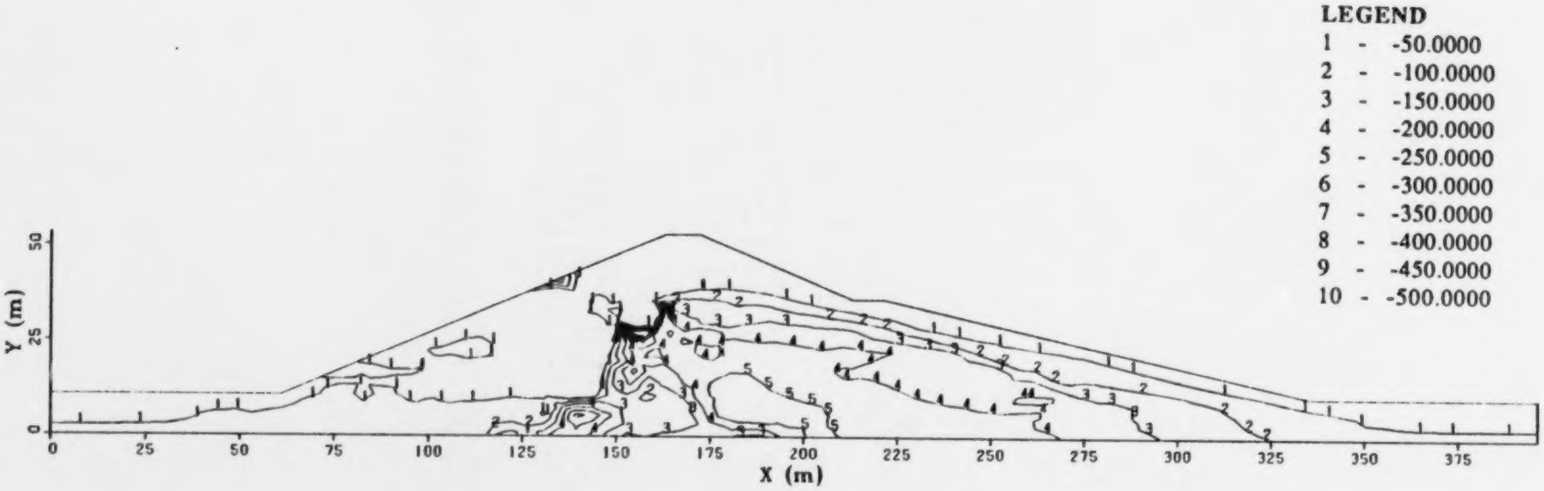

Fig. 7.4.5(a). Contours of Stress σ_x After Iteration of Unbalanced Load.

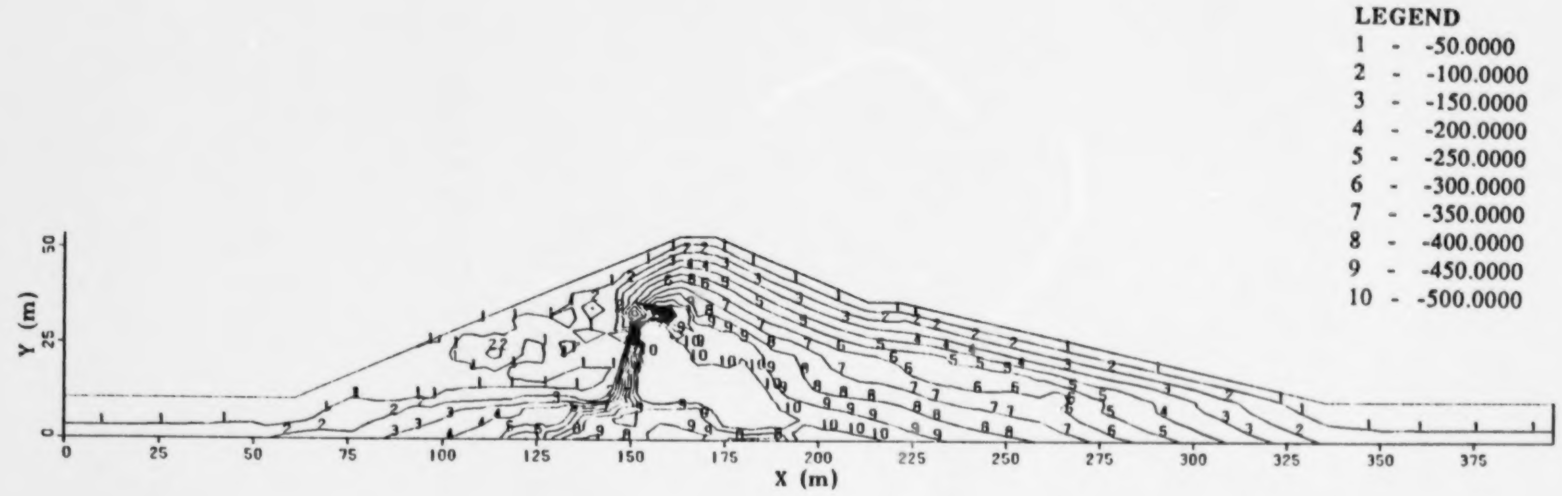

Fig. 7.4.5(b). Contours of Stress σ_y After Iteration of Unbalanced Load.

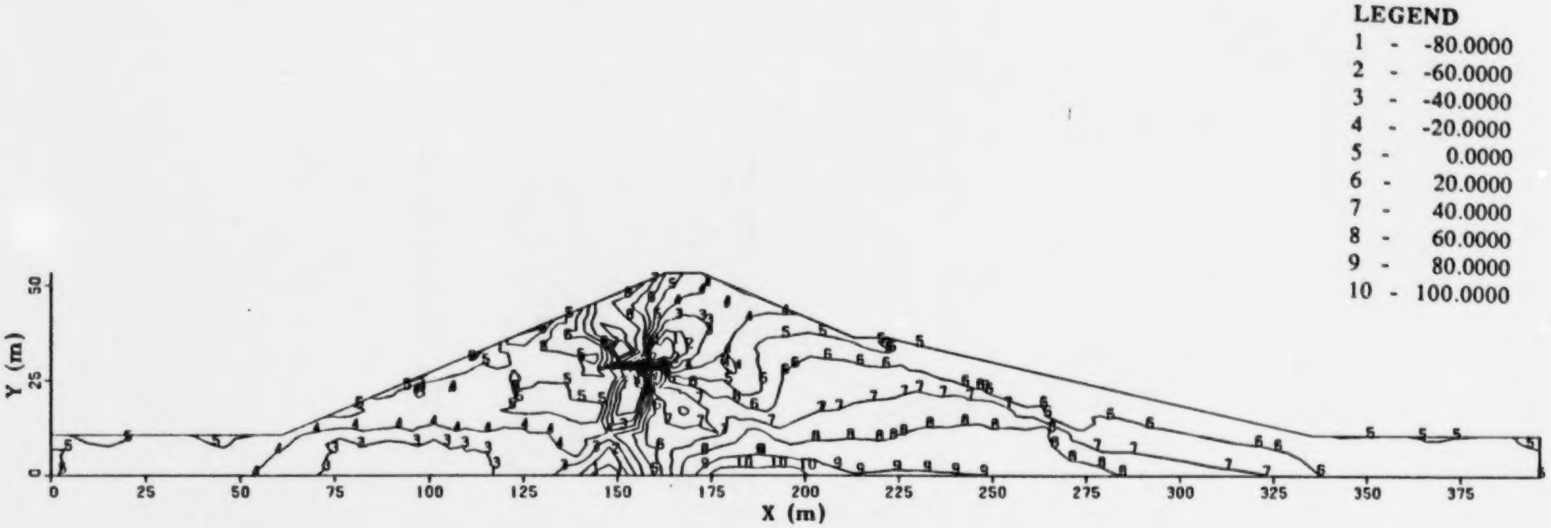

Fig. 7.4.5(c). Contours of Stress τ_{xy} After Iteration of Unbalanced Load.

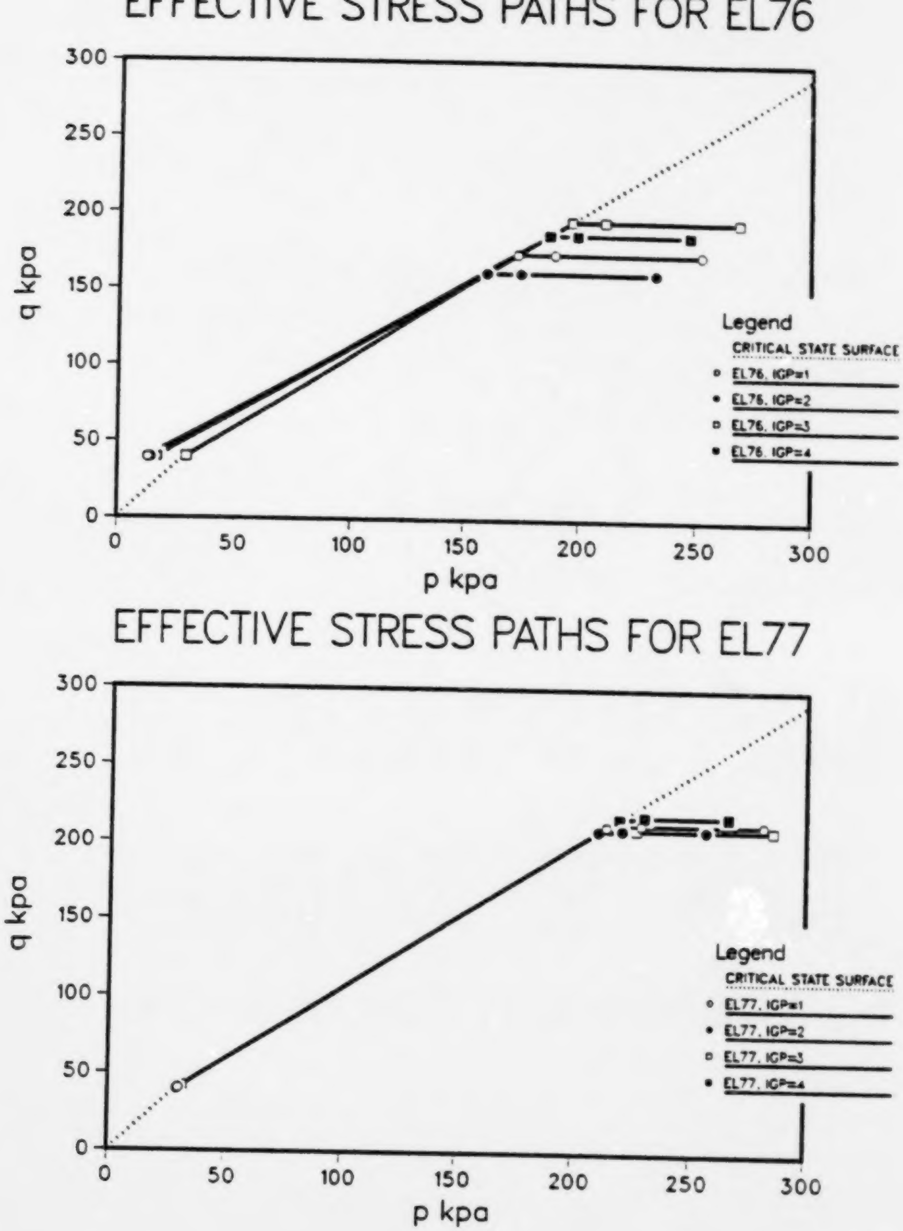

Fig. 7.4.6. **The effective stress paths for the elements liquefied directly by the excess pore water pressure generated by the earthquake**

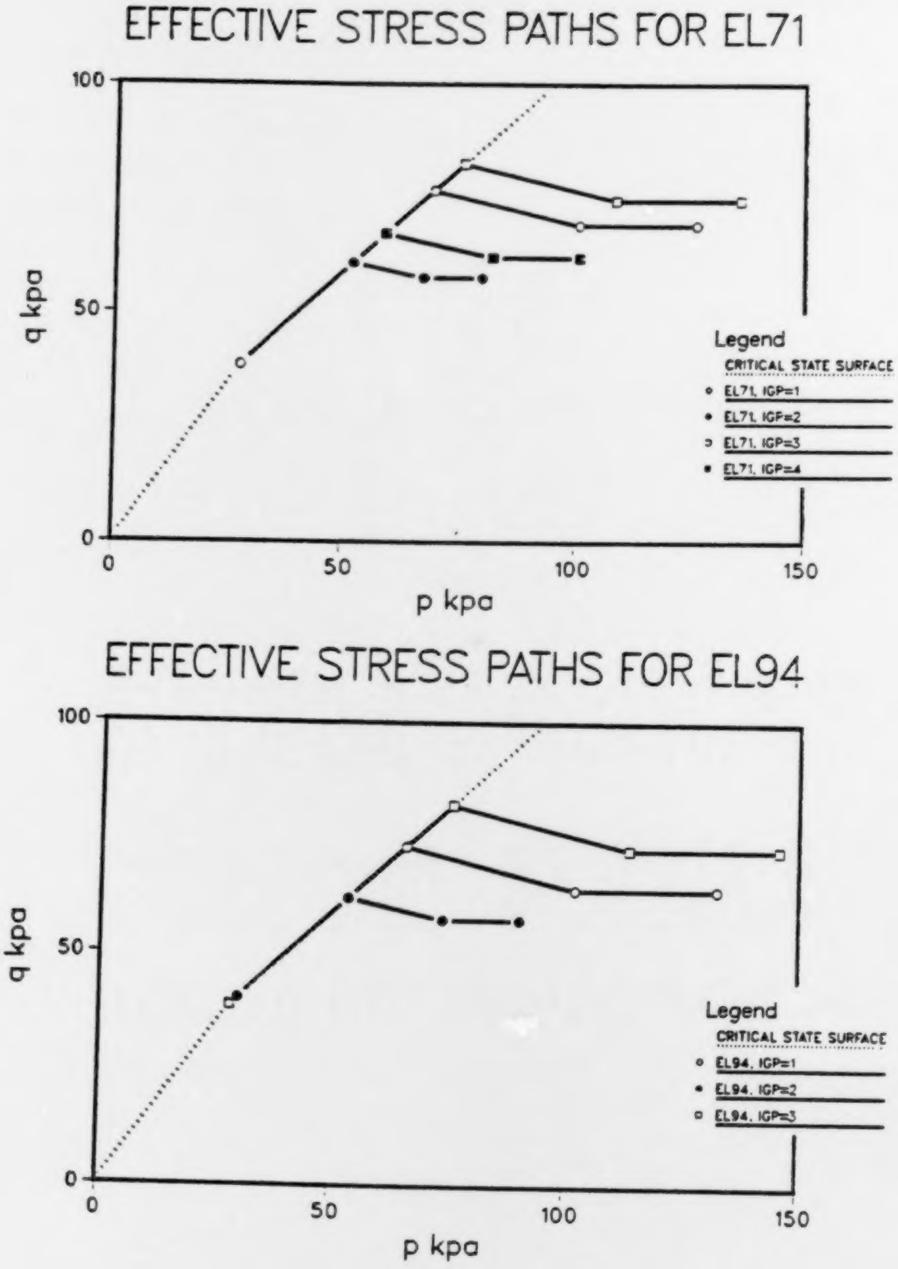

Fig. 7.4.7. **The effective stress paths for the elements liquefied by the stress re-distribution**

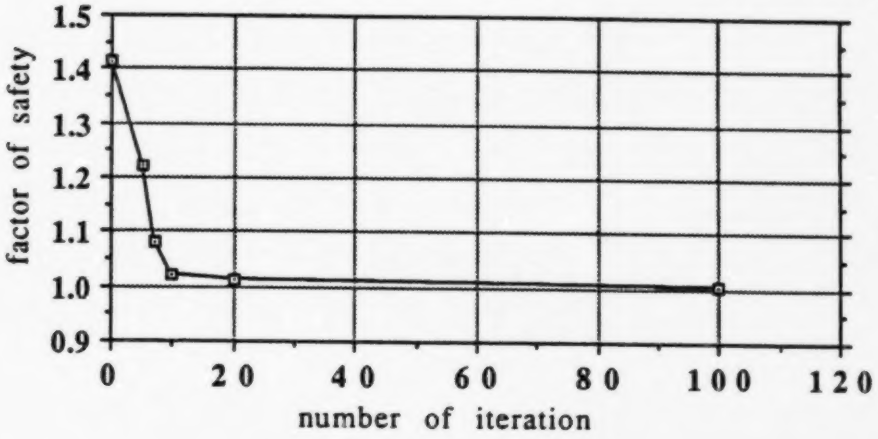

Fig. 7.4.8. **Factor of Safety During Iteration of Unbalanced Load.**

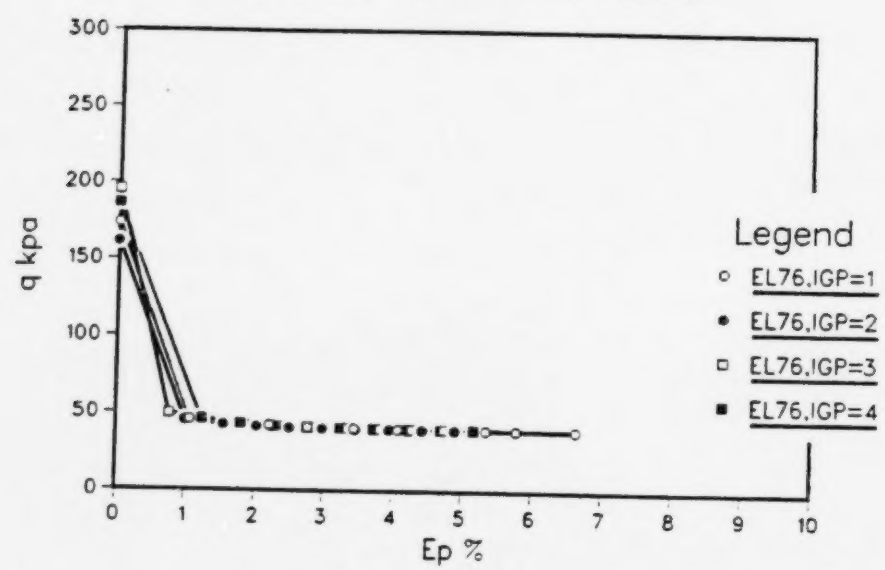
STRESS–STRAIN IN EL76

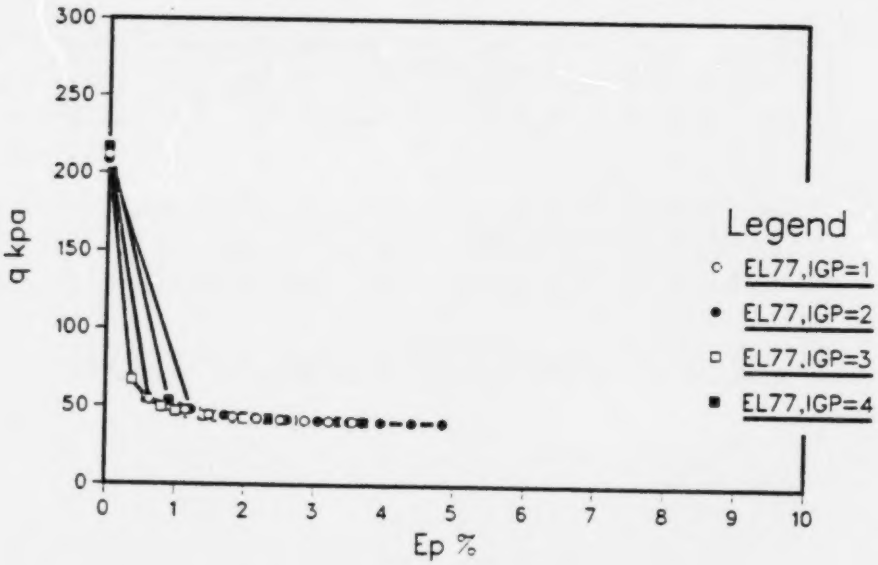
STRESS–STRAIN IN EL77

Fig. 7.4.9. Strain softening behaviour for the elements liquefied directly by the earthquake

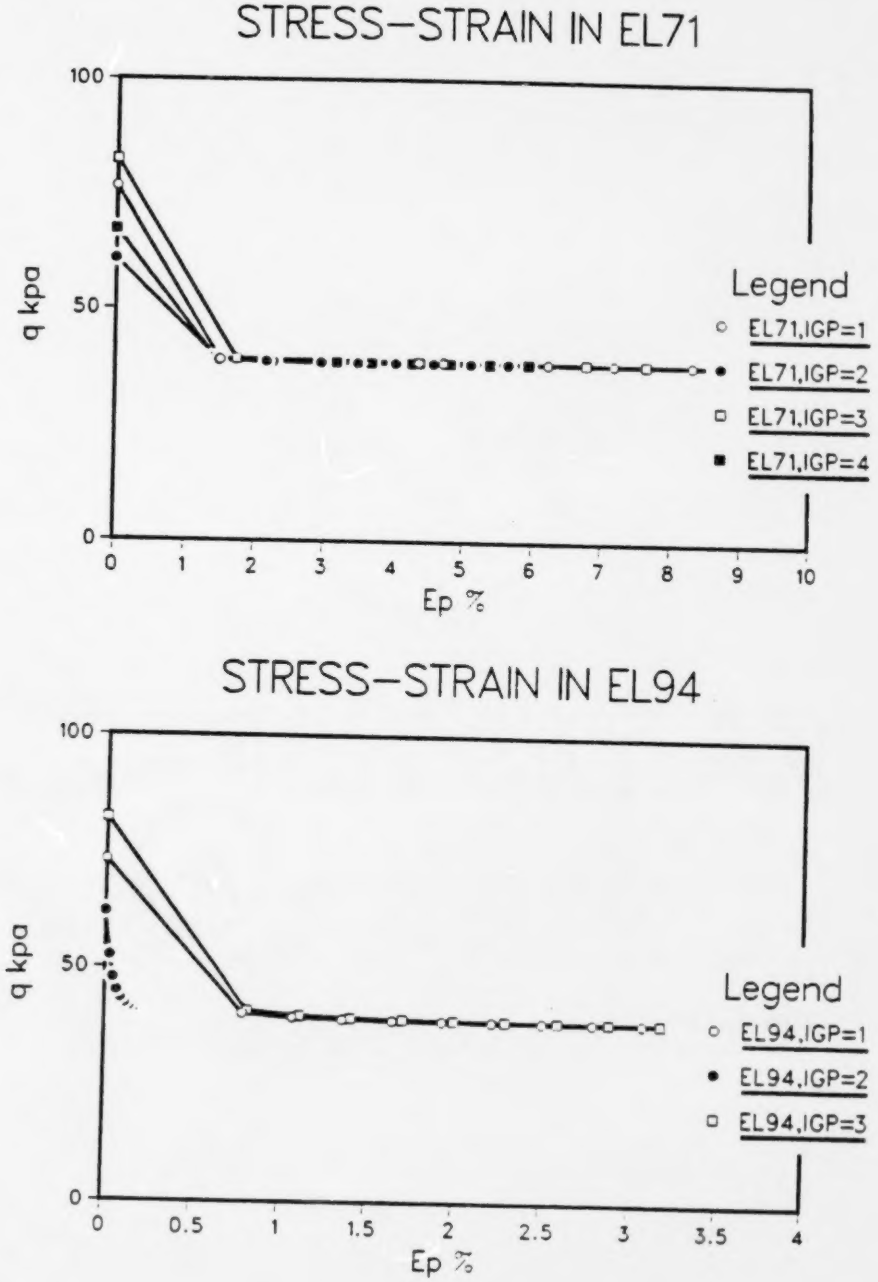

Fig. 7.4.10. Strain softening behaviour for the elements liquefied by the stress re-distribution

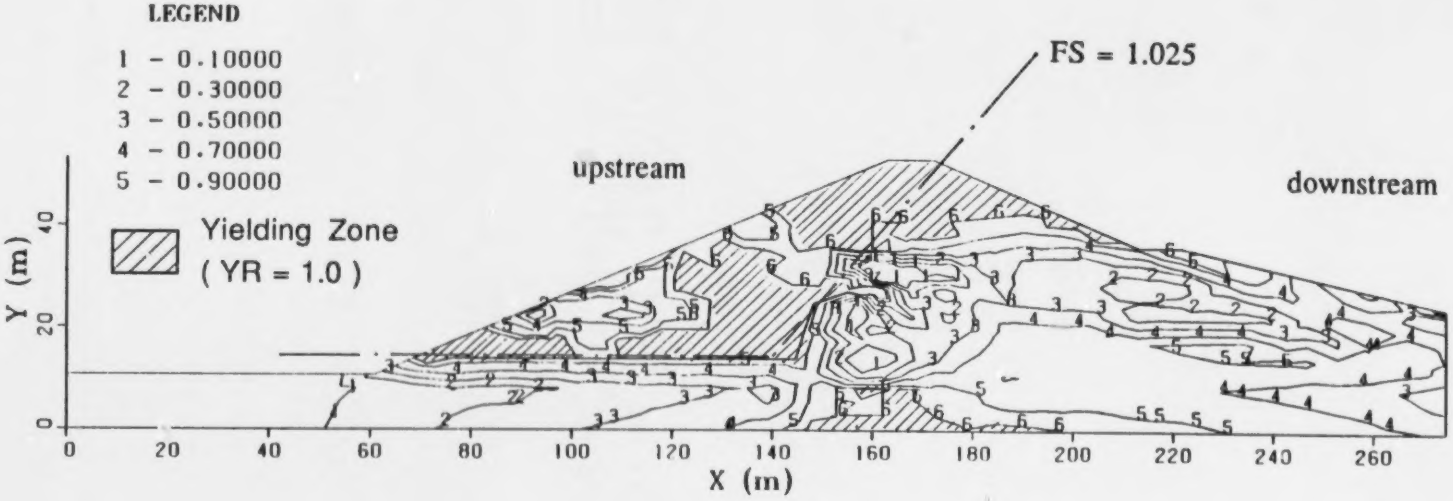

Fig. 7.4.11(a). Contours of Yield Ratio When Su = 21 kPa (441 psf).

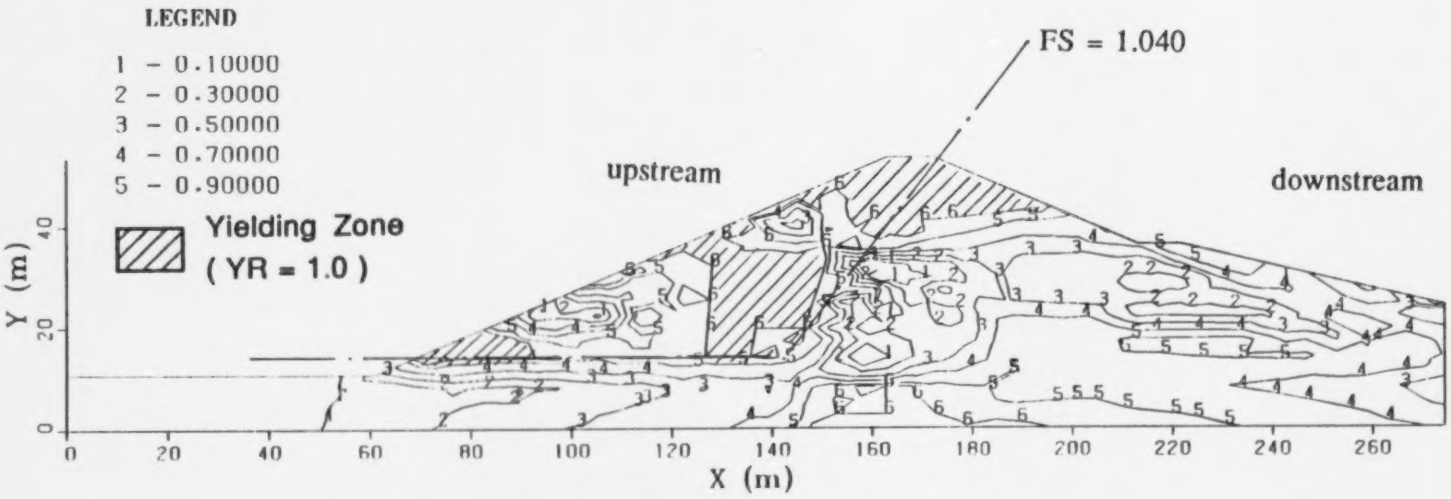

Fig. 7.4.11(b). Contours of Yield Ratio When Su = 28 kPa (580 psf).

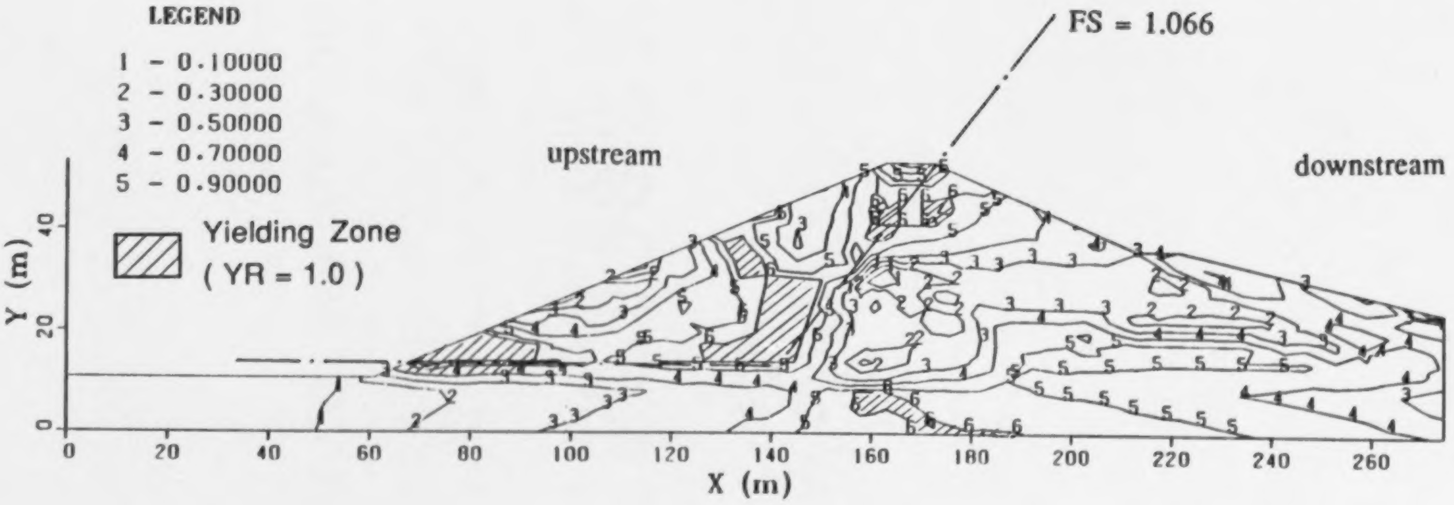

Fig. 7.4.11(c). Contours of Yield Ratio When Su = 33 kPa (690 psf).

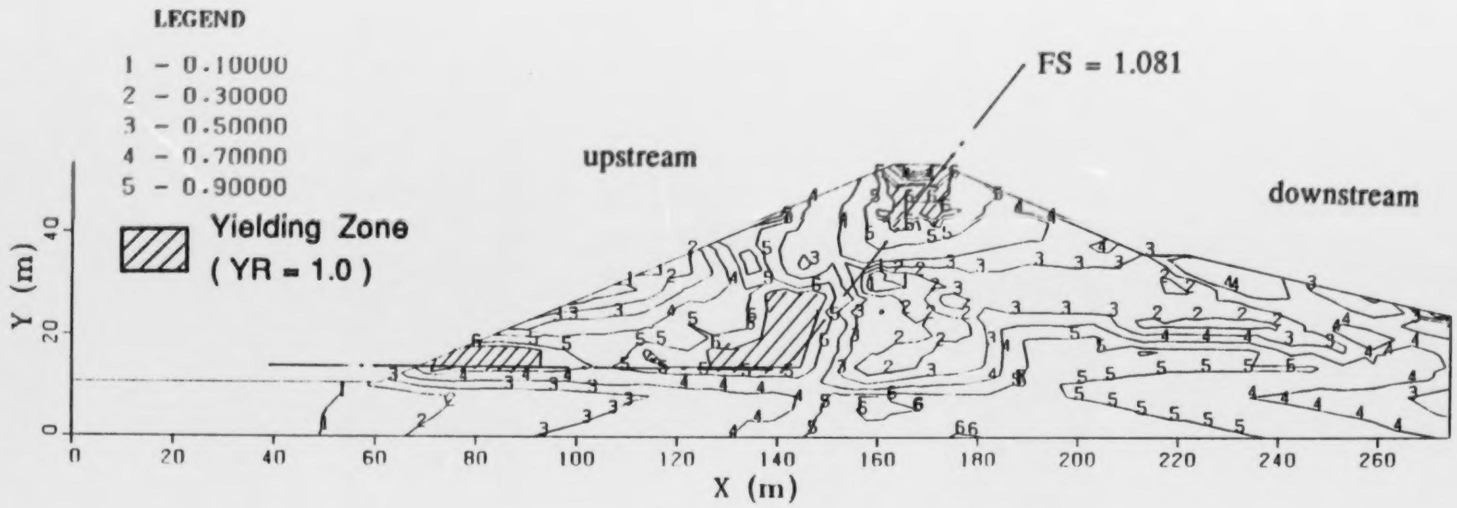

Fig. 7.4.11(d). Contours of Yield Ratio When Su = 36 kPa (745 psf).

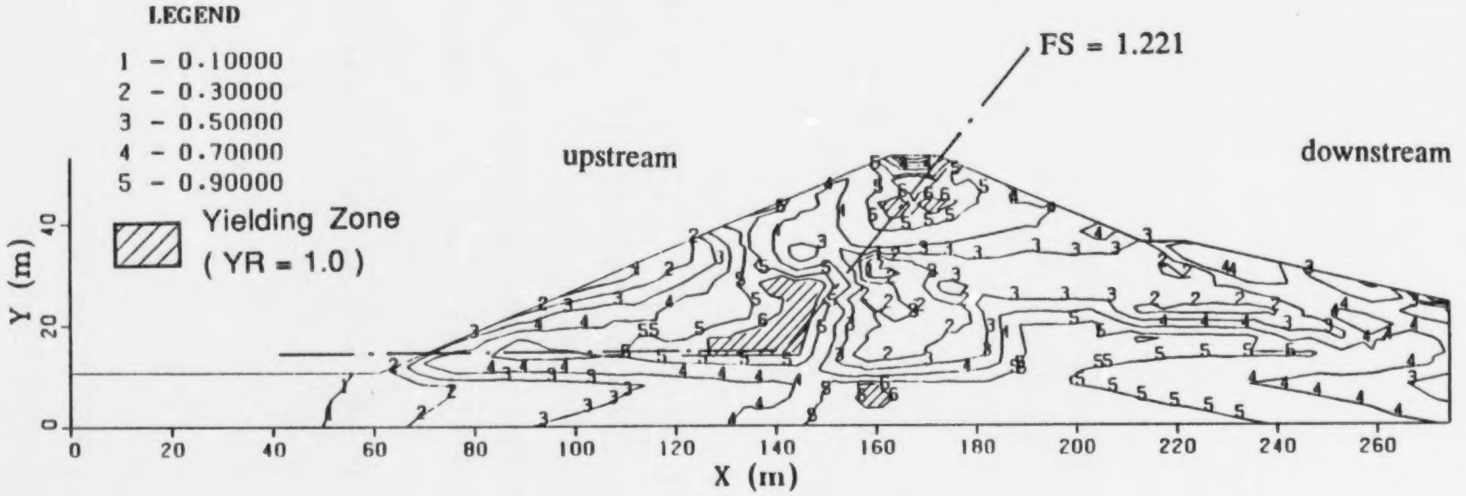

Fig. 7.4.11(e). Contours of Yield Ratio When Su = 38 kPa (800 psf).

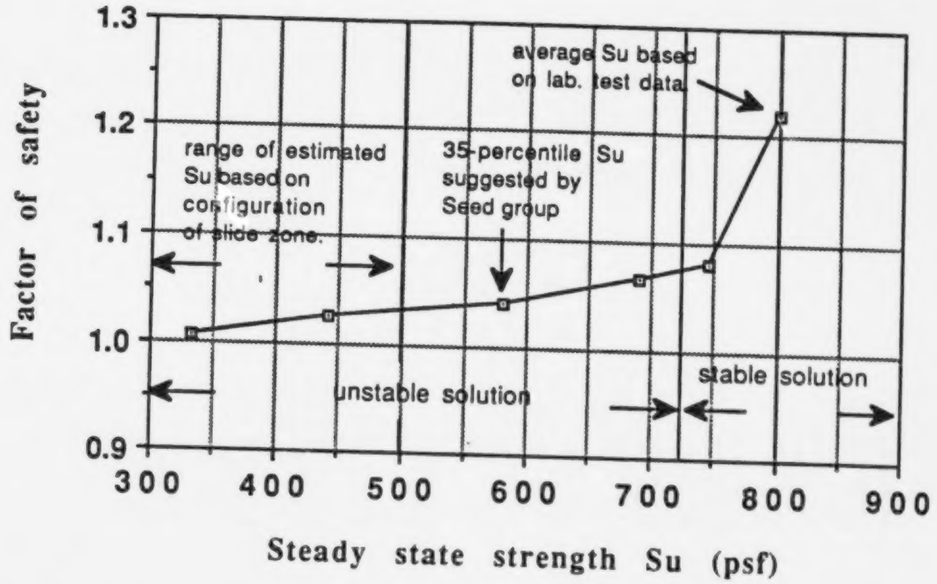

Fig. 7.4.12. **Factor of Safety vs Steady State Strength.**

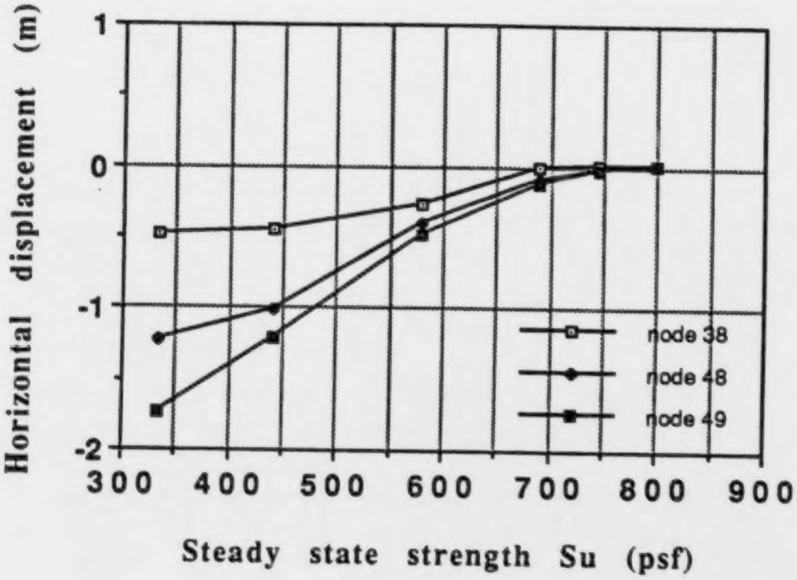

Fig. 7.4.13. **Horizontal Displacement vs Steady State Strength.**

8. POST-EARTHQUAKE DEFORMATION ANALYSIS OF THE WILDLIFE SITE, IMPERIAL VALLEY, CALIFORNIA.

8.1. Review of The Liquefaction Behaviour of The Wildlife Site.

The liquefaction behaviour of the Wildlife Site, Imperial Valley, California, during the1987 Superstition Hills earthquake is an important case to study the mechanism of liquefaction under level ground conditions. It is probably the only case history in which the site conditions, seismic response, and ground displacements are known, particularly, the simultaneous measurements of seismically induced pore water pressures and surface and subsurface accelerations were obtained (Holzer et.al, 1989).

After an earthquake (Ms=6.0) occurred on 26 April, 1981, in the Imperial Valley, near Westmorland, California, a group of tests were conducted in the area during 1982 to 1983(Bennett et.al, 1984). The goals of the testing were to define the sediment properties, identify the sediment susceptible to liquefaction and select a site for installation of accelerometers and piezometers to record ground-motion response and pore water pressures during future earthquake. The Wildlift site was selected for installation of the instruments.

The Wildlife site is located 3.2 km south of Calipatria in the Imperial Wildfowl Management Area. The site lies on the west side of the incised flood plain of the Alamo River. Sand boils developed on the flood plain during 1981 earthquake and 1987 earthquake.

Figure 8.1.1 shows a typical cross section (Units A to Unit D) and instrument locations at the Wildlife site (Bennette, et.al, 1984). Based on the looseness of the sediment, high water table, and similarity to sand boil material, the Unit B is identified to be the layer that liquefied and formed sand boils during 1981 earthquake. Therefore, five piezometers (pl to p5) were installed at different depths in Unit B. One piezometer P6 was installed in Unit D. Two three-component force-balance accelerometers, one (SM2) on the ground surface and one(SM1) downhole (at the top of Unit C) were also installed. During the November 24, 1987 earthquake(M=6.5), the instrumental response was monitored and recorded. Figure 8.1.2 shows the increase of normalized pore water pressures with time for piezometer Pl to P5 at the site shown in Figure.8.1.1. Excess pore water pressures began to develop when the peak horizontal ground acceleration reached 0.21g about 13.6 seconds after the accelerometers were triggered. The earthquake shaking lasted about 30 seconds, but the pore water pressures continued to climb for about 90 seconds. Almost half of the excess pore water pressures developed after the earthquake shaking. The liquefaction of Unit B did not actually occur until after the earthquake was over. The measurement of acceleration shows that the high frequency components of strong motion on the ground surface were especially degraded by excess pore water pressure generation. The measurement of piezometer p6 indicated that Unit D , a silt layer, did not liquefy during the 1987 earthquake.

Figure 8.1.3 shows the horizontal displacements measured on the ground surface at the Wildlife Site during 1987 earthquake(Youd and Bartlett, 1988). The displacements indicated that the upper layer slid in the N-E direction toward the river. Extensive cracking was observed on the ground that appears to have been caused by local slumping along the west bank of the Alamo River. The ejection of sand from some of these cracks confirms that they were associated with liquefaction. Figure 8.1.4 shows the sand boils observed on the ground surface during the 1987 earthquake.

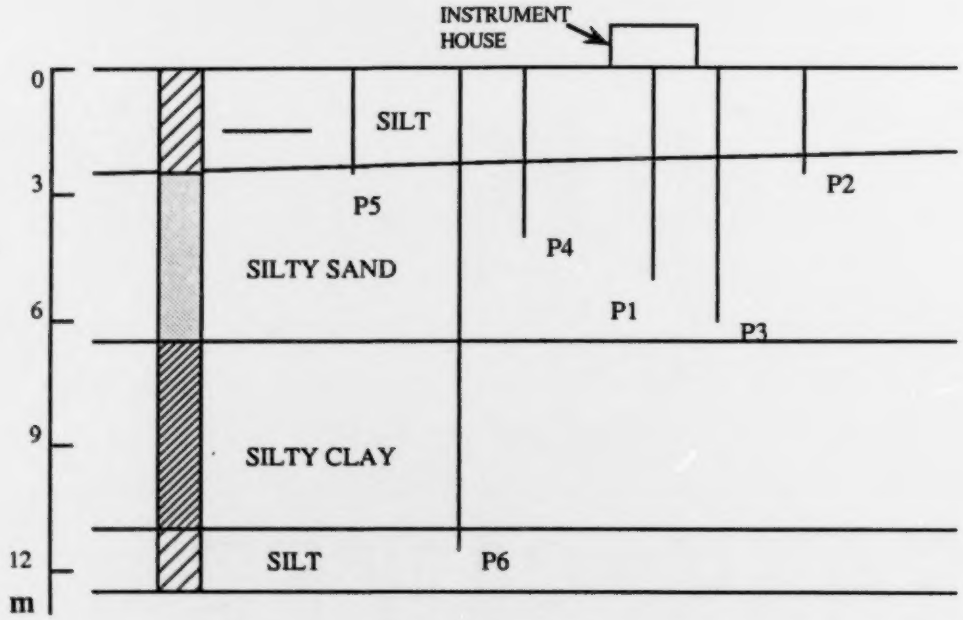
INSTRUMENT HOUSE
0
3
6
9
12
m
SILT
SILTY SAND
SILTY CLAY
SILT
P1
P2
P3
P4
P5
P6

Fig. 8.1.1. Cross Section of The Wildlife Site.

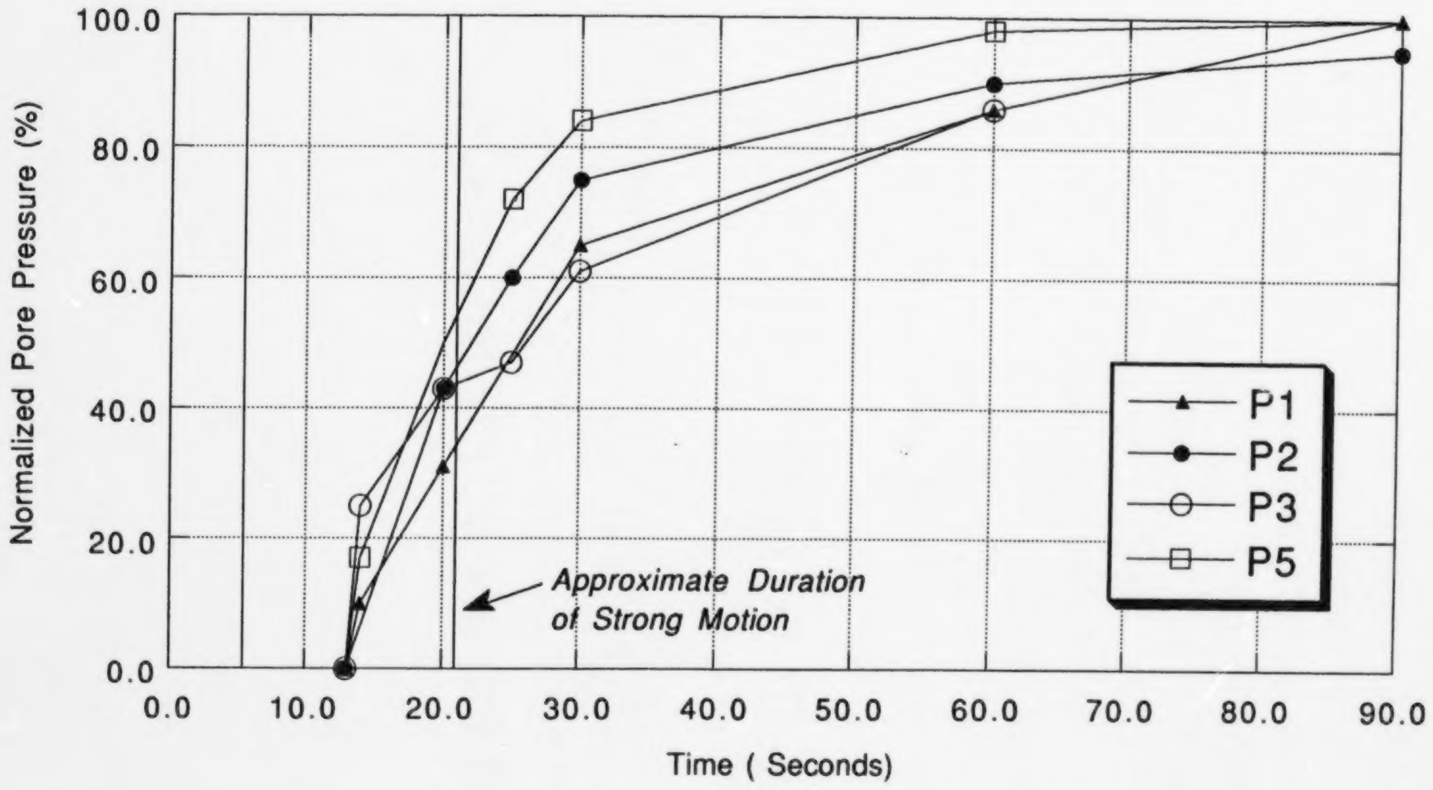

Fig. 8.1.2. Normalized Pore Pressure at The Wildlife Site.

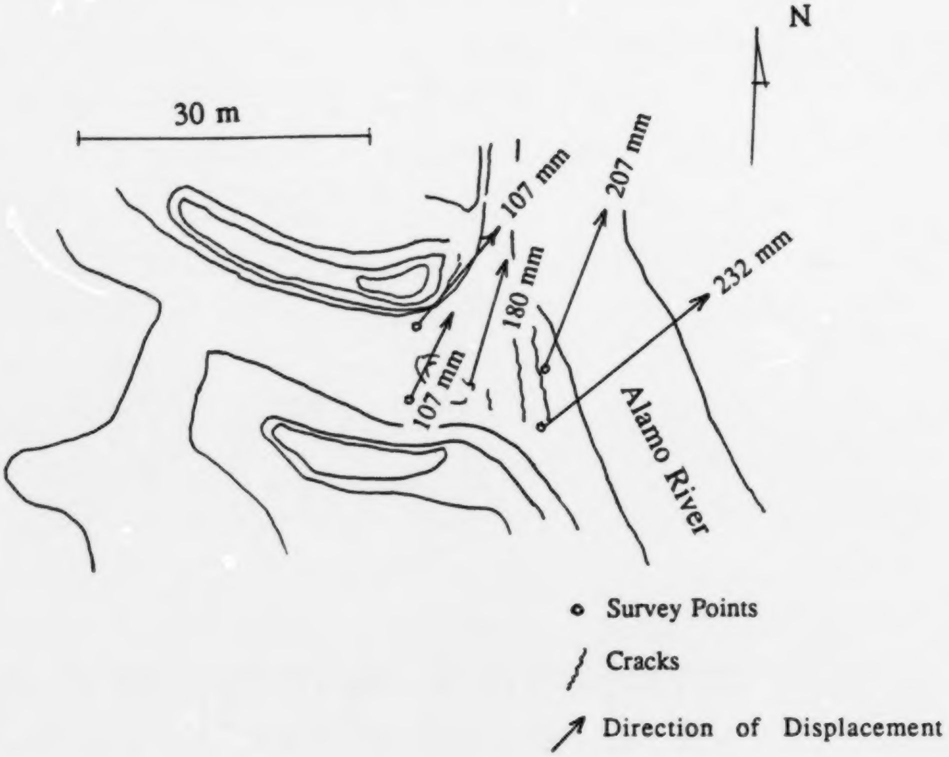
N
30 m
107 mm
207 mm
180 mm
232 mm
107 mm
Alamo River
Survey Points
Cracks
Direction of Displacement

Fig. 8.1.3. Displacements on Ground Surface of The Wildlife Site.

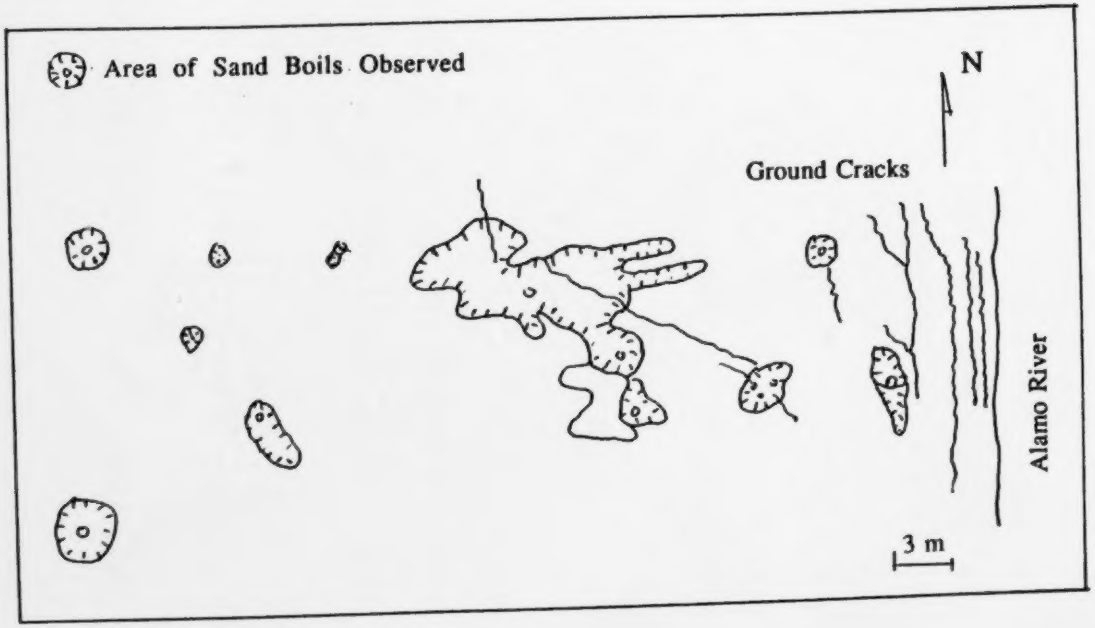
Area of Sand Boils Observed
N
Ground Cracks
Alamo River
3 m

Fig. 8.1.4. Sand Boils Observed at The Wildlife Sitr During 1987 Earthquake.

8.2. Characteristics of Sediments and Properties of Materials.

The sediment was classified by both field tests and laboratory tests. The field tests are CPT and SPT. The laboratory tests include grain size analysis and Atterberg limits. Grain size characteristics such as the median grain size(d50) and coefficients of uniformity (Cu) are used to describe the general size of sorting of sediment. The liquidity index(LI), calculated from the natural water content and the Atterberg limits, defines the physical state of the sediment. The following seven stratigraphic units were identified by the tests:

Unit A(0-2.5m) consists of very loose or very soft interbedded micaeous sandy silt, silt, and clayey silt. The liquidity index averages 1.6. CPT and SPT data also indicate a very loose or soft condition. The contact between unit A and B is gradational.

Unit B(2.5-6.8m) contains two subunits, B1(2.5-3.5m) and B2(3.5-6.8m). Subunit B1 consists of very loose to loose, dark grayish-brown, moderately sorted sandy silt. The contact between B1 and B2 is gradational. Subunit B2 consists of loose to medium dense, dark grayish-brown to dark brown, well-sorted silty sand to very fine sand. Subunit B2 is in sharp contact with underlying unit C.

Unit C(6.8-12m) contains two subunit, C1(6.8-7.5m) and C2(7.5-12m). Subunit C1 consists of medium to stiff clayey silt, and subunit C2 consists of medium to very stiff silty clay.

Unit D(12-17.5m) consists of medium dense silty with clayey and sandy beds.

Unit E(17.5-21.5m) is composed of moderately sorted, grey sand and reddish-gray clay silt and silty clay.

Unit F(21.5-24.3m) is mainly reddish-gray and reddish-brown clayey silt.

Unit G(24.3-26.5m) is composed of very stiff clayey silt and silty clay.

The sediments susceptible to liquefaction during 1981 earthquake were identified by Bennett et.al (1984) as follows:

Unit A is typical of flood-plain sediment. The low penetration resistance and liquidity index(greater than 1) indicate the sediment is susceptible to liquefaction. Approximately 20 percent of the sediment is liquefiable according to Seed and Idriss (1983) based on a liquidity index greater than 0.9, liquid limit less than 35, and a sediment fraction(0.005mm) less than 15 percent.

Unit B contains features characteristic of point bars such as a fining-upward grain size and an upward change from well-sorted to moderately sorted sediment. Based on the looseness of sediment, high water table, and similarty to sand boil material, Unit B is identified to be the layer that liquefied and formed sand boils.

The unit B was also identified as the liquefied layer during the 1987 earthquake by Holzer et.al (1989) according to the simultaneous measurments of seismically induced pore water pressure and surface and subsurface accelerations.

8.3. Initial Effective Stress Analysis.

The initial effective stresses are determined by finite element analysis. The survey of displacements on the ground surface (shown in Figure 8.1.4) and subsurface (Holzer et.al,1989) shows that the displacements on the ground surface are mainly due to the liquefaction of Unit B. Therefore, the liquefaction behavior based on a small finite element mesh composed of Unit A and Unit B will be mainly discussed in this analysis. Figure 8.3.1. shows the finite element mesh. The bottom was assumed a fixed boundary, the right and left side boundaries were assumed fixed in horizontal movement and the other boundaries including ground surface, river slope and river base were assumed free to move. A river base of 5 meter width was considered in this finite element mesh. In order to investigate the effects of boundary conditions, a larger finite element mesh was also used in this analysis as shown in figure 8.3.2. In this finite element mesh, the soil layer C including subunits C1 and C2 and a river base of 10 meter width was considered. Elastic models are used in this analysis. The initial shear stress is dependent upon the Poisson's ratio or Ko value. The Poisson's ratio usually decrease with increase of confining pressure. Table 8.3.1. shows the properties of materials used in this analysis. Figures 8.3.3 to 8.3.5 show the contours of stresses for the Wildlife site and Figure 8.3.6 shows the contours of yield ratio for the site under initial stress conditions.

8.4. Post-earthquake Deformation Due To Stress Redistributions.

During an earthquake, pore water pressures increase and the effective stresses decrease. If the soil is very loose, the soil grain structure can collapse and strain softening behaviour may occur. This strain softening causes stress re-distribution within the soil mass. Along with this re-distribution of stresses, there can be a re-distribution of pore water pressure. The re-distribution of stresses and pore water pressures may induce further liquefaction or yielding in surrounding areas. In nature, the process of strain softening, stress re-distribution and pore pressure re-distribution takes real time and can continue after the earthquake has ceased. Figure 8.4.1 illustrates in a schematic way a possible reason for the delayed behaviour of pore water pressure development at the Wildlife Site. Point b1 represents the initial stress state of a soil in Unit B1 with lower shear stress and steady state strength (average SPT blowcount of N = 3), and point b2 represents the stress state of a soil in Unit B2 with higher shear stress and steady state strength (average SPT blowcount of N = 8.3). During earthquake shaking, both soils move towards the collapse surface as defined by Sladen et.al (1985). The development of pore water pressure for the soil initially at b1 is faster than the soil initially at b2, as shown in figure 8.4.1(b), since the soil at b1 is looser than the soil at b2. Before the end of the earthquake, both soils have reached their respective collapse surfaces, i.e. the points e1 and e2, as shown in Figure 8.4.1. The collapse from points e1 and e2 to points s1 and s2 can take place either during or after the main earthquake shaking. Therefore, the pore water pressures can continue to increase after the earthquake shaking is over, as shown in Figure 8.4.1(b). A very similar behaviour in pore water pressure development can be observed by comparing soil b1 and b2 with piezometer p5 and p1 respectively between Figure 8.4.1(b) and Figure 8.1.3(a). Much longer delayed behaviours can be expected if the soils were brought to the collapse surface by re-distribution of stresses or excess pore water pressures rather than directly by the earthquake shaking as described in Figure 8.4.1.

To investigate the behaviour of the large lateral spreading of the ground surface and the pore water pressure generation at the Wildlife site, post-earthquake deformation analyses due to stress re-distribution were conducted under fully undrained conditions. In these analyses, the simplified undrained critical state boundary surface model described in chapter 2 was used to simulate the behaviour of liquefiable materials. In this analysis, the lateral spreading on the ground surface and the pore water pressure development during stress re-distribution are particularly interesting behaviour to be investigated. The finite element mesh shown in figure 8.3.1 was used in which the Unit A2, B1 and B2 are liquefiable soils. The elasto-plastic model with Mohr-Coulomb failure criterion is used for the soils in Unit A1. The boundary conditions are same as in the initial stress analyses. The parameters used in these analyses are given in table 8.3.1 in which two groups of steady state strength have been used to investigate the effects of steady state strength on post-earthquake deformation. The values of steady state strength in group 1 were determined based on the average SPT blowcount (Bennett et.al, 1984) and the relationship between SPT blowcount and steady state strength given by Seed(1987). The values of steady state strength in group 2 were determined under an assumption that the normalized pore water pressure for the soil in steady state should be very close to the in-situ measurement values reported by Holzer et.al(1989). The stress re-distribution analysis begins after the pore pressure ratio U/Um=1.0 is input for all elements of unit A2, B1 and B2, where Um is the maximum pore pressure defined by the horizontal distance between the initial effective stress state and the critical state boundary surface.

Lateral spreading and steady state strength Figure 8.4.2 shows the convergent results of displacement field when group 1 steady state strength were used after 91 iterations of unbalanced loads. Figure 8.4.3 shows the convergent result of displacement when group 2 steady state strengths were used after 183 iterations of unbalanced loads. The tolerance for the error in displacement for convergence in stress re-distribution analysis is set to be less than 0.005 in these analyses.

Figure 8.4.4 shows the horizontal displacements on the ground surface for the analysis results and the measured values. The magnitude of measured displacements are simply taken from Figure 8.1.4. The distances from the river bank shown in figure 8.4.4 are the distances between the measured points to the river bank along different directions of measured displacements showed in figure 8.1.4, In other words, the measured displacements in figure 8.4.4 neglected the difference in directions of the movements. Figure 8.4.4 also shows that the analysis horizontal displacements on ground surface are too small compared with the measured values when group 1 steady state strengths were used . A good agreement can be observed between the analysis results and the measurement displacements near the river bank when group 2 steady state strengths were used in the analysis. The distribution of ground surface movements illustrated in figure 8.4.4 seems to indicate that the amount of soils involved in the movement of the Wildlife Site may be larger than that predicted in the analysis. But one should notice that the measurement displacements shown in figure 8.4.4 were estimated from the measured values in figure 8.1.4 when the difference in directions of the movement has been neglected. In nature, the conditions for the movements at the Wildlife Site are much more complicated than the conditions that can be considered in a two-dimensional analysis. If we compare the measured displacements in one direction, e.g. E-W(east-west) direction, a very similar distribution of ground surface displacements can be observed as shown in figure 8.4.5.

Normalized Pore Water Pressure - Table 8.4.1 shows the comparison between the predicted normalized pore water pressures u/P_o' and the measured in-situ normalized pore water pressure u/σ_v' at similar locations reported by Holzer et.al (1984), where σ_v' is the overburden pressure. The predicted normalized pore water pressures during stress redistribution were obtained when group 2 steady state strength were used. The predicted normalized pore water pressures are defined as:

$$u/P_o' = (P_c' - P_o')/P_o' \qquad (8.4.1)$$

where: u is pore water pressure, P_o' is initial normal effective stress and P_c' is the current normal effective stress. The predicted normalized pore water pressures at two locations are given in Table 8.4.1. Location 1 is a location just in front of the movement obtained in stress re-distribution as shown in Figure 8.4.3. Location 2 is a location behind the movement.

Figure 8.4.6 shows the contours of yield ratio after stress re-distribution. The yield ratio is a ratio of the shear stress over the shear strength defined in chapter 6. Figure 8.4.6 reveals an interesting phenomenon that not all of the liquefiable soils collapse to steady state strength after they reach the collapse surface. Some of the soils unloaded elastically from the collapse surface (a contracting yield surface) to the elastic zone during stress re-distribution. Much higher pore water pressures are generated when the liquefiable soils collapse to steady state. Therefore, some relative lower pore water pressure pockets can be formed during stress re-distribution for the soils unloaded elastically from the collapse surface to the elastic zone.. The pore water pressure for the soils in these lower pore pressure pockets may continue to increase during further dissipation of excess pore water pressures. This is possibly another cause for the delayed behaviour in pore pressure development.

Another interesting phenomenon one may found by comparing the locations between the yield zones developed in liquefiable soils during stress re-distribution shown in figure 8.4.6 and the in-situ observed sand boils on ground surface shown in figure 8.1.5. The very good agreement between these two locations seems to indicate that the sand boils may generate on the ground surface above the yield zones of liquefiable soils due to the higher pore water pressures in these soils.

Figure 8.4.7 to Figure 8.4.9 show the contours of effective stresses after stress re-distributions. Significant changes in either normal stress or shear stress can be observed by comparing with the initial contours of effective stresses showed in figure 8.3.3 to figure 8.3.5. The changes in horizontal and vertical normal stresses are due to the generation of excess pore water pressures induced by earthquake shaking or stress redistributiuons. The changes in shear stress are directly due to the stress re-distribution.

Effects of Boundary Condition - To investigate the effects of boundary condition on lateral spreading on ground surface, a bigger finite element mesh was used as shown in Figure 8.3.2. Figure 8.4.10 shows the convergent results of displacement field after 183 iteration of unbalanced loads. There is no significant difference regarding the area of soils involved in movement beside the river bank in Figure 8.4.3 and Figure 8.4.10. In other words, the width of river base and the depth of considered soils in this analysis have no significant influence on the distribution of the displacement field. Figure 8.4.11 shows the comparison between the analysis results and the measured values of the horizontal movements on the ground surface. The analysis results of horizontal displacement for both finite element meshs are larger than the measured values. In nature, the actual conditions for liquefaction deformation are much more complicated than the undrained conditions used in these analyses. The dissipation of excess pore water pressures and hence the re-consolidation of liquefied soils may occur simultaneously with the stress re-distributions. The steady state strengths of liquefiable soils may increase during re-consolidation. The development of displacements may stop earlier than that under fully undrained conditions during stress re-distribution because the excess pore water pressures decrease and the steady state strength increases during re-consolidation. Figure 8.4.12 shows the contours of yield ratio when the bigger finite element mesh was used.

8.5. Post-earthquake Deformation Due to Reconsolidation.

Excess pore water pressure can be generated during earthquake shaking and stress re-distribution. If one allows the excess pore water pressure to dissipate, re-consolidation occurs. To investigate the effects of re-consolidation on the post-earthquake deformation of the Wildlife Site, a two-dimensional finite element analysis with Biot's theory was adopted. During re-consolidation, most of the soils will move away from the critical state boundary surface to the elastic zone and most of the effective stress paths will move on elastic walls defined by Roscoe et.al (1958). Therefore, elastic models were used in these analyses. The ground water table is assumed as the only pervious boundary. The same finite element mesh for stress re-distribution analyses was used for the re-consolidation analyses. The parameters used in these analyses are also shown in Table 8.3.1. The re-consolidation analysis started from the convergent result of stress re-distribution analysis when group 2 steady state strengths were used introduced in last section. To investigate the effects of drainage condition on post-earthquake deformation behaviour, different permeabilities were used for the unit A2 of top soils, as given in Table 8.3.1.

Settlement of The Ground Surface During Re-consolidation - In this analysis, unequal time steps were used. After 10 steps, about 5 hours dissipation, the excess pore water pressures reduced to almost zero again and the increments of settlements on ground surface became very small. Then the analysis was terminated. Figure 8.5.1 shows the final displacement field after re-consolidation. The results show that the horizontal movements due to re-consolidation are very small. The settlements during re-consolidation at some nodes on the ground surface are shown in Figure 8.5.2. This Figure shows that the final settlements of ground surface ranged from 0.63-0.91 cm are independent of the permeability of the top layer A2, but the rates of settlement are dependent upon the permeability of top layer A2. The settlement of the ground surface are faster when a higher permeability of the top layer A2 was used. Figure 8.5.3(a) shows the relationship between the settlements of ground surface and the normalized pore water pressures in underneath soils. The settlements are obviously dependent upon the excess pore water pressures developed during earthquake and stress re-distribution in underlying soils. Figure 8.5.3(b) shows the calculated settlements at some nodes on the ground surface obtained by using the relationship for Monterey sand with relative density Dr=50% given by Lee and Albaisa (1974). Obviously, the magnitude of settlements is also dependent on the compressibilty of materials. Larger settlements can be expected for looser materials.

Liquefaction During Re-consolidation - Figure 8.5.4(a) shows the typical normalized pore water pressures during re-consolidation for soils located in a yield zone, particularly, in front of the movement caused by stress re-distribution. No further increase in pore water pressures were observed during re-consolidation for the soils in these yield zones because of their relative higher pore water pressures generated during stress re-distributions.

Figure 8.5.4(b) shows the typical normalized pore water pressures during re-consolidation for soils located in the lower pore water pressure pockets formed during stress re-distribution. A considerable further increase of pore water pressures can be observed in the re-consolidation analysis when a lower permeability of the top layer A2 was used. Further liquefaction does occur in some elements during re-consolidation by re-distribution of excess pore water pressures. These results are also given in table 8.4.1. The normalized pore water pressures of equal to unity or even greater than unity may occur during dissipation of excess pore water pressures with poor permeable top soils. This replicate early observation of Ambraseys and Sarma (1969).

Figures 8.5.5 to 8.5.7 show the contours of stresses after re-consolidation. Significant changes in shear stress distribution can be observed by comparing Figure 8.5.7 with Figure 8.3.5. Figure 8.5.8 and Figure 8.5.9 show the typical effective stress paths for some elements. Figure 8.5.8 shows the effective stress paths for liquefied soils and Figure 8.5.9 shows the effective stress paths for soils in the lower pore water pressure pockets. Most of soil almost returns to their initial stress state after re-consolidation.

8.6. Discussion on the Liquefaction Behavior of Wildlife Site During 1987 Superstition Hills Earthquake.

The liquefaction behaviour observed at the Wildlife Site, in the Imperial Valley, during the 1987 Superstition Hills earthquake is an important case history to study the mechanism of liquefaction under level ground conditions. The large lateral spreading and the delay in pore water pressure development are particularly interesting observations. In order to investigate the effects of re-distribution in stresses, the post-earthquake deformation analyses of Wildlife Site have been conducted by finite element methods. The analyses consist of two parts: the post-earthquake deformation during stress re-distribution and the post-earthquake deformation during re-consolidation. The analysis results and conclusions can be made as follows:

(1) The agreements on both quantity and distribution of ground surface movement between the in-situ measured values and the analysis results reveal that the large lateral spreading towards the river in the Wildlife Site during 1987 earthquake is mainly due to the stress re-distribution caused by liquefied materials. The steady state strength for liquefied materials is the most important factor effecting the lateral movements on the ground surface.

(2) Not all of the liquefiable soils can collapse from their peak strengths to steady state strengths during stress re-distribution even though they have reached the collapse surface. Some of the soils may unload elastically during stress re-distribution. This behaviour is dependent upon the deformability of the structures. The soils in yield zones, particularly in front of the movements, obtained in stress re-distribution are more likely to collapse from their peak strengths to steady state strengths. The soils behind the movement may unload elastically after they have reached the collapse surface, during stress redistribution. For liquefiable materials, the pore water pressures will increase during the collapse from their peak strengths to steady state strengths. In nature, the collapse of liquefied soil and the re-distribution of stresses within an earth structure will take real time and they can continue to develop after the earthquake shaking is over. Therefore, the delayed behaviour in pore water pressure development may be caused by the collapse of the liquefied materials.

(3) Lower pore water pressure pockets may form during stress re-distribution depending on the uniformity of deposits and properties of materials. Therefore, the delayed behaviour in pore water pressure development may also be due to the re-distribution of excess pore water pressures. Increase of pore water pressures during re-consolidation, particular for the soils located in these lower pore water pressure pockets, can be expected in further re-consolidation analysis.

(4) The agreement between the locations of in-situ observed sand boils on ground surface and the locations of yielding zones for liquefiable soils in these analyses hints that the sand boils on ground surface may be generated by the higher pore water pressures in these yielding zones.

(5) The horizontal movements of ground surface at the Wildlife Site during re-consolidation are very small.

(6) Considerable increase of pore water pressures during re-consolidation, in particular for the soils located in those lower pore water pressure pockets, has been observed in these analyses.

(7) The settlements of ground surface associated with the lateral movements during stress re-distribution are located in a relatively small area beside the river. The settlements of ground surface during re-consolidation may occur in much larger areas depending on the excess pore water pressures development in the underneath soils during earthquake and stress redistribution.

(8) The rates of settlement are dependent upon the permeability of upper layer soils. The settlements of the ground surface with a higher permeability of upper layer soils are faster than the settlements with a lower permeability of upper layer soils.

(9) The drainage condition has a significant influence on further development of pore water pressures. Further liquefaction during re-consolidation is more likely to occur in soils under poor drainage conditions. Further liquefaction has been observed in this analysis when a lower permeability for the upper layer soil Unit A2 was used.

(10) The magnitude of settlements on the ground surface due to liquefaction depends on both the pore pressures in underlying soils and the compressibility of the soils.

Table 8.3.1. parameters for deformation analysis of Wildlife Site

soil	γ kN/ m^3	E $\times 10^4$ kN /m^2	μ_s	Su (psf)		c kPa	φ (o)	α_c (o)	a
				group 1	group 2				
A1	16.00	0.90	0.40	-	-	2	28	-	-
A2	9.28	0.90	0.48	15	8	2	28	48	0.001
B1	10.08	1.30	0.48	30	8	0	32	48	0.001
B2	10.08	1.55	0.48	70	15	0	34	48	0.001
C1	12.48	3.00	0.35	-	-	5	28	-	-
C2	12.48	3.40	0.35	-	-	10	28	-	-

Where: γ = unit weight, E = Young's modulus, μ_s = Poisson's ratio,
Su = steady state strength on $\sigma' - \tau$ plane, c = cohension,
φ = friction angle, α_c = angle of collapse surface on p'- q plane,
a = parameter for post peak behaviour.

Table 8.4.1. Normalized Pore Water Pressures During Post-earthquake Deformation Analysis.

location	* EL(IGP) Depth	relative piezometer Depth	measured in-situ $(\frac{u}{\sigma'_v})$			analysis results $(\frac{u}{p'_o})$		
			at the end of earthquake 20 sec	value at 60 sec	value at 90 sec	on collapse surface	after stress redistribution	during reconsolidation 10 sec
location 1 in front of the movement	20(3) 6.5m	P3 6.6m	0.42	0.85	0.93	0.48	0.97	0.61
	19(4) 5.5m	P1 5.0m	0.32	0.85	0.96	0.31	0.97	0.52
	47(3) 4.8m	P4 -	-	-	-	0.51	0.96	0.96
	75(4) 2.7m	P5 2.9m	0.55	0.98	1.00	0.20	0.96	1.03
	79(2) 2.7m	P2 3.0m	0.42	0.90	1.00	0.20	0.96	1.11
location 2 behind the movement	11(3) 6.5m	P3 6.6m	0.42	0.85	0.93	0.51	0.97	0.66
	11(2) 5.5m	P1 5.0m	0.32	0.85	0.96	0.32	0.96	0.50
	39(1) 4.8m	P4 -	-	-	-	0.54	0.96	0.92
	67(1) 3.3m	P5 2.9m	0.55	0.98	1.00	0.51	0.97	1.16
	70(3) 3.3m	P2 3.0m	0.42	0.90	1.00	0.51	0.50	0.98

* EL = Number of element, IGP = Number of Gaussian Integration Point.

LEGEND

A1 - Silt (above water table)
A2 - Silt
B1 - Silt sand
B2 - Silt Sand.

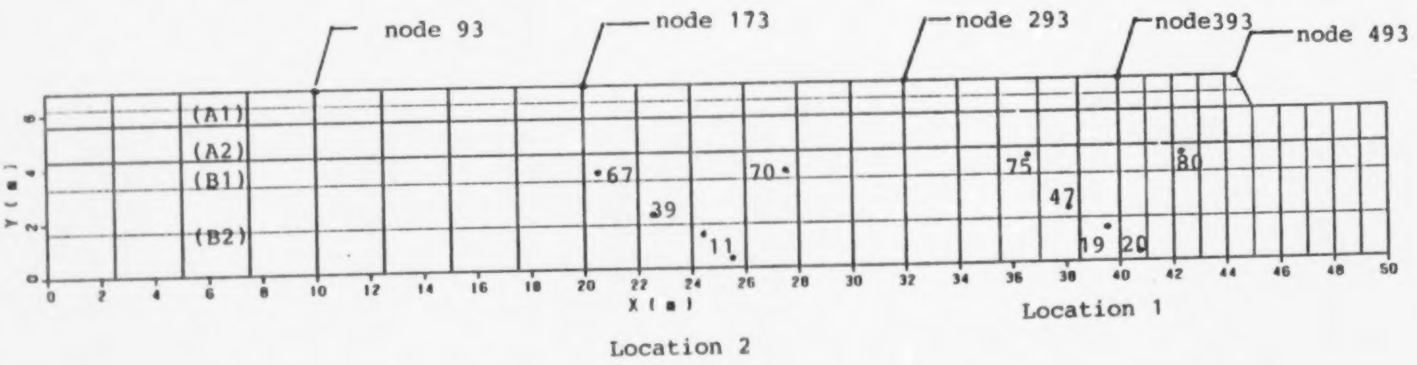
node 93
node 173
node 293
node393
node 493
(A1)
(A2)
(B1)
(B2)
67
39
11
70
75
47
19
20
80
Y (m)
0
2
4
6
X (m)
0
2
4
6
8
10
12
14
16
18
20
22
24
26
28
30
32
34
36
38
40
42
44
46
48
50
Location 1
Location 2

Fig. 8.3.1. Finite Elements and Material Distribution For Wildlife Site.

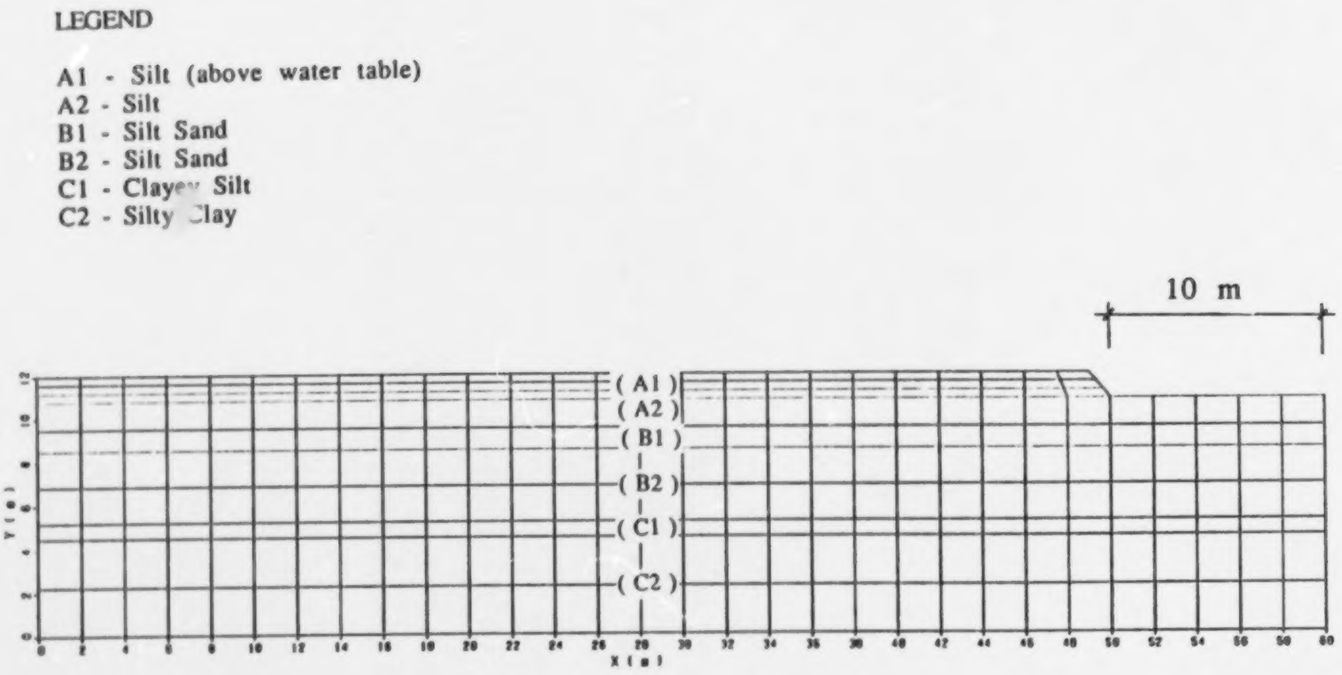
LEGEND
A1 - Silt (above water table)
A2 - Silt
B1 - Silt Sand
B2 - Silt Sand
C1 - Clayey Silt
C2 - Silty Clay
10 m
(A1)
(A2)
(B1)
(B2)
(C1)
(C2)
Y (m)
X (m)
0
2
4
6
8
10
12
14
16
18
20
22
24
26
28
30
32
34
36
38
40
42
44
46
48
50
52
54
56
58
60

Fig. 8.3.2. Larger Finite Element Mesh For Wildlife Site.

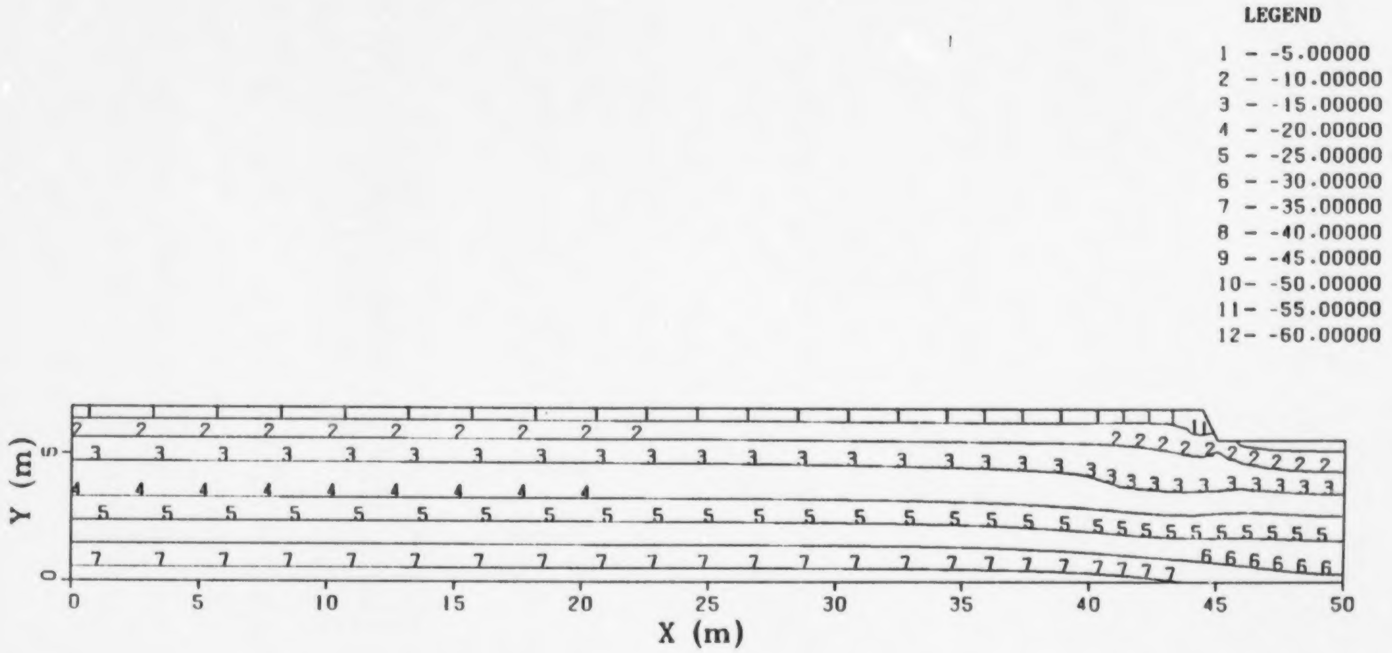

Fig. 8.3.3. Contours of Initial Effective Stress σ_x.

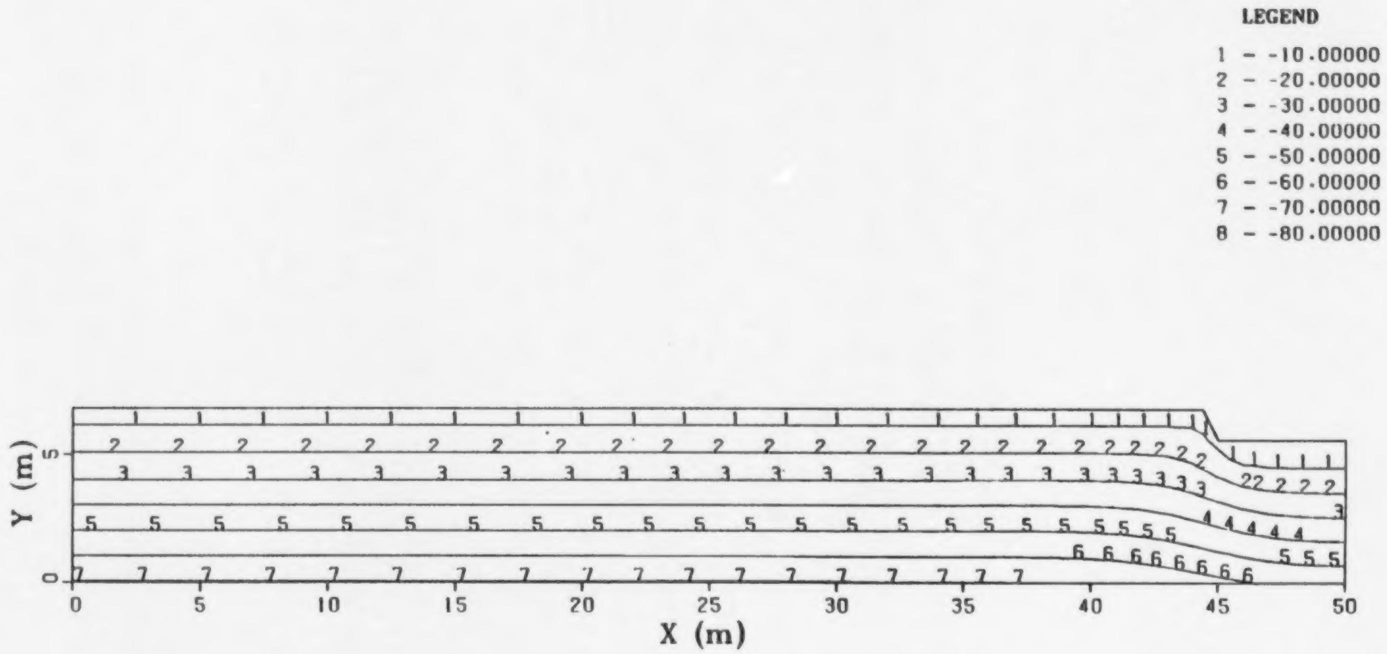

Fig. 8.3.4. Contours of Initial Effective Stress σ_y.

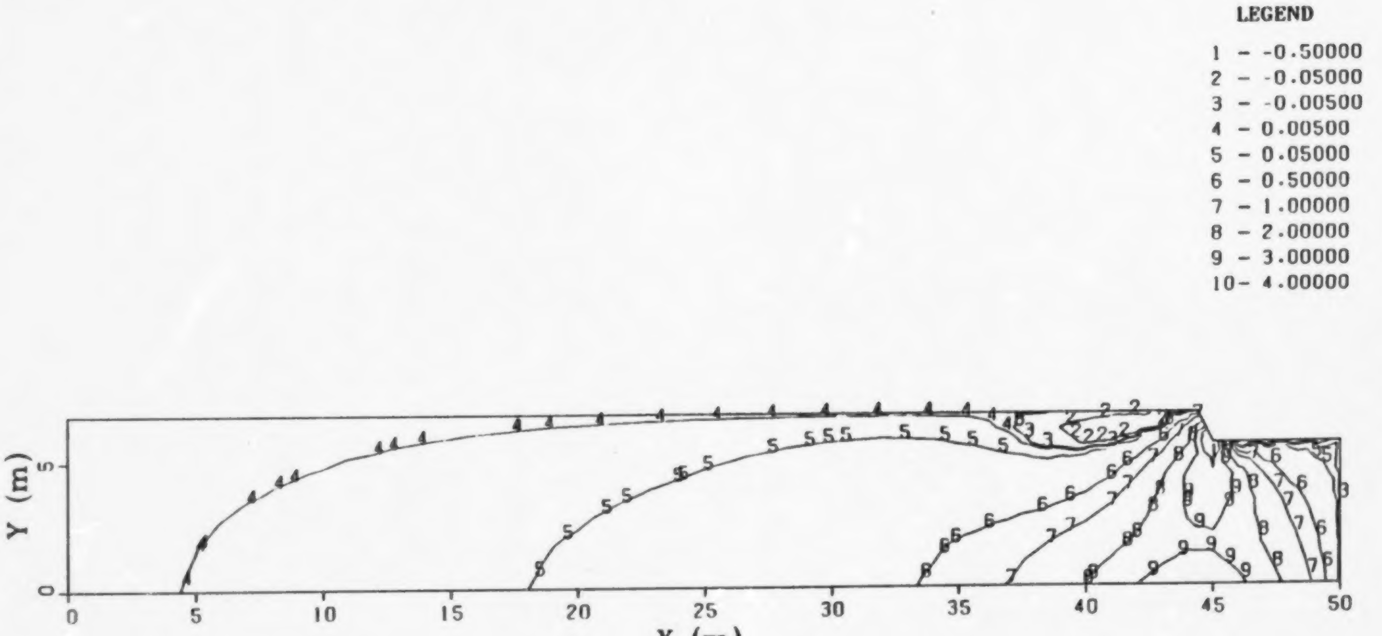

Fig. 8.3.5. Contours of Initial Effective Stress τ_{xy}.

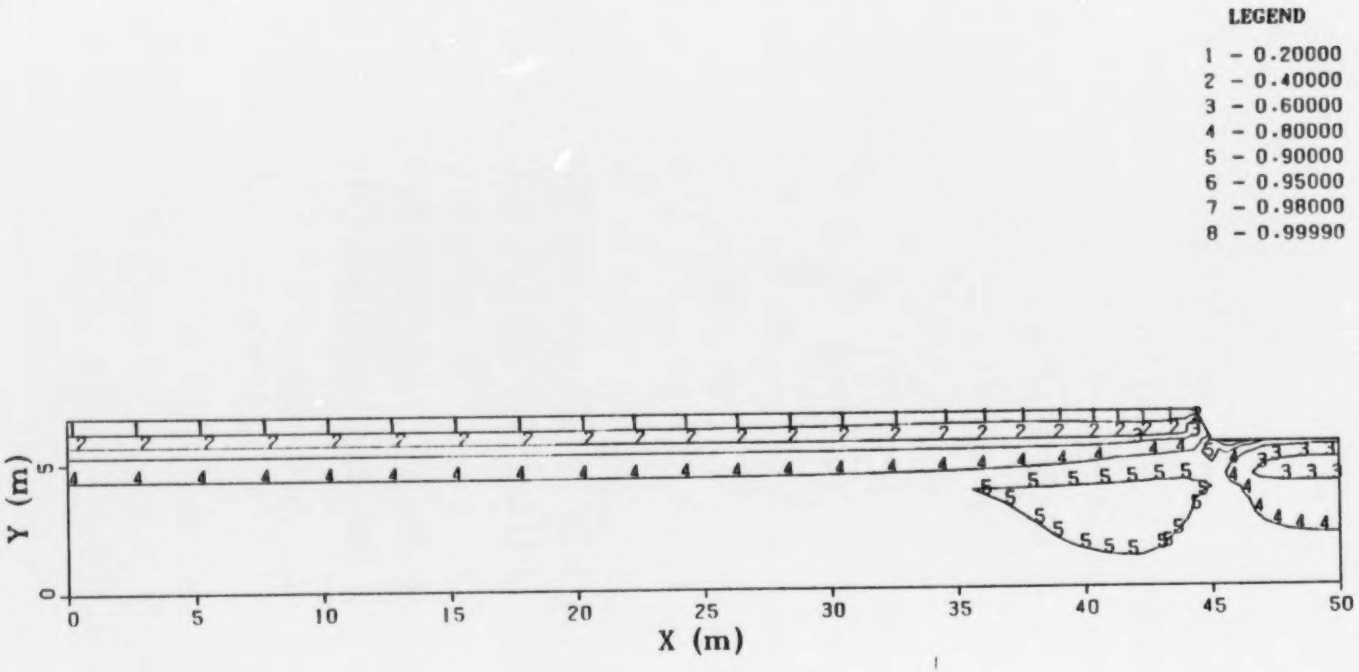

Fig. 8.3.6. Contours of Initial Yield Ratio.

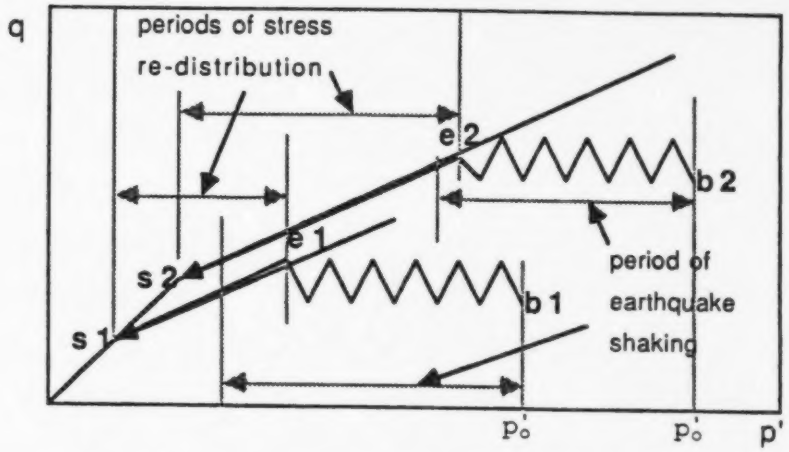
q
periods of stress
re-distribution
e2
b2
e1
s2
s1
b1
period of
earthquake
shaking
p'_o
p'_o
p'

(a) effective stress paths.

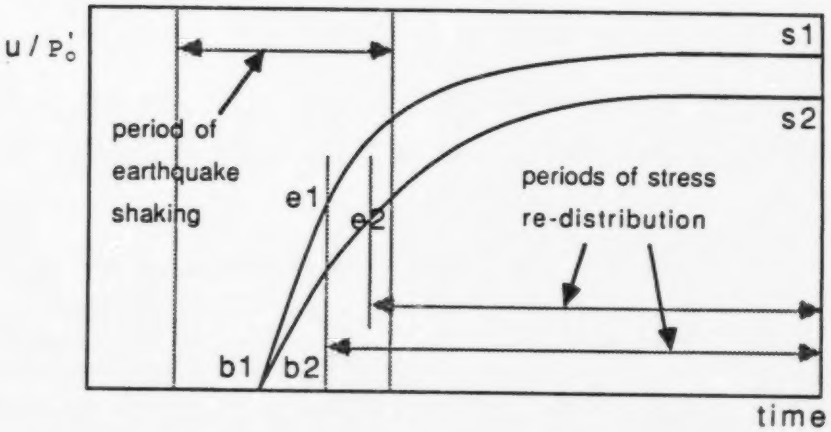
u / p'_o
s1
s2
period of
earthquake
shaking
e1
e2
periods of stress
re-distribution
b1
b2
time

(b) normalized pore water pressures.

Fig. 8.4.1. Delayed Behaviour Due To Stress Re-distribution.

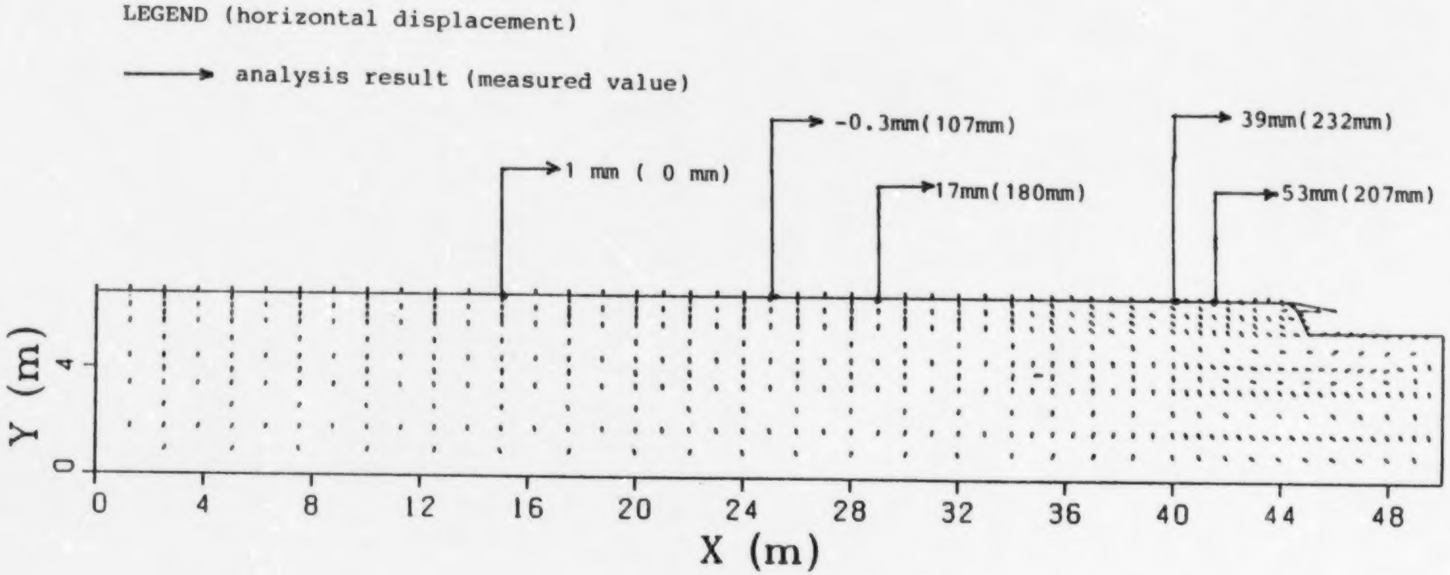

Fig. 8.4.2. Displacements After Stress Re-distribution For Group 1 Steady State Strength.

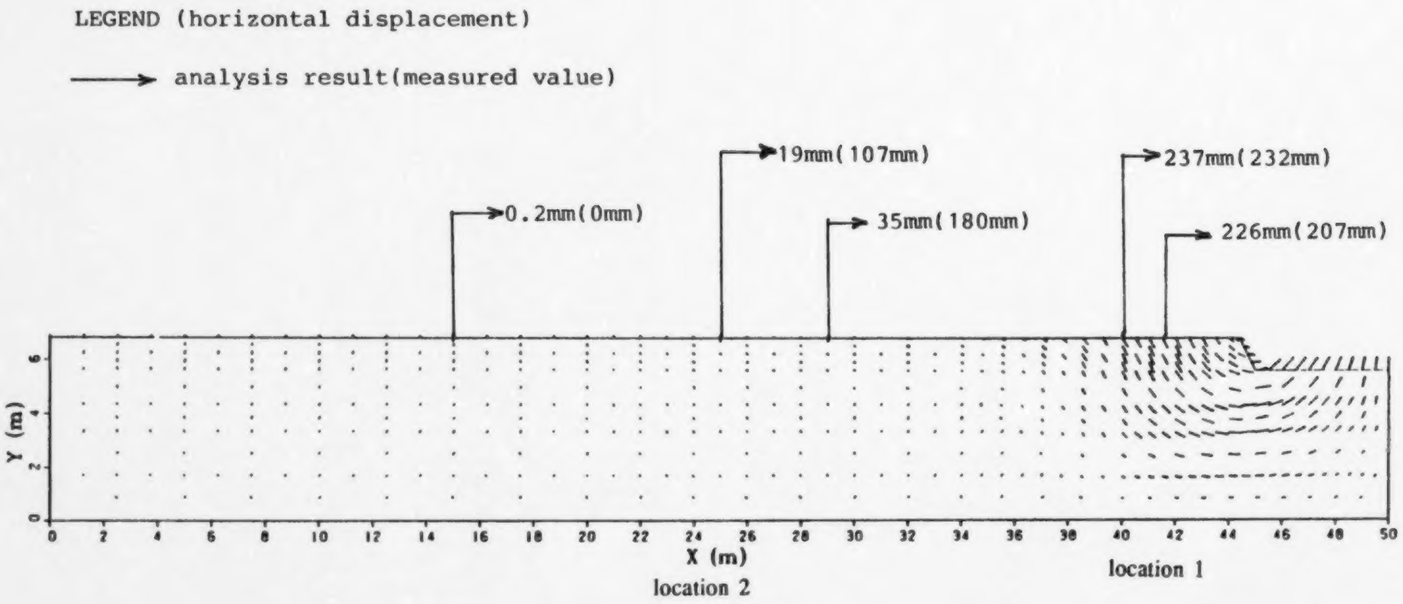

Fig 8.4.3. Displacements After Stress Re-distribution For Group 2 Steady State Strength.

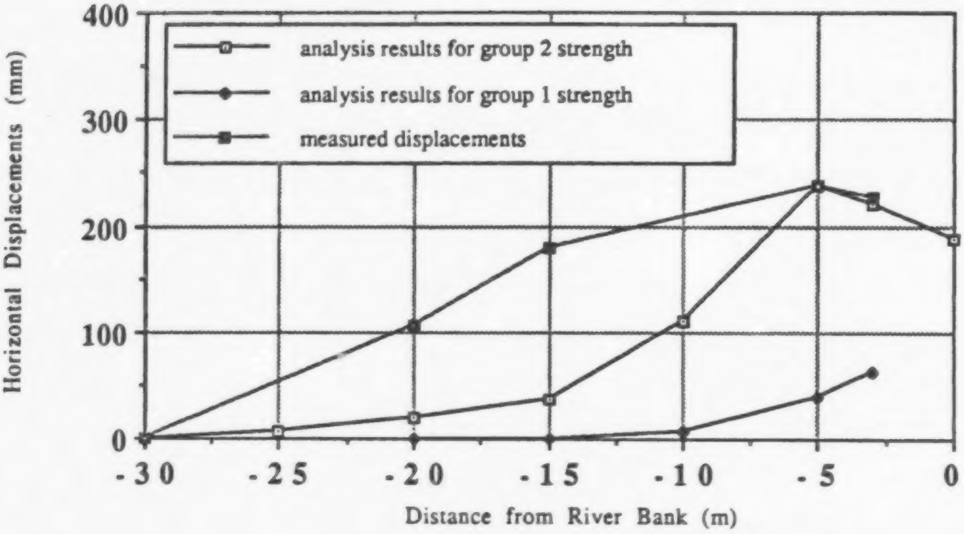

Fig. 8.4.4. **Distribution of Movement on Ground Surface.**

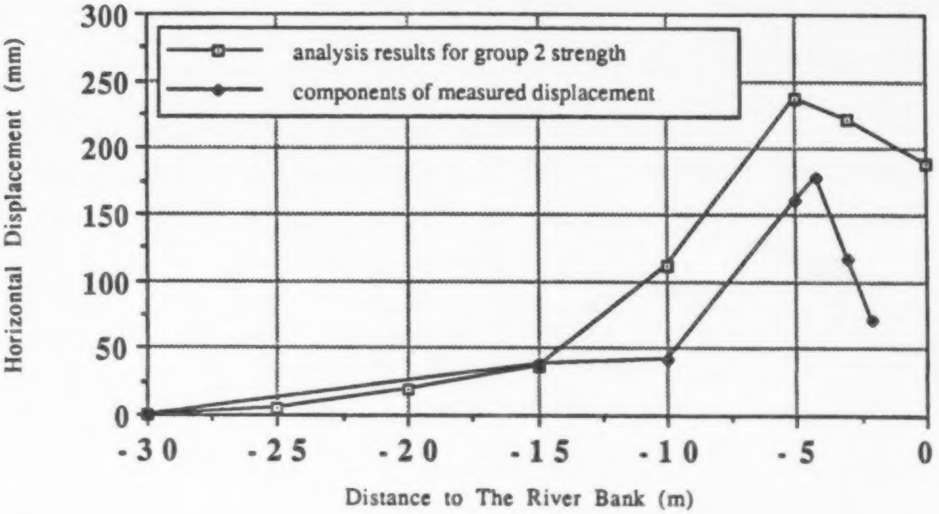

Fig. 8.4.5. E-W Components of Displacements on Ground Surface.

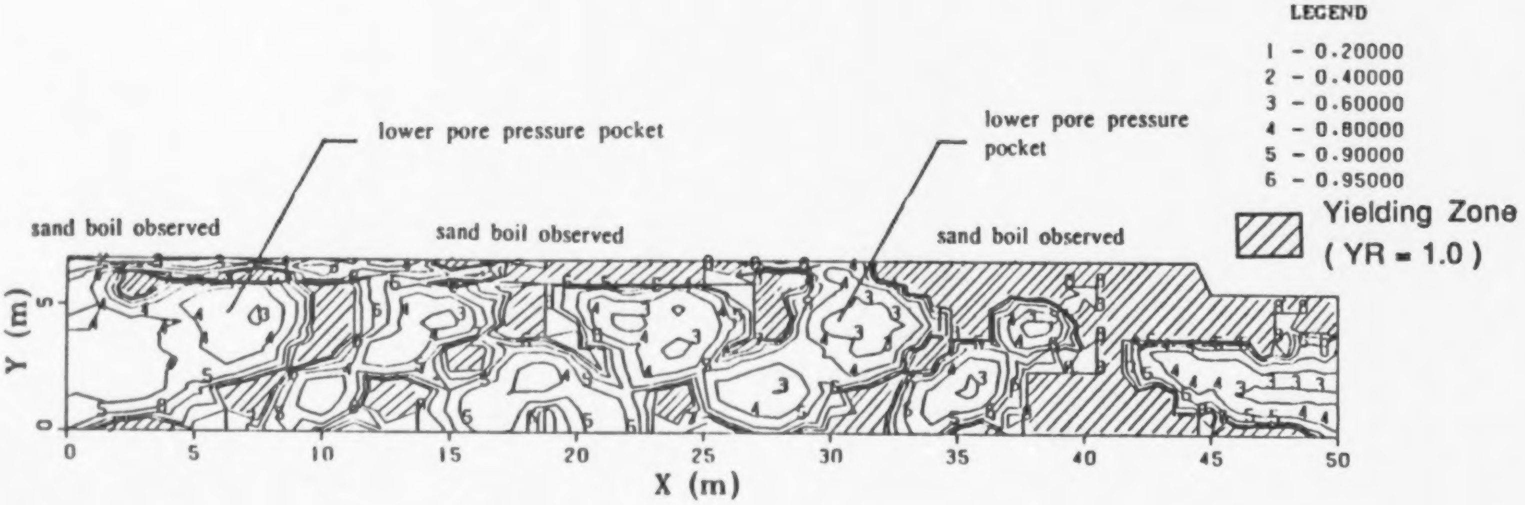

Fig. 8.4.6(a). Contours of Yield Ratio After Stress Re-distribution When Using Group 1 Steady State Strength.

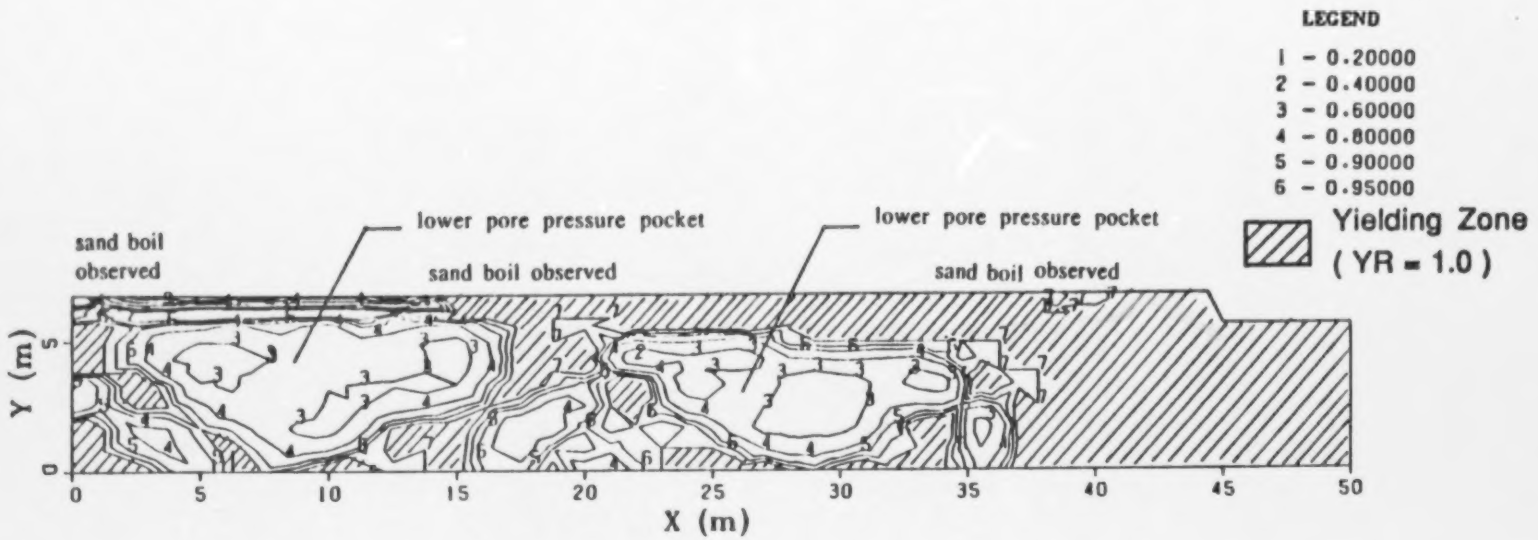

Fig. 8.4.6(b). Contours of Yield Ratio After Stress Re-distribution When Using Group 2 Steady State Strength.

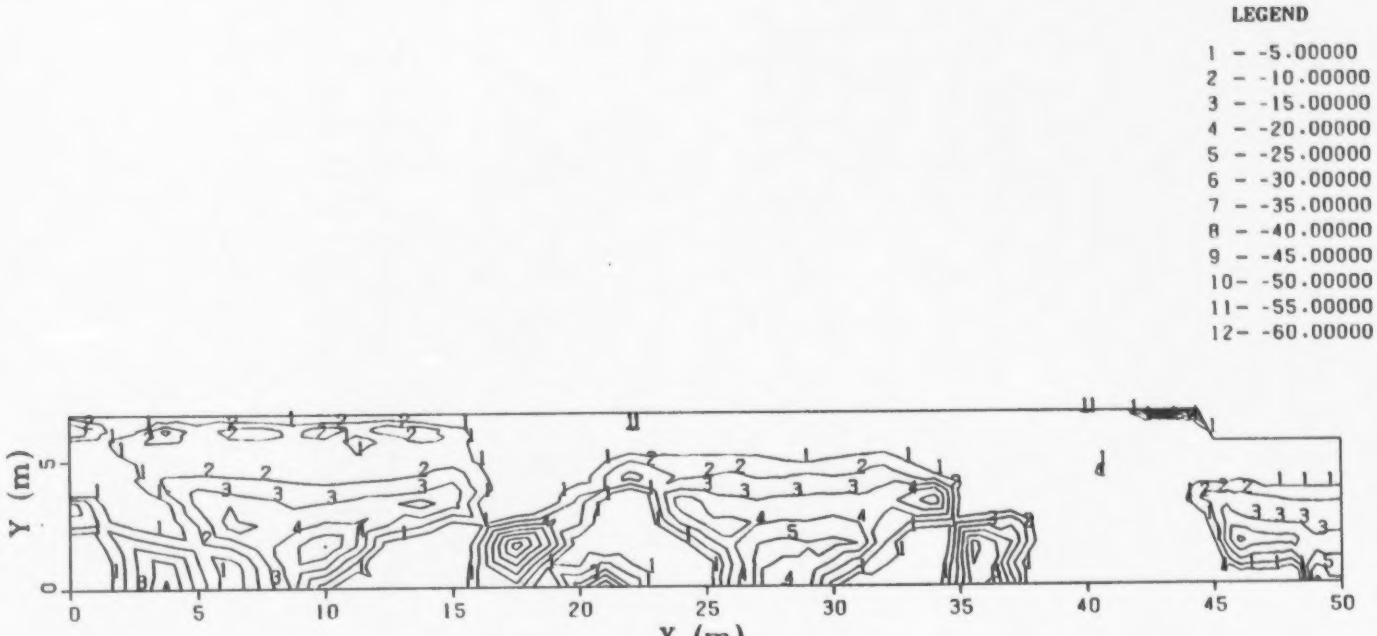

Fig. 8.4.7. Contours of Effective Stress σ_x After Stress Re-distribution.

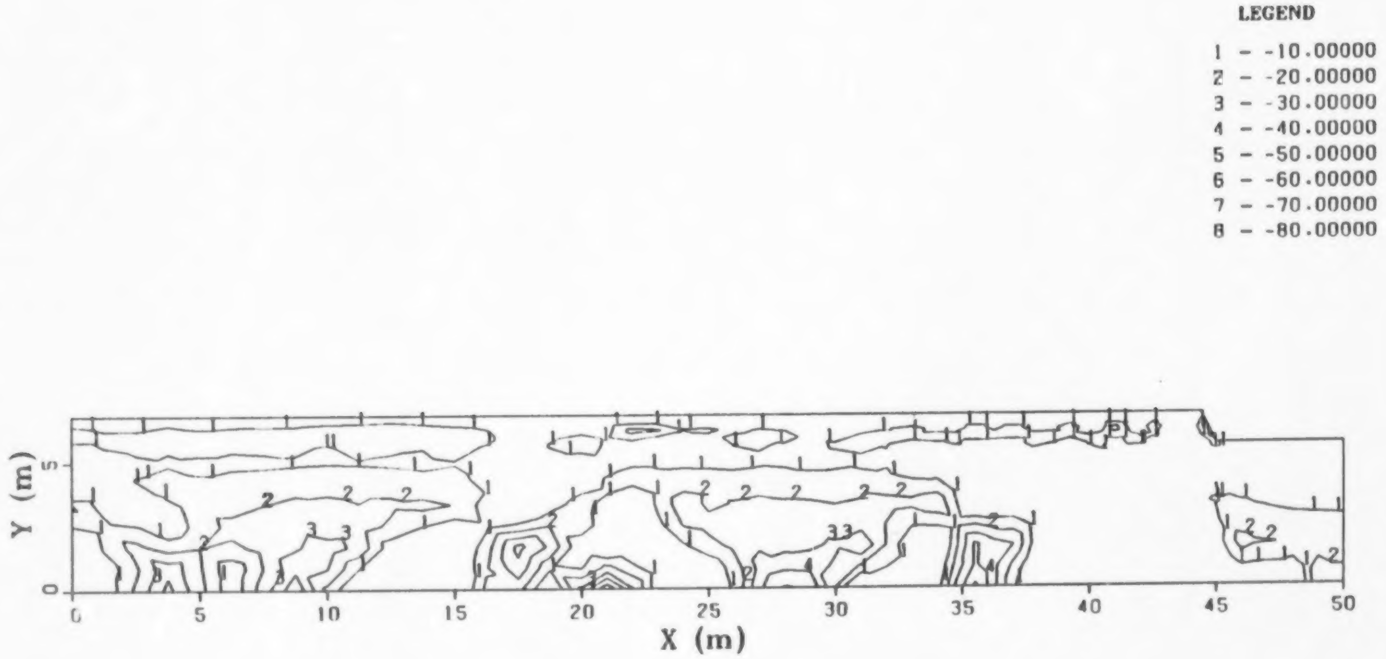

Fig. 8.4.8. **Contours of Effective Stress σ_y After Stress Re-distribution.**

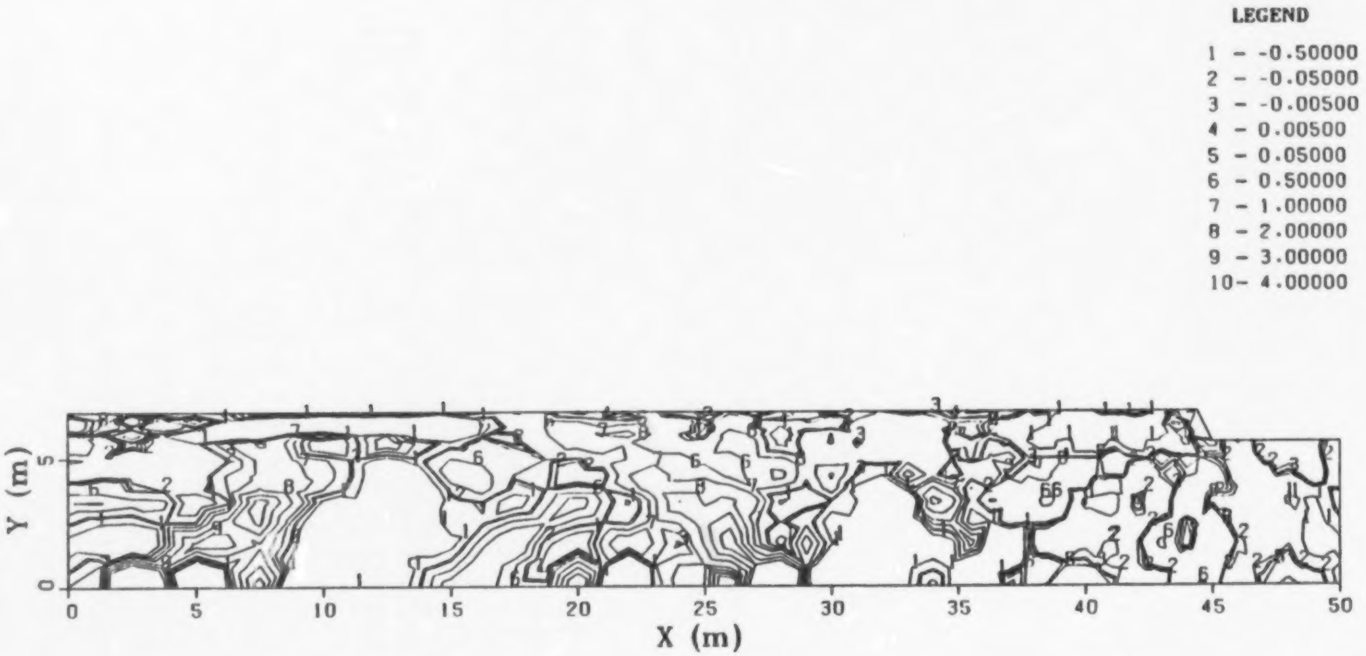

Fig. 8.4.9. Contours of Effective Stress τ_{xy} After Stress Re-distribution.

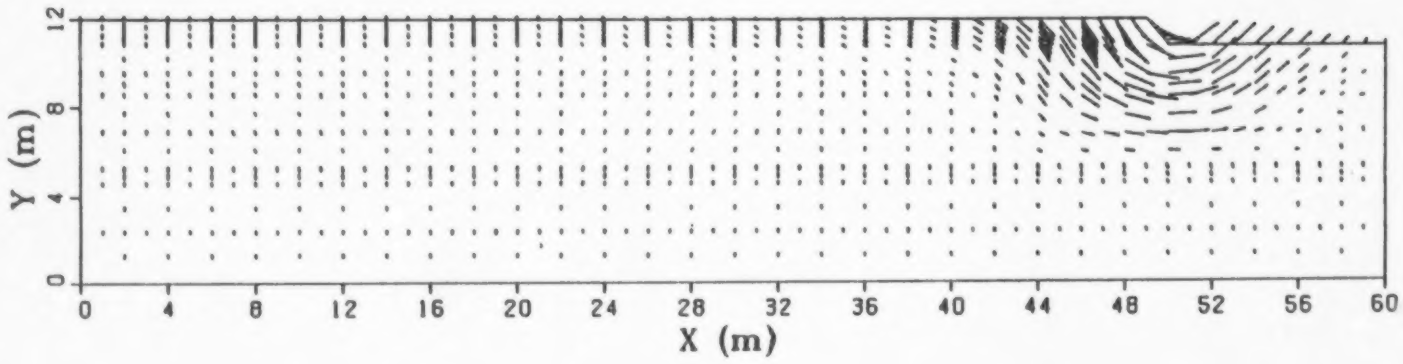

Fig. 8.4.10. **Displacement Field By Using Larger Finite Element Mesh.** (arrow=displ.x2)

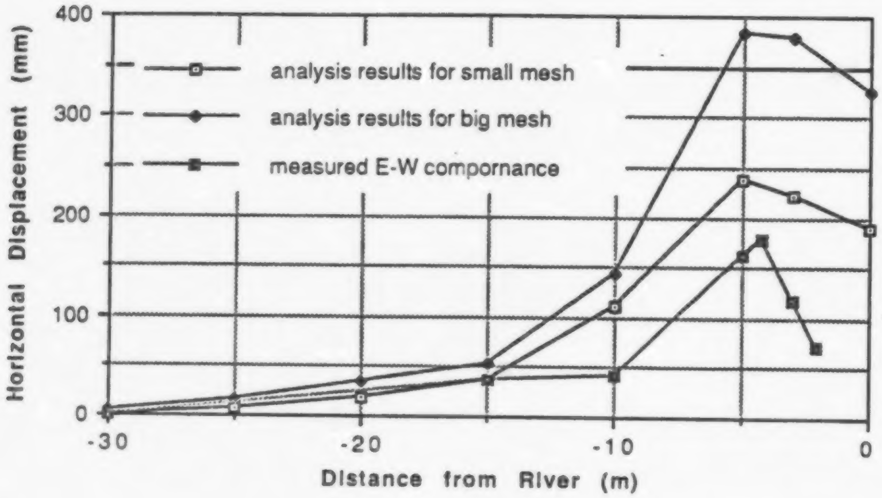

Fig. 8.4.11. Distribution of Displacement on Ground Surface.

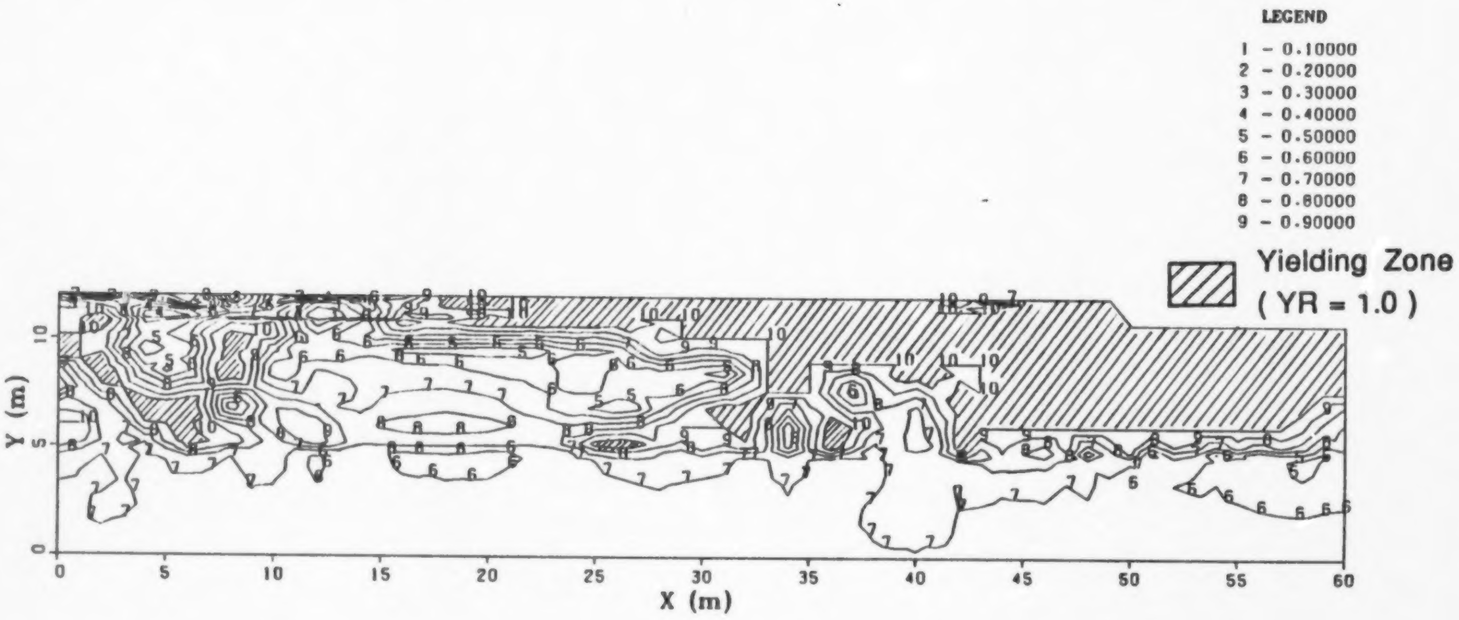

Fig. 8.4.12. Contours of Yield Ratio After Stress Re-distribution For Larger Finite Element Mesh.

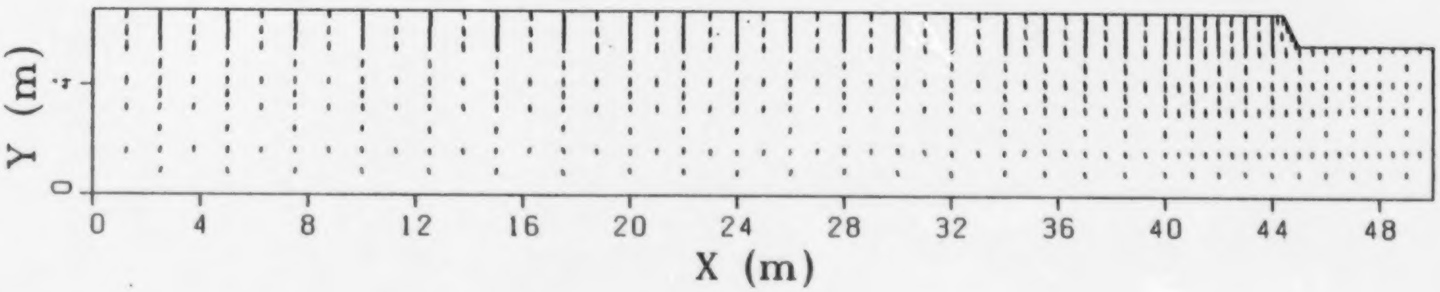

DISPLACEMENT AFTER RE-CONSOLIDATION(arrow=displx50)

Fig. 8.5.1. Displacement Field After Re-consolidation.

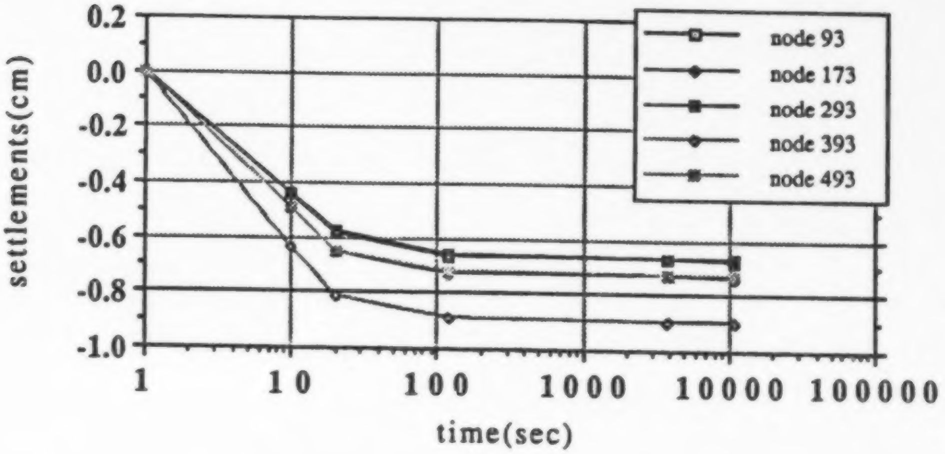

(a). settlements with large permeability(k=0.001) of top soil A2.

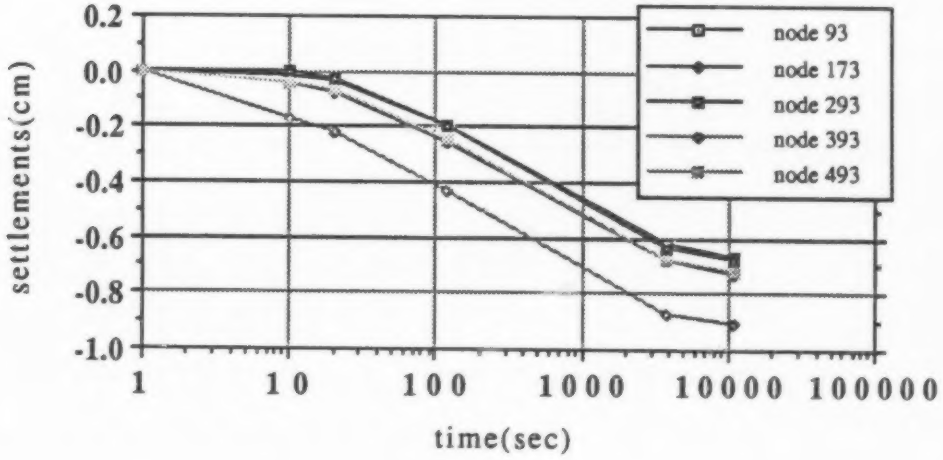

(b). settlements with small permeability(k=0.00001) of top soil A2.

Fig. 8.5.2. Settlements of Ground Surface During Re-consolidation.

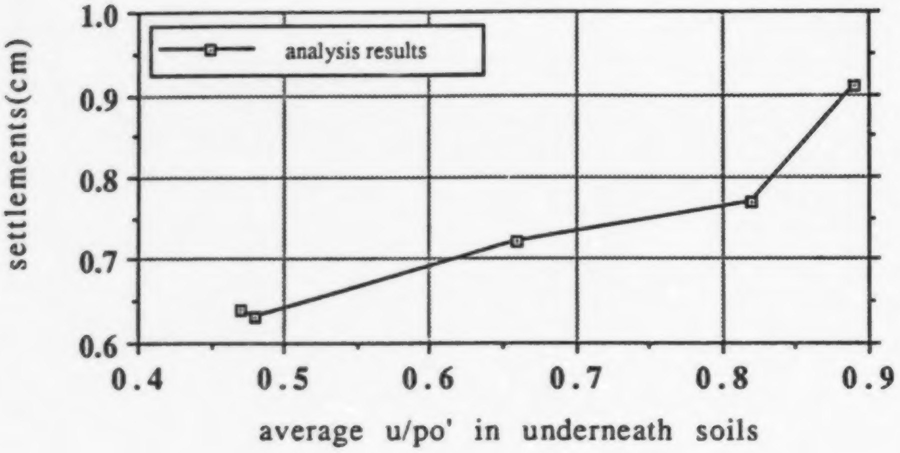

(a). settlements obtained in this analyses.

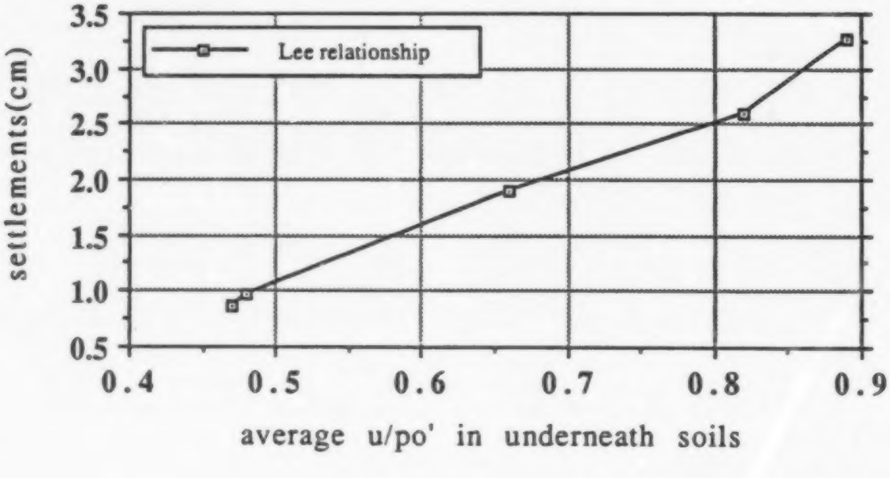

(b). calculated settlements using Lee and Albaisa's method.

Fig. 8.5.3. Relationship Between Settlements and Pore Pressures in Underneath Soils.

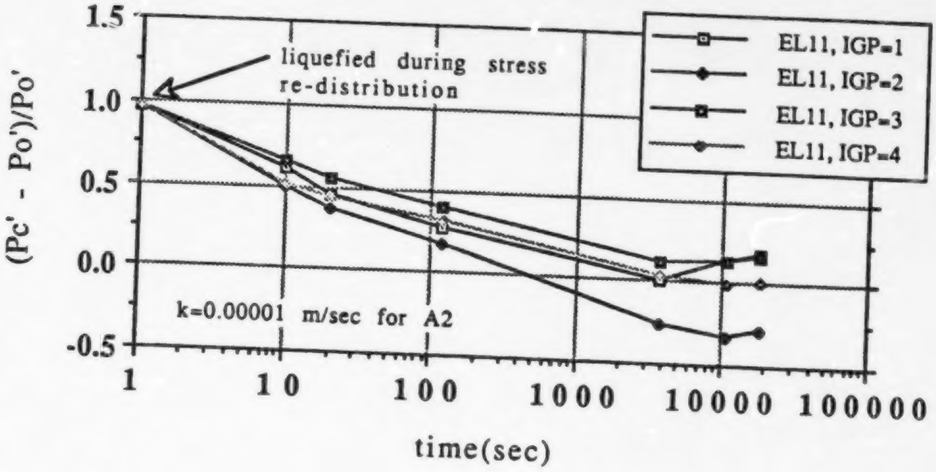

(a). pore pressures in yielding zones.

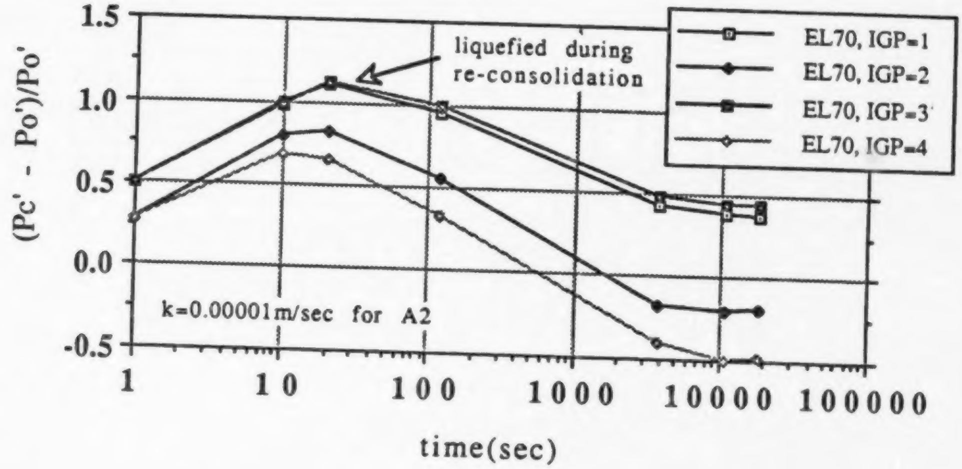

(b). pore pressures in lower pore pressure pockets.

Fig. 8.5.4. Pore Water Pressures During Re-consolidation.

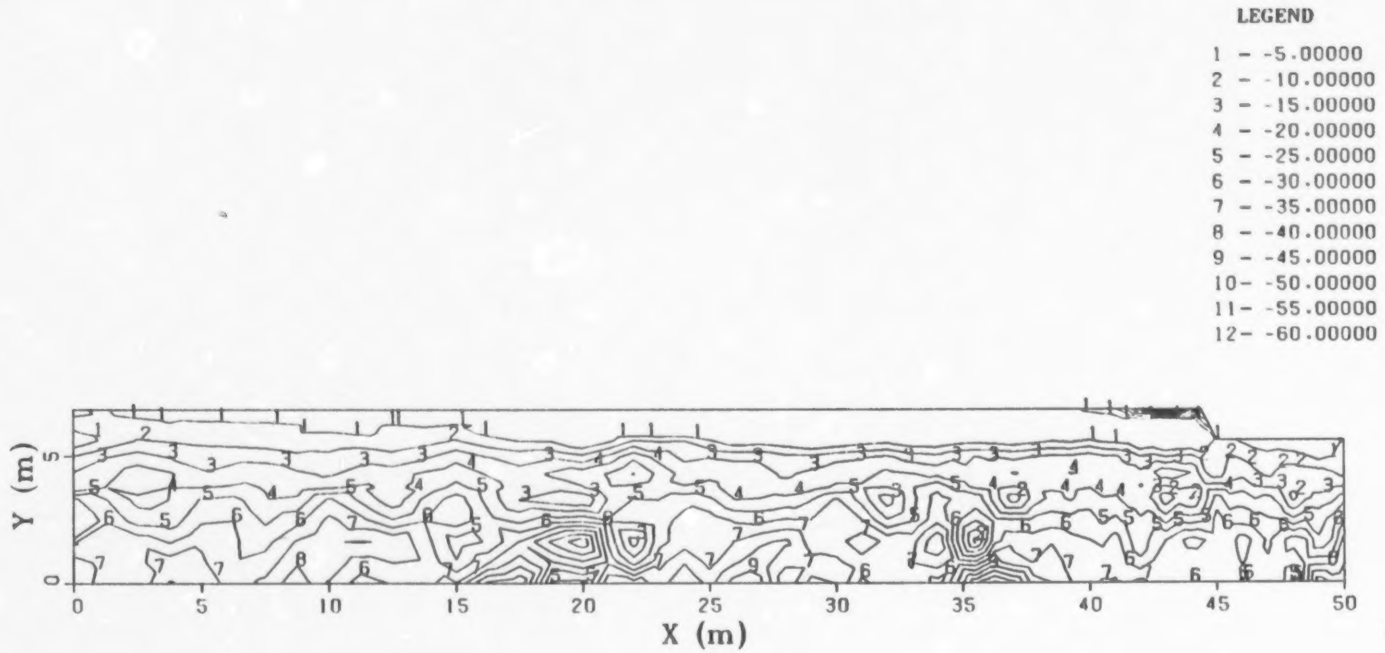

Fig. 8.5.5. Contours of Effective Stress σ_x After Re-consolidation.

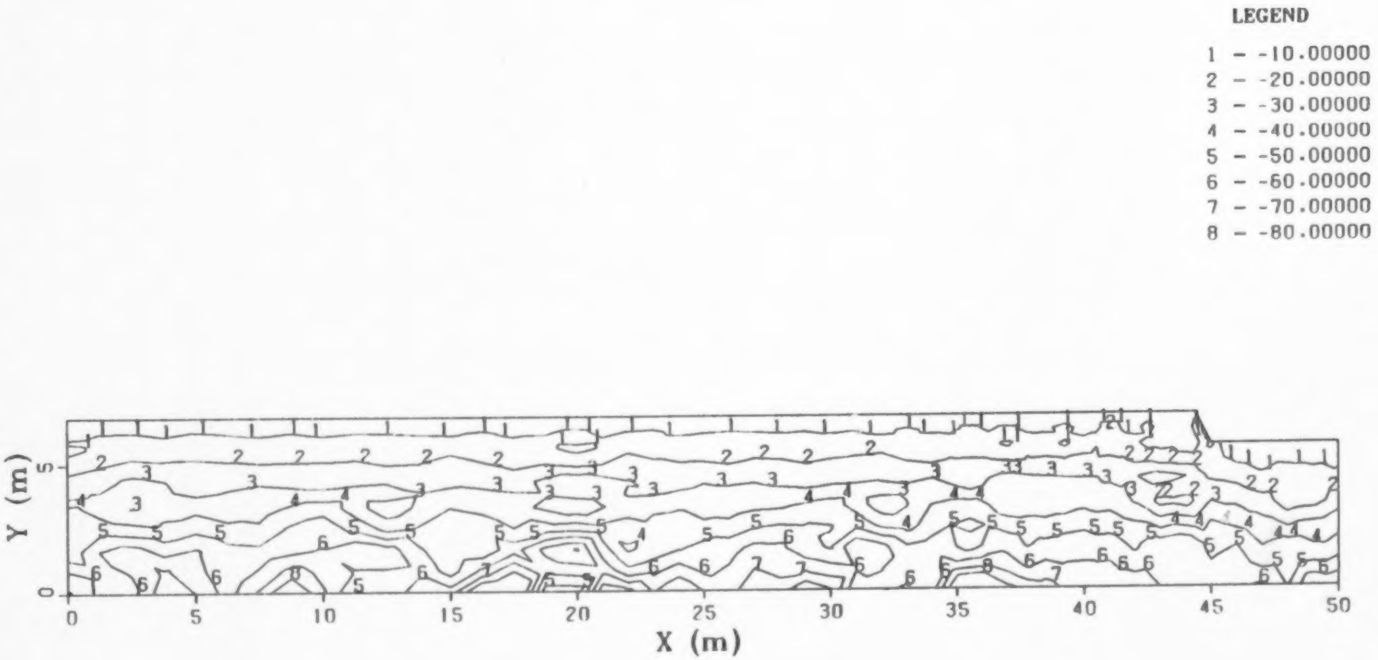

Fig. 8.5.6. **Contours of Effective Stress σ_y After Re-consolidation.**

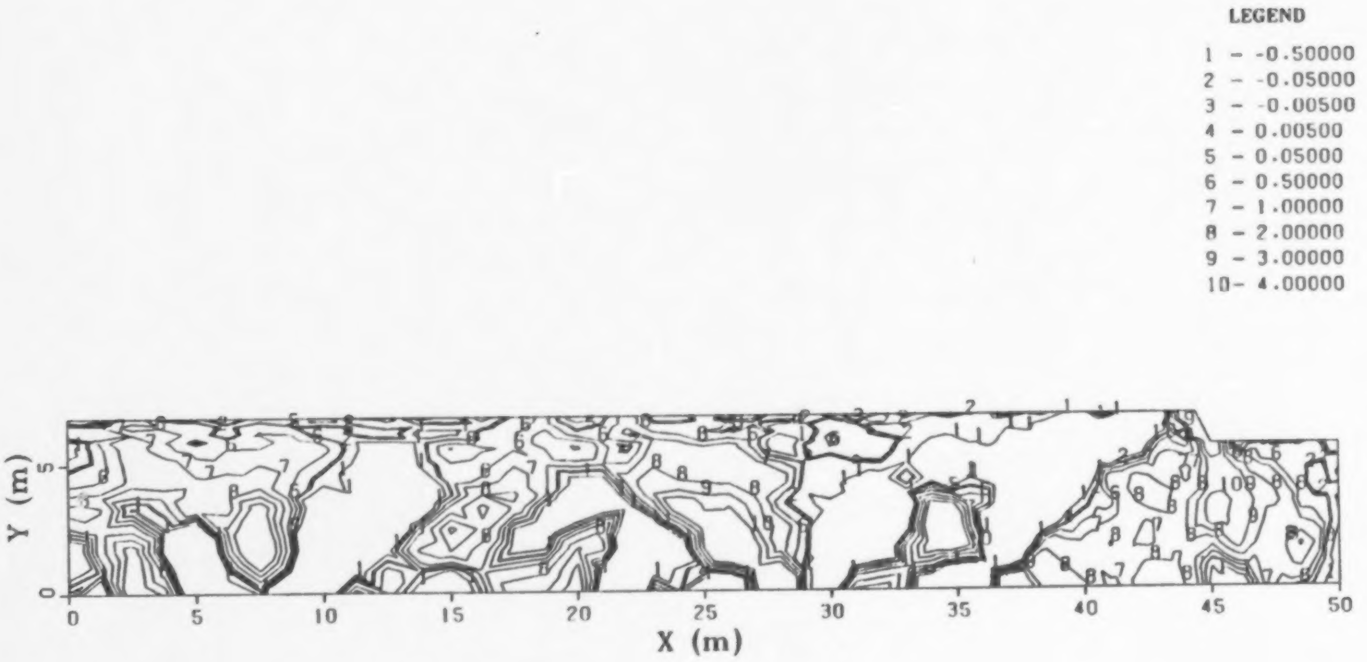

Fig. 8.5.7. Contours of Effective Stress τ_{xy} After Re-consolidation.

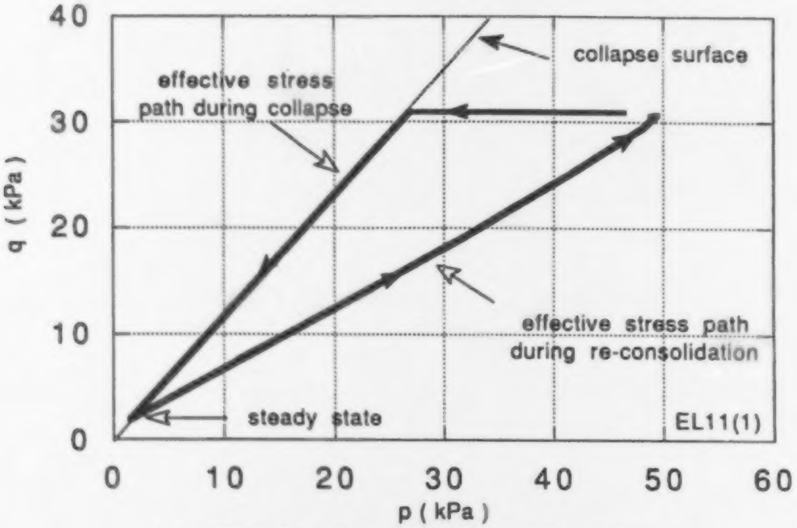

(a) Effective Stress Path For Element 11.

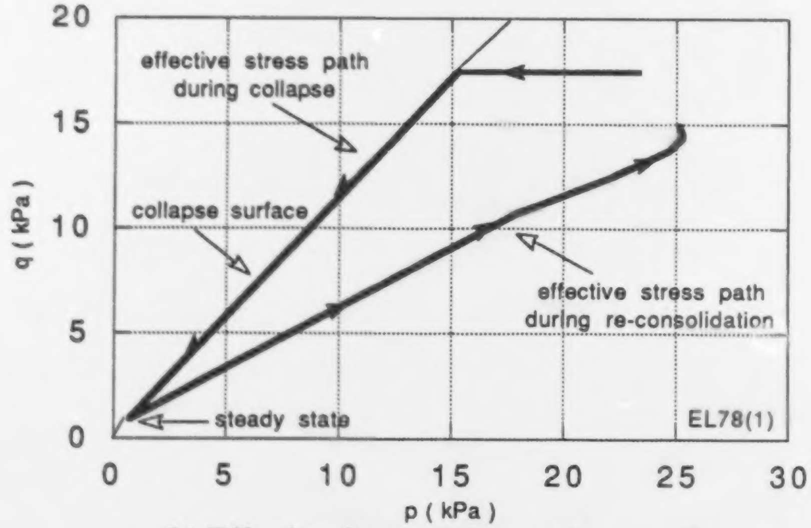

(b) Effective Stress Path For Element 78

Fig. 8.5.8. Effective Stress Paths For Soils in Liquefied Zone.

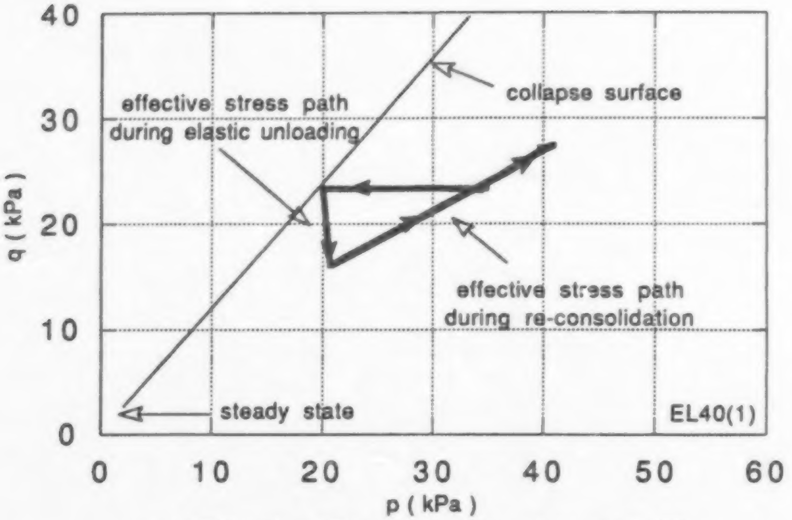

(a) Effective Stress Path For Element 40.

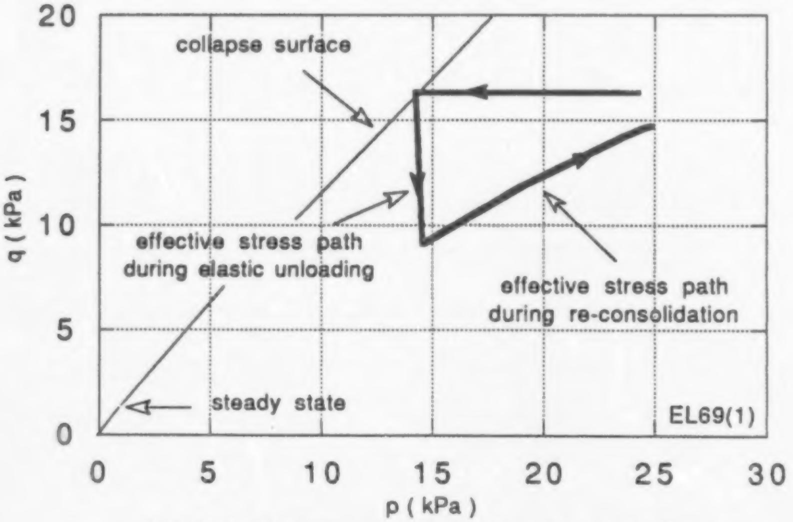

(b) Effective Stress Path For Element 69.

Fig. 8.5.9. Effective Stress Paths For Soils in Lower Pore Pressure Pockets

9. CONCLUSIONS.

9.1. Conclusions.

Liquefaction failure is a very complicated process involving dynamic loading, excess pore water pressure generation, stress re-distribution induced by strain softening of liquefied materials and re-consolidation caused by dissipation or re-distribution of the excess pore water pressures. The interactions among these problems make the process even more complicated. Liquefaction failure has attracted extensive attention since the liquefaction failure of many structures in the Niigata earthquake, 1964, in Japan and the liquefaction failure of the Lower San Fernanado Dam during the 1971 San Fernando earthquake. It is still difficulty to simulate the whole process of liquefaction failure. Most designs about liquefaction remain empirical methods. Deformation analyses by finite element methods is a powerful tool to study the mechanism of liquefaction failure of earth structures.

The behaviour of liquefiable soils has been discussed in more detail in chapter 2. Based on the concepts of the steady state deformation, the collapse surface, the critical state boundary surface model and the hyperbolic strain softening model, a simplified critical state boundary surface model is presented in chapter 3.

The simplifications in the post-earthquake deformation analyses presented in this thesis include the following two aspects:

(1). A simplified calculation scheme was introduced by separating the dynamic response analysis and static analysis. The static analysis includes stress re-distribution analysis and re-consolidation analysis. This simplification is based on the fact that delayed phenomena in liquefaction effects are common.

(2). A simplified critical state boundary surface model is established on an undrained plane. The undrained plane was defined by Roscoe et.al (1958) in the critical state boundary surface theory. The concept of steady state strength defined by Castro and Poulos et.al (1975,1981) and the collapse surface as a liquefaction triggering condition defined by Sladen et.al (1985) were adopted in this model. The hyperbolic strain softening model introduced by Chan and Morgenstern (1986,1989) was used to simulate the liquefaction behaviour of soils during collapse.

The governing equations for stress re-distribution analysis and the unbalanced loads caused by the strain softening behaviour of liquefied materials are presented in chapter 4. Both equilibrium conditions and the compatibilty conditions are satisfied approximately in finite element analysis during the iteration of the unbalanced loads caused by the strain softening of liquefied materials.

An iteration scheme has to be used in this analysis, because of the contracting yield surface to simulate the strain softening behaviour of liquefied materials and the development of excess pore water pressures during the static loadings caused by the stress re-distribution. The possible iteration schemes have been discussed in chapter 4.

The governing equations of Biot's theory for re-consolidation analysis were given in chapter 5. The incremental displacements and pore water pressures were determined by solving the coupled equilibrium equation and flow continuity equation in a finite element method. The elastic models were used in these analyses because most of soils will move away from the critical state boundary surfaces and the stress paths will move on the elastic walls during re-consolidation.

The liquefaction failure of an earth structure can be much more complicated than a slip surface failure of an earth structure. In some cases, it is even impossible to determine a slip surface as the failure of the Lower San Fernando Dam in which a few huge blocks of soils floating on the liquefied materials slide towards the reservoir about 46 meters. Therefore, some new definitions and methods to evaluate safety of dams have been considered in the analyses. The safety evaluation method by interpreting the expansion of contours of yielding ratio and the development of the displacement field was introduced in chapter 6.

The ability to simulate liquefaction failure by finite element methods have been demonstrated by the post-earthquake deformation analyses of the Lower San Fernando Dam in chapter 7 and the post-earthquake deformation analysis of the Wildlife Site in chapter 8.

The analyses in chapter 7 show that the liquefaction failure of the Lower San Fernando Dam can be successfully simulated by the finite element study. In these analyses, the progressive failure of the Lower San Fernando Dam was observed by the expansion of yielding zones and the development of the displacement field. The liquefied zone after stress re-distribution may be much larger than the initial liquefied zone caused directly by earthquake shaking. The commonly observed delayed failure of liquefied earth structures reinforces the conclusion that post-earthquake deformation and associated stress re-distribution are important considerations in liquefaction safety evaluation. The progressive failure and liquefaction instability of the Lower San Fernando dam studied in this analysis reveals that the liquefied zone necessary to trigger failure of an earth structure may be much smaller than previously expected. Progressive failure of liquefaction instability of an earth structure is produced by continual expansion of yielding zones. The continual expansion of yielding zones is dependent on the release in unbalanced load when the material strength drops from its peak to residual. Therefore, the location of the initial liquefied zone is an important factor for liquefaction stability evaluation. Progressive failure is more likely to occur when the initial liquefied zone is located in an area of high driving shear stress. The safety evaluation of an earth structure with liquefiable materials is not a simple limit equilibrium problem. The appropriate resistance depends on both stress path and material properties, in common with other progressive failure problems. The results of these analyses also show that the steady state strength is the most important factor in stability analysis of earth structures. The progressive failure in the Lower San Fernando Dam occurs when the steady state strength for the hydraulic fill is less than the average value based on the laboratory tests given by Seed et.al(1989). Failure would not occur if the steady state strength were larger than or equal to the average value (Su=800psf). This supports the conclusion made by Seed et.al(1989) in their re-evaluation of the Lower San Fernando Dam, which was that the steady state strength obtained in laboratory tests should be interpreted conservatively rather than simply taking an average value. In practice, realistic assessment of liquefaction stability should be sensitive to the actual distribution of the looser zones. This assessment can be accommodated in the type of analysis presented here.

The post-earthquake deformation analyses of the Wildlife Site during 1987 Superstition Hills earthquake in chapter 8 show that the deformation behaviour for liquefaction effects can be also predicted. The results presented a new explanation for the delayed behaviour in the liquefaction effects of the

Wildlife Site during 1987 Superstition Hills earthquake. The agreements on ground surface movements between the in-situ measured values and the analysis results reveal that the large lateral spreading towards the river in the Wildlife Site is mainly due to the stress re-distribution caused by liquefied materials. The steady state strength for liquefied materials is the most important factor effecting the lateral movements on the ground surface. In nature, the collapse of liquefied soil and the re-distribution of stresses within an earth structure will take real time and they can continue to develop after the earthquake shaking is over. Therefore, the delayed behaviour in pore water pressure development may be caused by the collapse of the liquefied materials. The results also show that not all of the liquefiable soils can collapse from their peak strengths to steady state strengths during stress re-distribution even though they have reached the collapse surface. Some of the soils unloaded elastically during stress re-distribution. For liquefiable materials, the pore water pressures will increase during the collapse from their peak strengths to steady state strengths. Lower pore water pressure pockets may form during stress re-distribution because of elastically unloaded soils. Therefore, the delayed behaviour in pore water pressure development may also be due to the re-distribution of excess pore water pressures. Considerable increase of pore water pressures and further liquefaction during re-consolidation, particular for the soils located in those lower pore water pressure pockets in the Wildlife site, has been observed in these analyses. The drainage condition has significant influence on further development of pore water pressures. Further liquefaction during re-consolidation is more likely to occur in the soils under poor drainage conditions.

9.2. Recommendations.

More case histories should be studied by the simplified method presented in this thesis even though the ability of the method has been testified by the post-earthquake deformation analyses for both the Lower San Fernando Dam and the Wildlife Site. Liquefaction failure is a such complicated problem that there is a need for more case histories to get a comprehensive evaluation of the methods and to understand the mechanism. This method can also be recommended to study slope stability problems relating to the pore water pressure generation such as the slope failure caused by change in ground water conditions.

To study the interaction between the dynamic response and the stress re-distributions, the more complicated calculation scheme described in chapter 1 is needed. In this scheme, a time dependent strain softening model for liquefiable materials is the key problem. The real process of stress re-distribution cannot be described by the simplified method presented in this thesis. If one wants to calculate the dynamic response, stress re-distribution and re-consolidation simultaneously, a time dependent general soil model may be needed. This general soil model should be able to present dynamic and also static soil behaviour under either drained or undrained conditions.

Laboratory tests on liquefaction, in particular the soil behaviour on the critical state boundary surfaces including the steady state deformation and the liquefaction triggering conditions, are very interesting and requise further studies.

The agreement between the analytical results and the in situ measured values for the liquefaction behaviours on the Wildlife Site shows that the deformation evaluation for liquefaction problem is not an unreachable goal. But one should also remember that the liquefaction behaviour in the Wildlife Site has its own special characteristics. Liquefaction failure is usually a large strain, large deformation and discontinuity problem. Therefore, the large strain, large deformation and discontinuity finite element methods should be developed to study the deformation behaviour of earth structures during liquefaction failure, particularly, for the cases in which the volume of slide materials rather than the stability is of more concern.

The possibility to capture the incipient failure of slopes by a small strain finite element method has been demonstrated in this thesis by the post-earthquake deformation analyses of the Lower San Fernando Dam. The safety evaluation method based on interpreting the expansion of yielding zones and the development of displacement fields can be very useful in the near future when the application of the finite element method becomes more and more popular. Much more work and studies are needed on this problem to reach the goal of acceptance in engineering practice.

BIBLIOGRAGHY

Ambraseys, N. N. and Sarma, S. K.(1969), "Liquefaction of Soils Induced by Earthquake," Bulletin of The Seismological Society of America, Vol.59, No.2, pp651-664.

Bathe, K.J. (1982), "Finite Element Procedure in Engineering Analysis", New Jerset, Prentice Hall Inc..

Bennett M.J., Mclaughlin P.V., Sarmiento J.S. and Youd T.L.(1984), "Geotechnical Investigation of Liquefaction Sites, Imperial Valley, California", United States Geological Survey, Open-file Report 84-252.

Bjerrum, L. (1967), "Progressive Failure in Slopes of Over-consolidated Plastic Clay and Clay Shales", Journal of the Soil Mechanics and Foundation Division, ASCE, Vol. 93, SM5, pp. 3-49.

Byrne, P. M. (1990), "A Model For Predicting Liquefaction Induced Displacements", Soil Mechanics Series No. 147, Department of Civil Engineering, The University of British Columbia, Canada.

Casagrande, A. (1936), "Characteristics of Cohesionless Soils Affecting The Stability of Slopes and Earth Fills," Journal of the Boston Society of Civil Engineers, reprinted in Contributions to Soil Mechanics, 1925 to 1940, Boston Society of Civil Engineers, 1940, pp257-276.

Casagrande, A.(1971), "On Liquefaction Phenomena," Geotechnique, Vol 21, pp197-202.

Castro, G. (1975), "Liquefaction and Cyclic Mobility of Saturated Sands,"Journal of the Geotechnical Engineering Division, ASCE, Vol.101, No. GT6, pp551-569.

Castro, G (1987), "On the Behavior of Soils During Earthquakes- Liquefaction", Soil Dynamics and Liquefaction, Edited by A.S. Cakmak, Elsevier Computational Mechanics Publications, pp169-204.

Castro, G., Keller, T. O. and Boynton, S. S.(1989), "Re-evaluation of The Lower San Fernando Dam, Report 1, An Investigation of The February 9, 1971 Slide," GEI Consultants Inc., Winchester, Massachusetts 01890-1943, September 1989. Contract Report GL- 89-2, US Army Corps of Engineers, Washington DC.20314-1000.

Chan, D. H. (1986), "Finite Element Analysis of Strain Softening Material," PhD Thesis, University of Alberta,1986.

Chan, D. H.and Morgenstern, N. R.(1989), "Bearing Capacity of Strain Softening Soil," Victor deMello Volume, Edited by J.E.Moreira, Rio de Janeiro, pp59-68.

Dafalias, Y. F. and Herrmann, L. R.(1982), "Bounding Surface Formulation of Soil Plasticity," Soil Mechanics---Transient and Cyclic Loads, Edited by G. N. Pande and O. C. Zienkiewicz, 1982, John Wiley & Sons Ltd., pp253-282.

Desai, C. S. and Li, G. C. (1983), "A Residual Flow Procedure and Application for Free Surface Flow in Porous Media," Advances in Water Resources, Vol.6, pp27-35.

Duncan, J. M. and Chang, C. Y. (1970), "Nonlinear Analysis of Stress and Strain in Soils," Journal of the Soil Mechanics and Foundations Division, ASCE, Vol.96, No. SM5, pp 1629-1653.

Finn, W.D. Liam and Byrne, P.M. (1976), "Liquefaction Potential of Mine Tailing Dams", Proceedings, 12th Int. Conf. on Large Dams, Mexico City, Vol.1, pp153-176.

Finn, W. D. Liam, (1981), "Liquefaction Potential: Developments Since 1976", International Conference on Recent Advances in Geotechnical Earthquake Engineering and Soil Dynamics", April, Rolla, Missouri, Vol.2, pp.655-681.

Finn, W. D. Liam, Yogendrakumar, M., Lo, R. C. and Ledbetter, R. H., (1990), "Seismic Response Analysis of Tailing Dams", International Symposium on Safety and Rehabilitation of Tailings Dams, Sydney, vol.1, pp.7-33.

Hinton, E., Scott, F. C. and Ricketts, R. E., (1975), "Local Least Squares Stress Smoothing for Parabolic Isoparametric Elements", Int. J. Num. Meth. Eng. Vol. 9, pp. 235-256.

Holzer,T.L., Youd,T.L. and Bennett,M.J.(1988), "In Situ Measurement of Pore Pressure Build-up During Liquefaction", 20th Joint Meeting of United States-Japan Panel on Wind and Seismic Effects, Gaithersburg, Maryland.

Holzer, T. L., Youd, T. L. and Hanks, T. C.(1989), "Dynamics of Liquefaction During the 1987 Superstition Hills, California Earthquake, " Science, Vol.244, pp56-59.

Ishihara, K., Tatsuoka, F. and Yasuda, S. (1975), "Undrained Deformation and Liquefaction of Sand Under Cyclic Stress," Soil and Foundations, 15(1), pp29-44.

Ishihara, K. (1984), "Post-earthquake Failure of a Tailings Dam Due toLiquefaction of the Pond Deposit", International Conference on Case Histories In Geotechnical Engineering, May 6-11, 1984, Vol.4, pp1129-1143.

Ishihara, K., Ramon Verdugo and Alexis A. Acacio,(1991) "Characterization of Cyclic Behavior of Sand and Post-seismic Stability Analyses", IX Asian Regional Conference on Soil Mechanics and Foundation Engineering, Bangkok, Thailand, 1991.

Kuwano J., Ishihara, K., Haya, H. and Izu, F. (1991), "Analysis On Fermanent Deformation of Embankments Caused By Earthquakes", Soils and Foundations, Vol. 31, No.3, pp.97-110.

Lee, K. L. and Albaisa, A.(1974) "Earthquake Induced Settlements in Saturated Sands", Journal of the Soil Mechanics and Foundations Division, ASCE, Vol. 100, GT4, April, 1974, pp. 387-406.

Lee, K. L., Seed, H. B. Idriss, I. M. and Makdis, F. I. (1975), "Properties of Soil in The San Fernando Hydraulic Fill Dams, " Journal of the Geotechnical Engineering Division, ASCE, Vol.101, GT8, pp 801-821.

Liu Hushan, and Qiao Taiping (1984),"Pile Foundation under Liquefied Soils", International Conference on Case Histories In Geotechnical Engineering, May 6-11, 1984, Vol.1, pp433-444.

Loudon, P. A., (1967) "Some Deformation Characteristics of Kaolin", PhD Thesis, University of Cambridge, 1967.

Martin, G.R., Finn Liam, W. D. and Seed, H. B. (1975), " Fundamentals of Liquefaction under Cyclic Loading", Journal of the Geotechnical Engineering Division, ASCE, Vol.101, No. GT5, pp. 423-438.

McRoberts, E. D. and Sladen, J. A. (1990), "Observations on Static and Cyclic Sand Liquefaction Methodologies," Prediction and Performance in Geotechnical, 43th Canadian Geotechnical Conference,Quebec, pp215-226.

Mohamad, R. and Dobry, R.(1986), "Undrained Monotonic and Cyclic Triaxial Strength of Sand," Journal of the Geotechnical Engineering Division, ASCE, Vol.112, GT10, pp941-957.

Morgenstern, N. R. and Price, V. E. (1965), " The Analysis of The Stability of General Slip Surface", Geotechnique, Vol.15, No.1, pp. 79-93.

Newmark, N. M. (1965), " Effects of Earthquakes on Dams and Embankments", Geotechnique, Vol.15, pp. 139-159.

Pastor, M. and Zienkiewicz, O. C. (1986), "A Generalized Plasticity, Hierarchical Model for Sand under Monotonic and Cyclic Loading," 2nd Int. Symposium on Numerical Models in Geomechanics, Ghent, M. Jackson & Son(Publishers) Ltd, pp131-150.

Poulos, S. J.(1981), "The Steady State of Deformation," Journal of the Geotechnical Engineering Division, ASCE, Vol.107, No. GT5, May, 1981, pp5513-5562.

Poulos, S. J., Robinsky, E. I. and Keller, T. O. (1985), "Liquefaction Resistance of Thickened Tailings," Journal of Geotechnical Engineering, Vol.111, No. GT12, December, 1985, pp1380-1394.

Prevost, J. H. and Hoeg, K. (1975), "Effective Stress-Strain-Strength Model for Soils," Journal of the Geotechnical Engineering Division, ASCE, Vol.101, GT3, 1975, pp259-278.

Roscoe, K. H., Schofield, A. N. and Wroth, C. P.(1958), "On the Yielding of Sands," Geotechnique, Vol.8, pp22-53.

Sangrey, D.A., Henkel, D.J. and Esrig, M.I. (1969),"The Effective Stress Response of a Saturated Clay Soil to Repeated Loading", Can. Geotechn. J., Vol.6, pp241-252.

Seed, H. B.(1966), "A Method for Earthquake Resistant Design of Earth Dams," Journal of the Soil Mechanics and Foundations Division, ASCE, Vol.92, SM1, pp13-41.

Seed, H.B. and Lee, K.L. (1969), "Porewater Pressures in Earth Slopes Under Seismic Loading Conditions", Proceedings, 4th world Conf. on Earthquake Engineering, Santiago, Session A5.

Seed, H. B., Idriss, I. M., Lee, K. L. and Makdisi, F. I.(1975), "Dynamic Analysis of The Slide in The Lower San Fernando Dam During The Earthquake of February 9,1971," Journal of the Geotechnical Engineering Division, ASCE, Vol.101, GT9, pp889-911.

Seed, H. B.(1979), Nineteenth Rankine Lecture: "Consideration in The Earthquake Resistance Design of Earth and Rockfill Dams", Geotechnique 29, pp215-263.

Seed,H.B.(1987), "Design Problem in Soil Liquefaction", Journal of Geotechnical Engineering, ASCE, Vol.113, GT7, pp827-845.

Seed, H. B., Seed, R. B., Harder, L. F. and Jong H. L. (1989),"Re-evaluation of The Lower San Fernando Dam, Report 2, Examination of The Post-earthquake Slide of February 9,1971." H. B. Seed Inc. 623 Crossridge Terrace Orinda, California 94563, Contract Report GL-89-2, US Army Corps of Engineers, Washington DC.20314-1000.

Sladen, J. A., D'Hollander, R. D. and Krahn, J. (1985), "The Liquefaction of Sands, A Collapse Surface Approach," Canadian Geotechnical Journal, Vol.22, pp564-578.

Terzaghi, K. (1950), " Mechanisms of Landslides", The Geological Survey of America, Engineering Geology (Berkey) Volume.

Vaid, Y. P.and Chern, J. C. (1985), "Cyclic and Monotonic Undrained Response of Saturated Sands," Advances in The Art of Testing Soils Under Cyclic Conditions, ASCE National Convention, Detroit, pp120-147.

Vasquez-Herrera, A. (1988), "The Behaviour of Undrained Contractive Sand and Its Effect On Seismic Liquefaction Flow Failures of Earth Structures", Ph.D Thesis, Rensselaer Polytechnic Institute, 1988.

Vasquez-Herrera, A. and Ricardo Dobry(1989), "Re-evaluation of The Lower San Fernando Dam, Report 3, The Behavior of Undrained Contractive Sand and Its Effects on Seismic Liquefaction Flow Failures of Earth Structures," Department of Civil Engrg, Rensselaer Polytechnic Institute, Troy, New York 12180-3590, Contract Report GL-89-2, US Army Corps of Engineers,Washington DC.20314-1000.

Youd T. L. and Bartlett S. F. (1988),"US Case Histories of Liquefaction-induced Ground Displacement", 1st Japan-United States Workshop on Liquefaction, Large Ground Deformation and Their Effects on Lifeline Facilities, Tokyo, Japan, November 16-19, 1988, pp22-31.

Zienkiewicz, O. C., Xie, Y. M., Schrefler, B. A., Ledesma, A. and Bicanic, N. (1990), "Static and Dynamic Behaviour of Soils: a Rational Approach to Quantitative Solutions. II. Semi-saturated problems", Proc. R. Soc. Lond. A429, pp. 311-321.

APPENDIX A

Finite Element Formulation for Post-earthquake Deformation Analysis

A.1. Formulation For Dynamic Analysis.

The equation of motion in effective stress including Reyleigh damping is:

$$\sigma'_{ij,j} + \delta_{ij}p_{,j} + \rho g_i = \rho\ddot{u}_i + a\rho\dot{u}_i \qquad \text{(A.1-1)}$$

The generalized Hook's law should be modified to account for the stiffness proportional damping effect:

$$\sigma'_{ij} = C_{ijkl}(u_{k,l} + b\dot{u}_{k,l}) \qquad \text{(A.1-2)}$$

where:

σ'_{ij} = effective stresses,

p = pore water pressure,

ρ = bulk unit mass of materials,

g_i= gravity acceleration,

u_i = displacement,

$\dot{u}_i$ = velocity,

$\ddot{u}_i$ = acceleration,

a, b = parameters for Rayleigh damping matrix.

The Rayleigh damping matrix can be expressed:

$$C = aM + bK \qquad \text{(A.1-3)}$$

where: C = viscous damping matrix, M = mass matrix, and K = stiffness matrix.

In case of a nonlinear system, K could respresent an initial tangent stiffness matrix, or C could be modified with each change in stiffness. The parameter a and b can be determined by two given modes. Let ω_r, ϕ_r be the eigenpairs corresponding to:

$$(K - \omega_r^2 M)\,\phi_r = 0 \qquad r=1,2,\ldots,N \qquad \text{(A.1-4)}$$

The orthogonality equations are:

$$\phi_r^T M \phi_s = M_r \delta_{rs} \qquad \text{(A.1-5a)}$$

$$\phi_r^T K \phi_s = \omega_r^2 M_r \delta_{rs} \qquad \text{(A.1-5b)}$$

By (A.1.3), we have:

$$\phi_r^T C \phi_s = (a + b\omega_r^2)\, M_r \delta_{rs} \qquad \text{(A.1-6)}$$

The modal damping factor defined as:

$$\zeta_r = \frac{C_r}{2M_r\omega_r} = \left(\frac{1}{2M_r\omega_r}\right)\phi_r^T C \phi_r \qquad \text{(A.1-7)}$$

i.e.

$$C_r = \phi_r^T C \phi_r = 2M_r\omega_r\zeta_r \qquad (A.1\text{-}8)$$

Therefore, the system damping factor are given by:

$$\zeta_r = \frac{1}{2}\left(\frac{a}{\omega_r} + b\omega_r\right) \qquad (A.1\text{-}9)$$

The Rayleigh damping is easy to define by choosing ζ_r for two modes and solving for a and b.

Assuming an approximate solution:

$$u = \sum_{k=1}^{n} N^k u^k \qquad (A.1\text{-}10a)$$

$$p = \sum_{k=1}^{n} N^k p^k \qquad (A.1\text{-}10b)$$

where: N^k is the isoparametric shape functions, u^k is the displacement at the node k of element and p^k is the pore water pressure at the node k of element.

By Galerkin method, from equation (A.1-1), one has:

$$\int_\Omega N^k(\sigma'_{ij,j} + \delta_{ij}p_{,j} + \rho g_i - \rho\ddot{u}_i - a\rho\dot{u}_i)\,d\Omega = 0 \qquad (A.1\text{-}11)$$

in which:

$$\int_{\Omega} N^k \sigma'_{ij,j} d\Omega = \int_{\Omega} (N^k \sigma'_{ij})_{,j} d\Omega - \int_{\Omega} N^k_{,j} \sigma'_{ij} d\Omega$$

$$= \int_{s} N^k \sigma'_{ij} l_j dS - \int_{\Omega} N^k_{,j} \sigma'_{ij} d\Omega$$

$$= \int_{s} N^k f_i dS - \int_{\Omega} N^k_{,j} \sigma'_{ij} d\Omega \tag{A.1-12}$$

$$\int_{\Omega} N^k (\delta_{ij} p_{,j}) d\Omega = \int_{\Omega} (N^k \delta_{ij} p)_{,j} \, d\Omega - \int_{\Omega} N^k_{,j} \delta_{ij} p \, d\Omega$$

$$= \int_{s} N^k \delta_{ij} p l_j \, dS - \int_{\Omega} N^k_{,j} \delta_{ij} p \, d\Omega$$

$$= \int_{s} N^k p l_i \, dS - \sum_{l=1}^{n} \int_{\Omega} N^k_{,i} N^l p^l \, d\Omega \tag{A.1-13}$$

$$\int_{\Omega} N^k \, \rho \, g \, d\Omega = \rho \, g \int_{\Omega} N^k \, d\Omega \tag{A.1-14}$$

$$\int_{\Omega} N^k \rho \ddot{u}_i \, d\Omega = \sum_{l=1}^{n} \int_{\Omega} N^k \rho N^l \, \ddot{u}_i^l \, d\Omega = \sum_{l=1}^{n} \int_{\Omega} N^k \rho N^l d\Omega \, \ddot{u}_i^l \tag{A.1-15}$$

$$\int_{\Omega} N^k a \rho \dot{u}_i \, d\Omega = a \sum_{l=1}^{n} \int_{\Omega} N^k \rho N^l d\Omega \, \dot{u}_i^l \tag{A.1-16}$$

and by:

$$\sigma' = D(\varepsilon + b\dot{\varepsilon}) = DB(U + b\dot{U}) \qquad \text{(A.1-17)}$$

Then we have:

$$KU + (aM + bK)\dot{U} + M\ddot{U} + QP = F_1 \qquad \text{(A.1-18)}$$

where: K is the stiffness matrix, Q is the connecting matrix, M is the mass matrix , F_1 is a vector of exterior forces, B is the strain matrix, D is the stress strain relationship, P is the vector of nodal pore water pressure and $U, \dot{U}, \ddot{U}$ are vectors of node displacements, velocities and accelerations.

$$K = \int_\Omega B^T \, D \, B \, d\Omega \qquad \text{(A.1-19)}$$

$$M_{kl} = \int_\Omega N^k \, \rho \, N^l \, d\Omega \qquad \text{(A.1-20)}$$

$$Q_{kl} = \int_\Omega N^k_{,i} \, N^l \, d\Omega \qquad \text{(A.1-21)}$$

$$F^k_l = \int_s N^k f_i dS + \int_s N^k p l_i dS + \rho g \int_\Omega N^k d\Omega \qquad \text{(A.1-22)}$$

For fluid flow, under the condition of neglecting the compressibility of solid grain and fluid between the solid skeleton and constant permeability, we have:

$$k(p_{,i})_{,i} - \dot{u}_{i,i} = 0 \qquad \text{(A.1-23)}$$

where: k is permeability.

By Galerkin method:

$$\int_\Omega N^k \left[\, k(p_{,i})_{,i} - \dot{u}_{i,i} \,\right] d\Omega = 0 \qquad \text{(A.1-24)}$$

in which:

$$\int_\Omega N^k k(p_{,i})_{,i}\, d\Omega = \int_\Omega k(N^k p_{,i})_{,i}\, d\Omega - \int_\Omega k N^k_{,i} p_{,i}\, d\Omega$$

$$= \int_s k N^k p_{,i} l_i\, dS - \sum_{l=1}^{n} \int_\Omega k N^k_{,i} N^l_{,i} p^l\, d\Omega \qquad \text{(A.1-25)}$$

$$\int_\Omega N^k \dot{u}_{i,i}\, d\Omega = \int_\Omega (N^k \dot{u}_i)_{,i}\, d\Omega - \int_\Omega N^k_{,i} \dot{u}_i\, d\Omega$$

$$= \int_s N^k \dot{u}_i l_i\, dS - \sum_{l=1}^{n} \int_\Omega N^k_{,i} N^l \dot{u}^l_i\, d\Omega \qquad \text{(A.1-26)}$$

Then, we have:

$$Q^T \dot{U} - HP = F_2 \qquad \text{(A.1-27)}$$

where: H is the permeability matrix and F_2 is a vector of exterior flow quantity.

$$H_{kl} = \int_{\Omega} k \, N^k_{,i} \, N^l_{,i} \, d\Omega \tag{A.1-28}$$

$$F_2^k = \int_s N^k \dot{u}_i l_i \, dS - \int_s N^k q_i l_i \, dS \tag{A.1-29}$$

For time domain solution, we can use Zienkiewicz-Chan method or Wilson-θ method.

In Zienkiewicz-Chan method, let:

$$U = U_n + \dot{U}_n \tau + \alpha \tau^2/2 \tag{A.1-30}$$

and

$$P = P_n + \beta \tau \tag{A.1-31}$$

By weighting residual method, from (A.1-18) and (A.1-27), we have:

$$\int_0^{\Delta t} W(KU + bK\dot{U} + QP + M\ddot{U} + aM\dot{U} - F_1)\, d\tau = 0 \tag{A.1-32}$$

$$\int_0^{\Delta t} W(Q^T\dot{U} - HP - F_2)\, d\tau = 0 \tag{A.1-33}$$

let:

$$\theta_1\Delta t = \frac{\int_0^{\Delta t} W\,\tau\,d\tau}{\int_0^{\Delta t} W\,d\tau} \qquad \text{(A.1-34)}$$

$$\theta_2\Delta t^2/2 = \frac{\int_0^{\Delta t} W\,\tau^2/2\,d\tau}{\int_0^{\Delta t} W\,d\tau} \qquad \text{(A.1-35)}$$

finally, we have:

$$\begin{bmatrix} Ma_1+Ka_2 & Qa_3 \\ Q^Ta_3 & -Ha_3 \end{bmatrix} \begin{bmatrix} \alpha \\ \beta \end{bmatrix} = \begin{bmatrix} \hat{F}_1 \\ \hat{F}_2 \end{bmatrix} \qquad \text{(A.1-36)}$$

where:

$a_1 = 1 + \theta_1\Delta ta$

$a_2 = \theta_2\Delta t^2/2 + b\theta_1\Delta t$

$a_3 = \theta_1\Delta t$

$\hat{F}_1 = F_1 - KU_n - (aM + bK + \theta_1\Delta tK)\dot{U}_n - QP_n$

$\hat{F}_2 = F_2 - Q\dot{U}_n + HP_n$

Solving equation (A.1-36), from equation (A.1-30) and (A.1-31), we can determine the displacement u and pore pressure p.

A.2. The Formulation of K M Q H.

(a) stiffness matrix K

From equation (A.1-19), the element stiffness matrix can be expressed as:

$$K^e = \int_{\Omega e} B^T \, D \, B \, d\Omega \qquad \text{(A.2-1)}$$

in which, the strain matrix B is:

$$B = [\ B_1 \ B_2 \ B_3 \cdots B_n \ ] \qquad \text{(A.2-2)}$$

where: n = nvar x node, and nvar = freedom of each nodal, node = number of nodes on the element.

For two-dimensional problem, we have:

$$B_i = \begin{bmatrix} \frac{\partial N^i}{\partial x} & 0 \\ 0 & \frac{\partial N^i}{\partial y} \\ \frac{\partial N^i}{\partial y} & \frac{\partial N^i}{\partial x} \end{bmatrix} \qquad \text{(A.2-3)}$$

The strain matrix B is derived from the following relationship:

$$\varepsilon = \begin{bmatrix} \varepsilon_x \\ \varepsilon_y \\ \varepsilon_{xy} \end{bmatrix} = \begin{bmatrix} \frac{\partial u}{\partial x} \\ \frac{\partial v}{\partial y} \\ \frac{\partial v}{\partial x} + \frac{\partial u}{\partial y} \end{bmatrix} = \sum_{i=1}^{np} \begin{bmatrix} \frac{\partial N^i}{\partial x} & 0 \\ 0 & \frac{\partial N^i}{\partial y} \\ \frac{\partial N^i}{\partial y} & \frac{\partial N^i}{\partial x} \end{bmatrix} \begin{bmatrix} u^i \\ v^i \end{bmatrix} = BU \tag{A.2-4}$$

where: np = number of nodes on an element.

From the definition of isoparameter shap function, we have:

$$x = \sum_{i=1}^{np} N^i x^i \tag{A.2-5a}$$

$$y = \sum_{i=1}^{np} N^i y^i \tag{A.2-5b}$$

Differentiating N with respect to the isoparameter ξ and η :

$$\frac{\partial N^i}{\partial \xi} = \frac{\partial N^i}{\partial x}\frac{\partial x}{\partial \xi} + \frac{\partial N^i}{\partial y}\frac{\partial y}{\partial \xi} \tag{A.2-6a}$$

$$\frac{\partial N^i}{\partial \eta} = \frac{\partial N^i}{\partial x}\frac{\partial x}{\partial \eta} + \frac{\partial N^i}{\partial y}\frac{\partial y}{\partial \eta} \tag{A.2-6b}$$

The equation can be re-written in matrix form:

$$\begin{bmatrix} \frac{\partial N^i}{\partial \xi} \\ \frac{\partial N^i}{\partial \eta} \end{bmatrix} = \begin{bmatrix} \frac{\partial x}{\partial \xi} & \frac{\partial y}{\partial \xi} \\ \frac{\partial x}{\partial \eta} & \frac{\partial y}{\partial \eta} \end{bmatrix} \begin{bmatrix} \frac{\partial N^i}{\partial x} \\ \frac{\partial N^i}{\partial y} \end{bmatrix} = [\,J\,] \begin{bmatrix} \frac{\partial N^i}{\partial x} \\ \frac{\partial N^i}{\partial y} \end{bmatrix} \tag{A.2-7}$$

where: [J] is the Jacobian matrix.

The inverse of (A.2-7) can be expressed as:

$$\begin{bmatrix} \frac{\partial N^i}{\partial x} \\ \frac{\partial N^i}{\partial y} \end{bmatrix} = [\,J\,]^{-1} \begin{bmatrix} \frac{\partial N^i}{\partial \xi} \\ \frac{\partial N^i}{\partial \eta} \end{bmatrix} = \frac{1}{\det(J)} \begin{bmatrix} \frac{\partial y}{\partial \eta} & -\frac{\partial y}{\partial \xi} \\ -\frac{\partial x}{\partial \eta} & \frac{\partial x}{\partial \xi} \end{bmatrix} \tag{A.2-8}$$

From (A.2-5a) and (A.2-5b), one has:

$$\frac{\partial x}{\partial \xi} = \sum_{i=1}^{np} \frac{\partial N^i}{\partial \xi} x^i \tag{A.2-9a}$$

$$\frac{\partial x}{\partial \eta} = \sum_{i=1}^{np} \frac{\partial N^i}{\partial \eta} x^i \tag{A.2-9b}$$

$$\frac{\partial y}{\partial \xi} = \sum_{i=1}^{np} \frac{\partial N^i}{\partial \xi} y^i \tag{A.2-9c}$$

$$\frac{\partial y}{\partial \eta} = \sum_{i=1}^{np} \frac{\partial N^i}{\partial \eta} y^i \tag{A.2-9d}$$

Then (A.2-8) becomes:

$$\begin{bmatrix} \frac{\partial N^i}{\partial x} \\ \frac{\partial N^i}{\partial y} \end{bmatrix} = \frac{1}{\det(\,J\,)} \begin{bmatrix} \sum_{j=1}^{np} \frac{\partial N^i}{\partial \eta} y^i & -\sum_{j=1}^{np} \frac{\partial N^i}{\partial \xi} y^i \\ -\sum_{j=1}^{np} \frac{\partial N^i}{\partial \eta} x^i & \sum_{j=1}^{np} \frac{\partial N^i}{\partial \xi} x^i \end{bmatrix} \begin{bmatrix} \frac{\partial N^i}{\partial \xi} \\ \frac{\partial N^i}{\partial \eta} \end{bmatrix} = f(\,\xi, \eta\,) \tag{A.2-10}$$

For elastic plane strain idealization, the stress-strain relationship or constitutive is:

$$D = D^e = \frac{E}{(1+\mu)(1-2\mu)} \begin{bmatrix} 1-\mu & \mu & 0 \\ \mu & 1-\mu & 0 \\ 0 & 0 & \frac{1-2\mu}{2} \end{bmatrix} \qquad \text{(A.2-11)}$$

For elastic plane stress idealization, the constitutive is:

$$D = D^e = \frac{E}{1 - \mu^2} \begin{bmatrix} 1 & \mu & 0 \\ \mu & 1 & 0 \\ 0 & 0 & \frac{1-\mu}{2} \end{bmatrix} \qquad \text{(A.2-12)}$$

For elasto-plastic problem, the generalized constitutive is:

$$D = D^{ep} = D^e - \frac{D^e n_g n^T D^e}{H + n_g^T D^e n} \qquad \text{(A.2-13)}$$

in which:

$$n = \frac{\partial F}{\partial \sigma} / \left| \frac{\partial F}{\partial \sigma} \right| \qquad \text{(A.2-14a)}$$

$$n_g = \frac{\partial g}{\partial \sigma} / \left| \frac{\partial g}{\partial \sigma} \right| \qquad \text{(A.2-14b)}$$

where: F is the yield surface, g is the plastic potential surface, and H is the plastic modulus.

The vectors in ξ and η direction can be expressed by the components in x-y coordinate system:

$$\overline{d\xi} = \left[\frac{\partial x}{\partial \xi} d\xi \quad \frac{\partial y}{\partial \xi} d\xi \right] \tag{A.2-15a}$$

$$\overline{d\eta} = \left[\frac{\partial x}{\partial \eta} d\eta \quad \frac{\partial y}{\partial \eta} d\eta \right] \tag{A.2-15b}$$

Therefore, we have:

$$d\Omega = | \overline{d\xi} \times \overline{d\eta} | = \det(\ J\ )\ d\xi\ d\eta \tag{A.2-16}$$

Then, the equation (A.2-1) can be expressed as:

$$K^e = \int_{\Omega e} B^T\ D\ B\ d\Omega = \int_{-1}^{1} \int_{-1}^{1} B^T\ D\ B\ \det(\ J\ )\ d\xi\ d\eta$$

$$= \int_{-1}^{1} \int_{-1}^{1} F(\xi,\eta)\ d\xi\ d\eta \tag{A.2-17}$$

By Gaussian quadrature:

$$K^e = \int_{-1}^{1} \int_{-1}^{1} F(\xi,\eta)\ d\xi\ d\eta = \sum_{i=1}^{ni} \sum_{j=1}^{nj} F(\xi_i,\eta_j) W_i W_j \tag{A.2-18}$$

where: ni, nj = number of integration (quadrature) points,

ξ_i, η_j = ith or jth integration point along ξ or η direction,

W_i, W_j = "weight" of the ith or jth integration point.

Finally, the general stiffness matrix K can be assembled by K^e according to the number of nodes in general element mesh.

(b). mass matrix M

From equation (A.1-20), the element mass matrix can be expressed as:

$$M^e = \left[M^{kl} \right] \qquad \text{(A.2-19)}$$

in which:

$$M^{kl} = \int_{\Omega e} N^k \rho N^l \, d\Omega \qquad \text{(A.2-20)}$$

From (A.1-15), we know the mass matrix is an i x i matrix, where i is motion freedom of nodes, e.g. for two-freedom nodal, we have:

$$M^{kl} = \begin{bmatrix} M_1^{kl} & 0 \\ 0 & M_2^{kl} \end{bmatrix} \qquad \text{(A.2-21)}$$

where:

$$M_1^{kl} = M_2^{kl} = \int_{\Omega e} N^k \rho N^l \, d\Omega \qquad \text{(A.2-22)}$$

By Gaussian quadrature:

$$M_1^{kl} = M_2^{kl} = \sum_{i=1}^{ni} \sum_{j=1}^{nj} N^k(\xi_i,\eta_j)\ \rho\ N^l(\xi_i,\eta_j)\ \det(\ J\ )\ W_i\ W_j \qquad \text{(A.2-23)}$$

The system mass matrix can be assembled by the element mass matrix according to the number of nodes in general element mesh. This matrix is called "consistent mass matrix". In early attempts to deal with dynamic problem, the element mass was usually arbitrarily lumped at nodes, resulting in a diagonal matrix. The lumped mass may lead to a poor approximation.

(c). connecting matrix Q.

From equation (A.1-21), we have the element connecting matrix as:

$$Q^e = [\ Q^{kl}\ ] \qquad \text{(A.2-24)}$$

in which:

$$Q^{kl} = \int_{\Omega_e} N^k_{,i}\ N^l\ d\Omega \qquad \text{(A.2-25)}$$

For two-dimensional prpblem:

$$Q^{kl} = \begin{bmatrix} Q_x^{kl} \\ Q_y^{kl} \end{bmatrix} \qquad \text{(A.2-26)}$$

where:

$$Q_x^{kl} = \int_{\Omega_e} \frac{\partial N^k}{\partial x} N^l \, d\Omega \tag{A.2-27a}$$

$$Q_y^{kl} = \int_{\Omega_e} \frac{\partial N^k}{\partial y} N^l \, d\Omega \tag{A.2-27b}$$

Therefore, $\underline{Q}^e$ is a 2n x n matrix, where n is the number of nodes on an element. By Gaussian method, the equation (A.2-27) can be re-written as:

$$Q_x^{kl} = \sum_{i=1}^{ni} \sum_{j=1}^{nj} \frac{\partial N^k}{\partial x}(\xi_i, \eta_j) \; N^l(\xi_i, \eta_j) \; \det(\, J \,) \; W_i \; W_j \tag{A.2-28a}$$

$$Q_y^{kl} = \sum_{i=1}^{ni} \sum_{j=1}^{nj} \frac{\partial N^k}{\partial y}(\xi_i, \eta_j) \; N^l(\xi_i, \eta_j) \; \det(\, J \,) \; W_i \; W_j \tag{A.2-28b}$$

Finally, the system matrix Q can be assembled by the element connecting matrix by the number of nodes in general element mesh.

(d). permeability matrix H.

From equation (A.1-28), the element permeability matrix can be expressed as:

$$H^e = [\; H^{kl} \;] \tag{A.2-29}$$

and

$$H^{kl} = \int_{\Omega e} k_i \; N^k_{,i} \; N^l_{,i} \; d\Omega \tag{A.2-30}$$

For two-dimensional problem:

$$H^{kl} = \int_{\Omega e} \left(k_x \frac{\partial N^k}{\partial x}\frac{\partial N^l}{\partial x} + k_y \frac{\partial N^k}{\partial y}\frac{\partial N^l}{\partial y} \right) d\Omega \tag{A.2-31}$$

By Gaussian numerical integration method:

$$H^{kl} = \sum_{i=1}^{ni} \sum_{j=1}^{nj} k_x \frac{\partial N^k}{\partial x}\frac{\partial N^l}{\partial x} + k_y \frac{\partial N^k}{\partial y}\frac{\partial N^l}{\partial y} \det(J) \; W_i \; W_j \tag{A.2-32}$$

Then, H can be assembled by the element permeability matrix according to the number of nodes in general element mesh.

A.3. Formulation of Static Analysis.

For static analysis, the equilibrium equation in effective stress form is:

$$\sigma'_{ij,j} + \delta_{ij} p_{,j} + \rho g_i = 0 \tag{A.3-1}$$

and the Hook's law is:

$$\sigma'_{ij} = C_{ijkl}\, u_{k,l} \tag{A.3-2}$$

The flow continuity equation (A.1-23) can be rewritten here:

$$k(p_{,i})_{,i} - \dot{u}_{i,i} = 0 \tag{A.3-3}$$

Therefore, equation (A.1-18) and (A.1-27) become:

$$KU + QP = F_1 \tag{A.3-4a}$$

$$Q^T\dot{U} - HP = F_2 \tag{A.3-4b}$$

where:

$$F_1^k = \int_s N^k f_i dS + \int_s N^k p l_i dS + \rho g \int_\Omega N^k d\Omega \tag{A.3-5a}$$

$$F_2^k = \int_s N^k \dot{u}_i l_i \, dS - \int_s N^k q_i l_i \, dS \tag{A.3-5b}$$

The equation (A.3-4a) and (A.3-4b) can be re-written in incremental form as:

$$K\ \Delta U + Q\ \Delta P = \Delta F_1 \tag{A.3-6a}$$

$$Q^T\ \Delta U - \Delta t\ H\ \Delta P = \Delta t\ H\ P_o + \Delta t\ F_2 \tag{A.3-6b}$$

in which:

$$\Delta F_1^k = \int_s N^k \Delta f_i dS + \int_s N^k \Delta p l_i dS + \Delta\rho g \int_\Omega N^k d\Omega \qquad \text{(A.3-7a)}$$

$$\Delta t F_2^k = \int_s N^k \Delta u_i l_i \, dS - \Delta t \int_s N^k q_i l_i \, dS \qquad \text{(A.3-7b)}$$

where: Δf_i is changes in boundary forces, Δp is changes in boundary pore pressures, $\Delta\rho$ is changes in material densities, Δu_i is changes in displacement boundary conditions and q_i is known flow quality boundary conditions. Known water head boundary condition can be inserted into equation (A.3-6a) and (A.3-6b) directly that resulting in a reduction in matrix size.

For steady state seepage analysis, an uncoupling form between displacements and pore water pressures can be obtained:

$$KU + QP = F_1 \qquad \text{(A.3-8a)}$$

$$HP = -F_2 \qquad \text{(A.3-8b)}$$

These two equation can be solved separately.

APPENDIX B

Finite Element Solution For Unstable Structures

In a limit design problem, one can either change the external load incrementally or adjust the strength incrementally to get a limit equilibrium solution. In the first scheme, the strength of material is usually known and constants. The limit external load is determined by a limit equilibrium condition. In the second scheme, the external load is usually known and the minimum strength is determined by the limit equilibrium condition. Figure B-1 shows the two schemes for a typical soil. For an earth structure, the load transfer or stress re-distribution can be generated by the unbalanced loads caused by changes in either external loads or strengths. Figure B-2 shows schematically the stress re-distributions between two typical soils.

During the stress re-distribution, both the equilibrium and compatible conditions should be always satisfied. Obviously, the incremental finite element method is a capable method to consider this stress re-distribution.

When the unbalanced loads for some material in an earth structure can not be transfered to anywhere else, the un-stable solution occurs. This phenomenon is usually observed when the yield zone expanded and reached at least two free boundaries and hence make part of materials in the earth structure kinematically movable.

Therefore, the un-stable solution or incipient failure can be captured by observing the expansion of yield zone during iteration of unbalanced loads in an incremental finite element analysis.

This analysis should be conducted with caution. In particular, the un-stable solution should be distinguished with the divergent solutions. One method to identify the un-stable solution and the divergent solution is to observe the displacement field or velocity field. For an un-stable solution, the distribution of displacement vectors should be reasonable to reflect the kinematically movement in the earth structure even though they may continue to increase during the iteration of unbalanced loads. Figure B-3 shows an typical solution for an un-stable structure.

For a divergent solution, some displacements may show unreasonable large and direction. Figure B-4 shows a typical divergent solution.

Generally speaking, three kinds of solution can be obtained by a finite element analysis. They are convergent solution for a stable structure, no convergent solution for an un-stable structure and divergent solution. The reasons for a divergent solution can be one in follows:

(1). geometrically error in finite element mesh caused by either a bad element mesh or input some data by mistake.

(2). physically error by input some un-reasonable parameters in material properties.

(3). tension in some elements.

(4). loading step is un-reasonable large.

(5). initial condition is unreasonable defined, particularly between loading and unloading.

(6). unreasonable boundary condition is used.

(7). unreasonable soil model is used.

(8). some mistakes in program codes.

The different behaviors for these three kinds of solution can be observed by plotting the errors of unbalanced load and displacement. Figure B-5 shows the errors of unbalanced load and displacement for a convergent solution in which both errors decrease rapidly after some iteration of unbalanced loads. Figure B-6 shows the errors for an unstable solution in which the error of unbalanced load oscillated around a constant and the error of displacement decrease very slowly after some iteration of unbalanced loads. Figure B-7 shows the errors for a divergent solution in which the error of displacement oscillated in a large magnitude and the error of unbalanced load increase continually.

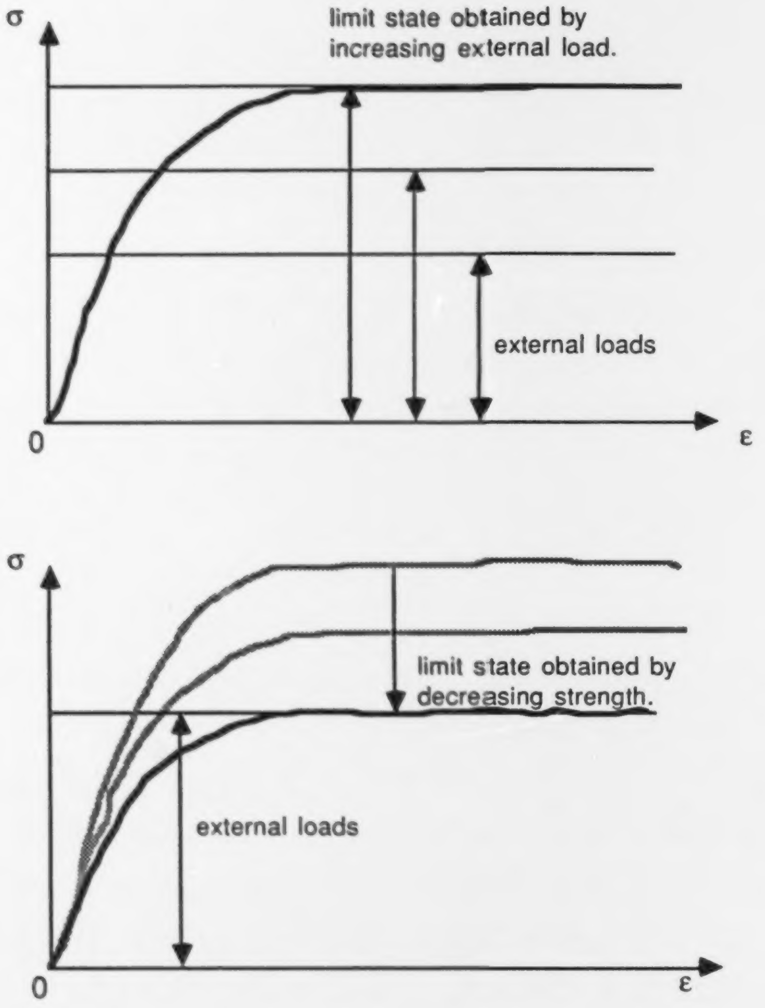
σ
limit state obtained by increasing external load.
external loads
0
ε
σ
limit state obtained by decreasing strength.
external loads
0
ε

Fig. B-1. Two Schemes For Limit Equilibrium Solution.

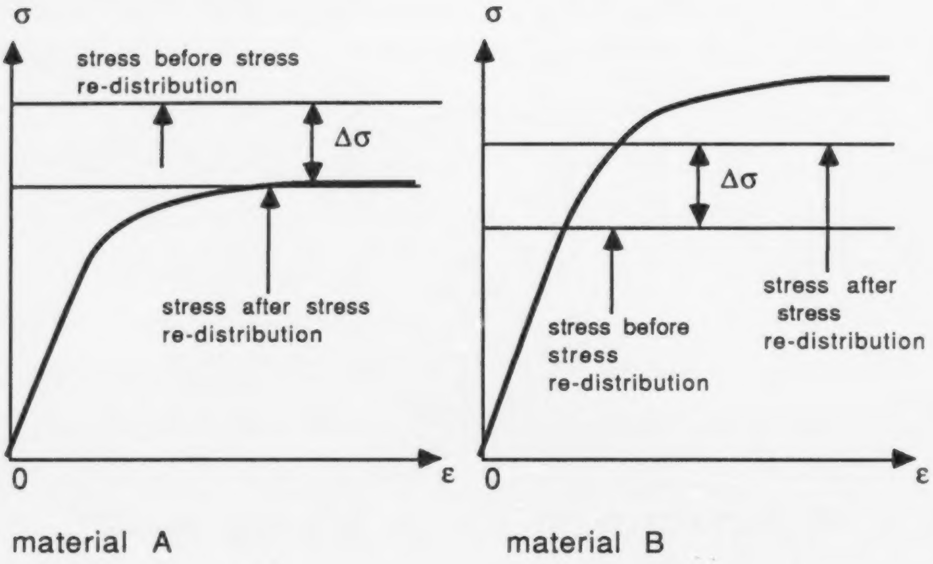
σ
stress before stress re-distribution
Δσ
stress after stress re-distribution
0
ε
material A
σ
Δσ
stress before stress re-distribution
stress after stress re-distribution
0
ε
material B

Fig. B-2. Load Transfer Between Two Materials.

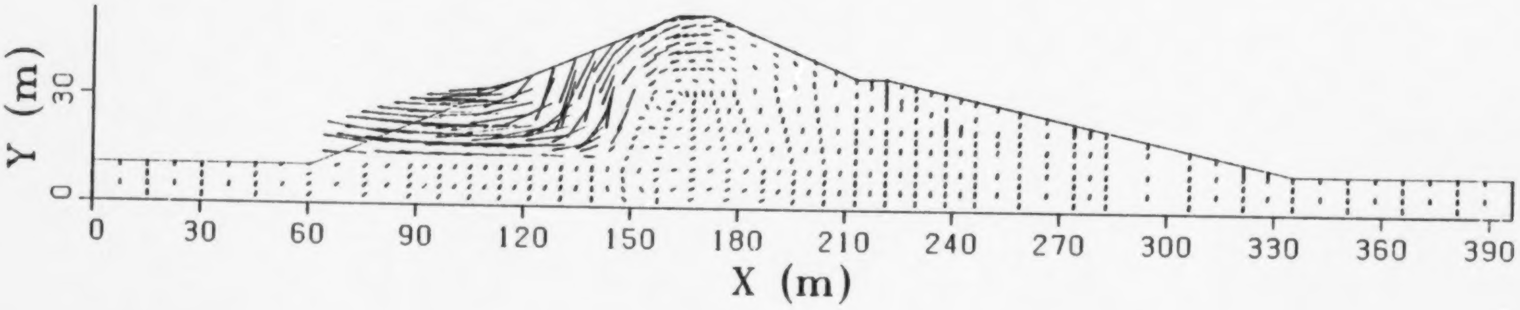

DISPLACEMENT DURING STRESS RE-DISTRIBUTION(it.=100,arrow=10xdispl.)

Fig. B-3. A Typical Finte Element Displacement Solution For an Un-stable Structure.

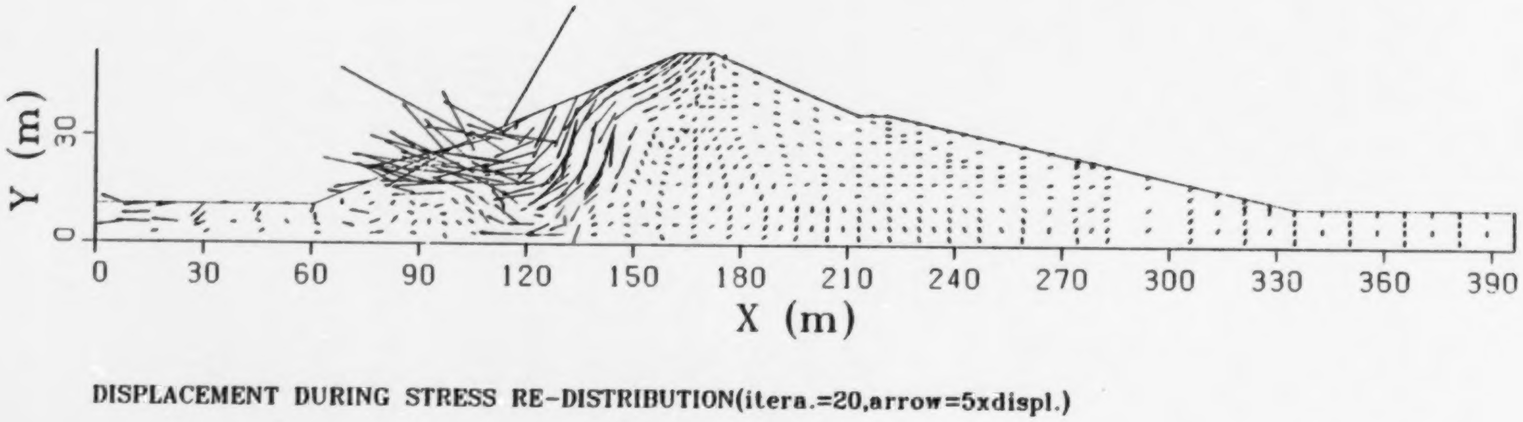

Fig. B-4. A Typical Diaplacement Distribution For a Divergent Result.

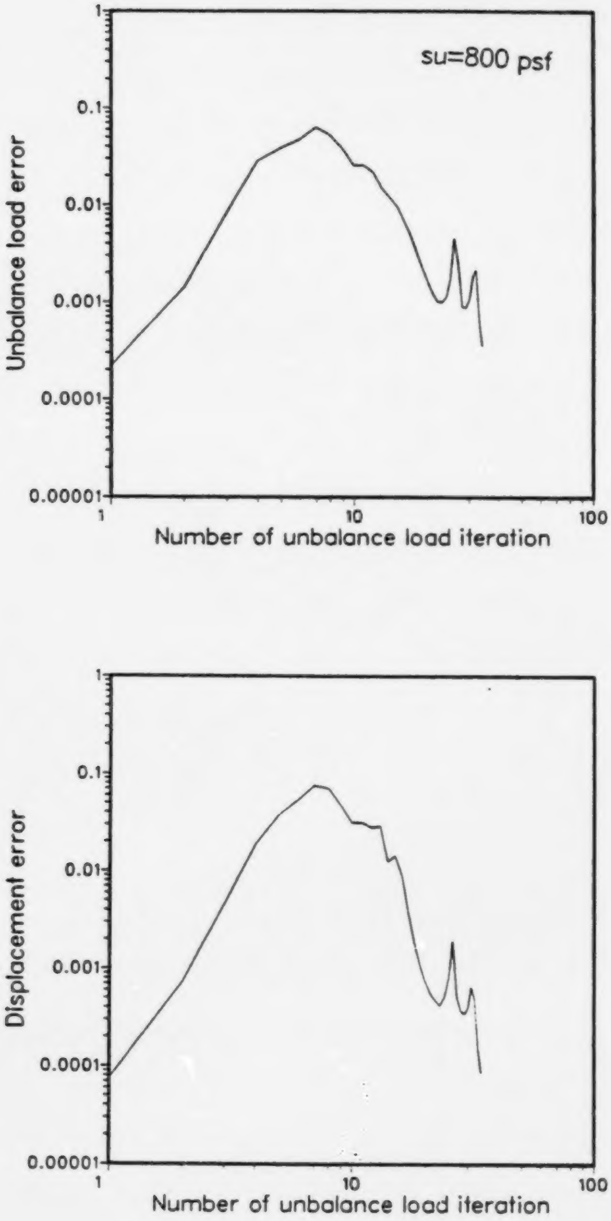

Fig. B-5. Errors During Iteration of Unbalanced Loads For A Convergent Solution.

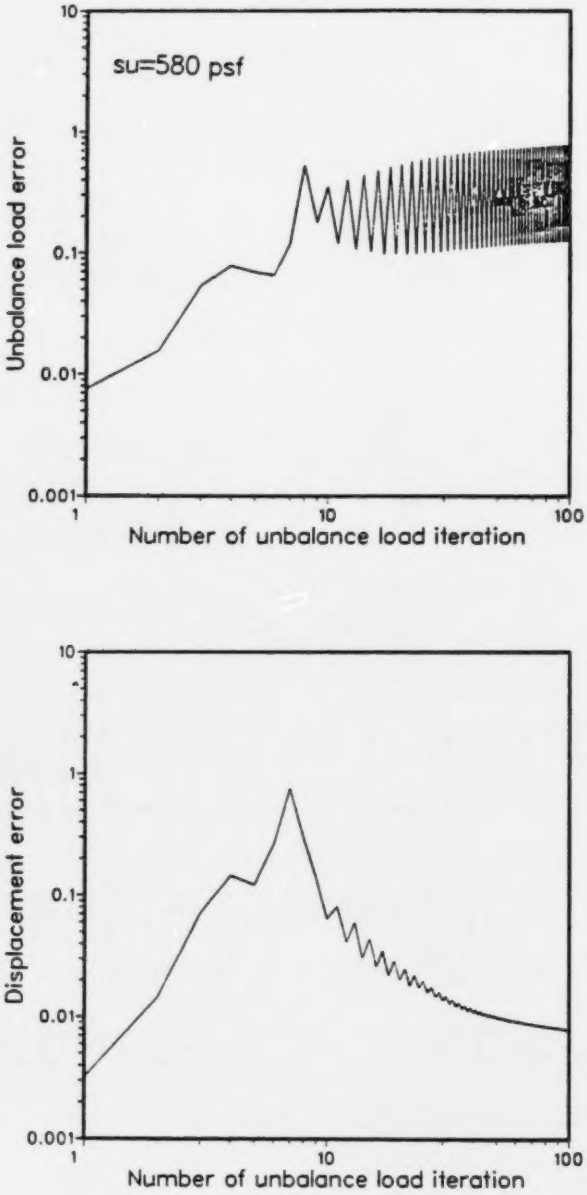

Fig. B-6. Errors During Iteration of Unbalanced Loads For an Un-stable Solution.

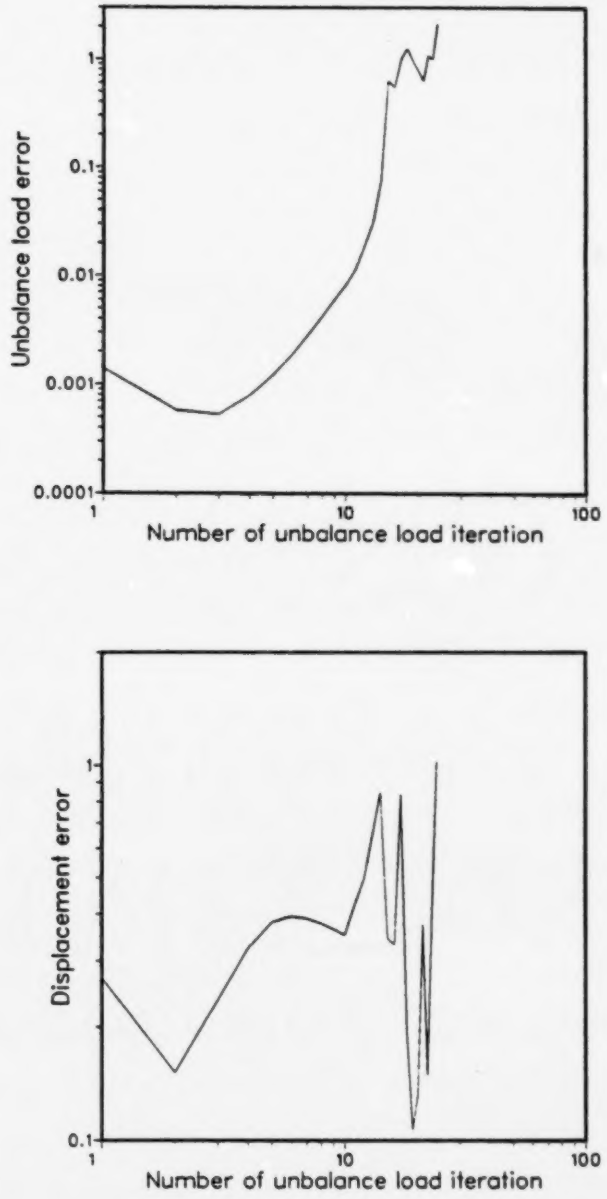

Fig. B-7. Errors During Iteration of Unbalanced Loads For a Divergent Solution.

APPENDIX C

Simplified Analysis Scheme

During an earthquake shaking, soil skeleton or grain structure can be fully or partly collapsed. The collapse will weaken the stiffness of the soil skeleton, then , part of load previously carried by the skeleton will be transfered to pore water, hence causing the excess pore water pressure. The excess pore water pressure will dissipate soon or later depended on the drainage boundary conditions. The material may be softening due to both dynamic loading and excess pore water pressure development. The stress re-distribution will occur due to changes in both material properties and pore water pressure. The stresses re-distribution and the pore water pressure generation and re-distribution will back influence the dynamic behavior of soils and hence the dynamic response of earth structures. It is an interaction problem between dynamic response and static behavior of earth structure. Obviously, this analysis is complicated and expensive. Figure C.1 shows the outline of the analysis. In this analysis, the dynamic response of earth structure, the excess pore water pressure generation during the dynamic loading, the stress re-distribution caused by strain softening and the excess pore water pressure and the re-consolidation caused by dissipation of the excess pore water pressure are considered to occur simultaneously and last to different periods. An iteration scheme or an incremental step scheme should be used in this analysis, because the dynamic properties of materials, hence the dynamic response of earth structure is usually related to the static effective stress state, yet the static stress state is also related to the dynamic response of earth structure and the re-consolidation caused by dissipation of the excess pore water pressures. Figure C.1 illustrates the interaction among the three parts of analyses.

To consider that the period of an earthquake is relative short comparing with the period of pore water pressure dissipation, and the delayed failure are common in liquefaction effects, the outline of analysis can be simplified. Fig. C.2 shows a simplified analysis scheme. In this scheme, the analysis consists of three parts. In the first part, i.e. the dynamic analysis, we neglected the dissipation of excess pore water pressures during the earthquake. The fully undrained condition is assumed during earthquake shaking. After the earthquake shaking, we allow the water to dissipate. The deformation caused by re-consolidation may develop. In the second part of analyses, i.e. static analysis, the stress re-distributions caused by liquefied materials is considered. In natural, the stress re-distribution and earthquake shaking may occur simultaneously and last to different periods. The separation between dynamic analysis and static analysis will make things on safe side, because the strain softening in stress re-distribution analysis will eases the earthquake shaking in either the liquefied zone or the zone above the liquefied area. In third part, the re-consolidation during dissipation of excess pore water pressures is considered. This is a relative long period comparing with either earthquake shaking or stress re-distributions. Further liquefaction may occurs during dissipation of excess pore water pressures even though most of soils are going to new stable states during re-consolidation. The stress re-distribution analysis may need to repeat if further liquefaction occurs during re-consolidation analysis.

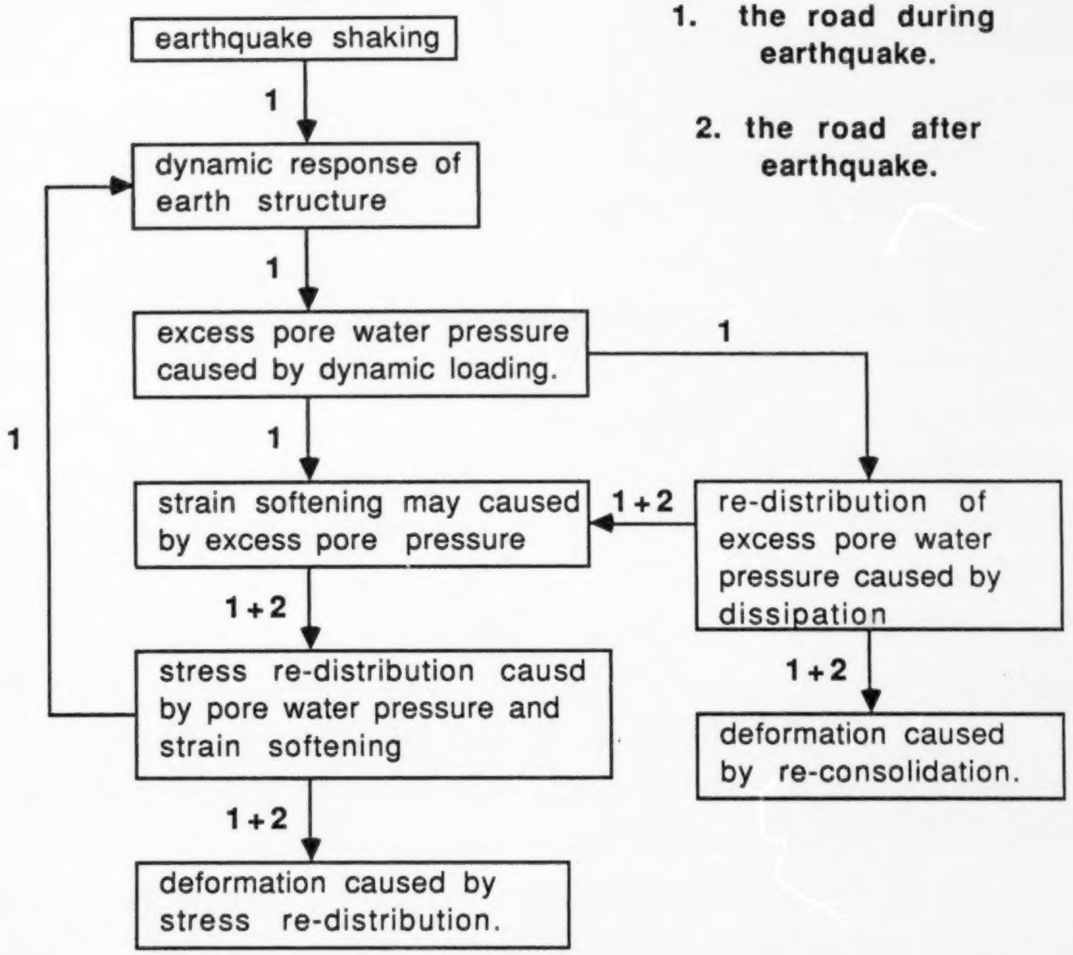
1. the road during earthquake.
2. the road after earthquake.
earthquake shaking
1
dynamic response of earth structure
1
excess pore water pressure caused by dynamic loading.
1
1
1
strain softening may caused by excess pore pressure
1+2
re-distribution of excess pore water pressure caused by dissipation
1+2
stress re-distribution causd by pore water pressure and strain softening
1+2
deformation caused by re-consolidation.
1+2
deformation caused by stress re-distribution.

Fig. C.1 Outline of Liquefaction Failure Analysis.

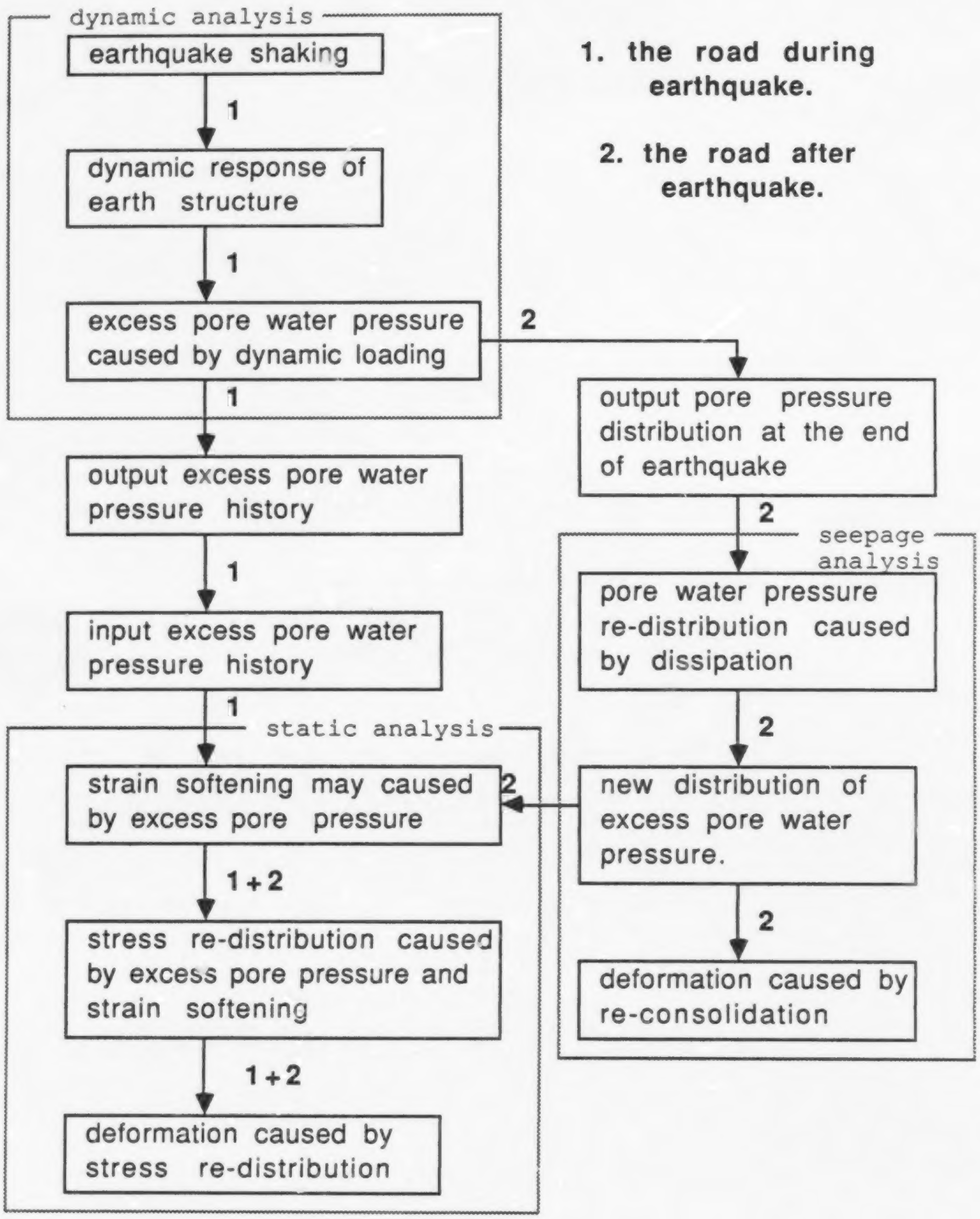
dynamic analysis
earthquake shaking
1
dynamic response of earth structure
1
excess pore water pressure caused by dynamic loading
1
output excess pore water pressure history
1
input excess pore water pressure history
1
static analysis
strain softening may caused by excess pore pressure
1+2
stress re-distribution caused by excess pore pressure and strain softening
1+2
deformation caused by stress re-distribution
1. the road during earthquake.
2. the road after earthquake.
2
output pore pressure distribution at the end of earthquake
2
seepage analysis
pore water pressure re-distribution caused by dissipation
2
new distribution of excess pore water pressure.
2
deformation caused by re-consolidation
2

Fig. C.2. Simplified Analysis Scheme.